

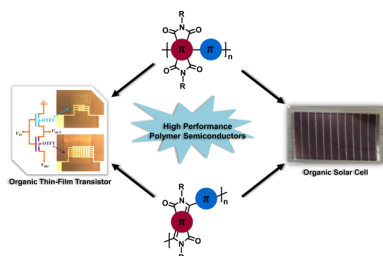
## Imide- and Amide-Functionalized Polymer Semiconductors

Xugang Guo,\*<sup>†</sup> Antonio Facchetti,\*<sup>‡,§</sup> and Tobin J. Marks\*<sup>‡</sup>

<sup>†</sup>Department of Materials Science and Engineering, South University of Science and Technology of China, No. 1088, Xueyuan Road, Shenzhen, Guangdong 518055, China

<sup>‡</sup>Department of Chemistry and the Materials Research Center, Northwestern University, 2145 Sheridan Road, Evanston, Illinois 60208, United States

<sup>§</sup>Polyera Corporation, 8045 Lamon Avenue, Skokie, Illinois 60077, United States



### CONTENTS

1. Introduction
  - 1.1. Prologue
  - 1.2. Organic Thin-Film Transistors
    - 1.2.1. OTFT Structure, Operation, and Characterization
    - 1.2.2. Semiconductor Design Rules for High-Performance OTFTs
  - 1.3. Organic Solar Cells
    - 1.3.1. OSC Structure, Operation, and Characterization
    - 1.3.2. Semiconductor Design Rules for High-Performance OSCs
  - 1.4. Why Imide/Amide-Functionalized Polymers Are of Interest
    - 1.4.1. Imide-Functionalized Small Molecules: High-Performance n-Channel Organic Semiconductors
    - 1.4.2. Imide/Amide-Functionalized Polymer Semiconductors: Attractions
2. Perylene Diimide-Based Polymer Semiconductors
  - 2.1. Synthesis of Dibrominated Perylene Diimide
  - 2.2. Perylene Diimide-Based Polymer Semiconductors for OTFTs
  - 2.3. Perylene Diimide-Based Polymer Semiconductors for OSCs
  - 2.4. Dithienocoronene Diimide-Based Polymer Semiconductors for OTFTs and OSCs
  - 2.5. Perylene Diimide-Based Nonconjugated Polymers for OTFTs and OSCs
  - 2.6. Summary
3. Naphthalene Diimide-Based Polymer Semiconductors
  - 3.1. Synthesis of Dibrominated Naphthalene Diimide
  - 3.2. Naphthalene Diimide-Based Polymer Semiconductors for OTFTs

B	3.3. Naphthalene Diimide-Based Polymers for OSCs	X
B	3.4. Naphthalene Diimide Isomers and Derivatives-Based Polymer Semiconductors for OTFTs and OSCs	Y
E	3.5. Summary	Z
D	4. Pyromellitic Diimide-Based Polymer Semiconductors	AA
E	4.1. Synthesis of Dibrominated Pyromellitic Diimide	AA
E	4.2. Pyromellitic Diimide-Based Polymer Semiconductors for OTFTs	AA
H	4.3. Summary	AB
I	5. Phthalimide-Based Polymer Semiconductors	AB
I	5.1. Synthesis of Dibrominated Phthalimide	AB
J	5.2. Phthalimide-Based Polymer Semiconductors for OTFTs	AB
J	5.3. Phthalimide-Based Polymer Semiconductors for OSCs	AD
L	5.4. Summary	AD
N	6. Thieno[3,4- <i>c</i> ]pyrrole-4,6-dione-Based Polymer Semiconductors	AD
R	6.1. Synthesis of Dibrominated Thieno[3,4- <i>c</i> ]pyrrole-4,6-dione and Its Dimer	AE
S	6.2. Thieno[3,4- <i>c</i> ]pyrrole-4,6-dione-Based Polymer Semiconductors for OTFTs	AF
S	6.3. Thieno[3,4- <i>c</i> ]pyrrole-4,6-dione-Based Polymer Semiconductors for OSCs	AH
T	6.4. Summary	AM
T	7. Bithiophene Imide-Based Polymer Semiconductors	AM
T	7.1. Synthesis of Dibrominated Bithiophene Imide	AM
L	7.2. Bithiophene Imide-Based Polymer Semiconductors for OTFTs and OSCs	AN
Q	7.3. Summary	AP
R	8. Thienoisooindoledione-Based Polymer Semiconductors	AP
S	8.1. Synthesis of Dibrominated Thienoisooindoledione	AP
S	8.2. Thienoisooindoledione-Based Polymer Semiconductors for OSCs	AQ
T	8.3. Summary	AQ

Received: April 23, 2014

9. Diketopyrrolopyrrole-Based Polymer Semiconductors	AQ
9.1. Synthesis of Dibrominated Diketopyrrolopyrrole	AR
9.2. Diketopyrrolopyrrole-Based Polymer Semiconductors for OTFTs	AR
9.3. Diketopyrrolopyrrole-Based Polymer Semiconductors for OSCs	AZ
9.4. Summary	BD
10. Isoindigo-Based Polymer Semiconductors	BE
10.1. Synthesis of Dibrominated Isoindigo	BE
10.2. Isoindigo-Based Polymer Semiconductors for OTFTs	BE
10.3. Isoindigo-Based Polymer Semiconductors for OSCs	BE
10.4. Isoindigo Derivatives-Based Polymer Semiconductors for OTFTs and OSCs	BF
10.5. Summary	BJ
11. Benzodipyrrolidone-Based Polymer Semiconductors	BK
11.1. Synthesis of Dibrominated Benzodipyrrolidone	BL
11.2. Benzodipyrrolidone-Based Polymer Semiconductors for OTFTs and OSCs	BL
11.3. Summary	BN
12. Other Imide/Amide-Functionalized Polymer Semiconductors	BN
13. Conclusions and Outlook	BN
Author Information	BR
Corresponding Authors	BS
Notes	BS
Biographies	BS
Acknowledgments	BT
References	BT

## 1. INTRODUCTION

### 1.1. Prologue

Organic molecular and polymeric semiconductors are attractive for fabrication of cost-effective, large-area, and mechanically flexible electronic devices via solution-based high-throughput patterning techniques such as slot-dye coating or printing.<sup>1,2</sup> Furthermore, the low-temperature processing enables device integration with flexible substrates,<sup>3–5</sup> such as fabrics or plastics, without compromising substrate functionalities.<sup>3,6</sup> In contrast to inorganic semiconductors, where the atoms are held together by strong covalent or ionic bonds,<sup>7</sup> organic semiconductors consist of discrete (macro)molecules, which are weakly organized via supramolecular van der Waals, dipole–dipole,  $\pi$ – $\pi$ , and hydrogen-bond interactions.<sup>8</sup> The energies of covalent or ionic bonds in inorganic materials are usually 1–3 orders of magnitude greater than those of supramolecular interactions in organic  $\pi$ -conjugated systems, resulting in distinctive differences in terms of materials processability and the corresponding optoelectronic device performance. The strong ionic or covalent bonds in inorganic semiconductors lead to formation of crystalline three-dimensional structures characterized by substantial orbital overlap. Hence, efficient charge transport can occur through highly delocalized bands. However, such structural motifs typically sacrifice materials processability from solution. Thus, inorganic semiconductors are usually deposited or patterned via energy-intensive and expensive methods including various high-

temperature, high-vacuum processes involving postdeposition lithographic steps for patterning.

Compared to inorganic semiconductors, organic semiconductors are low-dimensional materials in which the weaker supramolecular interactions between discrete (macro)molecules typically result in morphologically disordered films with limited intermolecular  $\pi$ -orbital overlap, hence lower charge carrier mobility.<sup>8,9</sup> Charge transport in less ordered organics follows a two-step process: first, intramolecular transport along single  $\pi$ -conjugated backbones; second, intermolecular hopping between discrete  $\pi$ -conjugated molecules.<sup>10</sup> The weak intermolecular interactions in organics lead to low charge carrier mobility. However, when considerable order is achieved such as in single crystals, organic semiconductors can exhibit transport through highly delocalized bands and far larger mobilities.<sup>11–13</sup> Despite transport limitations, organic semiconductors can be much easier to process from solution. Hence, electronic devices based on organic semiconductors are not aiming to replace inorganic electronic devices but to enable electronic device fabrication at lower costs and/or achieve completely new device functions such as large-area coverage, lightweight, mechanical flexibility, and integration with plastic foils.<sup>2,14,15</sup>

To date the applications of organic semiconductors include, but are not limited to, organic light-emitting diodes (OLEDs),<sup>16</sup> organic thin-film transistors (OTFTs),<sup>17</sup> organic solar cells (OSCs),<sup>18</sup> organic electrochromic devices (OECDs),<sup>19</sup> and sensors.<sup>20</sup> During the past two decades, organic optoelectronic device performance has advanced dramatically. Such progress is the result of interdisciplinary research efforts from organic synthetic chemists to device engineers. In fact, the device performance is not only determined by the semiconductors but also closely related to materials combinations and integration, multilayer film morphologies and microstructures,<sup>21</sup> as well as device structures.<sup>8,22</sup>

In this review, we focus on the applications of organic semiconductors in two of the most active fields of organic optoelectronics: organic thin-film transistors (OTFTs) and organic solar cells (OSCs). Specifically, we will discuss polymer semiconductors having a common structural component, the imide or amide functional group, connected to  $\pi$ -conjugated cores. Before entering into the detailed discussion of polymer synthesis, materials structure–property relationships, and device performance, an introduction to OTFTs and OSCs is given in the following sections with the basic concepts of OTFTs/OSCs and materials design principles.

### 1.2. Organic Thin-Film Transistors

**1.2.1. OTFT Structure, Operation, and Characterization.** The transistor is the fundamental building block of modern electronic devices and used to amplify and switch electronic signals.<sup>23</sup> The first transistor was invented by John Bardeen, Walter Brattain, and William Shockley at Bell Laboratories in 1947, and it has revolutionized the electronics industry in the 20th century. OTFTs are metal–insulator–semiconductor (MIS) field-effect transistors (FETs) in which the semiconductor is a  $\pi$ -conjugated organic material, a device architecture typically utilized for amorphous silicon FETs. A typical OTFT is composed of three main materials components (Figure 1a): (a) a conductor functioning as the gate, source, and drain electrodes; (b) a dielectric layer insulating the gate electrode; and (c) an organic semiconductor acting as the variable conductance element.

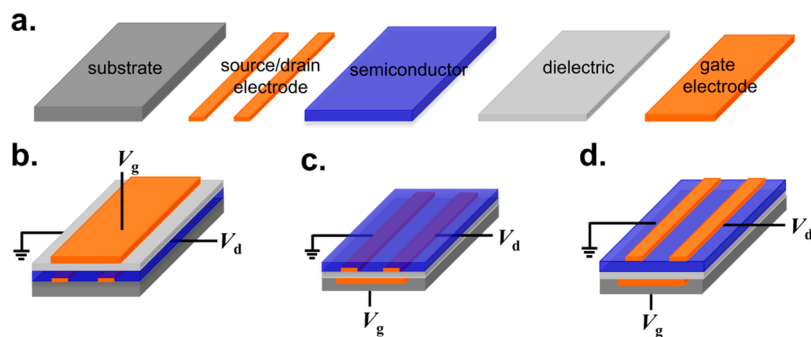


**Figure 1.** Device components and structures of organic thin-film transistors (OTFTs): (a) components of OTFTs, (b) top-gate/bottom-contact (TGBC) structure, (c) bottom-gate/bottom-contact (BGBC) structure, and (d) bottom-gate/top-contact (BGTC) structure.

Transistors can be constructed with a top-gate or bottom-gate architecture.<sup>24</sup> In the top-gate architecture (Figure 1b), source and drain electrodes are deposited on top of substrate, followed by deposition of the organic semiconductor, dielectric, and finally gate electrode. In such architectures, the semiconducting channel is enclosed between the dielectric and the substrate. In the bottom-gate architecture, the gate electrode lies directly on the substrate and highly doped silicon wafers are commonly used as both substrate and gate electrodes. Thermally grown  $\text{SiO}_2$  or other insulating layers serve as dielectrics and are situated on top of the gate. Two different structures can be further constructed from the bottom-gate architecture: bottom-contact and top-contact. In the bottom-gate/bottom-contact (BGBC) structure (Figure 1c), source and drain electrodes are located directly on top of the dielectric, followed by deposition of the semiconductor. In the bottom-gate/top-contact (BGTC) structure (Figure 1d), the semiconductor is deposited directly on the dielectric. Finally, the source and drain are patterned onto the organic semiconductor for device completion.

Each structure has its own advantages and disadvantages in regard to device fabrication and performance. The top-gate structure is particularly suitable for printed transistors in which every component can be deposited sequentially using printing. Conducting polymers such as doped polyaniline, poly(3,4-ethylenedioxythiophene):poly(styrene sulfonic acid) (aka PEDOT:PSS),<sup>25</sup> or metal nanoparticles<sup>26</sup> can be employed as electrodes. Insulating polymers, such as polyimides, poly(methyl methacrylate), or polystyrene can serve as dielectrics. Because the conduction channel is enclosed in top-gate structures, device environmental stability is improved due to device self-encapsulation. In the BGTC structure, organic films are deposited directly on a uniform dielectric and then source and drain electrodes are deposited on top of the semiconductor by thermal evaporation through a shadow mask. Contact resistance is minimized, and charge carrier mobility tends to be higher because of the intimate contact between semiconductor and source/drain electrodes. However, the BGTC structure has its own disadvantages. The vapor-phase evaporation of the metal electrodes can damage the organic layer, and the structure is not easily amenable to low-cost, large-scale, and high-throughput fabrication.<sup>27</sup> For BGBC OTFTs, the source and drain are prepatterned on top of the dielectric before semiconductor deposition. Due to the high contact resistance and irregular dielectric surface, charge carrier mobility tends to be lower than that in BGTC OTFTs.<sup>27</sup> However, the BGBC structure is readily integratable into low-cost and large-scale manufacturing processes, and smaller device features can be achieved through photolithographic technologies if necessary.

OTFT operation is depicted in Figure 2. The source electrode is grounded, and all other voltages (biases) are relative to this electrode. The OTFT operation relies on the charge carrier accumulation in the semiconductor enabled by applying a bias on gate. If the semiconductor is sufficiently pure and no gate voltage ( $V_g = 0 \text{ V}$ ) is applied there should be no free charge carriers in the conducting channel and the source–drain current should be near zero (“off” state) when a voltage is applied between the source and the drain. If a negative gate voltage ( $V_g < 0 \text{ V}$ ) is applied, positive charges (p-channel) will be created in close vicinity of the semiconductor/dielectric interface and the source–drain current ( $I_{ds}$ ) will dramatically increase (“on” state) as a consequence when a voltage ( $V_d$ ) is applied between them. If a positive gate voltage ( $V_g > 0 \text{ V}$ ) is applied, negative charges (n-channel) will accumulate at the semiconductor/dielectric interface. The  $I_{ds}$  in the conducting channel is manipulated by the gate voltage. Charge carrier polarity in the conducting channel determines whether the semiconductor is p-type, n-type, or ambipolar (functioning as both a p- and a n-type). After charge carriers accumulate, a commonly accepted transport model in less ordered organic semiconductors involves intramolecular charge migration within single molecules and intermolecular hopping between adjacent molecules.<sup>24</sup> Intermolecular hopping is the critical factor usually limiting OTFT mobilities, which relies on supramolecular self-assembly in the film state.<sup>8</sup>

Three critical OTFT performance parameters are charge carrier mobility ( $\mu$ ), current modulation ratio ( $I_{on}/I_{off}$ ), and threshold voltage ( $V_t$ ).<sup>28</sup>  $\mu$  describes how fast charge carriers drift in the active layer per unit electric field, which in turn determines the voltage to be applied and device power consumption.  $I_{on}/I_{off}$  is defined as the ratio of the source–drain current when the gate bias is maximal (“on” state) and there is no gate bias (“off” state).  $I_{on}/I_{off}$  is an indicator of material purity and its susceptibility to doping by its surroundings.  $V_t$  characterizes the critical voltage at which the field effect is operative. It can also serve as a measurement of the number of charge carrier traps at the semiconductor/dielectric interface. These traps must be filled before charge carriers can flow between the source and the drain;<sup>29</sup> therefore, high materials purity is a necessity for OTFT applications.

A BGTC OTFT structure with the reported key geometrical parameters is illustrated in Figure 3. The performance parameters can be derived from the OTFT output and transfer characteristics (Figure 4). In the output characteristics, two operation regions can be differentiated: a linear region at low drain voltage and a saturation region at high drain voltage. Charge carrier mobility ( $\mu$ ) and threshold voltage ( $V_t$ ) in the

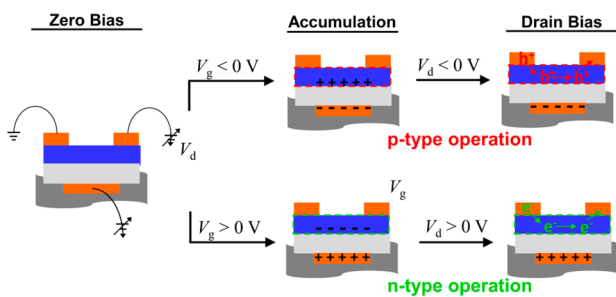


**Figure 2.** Schematic of p- and n-type (or channel) OTFT operation.

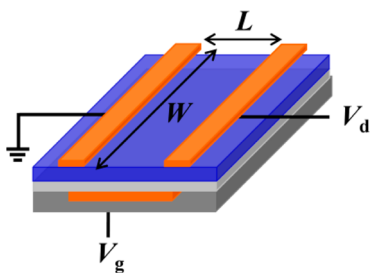


**Figure 3.** Schematic representation of an OTFT:  $V_g$ , gate voltage;  $V_d$ , drain voltage;  $L$ , channel length;  $W$ , channel width.

saturation region can be calculated from the transfer characteristic using the following equation

$$I_{ds} = \left( \frac{W}{2L} \right) \mu C_i (V_g - V_t)^2$$

where  $W$  is the channel width,  $L$  is the channel length (Figure 3),  $C_i$  is the dielectric capacitance,  $\mu$  is the mobility,  $V_g$  is the gate voltage, and  $V_t$  is the threshold voltage. The current modulation  $I_{on}/I_{off}$  can be derived from the quotient of “on” current divided by “off” current.

**1.2.2. Semiconductor Design Rules for High-Performance OTFTs.** On the basis of OTFT operation, it is essential to achieve facile charge injection from electrodes and promote charge transport in semiconductors in order to achieve high mobility and optimal transistor operation. Note that OTFT performance parameters are calculated by empirically fitting parameters in the  $I$ - $V$  equations, and the  $I$ - $V$  curves are derived from multicomponent devices rather than single materials. From material to device, there are different hierarchies of organization

and many interfaces are present in the transistors.<sup>8,30</sup> These organizations and interfaces are among the most critical issues for achieving optimal OTFT performance. Therefore, OTFT performance is influenced by many factors. These factors include the materials chemical structure, materials purity, supramolecular self-assembly, nature of the semiconductor/dielectric interface and semiconductor/electrode interface, device structure, and even device dimensions. Thus, controlling the structure at every structural hierarchy is essential for maximizing OTFT performance.

Organic synthetic chemists are highly skillful in tuning the optoelectronic properties of organic semiconductors at the molecule level via materials design and synthesis.<sup>31–33</sup> When transitioning from a single molecule to a micrometer-scale thin film device, supramolecular self-assembly plays a critical role. As a result, supramolecular approaches have been widely employed for achieving desired film morphologies with reduced grain boundaries<sup>34</sup> as well as well-aligned orientations<sup>35,36</sup> to facilitate charge transport. Interface engineering is found to be highly effective for lowering charge injection barriers<sup>37</sup> between the semiconductor and the electrode. Additionally, it is highly effective for minimizing the traps<sup>38</sup> between the semiconductor and the dielectric. For organic semiconductors, mobility is not a constant. It is a function of all of these factors rather than the intrinsic materials property. The sections below summarize the desirable properties of organic semiconductors for maximizing OTFT performance.

**1.2.2.1. Appropriate Frontier Molecular Orbitals.** In order to facilitate charge injection, semiconductors should have appropriate frontier molecular orbitals (FMOs) to form Ohmic contacts with electrodes. In p-channel OTFTs, the highest occupied molecular orbitals (HOMOs) of organic semiconductors should align with the Fermi levels of environmentally stable electrodes, such as Au or Ag, for efficient hole injection. For n-channel OTFTs, the lowest unoccupied molecular orbitals (LUMOs) should match the Au or Ag Fermi levels for optimal electron injection. In addition to charge injection, the semiconductor FMOs dominate OTFT stability. For p-type semiconductors, the HOMO empirical window for optimum performance is in the range from  $-4.8$  to  $-5.5$  eV.<sup>39,40</sup> Higher HOMOs lead to sizable off-currents and deterioration in device durability, and lower HOMOs result in substantial charge injection barriers and hence low measured mobility. For n-channel semiconductors, low LUMOs will facilitate electron

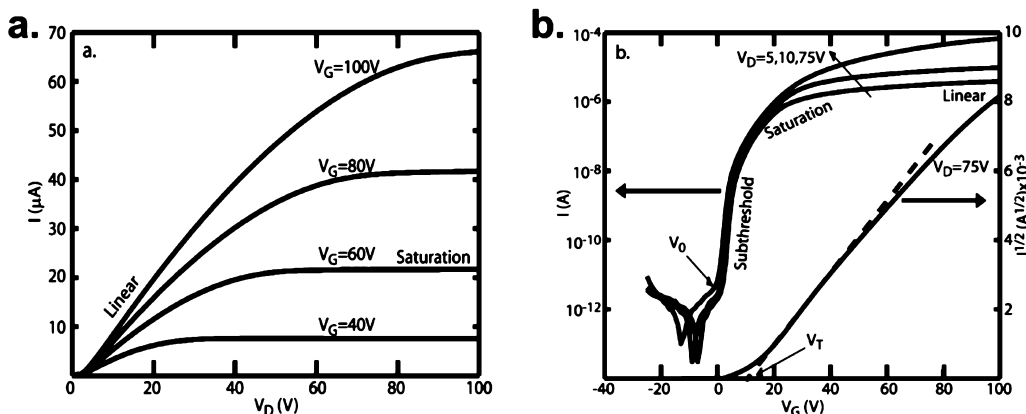


**Figure 4.** Example of output characteristics (a) and transfer characteristics (b) of an n-channel OTFT. Reprinted with permission from ref 28. Copyright 2004 American Chemical Society.

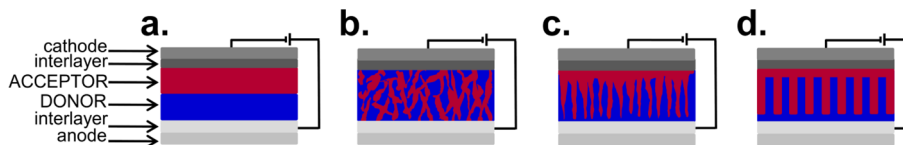


**Figure 5.** Device structures of various organic solar cells (OSCs): (a) bilayer flat bulk heterojunction solar cells, (b) disordered bulk heterojunction solar cells, (c) disordered bulk heterojunction solar cells with vertical phase gradation, and (d) ordered bulk heterojunction solar cells.

injection and stabilize electron transport, therefore resulting in enhanced device durability.<sup>41</sup> Note that semiconductors with ultralow LUMOs (<−4.60 eV) show materials instability due to attack by weak nucleophiles, such as water.<sup>42</sup> Hence, the ideal LUMO energy for n-type semiconductors is in the range from −3.6 to −4.5 eV.<sup>30,41</sup>

**1.2.2.2. High Degree of Backbone Coplanarity and Good Intermolecular  $\pi$ -Orbital Overlap.** In organic semiconductors, charge transport occurs between  $\pi$  orbitals; hence, the  $\pi$ -orbital overlap significantly affects charge carrier mobility. Intramolecular  $\pi$ -orbital overlap varies approximately with the cosine of molecular core dihedral angles, and departure from backbone coplanarity results in reduced  $\pi$ -orbital overlap.<sup>43</sup> Therefore, building blocks with minimal steric hindrance and semiconductors having appreciable backbone coplanarity are highly valued for enhancing mobility.<sup>9</sup> Theoretical computation and modeling are found to be particularly useful for predicting materials geometries.<sup>44</sup> Note that molecular coplanarity is related to charge transport efficiency within single molecules, whereas intermolecular charge hopping is found to be the limiting factor in determining solid-state charge carrier mobility in organic semiconductors.<sup>43,45</sup> Three-dimensional lamellar packing with close  $\pi$ – $\pi$  stacking is beneficial for intermolecular charge hopping. To achieve such packing, (macro)molecules should also have a high degree backbone coplanarity, which promotes self-assembly into ordered structures. It should be pointed out that achieving a high degree of backbone coplanarity can also greatly alter the energy levels of frontier molecular orbitals. This can lead to more facile charge injection and enhance mobility. Therefore, backbone coplanarity plays a profound role in determining the charge carrier mobility. This happens by facilitating charge injection via tuning frontier molecular orbitals, fostering intrachain transport, and maximizing intermolecular hopping. Among these three factors, maximizing intermolecular hopping via achieving a high degree of backbone coplanarity is paramount. Organic semiconductors having substantial charge injection barriers have still shown substantial mobility, while semiconductors having a high degree of backbone torsion usually show minimal mobility.

**1.2.2.3. Appropriate Film Morphologies and Microstructures.** Morphological studies carried out on high-performance semiconductors reveal that films with high degrees of crystallinity enable efficient charge transport,<sup>9,39,46</sup> which has guided materials synthetic efforts.<sup>39,40,47,48</sup> However, OTFT lateral dimensions are typically far larger than organic crystallite domains, meaning that many grain boundaries are present between the source and the drain. These boundaries act as charge trapping sites and hinder charge transport. For achieving high mobility, the films should have well-connected and aligned domains. For polymers, their molecular weights have a profound impact on film morphology and microstructure. High molecular weight batches of polymers usually have reduced grain boundaries, better domain connectivities, longer range orderings, and hence improved mobilities.<sup>49,50</sup> In OTFTs, charge migration

is parallel to the substrate; therefore, the semiconductors preferentially adopting edge-on orientations can provide improved  $\pi$ – $\pi$  stacking in the direction parallel to the substrate surface, and this generally results in enhanced mobility. The origin of organic molecular orientation is not fully understood but usually depends on the substrate surface energy and the interaction energetics between the semiconductor and the substrate. Minor structural modification can greatly affect the molecular orientation, and therefore, mobility varies.<sup>36,51</sup>

**1.2.2.4. Solubility and Materials Processability.** To fully realize cost-effective devices, semiconductors should be suitable for high-throughput film deposition via solution-based processing techniques. To achieve such processability, the commonly employed strategy is to functionalize  $\pi$ -conjugated systems with solubilizing chains, mainly hydrocarbon. However, introducing such chains may impose unfavorable steric hindrance, therefore reducing conjugation and sometimes ordering. To maintain solubility and achieve effective conjugation, solubilizing chains should be strategically manipulated, such as by controlling backbone regioregularity, e.g., the side chains in poly(3-alkylthiophenes),<sup>52</sup> or using unsubstituted spacer groups as pioneered by McCulloch and Ong in PBTTT<sup>47</sup> and PQT,<sup>53</sup> respectively, or using conformation “locks” such as the C center in cyclopentadithiophene<sup>54</sup> or the Si center in dithienosilole.<sup>55</sup>

### 1.3. Organic Solar Cells

**1.3.1. OSC Structure, Operation, and Characterization.** As an inexpensive and environmentally friendly energy source, organic solar cells (OSCs) have shown great potential for producing electrical energy directly from sunlight using photovoltaic technologies. Benefiting from materials development<sup>33,56</sup> and film morphology optimization,<sup>21,57</sup> significant advances have been made in the past two decades and power conversion efficiencies (PCEs) of >9% have recently been achieved.<sup>22</sup> However, the PCEs of OSCs are still lower than those of their inorganic-based counterparts.<sup>58</sup> To advance OSC applications to industrialization, the PCEs should surpass 10% with acceptable device durability. Along with materials development, device engineering has made a great contribution to performance enhancement.<sup>59–62</sup>

The photovoltaic effect in laminated organic systems was discovered by Kearns and Calvin in 1958,<sup>63</sup> and the first organic solar cell featuring a single flat bilayer heterojunction (Figure 5a) was invented by Tang in 1986,<sup>64</sup> in which an n-type perylene tetracarboxylic derivative acceptor semiconductor was stacked on top of a p-type copper phthalocyanine donor semiconductor. Please note that in order to avoid confusion, donor semiconductor and acceptor semiconductor are used to represent an electron-donor material (p-type) and an electron-acceptor material (n-type) in heterojunction solar cells, respectively, while donor and acceptor refer to the structural building blocks of organic semiconductors.<sup>65</sup> In flat bilayer OSCs, donor semiconductor and acceptor semiconductor are well separated from each other and selectively contact the device anode and cathode, respectively.<sup>66,67</sup> Once spatially well separated, the

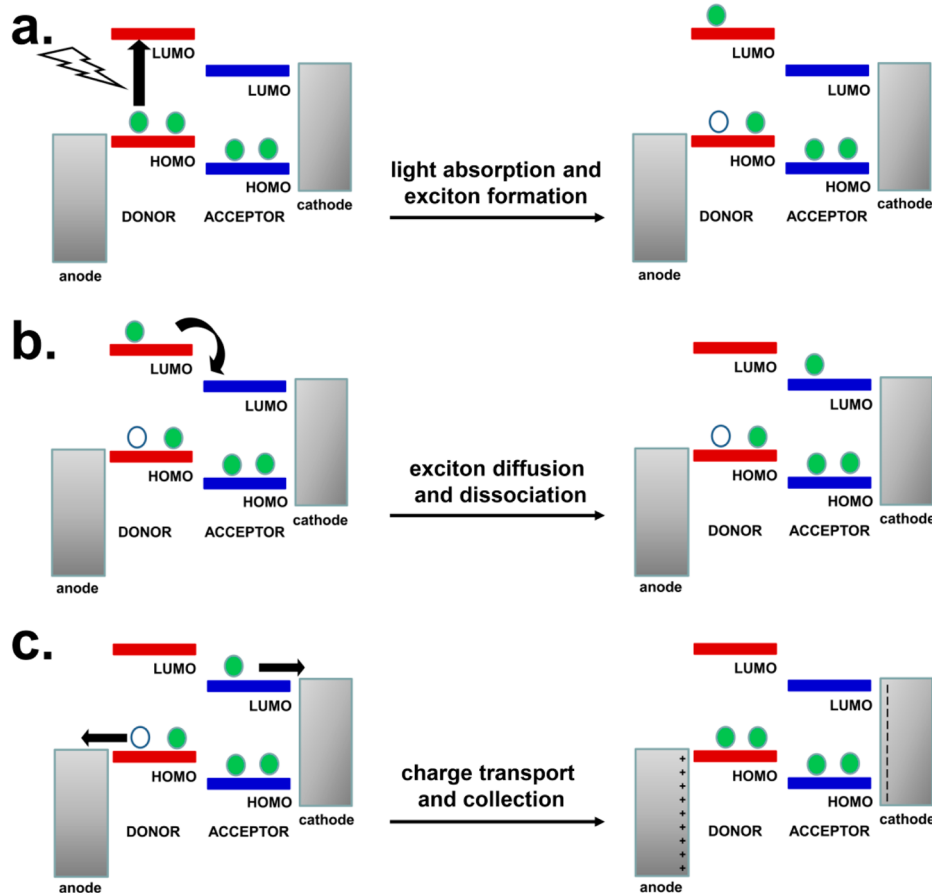


**Figure 6.** General mechanism of photoenergy conversion in OSCs.

electron and hole are unlikely to recombine. However, the area of the donor semiconductor/acceptor semiconductor interface (heterojunction) is limited in such structures, and only excitons (tightly bound electron–hole pairs) generated within a distance of 10–20 nm from the interface can reach the interface and separate into free charges. Excitons created away from the interface at distances greater than the exciton diffusion length cannot dissociate, which results in low PCEs.<sup>64,66,68,69</sup>

The bulk heterojunction (BHJ) solar cell concept was invented by Heeger<sup>70</sup> and Friend<sup>71</sup> in 1995, in which an intermingled network of a polymer as the donor semiconductor and a fullerene derivative as the acceptor semiconductor was created as the active layer (Figure 5b).<sup>70</sup> BHJ cells achieve greatly improved PCEs versus flat bilayer heterojunction cells, and solution processability offers reduced device fabrication costs and greater areal coverage.<sup>22,66</sup> Nanoscale phase separation in the bulk dramatically increases the donor semiconductor/acceptor semiconductor interfacial area, and therefore, excitons formed almost anywhere in the blend can reach the interface and dissociate to form free charge carriers.<sup>72</sup> The interpenetrating network in BHJ OSCs offers bicontinuous pathways for electrons and holes to migrate to their respective electrodes.<sup>73,74</sup> However, the donor semiconductor and acceptor semiconductor are in intimate contact with each other in the BHJ layer, and charge recombination can also occur along winding and disordered pathways, breaks, and dead ends. Recombination can also take place at the electrodes since the anodes and cathodes are in contact with both donor and acceptor semiconductor, which can lower device PCEs.

Disordered bulk heterojunction OSCs (Figure 5c) with vertical phase gradation are desirable for performance enhancement since it can effectively decrease electron and hole recombination.<sup>75</sup> The acceptor semiconductor-enriched layer on the cathode side of the heterojunction can block hole leakage to the cathode, and the donor semiconductor-enriched layer on the anode can block electron leakage to the anode. Such contact selectivity can thus reduce electron and hole recombination at the electrodes, as in the case of the bilayer solar cell.<sup>76,77</sup> Furthermore, the vertical phase gradation realizes matching between the photocurrent density and the charge carrier transport channel width, which can effectively suppress charge accumulation and recombination.<sup>75</sup> Several papers have reported vertical phase gradation and demonstrated improved performance by tuning the component surface energy and the interaction with the substrates,<sup>78,79</sup> using inverted device structures.<sup>62,80</sup> It should be pointed out that BHJ cells with this desired vertical phase separation may not always lead to enhanced device performance. Loo et al. reported comparable PCEs for the cells with desired vertical phase separation and the control cells with reversed films.<sup>81</sup> BHJ cells with vertical phase gradation are attracting a great deal of attention; deeper investigation is clearly needed to better understand its effects on device performance and to develop strategies to achieve such gradation.<sup>62,82</sup>

A highly ordered nanoscale BHJ structure (Figure 5d) was proposed to reduce charge recombination.<sup>73</sup> In such structures, the donor semiconductor and acceptor semiconductor domains are interspersed at length scales of about 10–20 nm equal to or less than the exciton diffusion length. The two phases are patterned in a regular interdigitated fashion to provide

continuous and direct pathways for charge transport to their respective electrodes. Moreover, the donor semiconductor and acceptor semiconductor are in specific and exclusive contact with the anode and cathode, respectively, which may prevent charge leakages to the “wrong” electrodes. However, construction of such well-organized nanostructures is a significant challenge, and very limited success has been demonstrated,<sup>83,84</sup> mainly in polymer and inorganic-based hybrid cells.<sup>85</sup>

Generally, three steps are involved in the process of the conversion of photon energy to electrical energy in OSCs (Figure 6):<sup>86</sup> (a) absorption of photons generates intramolecular excitons; (b) excitons diffuse to the donor semiconductor/acceptor semiconductor interface and dissociate via an electron-transfer process<sup>87</sup> to form a geminate pair; (c) separated charge carriers (electron and hole) migrate to their respective electrodes under the internal electric field and are collected at the electrodes. Thus, upon solar irradiation, electrons are excited from the HOMO to the LUMO, which leaves holes in the HOMO. As noted above, the resultant electron–hole pair is called an exciton, which is strongly bound Coulombically as a consequence of the low dielectric constants of organic materials. Exciton formation depends on the optical band gap of the absorbing materials. After formation, excitons diffuse in the active layer. In OSCs, excitons have limited lifetimes. In order to improve OSC performance, exciton dissociation must be maximized within the exciton lifetime. Therefore, achieving the correct morphology of the donor semiconductor/acceptor semiconductor blend film is crucial. The length scale of the phase-separated donor semiconductor and acceptor semiconductor domains should match the exciton diffusion length, typically  $\sim$ 10–20 nm in OSC active blend films. After the exciton reaches the interfaces, the abrupt difference in the LUMO energies between the two semiconductors provides the driving force for exciton dissociation. The optimal LUMO offset is found to be 0.3–0.4 eV, providing an efficient driving force for exciton dissociation.<sup>88</sup> After the excitons dissociate to free charge carriers there should be an interpenetrating bicontinuous network for the electron and hole to migrate to their respective electrodes and thus minimize recombination.<sup>89</sup>

OSC performance is derived from the device current–voltage data (Figure 7).<sup>74,83</sup> In the absence of light, there should be no substantial current flowing until the external voltage is greater than the open-circuit voltage (dashed line). Under light irradiation and without an external voltage applied, OSC generates an electrical current of magnitude  $J_{sc}$  (or the current density,  $J_{sc}$ ; short-current conditions). Upon application of an

external voltage, the current is reduced until it nullifies when the external voltage is equal to the magnitude of  $V_{oc}$  (open-voltage conditions). From the current–voltage curve, we can derive the maximum power point (MPP), where the product of current and voltage is the largest. The power conversion efficiency ( $\eta_e$ ) of an OSC can be calculated using the following equation,<sup>74</sup> where  $V_{oc}$  is the open-circuit voltage,  $J_{sc}$  is the short-circuit current density,  $FF$  is the fill factor, and  $P_{in}$  is the energy of incident light.

$$\eta_e = \frac{V_{oc} J_{sc} FF}{P_{in}}$$

$$FF = \frac{J_{mpp} V_{mpp}}{J_{sc} V_{oc}}$$

$J_{mpp}$  and  $V_{mpp}$  are the current and voltage at the maximum power point on  $J$ – $V$  curves, respectively. For an ideal cell, the  $J$ – $V$  curve should have a rectangular shape, and therefore, the  $FF$  approaches unity.

$V_{oc}$  is approximately proportional to the energy offset between the acceptor semiconductor LUMO and the donor semiconductor HOMO. Brabec<sup>90</sup> reported a linear correlation between  $V_{oc}$  and the acceptor LUMO energy. Scharber<sup>88</sup> likewise noted a linear relationship between  $V_{oc}$  and the donor semiconductor HOMO level. Malliaras reported that charge carrier losses at the electrodes lower  $V_{oc}$ , usually  $\sim$ 0.2 V at every electrode.<sup>91</sup> Other factors also affect  $V_{oc}$ , such as the film morphology<sup>92</sup> and surface composition.<sup>93</sup> A thin LiF layer was found to increase  $V_{oc}$ .<sup>74</sup> It was observed that  $V_{oc}$ s can also be tuned over a wide range via changing the alignment of interfacial dipole moments.<sup>94</sup> Hence,  $V_{oc}$ s depend on the materials used, but other factors also play significant roles.

$J_{sc}$  is a function of the active layer light absorption characteristics, the blend film morphology, and the charge carrier mobility of the donor and acceptor semiconductors. Compared to the bilayer devices, the bulk heterojunction (BHJ) OSCs have greatly increased interfacial area for exciton dissociation and therefore enhanced  $J_{sc}$ . Processing additives promote the nanoscale phase separation and the formation of interpenetrating bicontinuous networks,<sup>57</sup> which result in enhanced exciton dissociation and reduced charge recombination. OSCs fabricated with processing additives usually have enhanced  $J_{sc}$ s.<sup>57</sup> Thermal annealing and solvent annealing are also found to be effective for  $J_{sc}$  improvement.<sup>95,96</sup> Moreover,  $J_{sc}$  is related to the charge carrier mobility of the donor and acceptor semiconductors. Materials with increased mobilities can reduce charge accumulation and recombination and result in enhanced  $J_{sc}$ .<sup>97–99</sup> Furthermore, interfacial layers can serve as barriers to prevent leakage of undesired charges to wrong electrodes, reduce charge recombination at electrodes, and, hence, greatly enhance  $J_{sc}$ .<sup>22,100,101</sup>

Among OSC performance parameters, the  $FF$  is least understood at this moment, and achieving high  $FF$ s is challenging.<sup>89</sup> It was found that charge carrier mobility and lifetime, active layer morphology, and interfacial and bulk charge recombination play important roles.<sup>60</sup> After charge generation, a competition exists between charge transport to electrodes and charge recombination. Near the short-circuit condition, high charge mobility can facilitate its transport and reduce its accumulation. Near the open-circuit condition, long charge carrier lifetimes improve the charge extraction and thus the  $J$ – $V$  curve steepness.<sup>89</sup> Therefore, both charge carrier mobility and lifetime are parameters to be optimized for  $FF$  enhancement.

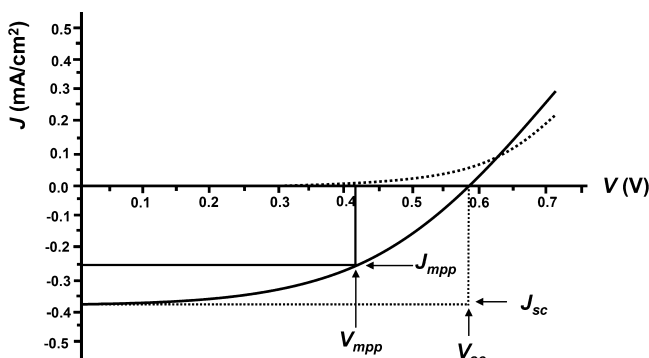


**Figure 7.** Example of current–voltage curve of OSCs (dark, dotted line; illuminated, solid line).

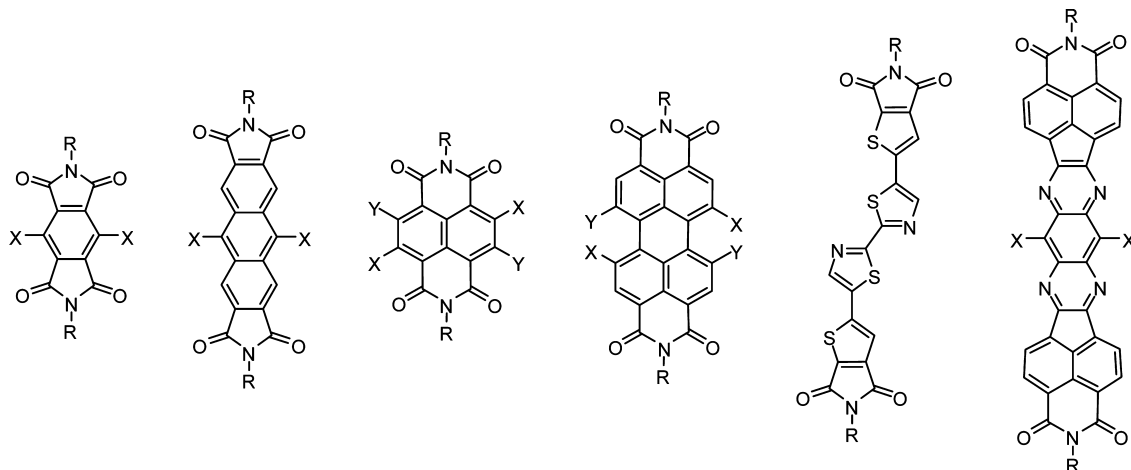


**Figure 8.** Chemical structures of representative imide-functionalized n-channel small molecule semiconductors. Structure modifications are realized by varying the N-imide substituent R and functionalizing the aromatic core with different electron-donating or -accepting groups (X and Y).

Note that a high *FF* of ~80% has recently been achieved in inverted solar cells fabricated with a high-mobility polymer.<sup>62</sup>

Although there are established strategies for increasing the magnitude of OSC performance parameters and for maximizing PCEs, there is also growing evidence that the PCEs of organic solar cells do not depend systematically on any one parameter. This is due to the intrinsic correlations among different performance parameters that in concert determine the solar cell performance.<sup>88,102</sup> Moreover, the dependencies observed in one material system do not necessarily translate to others. This reflects the structural complexity of organic solar cells.<sup>103–107</sup> The PCE is not only a function of the materials used but also a function of many other factors.<sup>8,22</sup>

In addition to PCE, an equally important consideration is solar cell stability. H<sub>2</sub>O and O<sub>2</sub> penetration, ITO corrosion by PEDOT:PSS, and low function work cathode oxidation erode device performance. Inverted OSCs have found success in improving device stability, which is attributed to use of more stable electrodes and elimination of PEDOT:PSS.<sup>108</sup> Note that ordered morphology degradation<sup>109</sup> also decreases OSC performance, especially at elevated temperature under irradiation. Since the PCEs of OSCs are approaching the threshold for commercialization, future research should focus on understanding those factors which govern device stability and developing strategies for achieving enhanced OSC stability.

**1.3.2. Semiconductor Design Rules for High-Performance OSCs.** One of the major challenges in OSCs is to develop organic semiconductors which synergistically integrate the desired molecular electronic structure and solid-state morphological properties to maximize device performance. The donor semiconductor and acceptor semiconductor should be capable of maximizing the efficiency of every step in the photoenergy to electricity conversion process. The section below summarizes the materials design rules for high-performance OSCs.

**1.3.2.1. Appropriate Band Gaps To Maximize the Absorption of Solar Irradiation.** Exciton generation in an OSC depends on the optical band gap of the photoactive layer. Since the peak of the solar flux is located at ~700 nm, small band-gap semiconductors with broad absorption and high absorption coefficients can facilitate exciton generation. Hence, many strategies have been developed to tune band gaps,<sup>110</sup> of which a particularly effective one is the synthesis of (macro)molecules having  $\pi$ -conjugated donor–acceptor groups. By synthesizing

building blocks with fine-tuned optoelectronic properties and coupling them together, large numbers of new semiconductors with greatly varied band gaps have been developed. This “mix-match” strategy in general leads to the most efficient OSC semiconductors.<sup>32,33</sup>

**1.3.2.2. Engineered Energy Levels of the Frontier Molecular Orbitals.** The device performance of organic semiconductors depends not only on their band gaps but also on their FMO energies. The donor (p-type) semiconductor having a low-lying HOMO usually shows higher  $V_{oc}$ s, which are beneficial to the PCE.<sup>88</sup> However, lowering the HOMO will widen the band gap, which underscores the trade-off between  $J_{sc}$  and  $V_{oc}$ . Exciton dissociation depends on the LUMO–LUMO energy offset between the donor and the acceptor semiconductors.<sup>88</sup> To drive exciton dissociation, the donor semiconductor LUMO should be >0.3 eV higher than that of the acceptor semiconductor to overcome the exciton Coulombic binding energy.<sup>111</sup> However, a greater offset will result in wasted light energy. Therefore, the donor semiconductor LUMO should be fine tuned when it is blended with different acceptor semiconductors. This donor–acceptor strategy has proven to be effective for tuning FMOs of the resulting semiconductors.

**1.3.2.3. Good Solubility and Desirable Film Morphology and Microstructure.** To realize cost-effective and large-area OSCs, semiconductors should have sufficient solubility for printing. Materials aggregation in solution should be suppressed in order to obtain uniform films with nanoscale phase separation. The resulting blend film should be of high quality and free from pinholes and dead ends. The charge transport characteristics of the blend film are critical to suppress charge recombination. Thus, semiconductors with high degrees of ordering are effective in facilitating charge sweep out from the blend. Different from the charge transport in OTFTs, which should be in parallel to the substrate, the transport in OSCs should be perpendicular to the substrate. Thus, materials having preferential face-on orientation to the substrate/electrode will generally enhance charge migration to the respective electrode. Polymer molecular weight ( $M_n$ ) is another important factor, with high  $M_n$  polymers usually showing enhanced  $J_{sc}$ , FFs, and PCEs.<sup>112</sup>

**1.3.2.4. Good Materials Purity and Stability.** The presence of impurities is detrimental to OSC performance by adversely affecting film morphology and microstructural order, thereby lowering carrier mobility.<sup>113</sup> Impurities act as charge traps and

lead to charge recombination. High-performance materials that give poor OSC performance may suffer from low concentrations of impurities.<sup>113</sup> Hence, the materials should be fully purified before performance evaluation. Moreover, it is important that semiconductors be stable in ambient (i.e., O<sub>2</sub>, H<sub>2</sub>O) for efficient handling and device fabrication. Lowering the frontier molecular orbital energies by appending electron-withdrawing substituents is a proven approach to increase resistance to degradation by atmospheric O<sub>2</sub> and H<sub>2</sub>O.

#### 1.4. Why Imide/Amide-Functionalized Polymers Are of Interest

**1.4.1. Imide-Functionalized Small Molecules: High-Performance n-Channel Organic Semiconductors.** The first imide-functionalized organic semiconductor, a perylene diimide, was used as an n-channel semiconductor for OTFTs with an electron mobility ( $\mu_e$ ) of  $1.5 \times 10^{-5}$  cm<sup>2</sup>/(V s) in 1996.<sup>114</sup> Next, imide-functionalized polycyclic arenes attracted a great deal of attention. Pyromellitic diimide (PMDI, Figure 8),<sup>115</sup> anthracene diimide (ADI),<sup>116</sup> naphthalene diimide (NDI),<sup>117</sup> perylene diimide (PDI),<sup>118</sup> and other diimide (or imide)-functionalized organic small molecules<sup>119,120</sup> containing various side chains were synthesized by condensation reaction of the corresponding anhydrides with various amines. Very promising OTFT n-channel performance has been achieved for this class of semiconductors, including  $\mu_{es} > 0.1$  cm<sup>2</sup>/(V s) in air for fluorinated alkyl NDI derivatives.<sup>117</sup> Chemical modifications on the imide groups do not significantly alter semiconductor optoelectronic properties due to the orbital nodes at the imide nitrogen atoms in the HOMOs and LUMOs. Further research efforts resulted in a new generation of imide-functionalized semiconductors utilizing core-substituted arenes. Core substitutions enable access to a class of semiconductors with tunable band gaps and lowered LUMOs for more facile charge injection and improved device stability.<sup>41,42,121</sup> Improved film morphology and microstructure ultimately led to a promising  $\mu_e$  of 3.50 cm<sup>2</sup>/(V s) for solution-deposited OTFTs.<sup>122</sup> To date, imide-functionalized small molecules constitute the most successful n-type organic semiconductors and enable their applications in p–n junctions, complementary inverters, and as electron acceptor semiconductors in OSCs.<sup>123,124</sup> Several reviews summarize the synthesis, structure–property correlations, and device performance of imide-functionalized small molecules for OTFTs<sup>123,125</sup> and OSCs.<sup>123,126</sup>

The remarkable n-channel performance of imide-functionalized small molecules is mainly attributed to the following factors: (a) a strong electron-withdrawing imide group, which lowers semiconductor LUMOs, facilitates electron injection, and stabilizes injected electrons; (b) good  $\pi$ -conjugation of the planar core; such electronic properties are beneficial for intramolecular charge transport; (c) solubilizing ability offered by N-imide substituents, which enables excellent solution processability and fine-tuned film morphology; (d) N-alkyl chains that are distant from the aromatic core, which minimizes steric hindrance; therefore, the n-channel semiconductors can achieve close intermolecular  $\pi$ – $\pi$  stacking for efficient charge carrier intermolecular hopping; (e) facile materials accessibility. The synthetic routes to these semiconductors are straightforward, usually in 1–4 steps with excellent yields from commercial sources. The combination of these factors renders the imide-functionalized arenes the most important n-channel organic semiconductors discovered to date.

**1.4.2. Imide/Amide-Functionalized Polymer Semiconductors: Attractions.** Polymer semiconductors have several advantages over their small molecule counterparts. First, polymers have better film-forming properties. Polymer films are generally smooth, uniform, and isotropic. Therefore, the devices fabricated from polymers can show minimal performance variation. Due to the differences in molecular weight ( $M_n$ ) and polydispersity index (PDI), polymers may show performance variations from batch to batch. Such variations can be suppressed by increasing the monomer purity and controlling the polymerization conditions. Second, for commercial applications, printing techniques require great control over the rheological properties, which are more easily tuned for polymer solutions than for the small molecule counterparts. Third, polymers are more suitable for fabricating flexible devices than small molecules considering their mechanical properties. Although high-performance polymers are actively pursued, the polymer-based devices normally show inferior charge transport to their small molecule counterparts mainly due to their low crystallinity.<sup>17,24,46</sup> Developing high-performance polymer semiconductors, particularly n-channel polymers with performance matching that of p-channel polymers, will expedite the commercialization of organic optoelectronics.<sup>127</sup>

The great success of imide-functionalized small molecules serves as a test bed for the use of imide-functionalized polymers as semiconductors in organic electronics. Note that depending on the structural connectivity (Figure 9), imide-containing

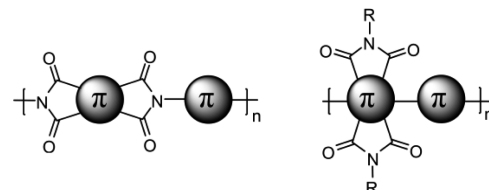
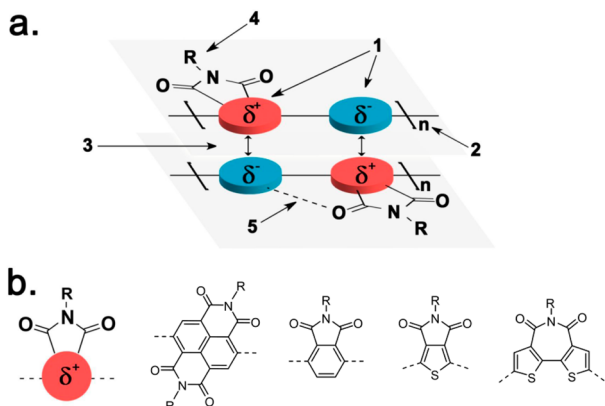


Figure 9. General chemical structures of polyimide insulators and imide-functionalized  $\pi$ -conjugated polymer semiconductors.

polymers can be semiconductors or insulators. Indeed, polyimides have been widely used as electrical insulators due to their synthetic accessibility, mechanical properties, thermal properties, and supramolecular self-assembly. Furthermore, nonconjugated polyimides show interesting photovoltaic performance when incorporated in OSCs.<sup>128</sup> Thus, some characteristics making polyimides superior insulators are also desired for organic semiconductors, such as the high electron deficiency and the capability to self-assemble into ordered structures.

In this review, we focus on a class of polymer semiconductors containing imide-functionalized arenes as  $\pi$ -conjugated electron-withdrawing units. Both diimide and monoimide-functionalized polymer semiconductors will be reviewed. As structural analogues, amide-functionalized polymers are also included. The combination of solubilizing substituent, electron-deficiency, and structure-enforcing geometry enables these polymer semiconductors to synergistically integrate desirable optoelectronic properties (Figure 10). First, the strong electron-withdrawing imide (or amide) groups enable effective tuning of polymer band gaps and FMOs, the primary concern for materials design in OSCs and OTFTs. Second,  $\pi$ -conjugated polymers are typically synthesized via Pd-mediated couplings,<sup>129</sup> and the dibrominated imide (or amide) monomers favor Pd(0) catalyst C–Br oxidative addition and subsequent transmetalation with electron-rich comonomers to yield high  $M_n$  polymers,<sup>129</sup> which usually show



**Figure 10.** (a) Imide-functionalized donor–acceptor (D–A) polymer semiconductors combining performance-enhancing characteristics for organic electronics. (1) D–A strategy for band-gap and frontier molecular orbitals tuning. (2) High molecular weights. (3) Close  $\pi$ – $\pi$  stacking. (4) Solubility and crystallinity via imide N-alkylation. (5) Conformational locking to promote  $\pi$ -system coplanarity via (thienyl)S···(carbonyl)O interactions or (thienyl)C–H···(carbonyl)O hydrogen bonds. (b) Representative imide-functionalized arenes as electron-deficient units for D–A polymer semiconductors. As structural analogues to imide-functionalized polymers, amide-functionalized polymers (structure not shown) should maintain these performance-enhancing characteristics. Reprinted with permission from ref 55. Copyright 2012 American Chemical Society.

improved performance than the low  $M_n$  analogues.<sup>49,50,112</sup> Third, the interchain donor–acceptor interactions should promote close  $\pi$ – $\pi$  stacking and facilitate intermolecular charge hopping. Fourth, facile N-alkylation on the imide (or amide) offers good materials solubility and promotes solid-state packing, which should benefit charge transport.<sup>130,131</sup> Moreover, the intramolecular S···O interactions (Figure 11a)<sup>44,132</sup> involving proximate imide (or amide) C=O and thienyl S or intramolecular H bonds (Figure 11b)<sup>133</sup> between the proximate imide (or amide) C=O and  $\beta$  H atom on the thienyl unit can serve as conformational “locks” to promote backbone coplanarity. Hence, the resulting semiconductors can achieve high-degrees of conjugation, reduced band gap, and enhanced charge carrier transport.

Various imide- and amide-functionalized arenes (Figure 12) have been incorporated into polymer semiconductors, which leads to the emergence of a new class of semiconductors with excellent device performance.<sup>134</sup> The arenes include historical

molecules produced from natural sources as well as their newly developed derivatives by modern organic synthetic methodologies. The unique combination of the performance-enhancing characteristics of imide- (and amide) functionalized polymer semiconductors results in superior performance OTFTs and OSCs. Among them, p-channel polymers exhibit hole mobility ( $\mu_h$ ) up to  $12 \text{ cm}^2/(\text{V s})$  with good device stability.<sup>135</sup> n-Channel polymers exhibit electron mobility ( $\mu_e$ ) approaching  $2 \text{ cm}^2/(\text{V s})$ ,<sup>136,137</sup> which greatly closes the performance gap between p- and n-channel polymers.<sup>17,30,127</sup> Substantial ambipolarity with  $\mu_h$  and  $\mu_e > 8$  and  $4 \text{ cm}^2/(\text{V s})$ , respectively, has also been obtained.<sup>138</sup> As donor semiconductors in OSCs, p-type polymers show PCEs of 8–9%<sup>61,139–141</sup> with unprecedented FFs approaching 80% in single-layer cells.<sup>62</sup> As acceptor semiconductors, n-type polymers enable PCE of 6.4% in all-polymer solar cells, the record value in this category cell.<sup>142</sup> Materials structure modification in parallel with device engineering will further improve device performance from this emerging class of polymers to advance OTFT and OSC technologies into the market.

## 2. PERYLENE DIIMIDE-BASED POLYMER SEMICONDUCTORS

The perylene diimide (PDI)-based chromophore was first reported in the early 1910s<sup>143,144</sup> and has been extensively studied in both industry and academia since then. PDI dyes exhibit strong absorption in the visible region,<sup>145</sup> and are widely used as high-grade industry colorants, particularly in carpet fibers and the automobile industry.<sup>144,146,147</sup> Recently, PDI small molecules were revitalized as n-channel semiconductors in OTFT with superior electron mobilities<sup>29,114,148</sup> and in OSCs with good PCEs.<sup>149,150</sup> The PDI core was successfully incorporated into nonconjugated polymers for light-emitting diodes,<sup>151</sup> but its incorporation into conjugated polymers was greatly delayed mainly due to the synthetic challenge of dihalogenation and the steric hindrance thought by materials synthetic chemists. Recently, a methodology developed for efficient bromination at the 1,7-positions of PDI allowed access to a large library of conjugated polymers for organic electronics.<sup>152</sup>

### 2.1. Synthesis of Dibrominated Perylene Diimide

The synthesis of dibrominated PDI was first disclosed in 1997.<sup>153</sup> According to the procedure of a BASF patent (Scheme 1), bromination of the perylene dianhydride **1** in  $\text{H}_2\text{SO}_4$  selectively

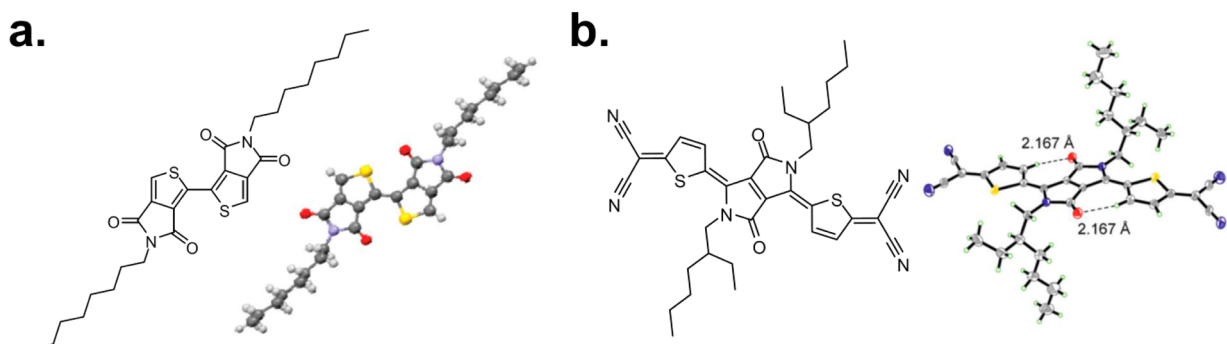


**Figure 11.** Chemical and single-crystal structures of (a) thieno[3,4-c]pyrrole-4,6-dione (TPD) dimer (Reprinted with permission from ref 132. Copyright 2010 American Chemical Society.) and (b) dihydropyrrolo[3,4-c]pyrrole-1,4-dione (DPP)-based semiconductors (Reprinted with permission from ref 133. Copyright 2012 American Chemical Society.). The (thienyl)S···(carbonyl)O interaction in TPD dimer and intramolecular H bonds (C–H···O, 2.167 Å) in DPP–semiconductor lead to their high backbone coplanarity.

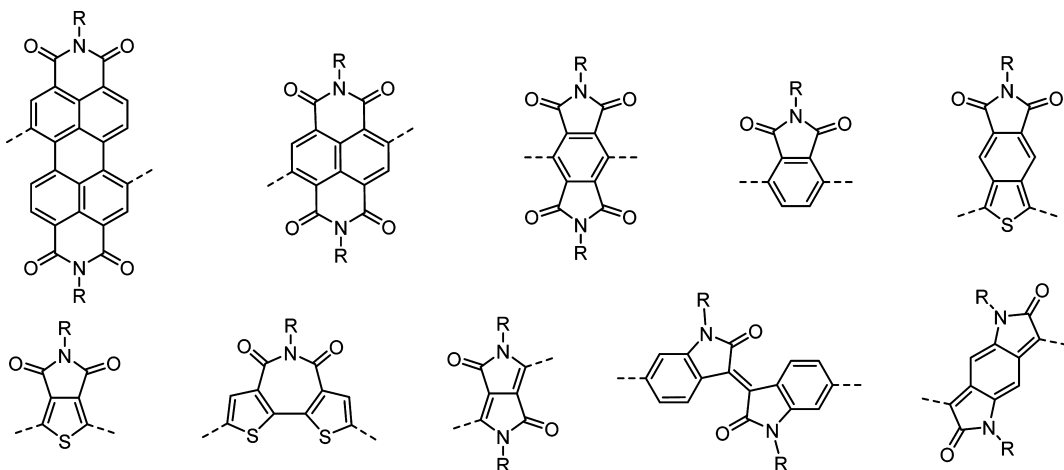
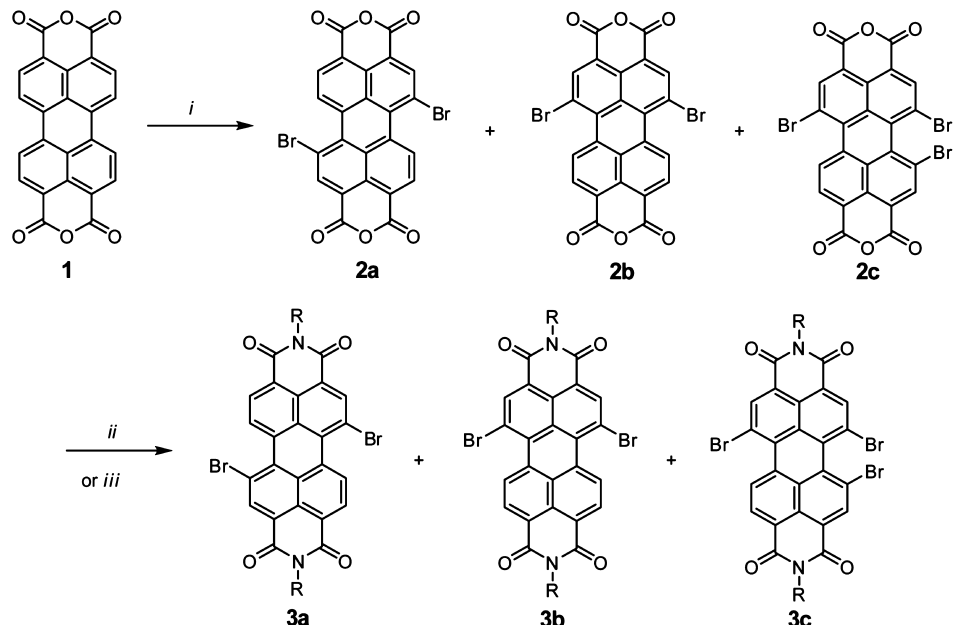


**Figure 12.** Chemical structures of imide- and amide-functionalized electron-deficient building blocks for polymer semiconductors.

**Scheme 1. Synthetic Route to Brominated Perylene Diimide from Perylene Dianhydride<sup>152 a</sup>**



<sup>a</sup>Reagent and conditions: (i)  $\text{Br}_2$ ,  $\text{I}_2$  (catalytic), 100%  $\text{H}_2\text{SO}_4$ , 85 °C; (ii) cyclohexylamine, *N*-methylpyrrolidinone, 85 °C; (iii) cyclohexylamine,  $\text{H}_2\text{O}/n\text{-PrOH}$  (2:1), 80 °C, Ar.

affords 1,7-dibromo dianhydride **2a**, and the subsequent imidization affords isomerically pure 1,7-dibrominated diimide **3a**. Würthner carefully examined BASF's procedure and revealed that the brominated dianhydride **2** was actually a mixture of 1,7-dibrominated **2a** (76%), 1,6-dibrominated **2b** (20%), and tribrominated **2c** (4%).<sup>152</sup> The overlooking of the regioisomer mixture is partially attributed to the insolubility of **2**, and the isomeric mixture of diimide **3** can only be detected using high-field NMR (>400 MHz). Imidizations (Scheme 1) are carried out by reacting dianhydride **2** with cyclohexylamine in *N*-methylpyrrolidinone or a 2:1 mixture of  $\text{H}_2\text{O}/n\text{-PrOH}$ , and similar results are obtained under both sets of conditions. During imidization, the accompanying nucleophilic displacement of bromines by amines leads to core-substituted amine byproducts (structures not shown), which lower the imidization yields. Such core-substituted byproducts have deep colors due to the electronic push-pull interactions.

Regioisomerically pure 1,7-dibromo PDI **3a** ( $\text{R} = \text{cyclohexylamine}$ ) can be obtained via column chromatography and recrystallization. Column chromatography allows removal of minor tribrominated byproduct **3c** (ca. 1% yield) to give a regioisomeric mixture of **3a** and **3b** in 61% yield. However, **3a** and **3b** (80:20) cannot be separated by column chromatography. Fortunately, the major isomer **3a** can be purified by repetitive recrystallization.<sup>152</sup> After recrystallization three times, **3a** is obtained in pure form as evidenced by 600 MHz  $^1\text{H}$  NMR (spectrum c in Figure 13); however, the minor regioisomer **3b** cannot be obtained in pure form but is enriched in the mother liquor (spectrum d in Figure 13). X-ray analysis of a **3a** single crystal confirms its structure. The approach developed by Würthner provides access to regioisomerically pure 1,7-dibromo PDI.

A modified procedure (Scheme 2) was developed for the synthesis of **3a** under mild conditions (organic solvents; without using  $\text{H}_2\text{SO}_4$ ).<sup>154</sup> Condensation of perylene dianhydride **1** with

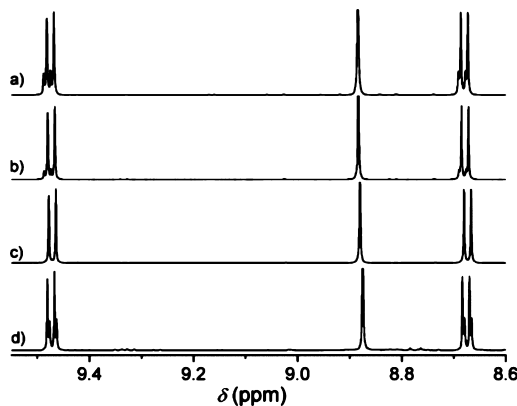
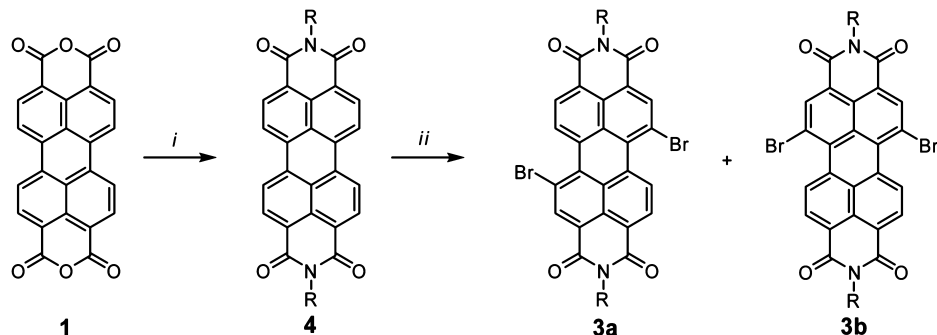


**Figure 13.**  $^1\text{H}$  NMR spectroscopic monitoring of recrystallization of regioisomer mixture of **3a** and **3b**; 600 MHz  $^1\text{H}$  NMR spectra of (a) a mixture before recrystallization, (b) after one and (c) after three repetitive recrystallizations; (d) spectra of mother liquor after concentration of the filtrate of the first recrystallization. Reprinted with permission from ref 152. Copyright 2004 American Chemical Society.

amine takes place in the presence of zinc acetate before bromination.<sup>155</sup> The novel method developed by Rybtchinski allows selective bromination by varying the reaction temperature to afford mono- and dibromo PDI or exclusively dibromo PDI with the 1,7-isomer as the major product, which can be purified by recrystallization.<sup>152</sup> It was found that the facility of bromination depends on the PDI aggregation propensities. For PDI with less bulky substituents, a harsher condition (higher temperature and longer reaction duration) is required for achieving exclusively dibrominated product.

Successful bromination of PDI enables access to a new class of polymer semiconductors. Controlled reaction condition and extensive purification lead to the availability of pure 1,7-dibromo PDI monomer rather than to the regioisomer mixture of 1,7-dibromo PDI and 1,6-dibromo PDI. In the following polymerizations, the pure 1,7-dibromo PDI monomer results in regioregular PDI polymer; while the PDI regioisomer mixture leads to regiorregular PDI polymer. This is because PDI can be incorporated into the polymer backbone in two different fashions, i.e., via a 1,7-linkage or a 1,6-linkage. Unless explicitly stated, the PDI polymers are regiorregular in this work.

**Scheme 2. Alternate Synthetic Route to Dibrominated Perylene Diimide from Perylene Dianhydride under Mild Condition<sup>154,155 a</sup>**



<sup>a</sup>Reagent and conditions: (i)  $\text{RNH}_2$ ,  $\text{Zn}(\text{OAc})_2$ , imidazole/quinoline, heating, or  $\text{RNH}_2$ , 1-n-butanol, heating; (ii)  $\text{Br}_2$ ,  $\text{CH}_2\text{Cl}_2$ , heating.

## 2.2. Perylene Diimide-Based Polymer Semiconductors for OTFTs

The first PDI-based conjugated polymer was reported by Marder et al. (Figure 14).<sup>156</sup> **P1** was synthesized by Stille coupling from a dibrominated PDI regioisomer mixture of **3a** and **3b** and distannylated dithienothiophene and had a number-average molecular weight ( $M_n$ ) of 10 kDa and a polydispersity index (PDI) of 1.5. The **P1** mobility was investigated by fabricating BGTC OTFTs using Al source/drain electrodes. The measured  $\mu_e$  in the saturation regime was  $1.3 \times 10^{-2} \text{ cm}^2/(\text{V s})$  with an  $I_{\text{on}}/I_{\text{off}} > 10^4$  and a  $V_t$  of 4.4 V under  $\text{N}_2$ . The good **P1**  $\mu_e$  is attributed to its low-lying LUMO of  $-3.9$  eV enabled by the PDI unit and good  $\pi$ -conjugation promoted by the fused PDI and dithienothiophene. Device optimization led to an improved  $\mu_e$  of  $0.06 \text{ cm}^2/(\text{V s})$  with an  $I_{\text{on}}/I_{\text{off}}$  of  $10^4$  in top-gate OTFTs fabricated by lamination using a polyacrylonitrile (PAN)/polystyrene (PS) dielectric.<sup>157</sup> Enabled by the encapsulation effect, the **P1** top-gate OTFTs showed enhanced device stability with a  $\mu_e$  of  $0.005 \text{ cm}^2/(\text{V s})$  and an  $I_{\text{on}}/I_{\text{off}}$  of  $10^4$  after 3 months storage in air.

Facchetti and co-workers reported PDI and bithiophene regiorregular **P2** having a  $M_n$  of  $\sim 11$  kDa and a PDI of  $\sim 3$ .<sup>158</sup> **P2** has a LUMO of  $-3.96$  eV and a band gap of  $1.65$  eV. BGTC OTFTs fabricated on OTS/SiO<sub>2</sub>/Si substrate show a  $\mu_e$  of  $2 \times 10^{-3} \text{ cm}^2/(\text{V s})$  with an  $I_{\text{on}}/I_{\text{off}}$  of  $10^5$  in vacuum. The lower  $\mu_e$  of **P2** versus that of **P1** is likely due to the larger electron injection barrier in **P2** OTFTs since Au is used as source/drain. **P2** OTFTs show rapid performance degradation when exposed to air because the **P2** LUMO is on the borderline for ambient OTFT operation.<sup>41</sup>

**P3** and **P4** containing the dithienopyrrole donor with different solubilizing chains on the imide moiety were synthesized by Zhan.<sup>159</sup> The strong electron-donor dithienopyrrole elevates the polymer HOMOs and decreases the band gaps. It is interesting to note that the band gap of **P4** (1.30 eV) is smaller than that of **P3** (1.37 eV), and is accompanied by a higher HOMO ( $-5.31$  eV) than that of **P3** ( $-5.54$  eV). The **P4** HOMO matches the Au Fermi level; therefore, **P4** shows ambipolarity with a  $\mu_e/\mu_h$  of  $4 \times 10^{-4}/4 \times 10^{-5} \text{ cm}^2/(\text{V s})$  in air. However, **P3** only shows n-channel performance with a  $\mu_e$  of  $5 \times 10^{-3} \text{ cm}^2/(\text{V s})$ . The **P4** ambipolar OTFT can operate in ambient, while **P3** n-channel OTFT performance can only operate under  $\text{N}_2$ . Further increasing the electron-donating ability of the donor leads to **P5**, which shows a band gap of 1.24 eV, a HOMO of  $-5.38$  eV,

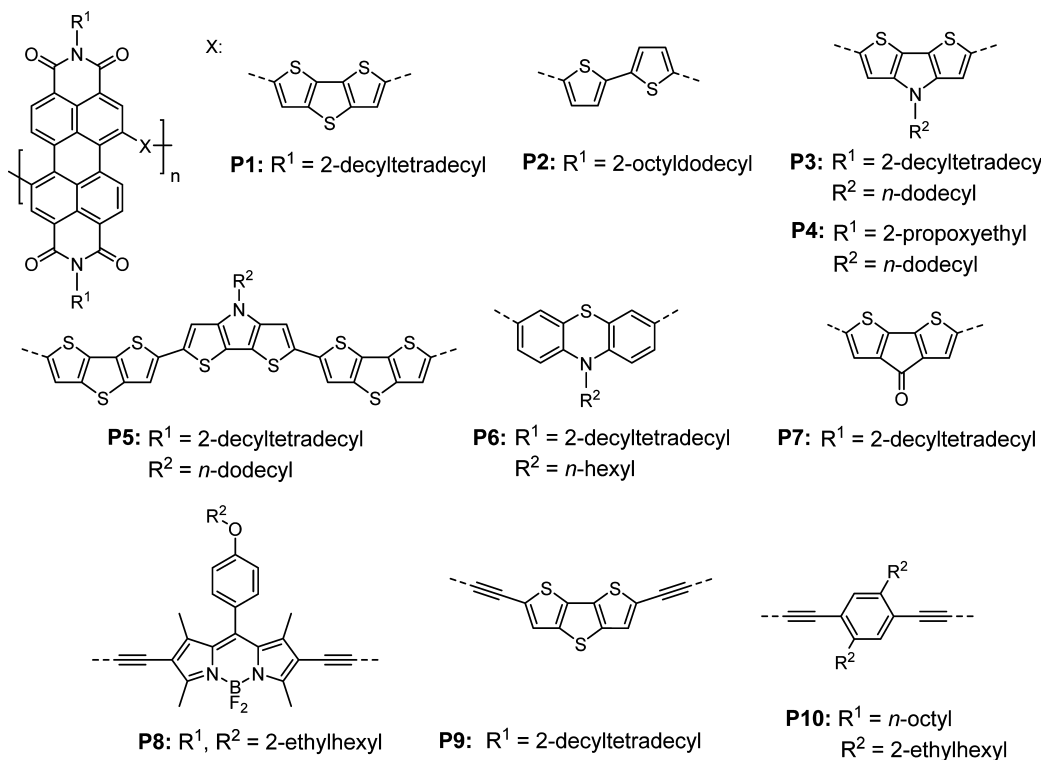


**Figure 14.** Chemical structures of PDI-based polymers for OTFTs.

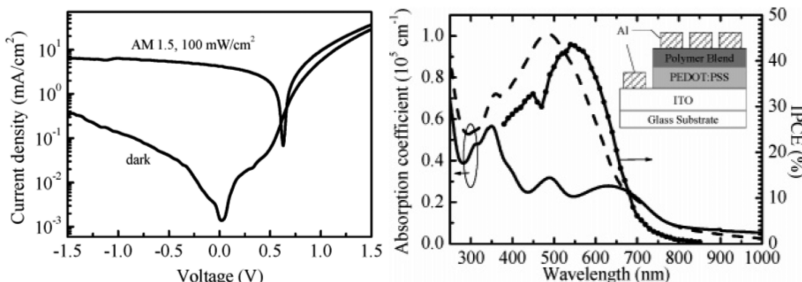


**Figure 15.** (Left) Current density–voltage ( $J$ – $V$ ) characteristics of an all-polymer solar cell having the structure ITO/PEDOT:PSS/**P1:D1** (1:1, w/w)/Al in the dark and under illumination of an AM 1.5 solar simulator, 100 mW/cm<sup>2</sup>. (Right) Absorption spectra of films of **P1** (plain line) and of a **P1:D1** (1:1, w/w) blend (dashed line) spin coated from chlorobenzene, and plot of incident photon to current conversion efficiency (IPCE) as a function of wavelength. Reprinted with permission from ref 156. Copyright 2007 American Chemical Society.

and ambipolar transport with a  $\mu_e/\mu_h$  of  $3 \times 10^{-4}/4 \times 10^{-5} \text{ cm}^2/(V \text{ s})$ .<sup>159</sup>

**P6** was synthesized under Suzuki coupling using a dibrominated PDI regiosomer mixture and 10-hexyl-2,8-bis-(4,4,5,5-tetramethyl-1,3,2-dioxaborolan-2-yl)phenothiazine.<sup>160</sup> Phase-transfer catalyst Aliquat 336 can improve the polymer  $M_n$  and lower the PDI. UV absorption spectra show that the low energy charge-transfer band of the high  $M_n$  batch has a  $\sim 10$  nm red shift in comparison to that of the low  $M_n$  one. BGTC OTFTs of **P6** ( $M_n = 10$  kDa; PDI 1.53) with Au electrodes show the highest  $\mu_e$  of  $0.05 \text{ cm}^2/(\text{V s})$  in  $N_2$ , while the low  $M_n$  batch ( $M_n = 5$  kDa; PDI 1.95) OTFTs exhibit a  $\mu_e$  of  $0.02 \text{ cm}^2/(\text{V s})$ . AFM investigation reveals that **P6** films are very smooth and exhibit amorphous microstructures without any crystalline domains.

A new acceptor–acceptor-type copolymer **P7** bearing PDI and fluorenone was synthesized by Suzuki coupling.<sup>161</sup> Compared to **P1**, **P7** has a larger band gap of 1.96 eV but the LUMO is lowered by 0.1 eV. **P7** OTFTs show a  $\mu_e$  of  $\sim 0.01 \text{ cm}^2/(\text{V s})$  in air; however, **P1** does not function under identical conditions. The

enhanced **P7** OTFT stability is attributed to its lower LUMO and denser packing. By incorporating an acetylene linker, a novel 4,4-difluoro-4-borata-3a-azonia-4a-aza-s-indacene dye (BODIPY) and PDI copolymer **P8** was synthesized via Sonogashira polymerization.<sup>162</sup> **P8** shows broad absorption in the visible region (350–800 nm) while retaining the intense absorption characteristics of both BODIPY and PDI. The electron-deficient PDI leads to a low-lying LUMO/HOMO of  $-4.09/-5.73$  eV. Preliminary charge transport investigations of **P8** show a low  $\mu_e$  of  $1.3 \times 10^{-5} \text{ cm}^2/(\text{V s})$  with an  $I_{on}/I_{off}$  of  $10^4$  in BGTC OTFTs. **P9** was synthesized via Sonogashira coupling. The rod-like ethynylene spacer greatly reduces steric hindrance and promotes backbone  $\pi$ -conjugation and coplanarity. As compared to **P1** without the linker, **P9** shows an 89 nm red-shifted low-energy absorption band and a 0.1 eV lower LUMO. **P9** BGTC OTFTs achieve a  $\mu_e$  of  $0.06 \text{ cm}^2/(\text{V s})$  in air; however, the **P1** devices do not function under the same structure. In ambient, BGBC OTFTs exhibit  $\mu_e$ s of 0.075 and  $0.034 \text{ cm}/(\text{V s})$  for **P9**- and **P1**-based OTFTs, respectively. Moreover, **P9** demonstrates

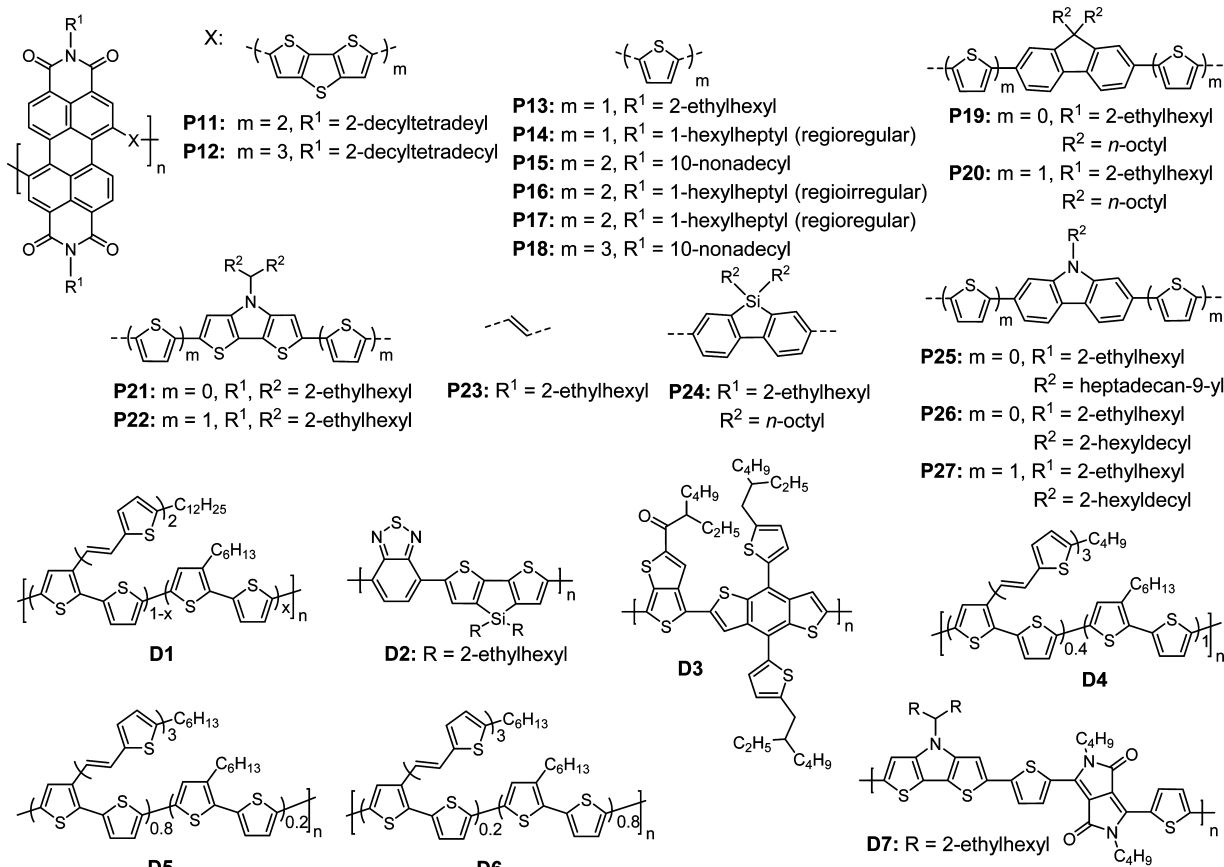


**Figure 16.** Chemical structures of PDI-based polymers for all-polymer solar cells. Chemical structures of donor semiconductors **D1–D7** used in all-polymer solar cells are also included.

enhanced OTFT stability versus **P1** under similar storage conditions. Grazing incidence X-ray diffraction (GIXRD) reveals that **P9** is crystalline while **P1** is amorphous, due to the reduced steric hindrance of the ethynylene link in **P9**. PDI-containing poly(phenylene ethynylene)-type polymer **P10** was also synthesized, which shows good solubility but a strong tendency to aggregate.<sup>163</sup> In chloroform, **P10** undergoes self-assembly at room temperature to form nanowires. Films fabricated from **P10** nanowire suspensions show highly ordered microstructures and a high degree edge-on orientation with respect to the film plane. Such morphology leads to a substantial  $\mu_e$  of  $0.1 \pm 0.05 \text{ cm}^2/(\text{V s})$  with a high  $I_{on}/I_{off}$  of  $4 \times 10^6$  and a low  $V_t$  of 8 V in BGTC OTFTs after the nanowire OTFTs are annealed at 200 °C. The results demonstrate that PDI polymer nanowires are suitable materials for fabricating high-performance OTFTs via simple solution coating.

### 2.3. Perylene Diimide-Based Polymer Semiconductors for OSCs

The low LUMO, good electron transport, and broad absorption render PDI polymers as promising candidates for all-polymer solar cells. **P1** (Figure 14) was first used as the acceptor semiconductor with bis(thienylenevinylene)-substituted polythiophene donor semiconductor **D1** (Figure 16)<sup>164</sup> to fabricate OSCs having the structure ITO/PEDOT:PSS/**D1:P1** (1:1; w/w)/Al. The incident photon to converted current efficiency curve indicates photon-to-current conversion up to 850 nm, manifesting photocurrent generation from **P1** absorption (Figure 15). A PCE of ~1% with a  $J_{sc}$  of 4.2 mA/cm<sup>2</sup>, a  $V_{oc}$  of

0.63 V, and a  $FF$  of 39% is achieved, which was among the highest for all-polymer OSCs at that time.<sup>156</sup>

**P1** was next incorporated into inverted cells, in which benzothiadiazole–dithienosilole copolymer **D2** (Figure 16) was used as donor semiconductor.<sup>165</sup> The optimized inverted cells having the structure ITO/ZnO/**D2:P1/PEDOT:PSS/Ag** achieve a moderate PCE of 0.63% with a  $J_{sc}$  of 2.41 mA/cm<sup>2</sup>, a  $V_{oc}$  of 0.60 V, and a  $FF$  of 43%, which is higher than that in conventional cells. The roll-to-roll (R2R) fabricated large-area cells (4.2 cm<sup>2</sup>) show a PCE of 0.20% using the same device structure.<sup>165</sup> Zhan and co-workers recently developed a novel all-polymer solar cell containing **P1** as the acceptor semiconductor and a high-performance benzodithiophene and thienothiophene copolymer **D3** as the donor semiconductor.<sup>166</sup> The optimized cells show a PCE up to 3.45% with a  $J_{sc}$  of 8.55 mA/cm<sup>2</sup>, a  $V_{oc}$  of 0.752 V, and a  $FF$  of 52%. It was found that binary additives synergistically boosted cell performance. The nonvolatile additive PDI-2DTT, which is the repeating unit of **P11** (Figure 16), suppressed **P1** aggregation and enhanced **D3:P1** mixing. Adding 2% PDI-2DTT additive in 1,2-dichlorobenzene led to PCE enhancement from 1.16% to 1.43%. The second additive, 1,8-diiodooctane (DIO), facilitated the **D3** aggregation and crystallization and improved phase separation. Hence, adding 6% DIO in 1,2-dichlorobenzene resulted in a substantial PCE improvement from 1.16% to 2.92%. A combination of PDI-2DTT and DIO significantly boosted the PCE to 3.45%, which was attributed to suitable phase separation and balanced charge transport.<sup>166</sup>

The polymer structure was next modified by changing the donor to the dithienothiophene dimer. The resultant **P11** (Figure 16) when combined with the polythiophene donor semiconductor **D4** showed a  $J_{sc}$  of  $5.02 \text{ cm}^2/(\text{V s})$ , a  $V_{oc}$  of  $0.69 \text{ V}$ , a  $FF$  of  $43\%$ , and a PCE of  $1.50\%$ .<sup>167</sup> As the conjugation length of the donor counter unit was further increased to the dithienothiophene trimer, the polymer band gap was further decreased for **P12**. All-polymer cells having a **D4:P12** active layer showed a  $J_{sc}$  of  $2.80 \text{ cm}^2/(\text{V s})$ , a  $V_{oc}$  of  $0.69 \text{ V}$ , a  $FF$  of  $40\%$ , and a PCE of  $0.77\%$ , which was lower than that of the **D4:P11** cells.<sup>167</sup> The ICPE curves of **P1**, **P11**, and **P12** cells indicated that excitation from the acceptor semiconductors had a limited contribution to photocurrent, which could be ascribed to the following factors: (a) although the PDI polymers show absorption extending into the near-IR region, the absorption coefficient in this region is small; (b) the PDI polymers usually have a short excited-state lifetime, which hampers intermolecular charge transfer and limits exciton dissociation.<sup>168</sup>

PDI and oligothiophene copolymers were also synthesized for all-polymer solar cells.<sup>169</sup> **P13** having a monothiophene donor was synthesized, and an optimal PCE of  $0.97\%$  was achieved when **P13** was blended with polythiophene derivative **D5**.<sup>170</sup> **P15** with a bithiophene donor or **P18** with a terthiophene donor was incorporated into all-polymer cells having the structure ITO/PEDOT:PSS/P3HT:**P15** (or **P18**)/Al. Without extensive optimizations, the cells achieved PCEs of  $0.4\%$  and  $0.8\%$  for **P15** and **P18**, respectively.<sup>169</sup> Pei and co-workers later reported similar PDI-bithiophene copolymers **P16** and **P17** but having different alkyl chains than **P15** and investigated the effect of polymer purity and regioregularity on device performance.<sup>80</sup> Regioirregular **P16** was synthesized from the regiosomer mixture. It contained both 1,7-dibromo PDI and 1,6-dibromo PDI. However, regioregular **P17** was polymerized from only 1,7-dibromo PDI. Therefore, the **P16** polymer backbone grew in two different fashions, i.e., via 1,7-linkage or 1,6-linkage. In contrast to Würthner's procedure,<sup>152</sup> the 1,7-dibromo PDI monomer was purified by repeated column chromatography. It is interesting to note that **P16** and **P17** have nearly identical optoelectronic properties. The swallow-tail 1-hexylheptyl chains can greatly suppress polymer aggregation and promote phase segregation with the donor semiconductor P3HT. All-polymer cells using regioirregular **P16** as the acceptor semiconductor blended with P3HT showed a PCE of  $0.45\%$  in a conventional device having the structure ITO/PEDOT:PSS/P3HT:**P16**/LiF/Al, while the P3HT:**P17** cells showed an improved PCE of  $0.94\%$  in the same structure. Further optimization led to greatly improved PCEs of  $1.55\%$  and  $2.17\%$  for **P16** and **P17** cells, respectively, but in inverted devices having the structure ITO/ZnO/P3HT:**P16** (or **P17**)/MoO<sub>3</sub>/Ag. The mobility measurement in the SCLC regime showed that **P17** had slightly improved  $\mu_e$  ( $5 \times 10^{-4} \text{ cm}^2/\text{V s}$ ) over that ( $3 \times 10^{-4} \text{ cm}^2/\text{V s}$ ) of **P16**, which led to a larger  $J_{sc}$  and improved PCE for **P17** cells. The result reveals the significance of polymer regioregularity for performance enhancement. Compared to conventional cells, inverted cells show reduced series resistance and improved  $J_{sc}$ s and  $FF$ s. An X-ray photoelectron spectroscopy (XPS) investigation showed spontaneous vertical phase gradation with a P3HT-rich layer on the top surface of the blend film spin cast onto PEDOT:PSS or ZnO substrate. The favorable connection between the P3HT-rich layer and the anode in inverted cells suppresses charge recombination and improves charge collection. Therefore, the  $FF$ s,  $J_{sc}$ s, and PCEs were improved in inverted cells.<sup>62,80</sup>

PDI side chain and regioregularity play important roles in OSC performance;<sup>80</sup> therefore, regioregular PDI containing a swallow-tail-like 1-hexylheptyl chain was copolymerized with monothiophene to afford **P14**.<sup>171</sup> Narrow band-gap polymer **P302**<sup>172</sup> (Figure 48) was chosen as the donor semiconductor for all-polymer cells having the inverted structure ITO/ZnO/**P302:P14/MoO<sub>3</sub>/Ag**. Although the LUMO–LUMO offset is only  $0.1 \text{ eV}$  between **P302** and **P14**, the OSCs show a promising PCE of  $3.48\%$  with a  $J_{sc}$  of  $6.91 \text{ mA/cm}^2$ , a  $V_{oc}$  of  $1.01 \text{ V}$ , and a  $FF$  of  $50\%$ .<sup>171</sup> Film morphology characterization suggests that the phase separation domain size is the most critical factor limiting the device performance of all-polymer OSCs. Therefore, **P330**<sup>173</sup> (Figure 49) containing a small fraction of polystyrene side chain is used as the donor semiconductor to control phase separation in all-polymer blend, and the resulting **P330:P14** cells show an enhanced PCE of  $4.21\%$  with a  $J_{sc}$  of  $8.77 \text{ mA/cm}^2$ , a  $V_{oc}$  of  $1.04 \text{ V}$ , and a  $FF$  of  $46\%$ . In comparison to the domain size ( $54 \text{ nm}$ ) of **P302:P14** cells, the **P330:P14** cells show a median size of  $30 \text{ nm}$ .<sup>171</sup> The PCE is among the highest for all-polymer cells, and the results demonstrate that PDI polymers are promising acceptor semiconductors for all-polymer solar cells.

Using fluorene or dithienopyrrole donor with/without a thiophene spacer, four copolymers **P19–P22** were synthesized having tunable band gaps.<sup>174</sup> The fluorene-based **P19** has a wider band gap than the thienopyrrole-based counterpart **P21** due to the higher steric hindrance, weaker electron-donating ability, and higher degree of aromaticity of fluorene in **P19**, which limits the population of the quinoidal form. Introduction of thiophene spacers reduces steric hindrance and enhances conjugation for **P20** and **P22**. **P22** has the narrowest band gap of  $1.24 \text{ eV}$ . **P19–P22** are then blended with **D6** or a dihydropyrrolo[3,4-*c*]pyrrole-1,4-dione (DPP)-based low-band-gap **D7** for all-polymer solar cells. Fluorene-based **P19** and **P20** achieve higher  $V_{oc}$ s than dithienopyrrole-based **P21** and **P22**. The champion cell having a  $J_{sc}$  of  $3.05 \text{ mA/cm}^2$ , a  $V_{oc}$  of  $0.66 \text{ V}$ , a  $FF$  of  $46\%$ , and a PCE of  $0.93\%$  is achieved from **D6:P21** cells.

Using various donors including vinylene (**P23**), thiophene (**P13**), dithienopyrrole (**P21**), fluorene (**P19**), dibenzosilole (**P24**), and carbazole (**P25**), Hashimoto et al. systematically investigated a series of PDI polymers to fine tune their optoelectronic properties.<sup>170,174</sup> The changes in the donors result in tailored LUMOs varying from  $-4.05$  (**P23**) to  $-3.61 \text{ eV}$  (**P19**). Without optimization, these polymers exhibit good  $\mu_e$ s of  $10^{-4}$ – $10^{-3} \text{ cm}^2/(\text{V s})$  in OTFTs. All-polymer cells having the structure ITO/PEDOT:PSS/active layer/cathode are then fabricated and optimized, in which the active layer comprises a polythiophene derivative or P3HT as the donor semiconductor and PDI polymer as the acceptor semiconductor. In most cases using chlorobenzene, a Ca/Al cathode, and a donor semiconductor:acceptor semiconductor weight ratio of 2:1 without postannealing, results in optimal performance. It was found that the toluene:chloroform (9:1) mixed solvent can greatly improve film morphology, and the best performing **D5:P25** cell using this solvent mixture yields a  $V_{oc}$  of  $0.70 \text{ eV}$ , a  $J_{sc}$  of  $6.35 \text{ mA/cm}^2$ , a  $FF$  of  $50\%$ , and a PCE of  $2.23\%$ . The PCE was among the highest for all-polymer cells at that time. The  $0.83 \text{ eV}$  LUMO–LUMO offset between **D5** and **P25** indicates that there is great room for  $V_{oc}$  enhancement by structural modifications of donor semiconductor and/or acceptor semiconductor. In comparison to **P25**, **P26** and **P27** having a less bulky 2-hexyldecyl on carbazole show degraded PCEs of  $0.1\%$  and  $0.68\%$ , respectively, when blended with P3HT, which are attributed to the coarse phase separation at  $\sim 100 \text{ nm}$ .

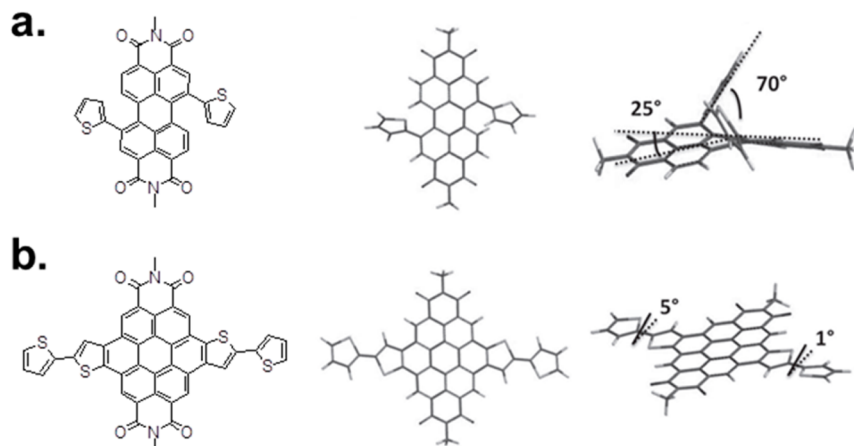
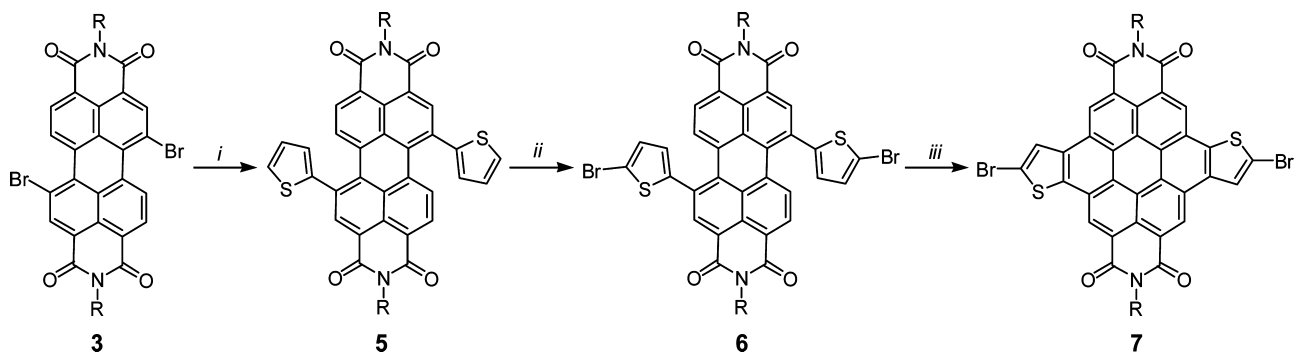


**Figure 17.** Chemical structures and DFT-calculated molecular geometries of (a) thiophene-substituted perylene diimide and (b) thiophene-substituted dithienocoronene diimide illustrating dihedral angles. Reprinted with permission from ref 175. Copyright 2012 Wiley-VCH Verlag GmbH & Co. KGaA.

**Scheme 3. Synthetic Route to Dibrominated Dithienocoronene Diimide from Dibrominated Perylene Diimide<sup>175a</sup>**



<sup>a</sup>Reagent and conditions: (i) 2-(Tributylstannyl)thiophene,  $\text{Pd}(\text{PPh}_3)_4\text{Cl}_2$ , toluene, 80 °C; (ii) NBS, DMF; (iii)  $\text{h}\nu$  (300 nm), I<sub>2</sub>, benzene. R = 12-tricosanyl.

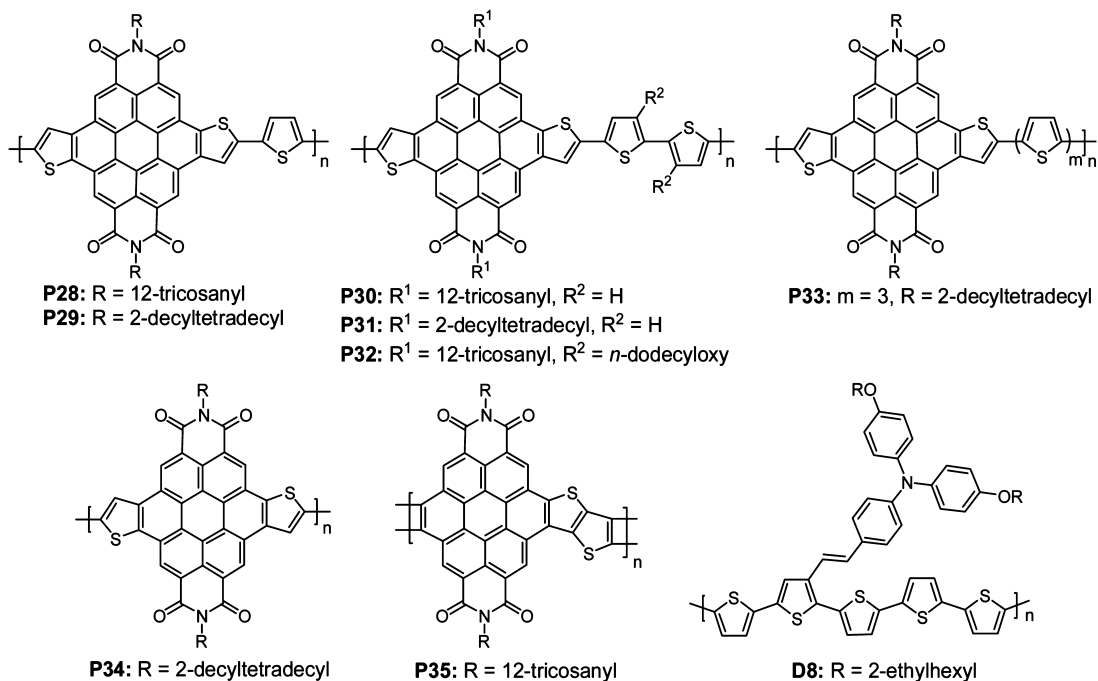


**Figure 18.** Chemical structures of dithienocoronene diimide-based polymers for OTFTs and OSCs. Chemical structure of donor semiconductor D8 used in all-polymer solar cell is also included.

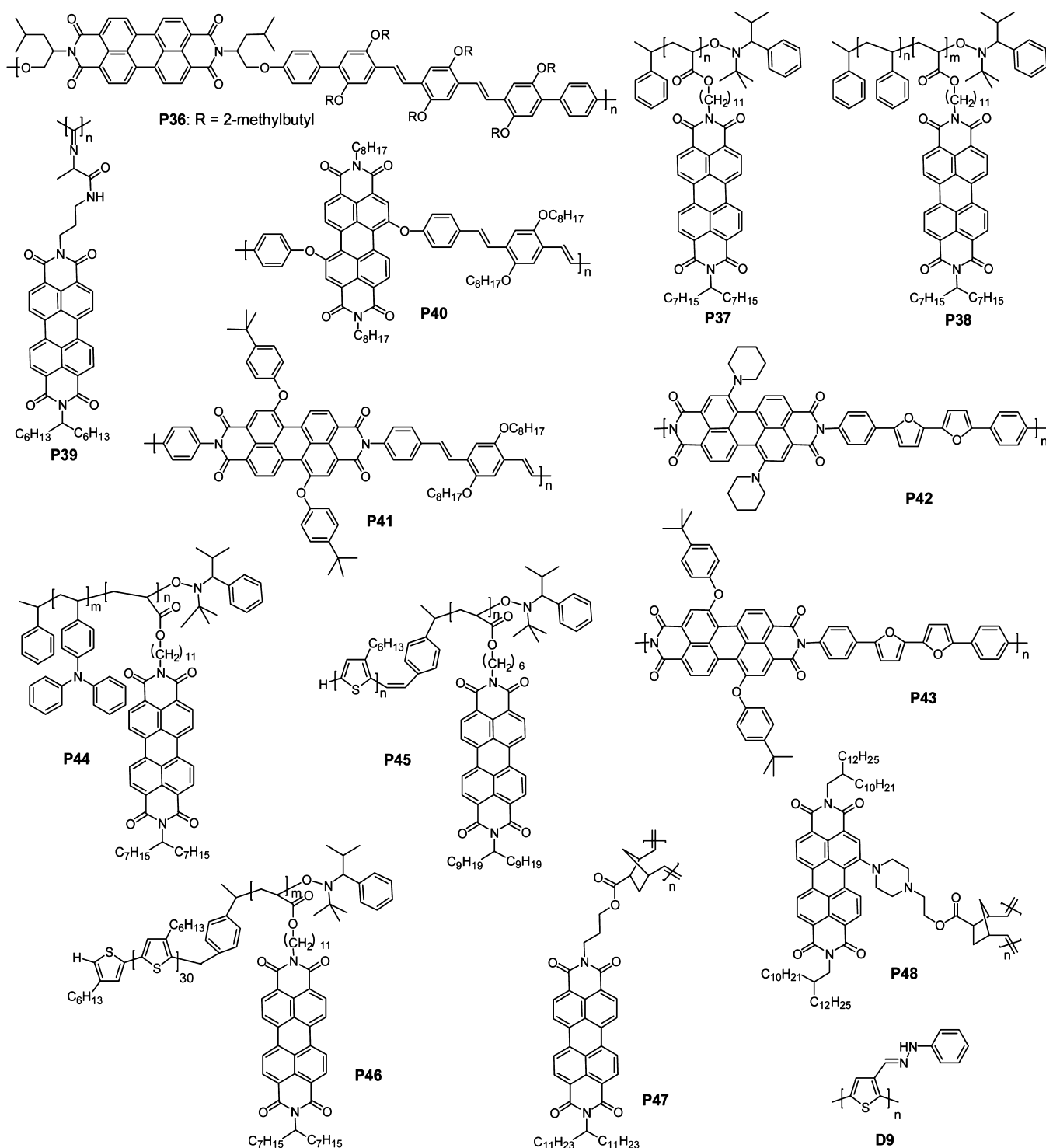


**Figure 19.** The chemical structures of nonconjugated perylene diimide-based polymers for OTFTs and OSCs. The chemical structure of donor semiconductor D9 used in all-polymer solar cell is also included.

#### 2.4. Dithienocoronene Diimide-Based Polymer Semiconductors for OTFTs and OSCs

PDI polymers have shown promising OTFT and OSC performance. However, the optoelectronic property and microstructure investigations unambiguously manifest a low degree of backbone coplanarity and materials crystallinity of PDI polymers. DFT computation indicates that the sterically encumbered PDI bay region causes substantial backbone torsion with a dihedral angle of  $\sim 25\text{--}70^\circ$  (Figure 17a) between the PDI and the

neighboring thiophene, which decreases film ordering and lowers charge carrier mobility.<sup>175</sup> Coronene is a rigid and coplanar aromatic system, and the fused six-membered rings in the bay region greatly increase the core coplanarity.<sup>176</sup> As a PDI derivative, dithienocoronene diimide (DTCDI) was first designed by Usta and coworkers.<sup>175</sup> Presynthesis computation indicates that DTCDI has greatly reduced steric hindrance and a high degree of core coplanarity (Figure 17b). Moreover, in comparison to dibrominated PDI, dibrominated DTCDI should

have a more linear monomer-linkage geometry with negligible angle difference between syn and anti regioisomers. The high backbone coplanarity and linear geometry should promote polymer packing and ordering and increase the charge carrier mobility.

The synthetic route to the dibrominated DTCDI is depicted in Scheme 3. Dibrominated PDI **3** is coupled with 2-(tributylstannyl)thiophene under Stille coupling to yield **5** in high yield. Please note that the starting material **3** is a mixture of the 1,6- and 1,7-regioisomers (**3a** + **3b**, Scheme 1), but only 1,7-dibrominated monomer (**3a**) is shown in Scheme 3 for simplicity. The coupling product **5** shows improved solubility over **3** due to the suppressed  $\pi$ - $\pi$  stacking (Figure 17a) induced by the backbone torsion of **5**. The following  $\alpha$ -bromination using NBS in DMF affords compound **6**, which undergoes photocyclization reaction ( $\lambda = 300$  nm) in the presence of  $I_2$  to provide the dibrominated monomer **7** in quantitative yield (98%). The highly effective photocyclization has been employed in the synthesis of PDI-based ladder-type polymer **P35** (Figure 18).<sup>177</sup> It is interesting to note that the  $^1H$  NMR spectra of monomer **7** are concentration dependent. A model compound thiophene-flanked **7** was also synthesized, and the  $^1H$  NMR spectra show that the hydrogen signals assigned to the aromatic core shift upfield and become wider as the concentrations increase, indicating a shielding effect caused by staggered  $\pi$ - $\pi$  stackings. Such stacking will benefit charge transport, as seen in disc-like hexabenzocoronene-based semiconductors.<sup>178</sup> It was found that cyclization leads to destabilized LUMOs by 0.3–0.4 eV for DTCDIs, which is attributed to the electron-rich thiophene annulation to the bay region.<sup>177</sup>

DTCDI polymers **P28**, **P30**, and **P32** (Figure 18) were synthesized via Stille coupling. Among them, **P28** and **P32** achieved decent  $M_n$ s of 11 and 51 kDa with good solubilities in common organic solvents, respectively.<sup>175</sup> However, **P30** was insoluble, which prevented its characterization and application in organic electronics. Optoelectrical investigation of these polymers indicated that the DTCDI polymers have wider band gaps and higher LUMOs than the PDI polymer counterparts.<sup>179</sup> The **P28** and **P32** LUMOs are  $-3.70$  eV, comparable to that of DTCDI monomer **7** ( $-3.74$  eV), while the polymer HOMOs are  $-5.56$  and  $-5.01$  eV for **P28** and **P32**, respectively. TGBC OTFTs were fabricated using a poly(methyl methacrylate) (PMMA) dielectric and Au as the source/drain. All device fabrications and characterization were performed in ambient. **P28** and **P32** showed clear ambipolarity. **P28** OTFTs exhibited a maximum  $\mu_e/\mu_h$  of  $0.30/0.04$  cm $^2$ /(V s), and **P32** OTFTs showed lower performance with a maximum  $\mu_e/\mu_h$  of  $0.03/0.003$  cm $^2$ /(V s). The OTFTs showed good current modulation ( $I_{on}/I_{off}$ ) of  $10^{5-6}$  for n-channel operation and of  $10^{3-5}$  for p-channel operation.<sup>175</sup> The DTCDI polymers have a  $\sim 10$  times higher  $\mu_e$  ( $10^{-3}-10^{-1}$  cm $^2$ /(V s)) than the PDI polymer counterparts,<sup>156,158</sup> which is attributed to the higher degree of backbone coplanarity of the DTCDI polymers. The performance was among the best for ambipolar OTFTs with TGBC structure in ambient at that time. The **P28** and **P32** performance difference is in good agreement with the film microstructures due to the different alkyl densities and varied short/long-range intra/interchain interactions. Both polymer TGBC OTFTs show negligible performance degradation after 1 week storage in ambient, which is attributed to the interplay of the polymer electronic structures, film morphologies, and self-encapsulated top-gate OTFT structures.

Zhan et al. reported a series of DTCDI polymers having varied oligothiophene conjugation length for all-polymer solar cells.<sup>180</sup> The n-type polymers **P29**, **P31**, **P33**, and **P34** were synthesized via Stille coupling with  $M_n$ s of 9.8–15.8 kDa and showed good solubility in organic solvents except for **P33**. As the thiophene number increases the polymer band gap decreases. The band gaps derived from the absorption onsets are 1.93, 1.83, and 1.78 eV for **P34**, **P29**, and **P31**, respectively. The cyclic voltammetry derived LUMOs of all these polymers are around  $-3.5$  eV, 0.4–0.5 eV higher than those of the PDI polymer counterparts.<sup>156</sup> All-polymer cells are fabricated having the structure ITO/PEDOT:PSS/active layer/Ca/Al using **P34**, **P29**, or **P31** as the acceptor semiconductor and a polythiophene derivative **D8** as the donor semiconductor. PCEs of 0.31%, 0.41%, and 0.84% are achieved for **P34**, **P29**, and **P31** cells, respectively, with large  $V_{oc}$ s of  $\sim 0.90$  eV. The  $V_{oc}$ s are much higher than that (0.68 eV) of **D8:PC<sub>70</sub>BM** cells,<sup>181</sup> in agreement with the higher LUMOs of these DTCDI polymers. Morphological characterization indicates that improved phase separation should be achieved for further performance optimization.

A novel DTCDI ladder-type polymer **P35** was synthesized in quantitative yield from perylene diimide and thienothiophene copolymer using photocyclization catalyzed by  $I_2$  and sunlight.<sup>177</sup> Postpolymerization photocyclization is similar to the reaction used for conversion of compound **6** to **7** in Scheme 3. After cyclization, the ladder polymer **P35** maintains good solubility (7 mg/mL in chloroform) but exhibits very strong aggregation. No OTFT and OSC performance is reported for this material to date.

## 2.5. Perylene Diimide-Based Nonconjugated Polymers for OTFTs and OSCs

PDI has also been incorporated into nonconjugated polymers for organic electronics due to its extended  $\pi$ -core. In 2003, Janssen reported **P36** (Figure 19) containing PDI and oligo(phenylene vinyl) chromophores linked via a saturated spacer.<sup>128</sup> Importantly, **P36** exhibited photoinduced singlet energy transfer, and OSCs having the structure ITO/PEDOT:PSS/**P36**/LiF/Al were fabricated using a single **P36** layer. The cells showed a high  $V_{oc}$  of  $\sim 1$  V, but the  $J_{sc}$  was extremely low (<0.01 mA/cm $^2$ ). Thereafter, various PDI-containing nonconjugated polymers were developed,<sup>182</sup> in which the PDIs were incorporated into backbones or were pendant groups. The resulting polymers show interesting optoelectronic properties, self-assembly, and promising device performance.<sup>182</sup>

Thelakkat investigated the charge transport properties of the homopolymer poly(perylene diimide acrylate) **P37** and diblock copolymer polystyrene-block-poly(perylene diimide acrylate) **P38**.<sup>183</sup> The PDI moiety was attached to the polyacrylate backbone via a C11 spacer with another end having a swallow-tail-like undecan-6-yl chain. **P37** and **P38** have a LUMO of  $-3.9$  eV, imparted by the PDI moiety. The homopolymer **P37** was crystalline with a melting point of 190 °C induced by strong PDI  $\pi$ - $\pi$  stacking. **P37** OTFTs exhibited a  $\mu_e$  of  $1.2 \times 10^{-3}$  cm $^2$ /(V s) with an  $I_{on}/I_{off}$  of  $10^4$  in a glovebox. Interestingly, the block copolymer **P38** containing 30% polystyrene showed identical performance. Therefore, dilution of the active poly(perylene diimide acrylate) by insulating polystyrene did not impair charge transport, which was likely due to migration of the PDI-containing block microdomains onto the dielectric surface. The PDI-substituted rigid and helical polyisocyanopeptides **P39** was synthesized via nickel-catalyzed polymerization of isocyanide, in which the polyisocyanopeptides functioned as a scaffold to tailor

interchromophore interactions among the PDI groups.<sup>184</sup> **P39** formed “supercoils”, stabilized by its strong intermolecular or long-range intramolecular interactions. **P39** BGTC OTFTs showed a  $\mu_e$  of  $10^{-3}$  cm<sup>2</sup>/(V s). The studies pointed toward effective  $\pi-\pi$  stackings, and substantial  $\mu_e$ s can be achieved through developing innovative supramolecular materials with precisely tailored functionalities.

Li and co-workers studied **P40** containing oligo(phenylene vinylene) connected to the PDI 1,7-bay positions through ether linkage.<sup>185</sup> **P40** was synthesized by a Wittig reaction and had a  $M_n$  of 6.8 kDa. OSCs having the structure ITO/PEDOT:PSS/**P40**/Ca/Al show a PCE of 0.07% with a single-component active layer.<sup>185</sup> **P40** bears all functionalities required for light absorption, exciton separation, and charge transport. An alternating polymer **P41** containing PDI and oligo(phenylene vinylene) in the backbone was synthesized by Heck coupling having a  $M_n$  of 8 kDa and a PDI of 2.4.<sup>186</sup> **P41** showed broad absorption with a band gap of 1.66 eV, but the absorption coefficient in long wavelength is much lower than that in short wavelength. An average  $\mu_e$  of  $8.5 \times 10^{-3}$  cm<sup>2</sup>/(V s) was measured from the SCLC regime in an electron-only device. Using **D9** (Figure 19) as the donor semiconductor, all-polymer cells having the structure ITO/**D9**:**P41**/Al show a PCE of 2.32% with a  $J_{sc}$  of 2.98 mA/cm<sup>2</sup>, a  $V_{oc}$  of 0.60 V, and a FF of 39% under illumination of white light (intensity of 30 mW/cm<sup>2</sup>).

**P42** and **P43** were synthesized via polycondensation between perylene dianhydride and 5,5'-bis(4-aminophenyl)-2,2'-bifuran and have a low  $M_n$  of 1.5 kDa and a narrow PDI of 1.02.<sup>187</sup> The PDI is functionalized with electron-rich piperidinyl and 4-*tert*-butylphenoxy at the 1,7-positions for better absorption through push–pull interaction.<sup>188</sup> The strong electron-donating piperidinyl results in a greatly red-shifted absorption of **P42** as compared to that of **P43**. Under AM 1.5 G illumination, OSCs having the structure ITO/PEDOT:PSS/**P42**(or **P43**)/Ca/Al show a PCE of 1.23% with a  $J_{sc}$  of 2.16 mA/cm<sup>2</sup>, a  $V_{oc}$  of 1.24 V, and a FF of 46% for **P42** cells and a PCE of 1.18% with a  $J_{sc}$  of 2.65 mA/cm<sup>2</sup>, a  $V_{oc}$  of 1.11, and a FF of 42% for **P43** cells.<sup>187</sup> The remarkable  $V_{oc}$ s (>1.10 V) of **P42** and **P43** cells are attributed to the elevated LUMOs (~3.8 eV) enabled by the electron-donor substituents on the 1,7-positions of the PDI core.

Diblock copolymer **P44** containing poly(vinyltriphenylamine) and poly(perylene diimide acrylate) segments can self-assemble into nanostructure, providing charge-separating interfaces at the nanoscale.<sup>189</sup> OSCs having the structure ITO/PEDOT:PSS/**P44**/Al show a PCE of 0.07%, which is one order higher than that of solar cells using a poly(vinyltriphenylamine):poly(perylene diimide acrylate) blend as the active layer.<sup>189</sup> The single active layer OSCs were obtained by self-assembly of a diblock copolymer to achieve functionalities of exciton formation and dissociation and charge transport, which usually require two components.<sup>74</sup> While the absolute PCE of **P44** single active layer OSCs is much lower than that of the state-of-the-art OSCs, the concept of nanostructured BHJ OSCs based on a single block copolymer is a breakthrough in the design of organic electronic devices.<sup>189</sup> Double-crystalline diblock copolymer **P45** bearing poly(3-hexylthiophene) as the electron-donor semiconductor block and poly(perylene diimide acrylate) as the electron-acceptor semiconductor block was synthesized via combination of Grignard metathesis polymerization and controlled free radical polymerization.<sup>190</sup> **P45** was designed for better absorption and higher mobility in comparison to **P44**.<sup>189</sup> OSCs having the structure ITO/PEDOT:PSS/**P45**/LiF/Al showed an enhanced PCE of 0.49% with 100 mA/cm<sup>2</sup>

illumination (AM 1.5 G).<sup>189</sup> As a **P45** analogue, **P46** with pentadecan-8-yl on imide exhibited switching behavior of charge transport in OTFTs. The electrically active poly(3-hexylthiophene) and poly(perylene diimide acrylate) can self-assemble into continuous microdomains and form percolation channels for transport of an electron or a hole or both with a moderate mobility of  $10^{-5}$  cm<sup>2</sup>/(V s), depending on the block ratio ( $m$ , Figure 19) and the processing conditions.<sup>191</sup>

Polynorbornenes **P47** and **P48** containing PDI pendants were synthesized via ring-opening metathesis polymerizations.<sup>192</sup> For **P47** with PDI–norbornene linkages via the imide nitrogen, UV-vis absorption spectra showed significant PDI–PDI aggregation and XRD diffractions exhibited  $\pi-\pi$  stacking. **P47** OTFTs show weak n-channel performance with a  $\mu_e$  of  $3 \times 10^{-5}$  cm<sup>2</sup>/(Vs), and all-polymer OSCs exhibited a PCE of 0.38% when blended with P3HT. In contrast, the “bay”-linked polymer **P48** had monomer-like absorption, indicating minimal  $\pi-\pi$  stacking. **P48** OTFTs showed no measurable transistor performance, and OSCs containing a P3HT:**P48** active layer showed a PCE of 0.04%. In comparison to the PCE of **P47**, the degraded performance of **P48** is due to the nonplanarity of bay-substituted PDIs of **P48**.

## 2.6. Summary

PDIs were successfully incorporated into polymer semiconductors, which have exhibited promising OTFT and OSC performance. As the first diimide-functionalized conjugated polymer family, the introduction of PDI polymers has generated great interest in developing high-performance n-channel polymers as well as encouraging the design and implementation of various imide-functionalized arene-based polymers. The planar and extended electron-deficient PDI greatly promotes electron injection and transportation in both conjugate and nonconjugated polymer semiconductors. On the basis of the optoelectrical studies and film morphology/microstructure characterization, the device performance of PDI polymers is mainly limited by the backbone torsion due to the sterically encumbered PDI bay region. To attenuate such steric hindrance, dithienocoronene diimide polymers have been developed and show encouraging device performance. Further materials modifications should focus on increasing PDI polymer coplanarity and crystallinity.

## 3. NAPHTHALENE DIIMIDE-BASED POLYMER SEMICONDUCTORS

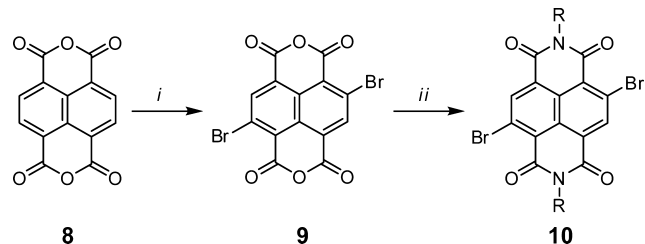
As a structural analogue to perylene diimides, 1,4,5,8-naphthalene diimides (or simplified as naphthalene diimides) show comparable LUMOs and the OTFT performance of naphthalene diimide (NDI) small molecules is among the best n-channel semiconductors.<sup>123,127,156</sup> From energetic considerations, NDI polymers should be promising n-channel semiconductors. There are several advantages of NDI polymers. First, NDI polymers can be easily obtained in a regiosomERICALLY pure form.<sup>193</sup> Second, NDI polymers should have better solubilities and hence higher  $M_n$ s in comparison to PDI polymers due to the smaller NDI core. Third, the 2,6-positions of NDI should allow the polymers to achieve a more planar backbone than bridging via the sterically congested PDI bay positions. The similar LUMO, improved solubility, and higher degree of backbone coplanarity make NDI polymers more attractive than PDI polymer counterparts as n-channel semiconductors. A variety of NDI polymers have been designed and systematically investigated for structure–property–device performance correlations,

and highly promising OTFT and OSC performance has been obtained from NDI polymers.

### 3.1. Synthesis of Dibrominated Naphthalene Diimide

The synthesis of dichloronaphthalene dianhydride was first reported by Vollmann;<sup>194</sup> the subsequent imidization afforded dichloro NDI. However, the five-step procedure from pyrene to dichloro NDI is cumbersome, and the dichloro NDI is not active for Pd-mediated coupling. A two-step synthetic route to dibromo NDI was developed by Würthner (Scheme 4).<sup>193</sup> Naphthalene

**Scheme 4. Synthetic Route to Dibrominated Naphthalene Diimide from Naphthalene Dianhydride<sup>193 a</sup>**



<sup>a</sup>Reagent and conditions: (i) DBI, oleum (20%  $\text{SO}_3$ ); (ii)  $\text{RNH}_2$ , glacial  $\text{HOAc}$ , 120 °C.

dianhydride **8** is first brominated in oleum (20%  $\text{SO}_3$ ) using a strong brominating agent, dibromo isocyanuric acid. Bromination with a stoichiometric amount of dibromo isocyanuric acid then affords a mixture consisting of mainly 2,6-dibromo naphthalene dianhydride **9** and 2-monobromo and 2,3,6-tribromo naphthalene dianhydride as well as some unreacted **8**. Intermediate **9** can be enriched by recrystallization of the mixture in various polar aprotic solvents, however this was found unnecessary since the separation is readily accomplished by column chromatography after imidization. The mixed brominated dianhydride is converted to a mixture of brominated NDIs after condensation with amines in glacial acetic acid. The amine is protonated by acetic acid; hence, aromatic nucleophilic substitution on the bromine atoms is greatly suppressed and imidization is favored. The regiosomerically pure 2,6-dibromo NDI **10** can be readily separated from the byproducts of nucleophilic aromatic substitutions and monobromo and tribromo NDIs via simple flash chromatography and/or recrystallization.

### 3.2. Naphthalene Diimide-Based Polymer Semiconductors for OTFTs

The first solution-processable NDI-based conjugated polymers were developed by Watson (**P49**)<sup>179</sup> and Facchetti (**P50**),<sup>158</sup> independently. **P49** and **P50** (Figure 20) show substantially high  $M_n$ s due to the favorable Stille coupling and good polymer solubility. Watson reported a series of NDI polymers having different conjugation lengths and substituents on oligothiophenes and studied polymer optoelectronic properties and film microstructures. The energies of the polymer LUMOs are invariant and dictated by the NDI unit, while the HOMOs are a function of thienyl donor counts and polymer backbone conformation.<sup>179</sup> The UV-vis absorption and film microstructure characterization demonstrated that NDI polymers could achieve a high degree of backbone coplanarity, depending on donor counts.<sup>179</sup>

Facchetti et al. first reported the OTFT performance of NDI polymer **P50** and compared its optoelectronic properties with the PDI polymer counterpart **P2** (Figure 14).<sup>158</sup> In comparison

to **P2**, **P50** showed structured absorption and a greatly red-shifted absorption maximum (Figure 21), which was attributed to the higher degree of backbone coplanarity and regioregularity of the NDI polymer. PDI polymers show greater backbone torsion due to the congested structure in the PDI bay region (Figure 17).<sup>175,195</sup> The higher degree of coplanarity has profound implications for the device performance. BGTC OTFTs fabricated on OTS/Si/SiO<sub>2</sub> exhibit  $\mu_e$ s of 0.06 and 0.002  $\text{cm}^2/(\text{V s})$  for **P50** and **P2** in vacuum, respectively. When measured in ambient, the **P50** OTFTs function 14 weeks with a  $\mu_e$  of 0.01  $\text{cm}^2/(\text{V s})$  while the **P2**  $\mu_e$  drops to  $2 \times 10^{-4} \text{ cm}^2/(\text{V s})$  within 1 week. Therefore, NDI polymers show enhanced device stability. The improved **P50**  $\mu_e$  and enhanced device stability are attributed to its regioregularity and more compact film morphology, which creates a kinetic barrier for  $\text{H}_2\text{O}$  and  $\text{O}_2$  penetration. **P49** having more branched 2-decyldodecyl on the imide groups shows a slightly lower  $\mu_e$  of 0.033  $\text{cm}^2/(\text{V s})$  in the same device structure.<sup>196</sup>

The good  $\mu_e$  combined with its high solubility (~60 g/L) renders **P50** highly suitable for printed electronics.<sup>197</sup> **P50** exhibits unprecedented  $\mu_e$ s of up to 0.85  $\text{cm}^2/(\text{V s})$  under ambient in top-gate OTFTs having Au source/drain with various polymer dielectrics. Printed flexible OTFTs have  $\mu_e$ s of 0.1–0.65  $\text{cm}^2/(\text{V s})$ . The low-lying LUMO/HOMO and self-encapsulation of top-gate structure enable **P50** OTFTs with remarkable storage and operation/stress stability (Figure 22a). The achievement of  $\mu_e$  approaching 1  $\text{cm}^2/(\text{V s})$  greatly reduces the performance gap between n- and p-type polymers. All-printed polymeric complementary inverters show voltage gains of 25–65, in which **P50** and P3HT are used as n- and p-channel materials.<sup>197</sup>

The promising **P50** mobility inspires NDI polymer structural modifications for performance enhancement. Luscombe and co-workers developed a series of NDI polymers (Figure 20) having oligothiophene donors.<sup>198</sup> The homopolymer **P51** was synthesized via Yamamoto coupling, while copolymers **P50**, **P52**, and **P53** were synthesized under Stille coupling. As the thiophene number increases, the polymer HOMO is gradually elevated while the LUMO remains unchanged, accompanied by improved crystallinity and ordering as revealed by X-ray diffraction (XRD). **P51** shows the lowest  $\mu_e$  of  $6 \times 10^{-4} \text{ cm}^2/(\text{V s})$  in the series, and the highest  $\mu_e$  of 0.076  $\text{cm}^2/(\text{V s})$  is obtained from NDI–terthiophene copolymer **P53** in BGBC OTFTs, which is higher than the  $\mu_e$  of  $3.9 \times 10^{-2} \text{ cm}^2/(\text{V s})$  from **P50**. Therefore, increasing the thiophene number in the donors gradually enhances the film crystallinity and electron mobility in NDI–oligothiophene copolymers. When n-dodecyl is installed at the 3,3'-position of bithiophene, the resultant **P54** shows a greatly blue-shifted absorption and an amorphous film morphology, which leads to a lower  $\mu_e$  of 0.012  $\text{cm}^2/(\text{V s})$  in comparison to that of **P50**. **P55** and **P56** bearing thienothiophene and dithienothiophene show  $\mu_e$ s of  $3.6 \times 10^{-3}$  and  $9.6 \times 10^{-3} \text{ cm}^2/(\text{V s})$  in BGTC OTFTs, respectively.<sup>196</sup> The low  $\mu_e$ s are associated with their reduced film crystallinity. Incorporation of fused thiophenes leads to low polymer solubility and strong aggregation, which would lower the degree of conformational freedom and adversely impact polymer self-assembly into an ordered microstructure. Further extending the conjugation length of the fused thiophene donor affords **P57**.<sup>199</sup> In order to achieve the desired solubility, n-dodecyl chains are installed on the quaterthiophene. Please note that attachment of the alkyl chain does not induce substantial backbone torsion, and **P57** shows the lowest band gap of 1.37 eV and highest crystallinity

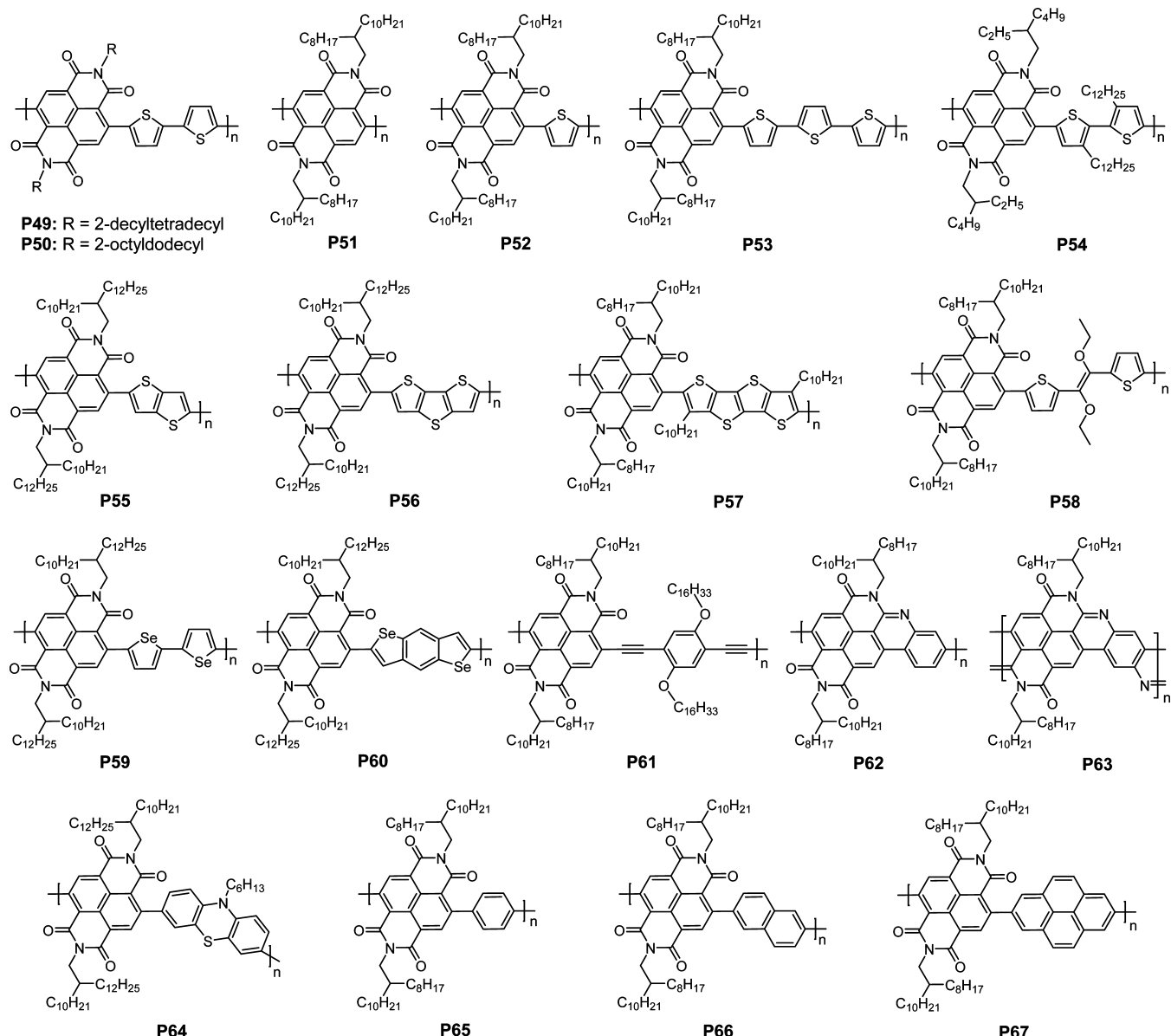


**Figure 20.** Naphthalene diimide-based polymer semiconductors for n-channel OTFTs.

among P55–P57. Note that P57 BGTC OTFTs exhibit the highest  $\mu_e$  of  $0.012 \text{ cm}^2/(\text{V s})$  in the series, in parallel with a good current modulation ( $I_{\text{on}}/I_{\text{off}} > 10^5$ ). The results highlight the significance of achieving good materials solubility for performance enhancement.

A novel bithienylene vinylene-containing donor was incorporated into P58.<sup>200</sup> Alkoxy functionalization at C=C not only enable a weak intramolecular S···O “conformation lock” to promote backbone coplanarity but also lowered the polymer HOMO in comparison to alkoxy functionalization at thiophene in P68 (Figure 23). The low-lying HOMO enables enhanced materials and device stability and unipolar n-channel performance for P58. Moreover, the alkoxy chain enhances polymer solubility. Cyclic voltammetry measurements show that P58 has a LUMO/HOMO of  $-4.0/-5.4 \text{ eV}$ . XRD indicates that P58 has a high degree of ordering with a  $\pi-\pi$  stacking of  $4.11 \text{ \AA}$ . P58 BGTC OTFTs show a  $\mu_e$  of  $0.2 \text{ cm}^2/(\text{V s})$  after annealing at  $200^\circ\text{C}$ , which is higher than that of P50 OTFTs in the same

structure. TGBC OTFTs afford a further increased  $\mu_e$  of  $0.5 \text{ cm}^2/(\text{V s})$ .<sup>200</sup>

Selenophene derivatives were incorporated into NDI polymers.<sup>201,202</sup> Compared to sulfur, selenium has a larger p orbital, which should promote orbital overlap and increase mobility. Biselenophene-containing P59 shows a  $\sim 0.1 \text{ eV}$  lower LUMO,  $0.1 \text{ eV}$  smaller band gap, and  $50 \text{ nm}$  broader width of half-maximum of the absorption peak in comparison to those of P49. Morphological investigation reveals the highly ordered lamellar crystallinity of P59 thin films. P59 BGTC OTFTs show a  $\mu_e$  of  $0.07 \text{ cm}^2/(\text{V s})$  with an  $I_{\text{on}}/I_{\text{off}}$  of  $10^5$  and a  $V_t$  of  $15 \text{ V}$ .<sup>201</sup>  $\mu_e$  is higher than that ( $0.04 \text{ cm}^2/(\text{V s})$ ) of bithiophene copolymer P49, which could be attributed to enhanced P59 film crystallinity due to Se–Se interaction. It is interesting to note that the phenyl end-capped P59 shows a 3.4-fold higher  $\mu_e$  of  $0.24 \text{ cm}^2/(\text{V s})$ .<sup>202</sup> The improved  $\mu_e$  of the end-capped polymer is attributed to minimization of charge traps. Benzo[1,2-*b*:4,5-*b'*]diselenophene-containing P60 shows an enlarged band gap of  $1.55 \text{ eV}$  in comparison to that ( $1.40 \text{ eV}$ ) of P59 due to the less favored

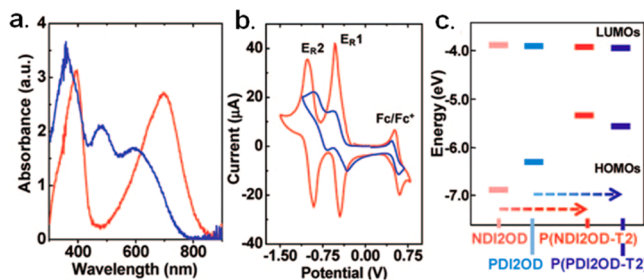


**Figure 21.** (a) UV–vis absorption spectra of spin-coated NDI polymer P50 (aka P(NDI2OD)-T2, red line) and PDI polymer P2 (aka P(PDI2OD)-T2, blue line) films on glass. (b) Thin-film cyclic voltammetry [Fc (+0.54 V vs SCE) internal standard] of P50 (red line) and P2 (blue line) thin films on a Pt electrode.  $E_{R1}$  values of *N,N'*-bis(2-octyldecyl)-naphthalene-1,4,5,8-bis(dicarboximide) (NDI2OD) and *N,N'*-bis(2-octyldecyl)-perylene-3,4,9,10-bis(dicarboximide) (PDI2OD) are  $-0.49$  and  $-0.46$  V vs SCE, respectively. (c) Energy diagram for the specified NDI and PDI monomers and polymers. Reprinted with permission from ref 158. Copyright 2008 American Chemical Society.

quinoidal population of P60. P60 OTFTs show a  $\mu_e$  of  $0.1 \text{ cm}^2/(\text{V s})$ , much lower than that of P59 OTFTs, which is likely related to the low  $M_n$  (27 kDa) of P60 compared to that (107 kDa) of P59.

A poly(phenylene ethynylene)-type polymer P61 was synthesized via Sonogashira coupling and showed a moderate  $\mu_e$  of  $3.7 \times 10^{-3} \text{ cm}^2/(\text{V s})$  in OTFT.<sup>203</sup> The mobility is likely related to the limited conjugation and suppressed electron delocalization, seen in most poly(phenylene ethynylene)-type polymers.<sup>204,205</sup> The P61 mobility is considerably lower than that ( $0.1 \pm 0.05 \text{ cm}^2/(\text{V s})$ ) of the PDI polymer counterpart P10 (Figure 14).<sup>163</sup> The extended PDI  $\pi$  system in P10 leads to greater  $\pi$ -orbital overlap and provides a more efficient pathway for interchain charge hopping. Luscombe et al. designed solution-processable NDI-based ladder polymers,<sup>206</sup> P62 and P63, which were synthesized by forming an intramolecular imine bridge after polymerization. After ladderizations, both polymers maintained good solubilities. UV–vis absorption and DFT computation show that ladderization leads to greatly enhanced backbone coplanarity. In comparison to unladdered polymer counterparts, P62 and P63 have raised LUMOs of  $-3.54$  eV due to the reduced electron deficiency as a result of imine-bridge formation in place of the more electron-deficient carbonyl group. The P62 and P63  $\mu_e$ s measured from BGTC OTFTs are  $4 \times 10^{-7}$  and  $2.6 \times 10^{-3} \text{ cm}^2/(\text{V s})$ , respectively. The lower P62  $\mu_e$  is due to the partial ladder structure, which results in substantial

backbone torsion. The P63  $\mu_e$  is improved by 3 orders of magnitude compared to the nonladdered polymer precursor having a  $\mu_e$  of  $1.9 \times 10^{-6} \text{ cm}^2/(\text{V s})$ . Despite the high degree of backbone coplanarity, the moderate P63  $\mu_e$  is likely due to its unfavorable LUMO ( $-3.54$  eV), low  $M_n$  (14 kDa), and amorphous film microstructure.<sup>206</sup> P64 containing phenothiazine was synthesized via Suzuki coupling. The band gap (1.4 eV)<sup>160</sup> of P64 is smaller than that (1.5 eV) of the PDI polymer P6. BGTC P64 OTFTs show the highest  $\mu_e$  of  $0.05 \text{ cm}^2/(\text{V s})$ , comparable to that of P6 OTFTs in the same device structure, in good accordance with their band gaps and film morphologies.

A family of NDI polymers having various acenes, i.e., benzene, naphthalene, and pyrene, was designed to systematically investigate structure–property correlations in this family.<sup>207</sup> P65–P67 (Figure 20) were synthesized via Suzuki coupling and showed  $M_n$ s in the range of 3–31 kDa. UV–vis absorption spectra show that thiophene-free P65–P67 have largely blue-shifted absorption than thiophene-containing P52 due to the reduced electron-donating ability of the acene than thiophene heteroacene. The  $\mu_e$ s measured from BGTC OTFTs are  $8.0 \times 10^{-3}$ ,  $5.6 \times 10^{-2}$ , and  $7.6 \times 10^{-3} \text{ cm}^2/(\text{V s})$  for P65, P66, and P67, respectively. The highest  $\mu_e$  from P66 could be due to the centrosymmetric geometry versus the axisymmetric structures of P65 and P67.<sup>208</sup> The most promising OTFT performance is usually achieved from polymers bearing thiophene or selenophene, and thiophene-free copolymers usually show lower mobilities. However, the P66  $\mu_e$  is comparable to that of NDI–bithiophene copolymer P49 in the same device structure. The results clearly indicate that NDI is a versatile building block for enabling high-performance n-channel OTFT polymers with various donor counits.<sup>207</sup>

The low-lying LUMOs and favorable film morphologies enable good n-channel OTFT performance for NDI polymers. Modifying donors should lead to NDI polymers with promising ambipolar transport when the HOMO approaches the work function of source/drain electrodes.<sup>28,30</sup> P68 (Figure 23) bearing a strong donor, 3,3'-dialkoxy-2,2'-bithiophene, shows a LUMO/HOMO of  $-3.7$ / $-5.1$  eV with a small band gap of 1.16 eV.<sup>179,209</sup> The narrow band gap reflects its strong donor–acceptor makeup and high degree of backbone coplanarity promoted by the intramolecular (thienyl)S...-(carbonyl)O interactions.<sup>131,179</sup> The  $-5.1$  eV HOMO facilitates hole injection, and hence, P68 BGBC OTFTs show substantial ambipolar transport with a  $\mu_e/\mu_h$  of  $0.04/0.003 \text{ cm}^2/(\text{V s})$  in a  $\text{N}_2$ -purged glovebox (Figure 24). In comparison to P58, installation of alkoxy on thiophene elevates the P68 HOMO. Ambipolarity simplifies the fabrication of complementary-like inverters in comparison to inverters

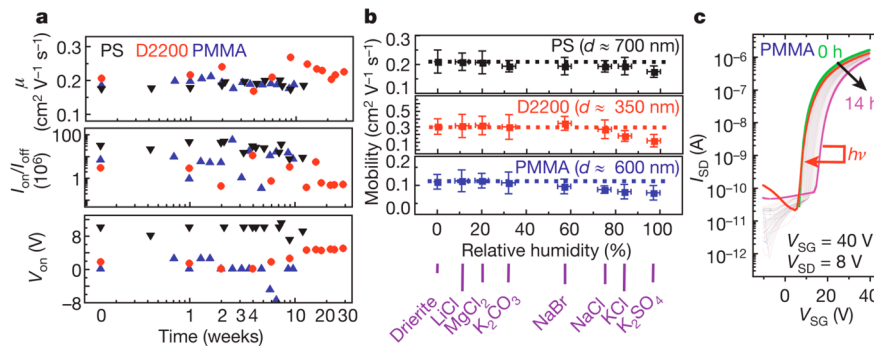


**Figure 22.** Stability and bias stress in ambient of representative TGBC OTFTs with spin-coated P50 semiconductor and several gate dielectrics: PS, D2200, and PMMA. Reprinted with permission from ref 197. Copyright 2009 Rights Managed by Nature Publishing Group.

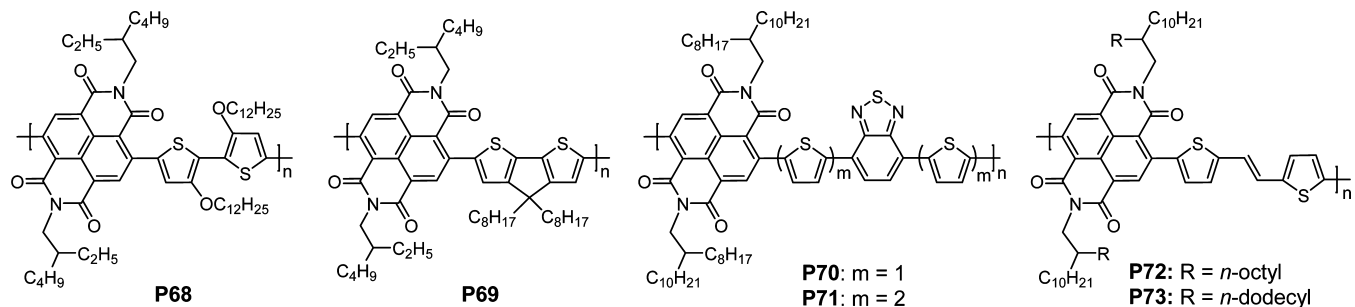


Figure 23. Naphthalene diimide-based polymer semiconductors for ambipolar OTFTs. P71 shows unipolar p-channel performance.

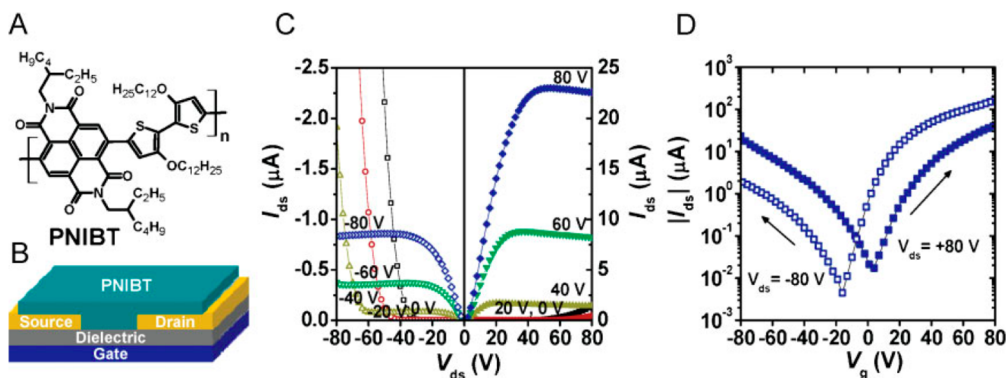


Figure 24. (A) Chemical structure of NDI polymer P68 (PNIBT). (B) Schematic of BGBC OTFTs. (C) Output and (D) transfer characteristics of the P68 OTFTs after annealing at 200 °C. Saturation mobilities in the specific devices are  $0.042 \text{ cm}^2/(\text{V s})$  for electron and  $0.0026 \text{ cm}^2/(\text{V s})$  for hole. Reprinted with permission from ref 209. Copyright 2010 Wiley-VCH Verlag GmbH & Co. KGaA.

fabricated using distinct p- and n-channel semiconductors. The inverters using P68 as the channel material show a sharp signal switching with a high voltage gain of 30. Cyclopentadithiophene was incorporated into P69, which has a band gap of 1.20 eV and a HOMO of  $-5.42 \text{ eV}$ . The HOMO is higher than that ( $-5.77 \text{ eV}$ ) of P50 by a large margin, in good accordance with the stronger electron-donating characteristics of cyclopentadithiophene as compared to bithiophene. P69 BGBC OTFTs show ambipolarity with a  $\mu_e/\mu_h$  of  $5.6 \times 10^{-3}/1.0 \times 10^{-3} \text{ cm}^2/(\text{V s})$ .<sup>196</sup> As compared to P68, the lower P69 mobilities are due to the out-of-plane orientation of the alkyl chains on the  $\text{sp}^3$  carbon bridge.<sup>210</sup>

Covalently connecting NDI with electron-deficient benzothiadiazole via a thiophene linker affords P70 and P71, which have  $M_n$ s of 31 and 12 kDa, respectively.<sup>211</sup> The synthetically accessible  $M_n$ s are limited by the polymer solubility. P70 has a band gap of 1.49 eV with a LUMO/HOMO of  $-4.17/-5.73 \text{ eV}$ . Extending the linker from thiophene to bithiophene, P71 exhibits a smaller band gap of 1.33 eV but an elevated LUMO/HOMO of  $-4.05/-5.50 \text{ eV}$ . P70 BGTC OTFTs with Au electrodes show a balanced  $\mu_h/\mu_e$  of  $0.1 \pm 0.03/0.05 \pm 0.02 \text{ cm}^2/(\text{V s})$  in ambient, while P71 containing a bithiophene linker exhibits unipolar p-channel performance with a  $\mu_h$  of  $0.07 \pm 0.02 \text{ cm}^2/(\text{V s})$ . The absence of n-channel response of P71 is due to its elevated LUMO, which lies at the borderline for air-stable n-channel performance.<sup>41</sup> The slightly lower P70 LUMO leads to its good n-channel performance in air. Moreover, P70 and P71 OTFTs show good air stability with negligible OTFT performance degradation after being stored in air for 3 months.<sup>211</sup>

By incorporating (E)-2-(2-(thiophen-2-yl)vinyl)thiophene, the resulting P72 shows a HOMO of  $-5.61 \text{ eV}$ , which lowers the hole injection barrier as compared to bithiophene polymer P50 having a HOMO of  $-5.82 \text{ eV}$ .<sup>212</sup> P72 BGTC OTFTs fabricated on octadecyltrichlorosilane (OTS)-modified Si/SiO<sub>2</sub>

show pronounced ambipolarity with an average  $\mu_e/\mu_h$  of  $0.70/0.12 \text{ cm}^2/(\text{V s})$  under N<sub>2</sub>. The  $\mu_e$  of P72 is much higher than that ( $0.18 \text{ cm}^2/(\text{V s})$ ) of P50.<sup>212</sup> Therefore, vinyl group incorporation improves charge transport. Device optimization further improves P72 OTFT performance using a TGBC structure with a PMMA dielectric; the highest  $\mu_e$  and  $\mu_h$  reach  $1.13$  and  $0.23 \text{ cm}^2/(\text{V s})$ , respectively. Under the same device structure, P73 having a longer alkyl chain on the imide group shows a  $\mu_e/\mu_h$  of  $1.57/0.30 \text{ cm}^2/(\text{V s})$ . P73 OTFTs show good air stability;  $\mu_e/\mu_h$  maintain  $1.03/0.13 \text{ cm}^2/(\text{V s})$  when the devices are stored 1 month in ambient (20–40% humidity). The CMOS-like inverters by integrating two identical ambipolar P72 OTFTs show a voltage gain of 155, which is among the highest for complementary-like inverters using a single ambipolar polymer.<sup>212</sup> TGBC P73 OTFTs with a Cs<sub>2</sub>CO<sub>3</sub>-treated Au source/drain exhibit unipolar n-channel performance with a  $\mu_e$  of  $1.8 \text{ cm}^2/(\text{V s})$  and an  $I_{on}/I_{off}$  of  $10^6$  after annealing at 150–210 °C.<sup>136</sup> The p-channel character in the ambipolar P73 OTFTs completely disappears after Cs<sub>2</sub>CO<sub>3</sub> insertion due to its hole-blocking property.<sup>37</sup> The  $\mu_e$  is among the highest for n-channel polymers. In comparison to P50, P73 shows enhanced air and bias stability due to its closer  $\pi-\pi$  stacking (3.80 Å), shorter lamellar distance, and more crystalline film morphology, which promote charge transport and prevent H<sub>2</sub>O and O<sub>2</sub> penetration.

OTFT performance is not only a function of intrinsic materials characteristics but also highly dependent on the materials processing and device structure.<sup>8</sup> Noh and co-worker reported remarkable enhancement of hole injection and transport in TGBC OTFTs using a high- $k$  dielectric.<sup>213</sup> The top-gate P50 (Figure 20) OTFTs using a high-permittivity ( $k$ ) fluorinated dielectric, poly(vinylidenefluoride-trifluoroethylene) (P(VDF-TrFE)), show remarkable ambipolarity with a  $\mu_e/\mu_h$  of  $0.093/0.11 \text{ cm}^2/(\text{V s})$ . The directional interface state modulation by

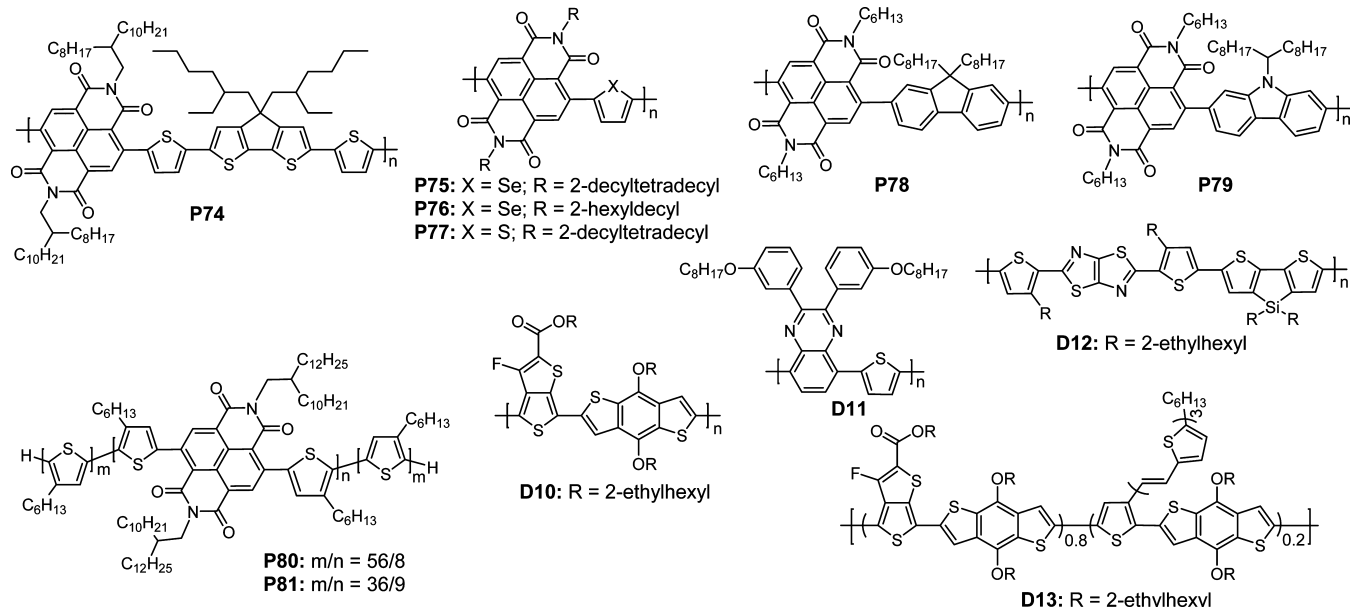


**Figure 25.** Naphthalene diimide-based polymer semiconductors for all-polymer solar cells. Chemical structures of donor semiconductors D10–D13 used in all-polymer solar cells are also included.

C–F dipoles greatly increases hole density and decreases the hole injection barrier from source/drain. High-performance P50 inverters with a voltage gain of 25 and high-speed ring oscillators with an oscillation frequency of  $\sim 3.5$  kHz are demonstrated. The study demonstrates that engineering dielectric interfaces is an efficient avenue to achieve ambipolarity of conjugated polymers.

### 3.3. Naphthalene Diimide-Based Polymers for OSCs

The small band-gap, low-lying LUMO, and good electron mobility of NDI polymers herald their potential as acceptor semiconductors in OSCs. Loi reported all-polymer cells having the structure ITO/PEDOT:PSS/P3HT:P50 (1:2; w/w)/LiF/Al, which showed a PCE of 0.16% with a  $J_{sc}$  of 0.48 mA/cm<sup>2</sup>, a  $V_{oc}$  of 0.50 V, and a FF of 67% using *o*-dichlorobenzene as solvent.<sup>214</sup> The 67% FF is the highest for all-polymer cells, which is attributed to the high and balanced  $\mu_e$  and  $\mu_h$  of  $\sim 3 \times 10^{-3}$  cm<sup>2</sup>/V s measured in the OTFT regime.<sup>215</sup> Therefore, the high  $\mu_e$  of P50 enables the FF of all-polymer cells comparable to that of polymer:fullerene cells. The  $J_{sc}$  is mainly limited by monomolecular (geminate pair) recombination.<sup>214</sup> Using xylene as the solvent, P3HT:P50 OSCs show an improved PCE of 0.62%. ICPE spectra show photocurrent generation from P50. Steady state and transient optical spectroscopy and scanning X-ray transmission microscopy study revealed that the P3HT:P50 system has a hierarchical morphology with impure P3HT-rich and P50-rich domains with sizes of 0.2–1  $\mu$ m. Such morphology leads to charge localization, increases geminate recombination, prevents charge sweep out, and hence limits  $J_{sc}$ .<sup>216</sup> Schubert systematically optimized P3HT:P50 cells. It was found that PCEs could be greatly enhanced when formation of large and well-ordered crystallites was suppressed. The optimized cells prepared from nonaggregated solutions in xylene/chloronaphthalene (1:1) showed PCEs reaching 1.4% with a FF of 65%.<sup>217</sup> P50 preaggregation was completely suppressed in solution, which prevented formation of large and well-ordered P3HT crystallites and facilitated formation of an interpenetrating network having nanoscale crystalline polymer domains.<sup>217</sup>

As the most efficient p-type polymer in OSCs, D10 (aka PTB7,<sup>22,218</sup> Figure 25) was blended with acceptor semi-

conductor P50, and the resulting cells showed a PCE of 1.1% with a  $J_{sc}$  of 3.4 mA/cm<sup>2</sup>, a  $V_{oc}$  of 0.62 V, and a FF of 39%. The  $V_{oc}$  of D10:P50 cells was greater than that of P3HT:P50 cells along with a better spectral response to the solar spectrum. The moderate performance was attributed to the lack of mesoscale phase separation and unoptimized morphology.<sup>219</sup> This preliminary result indicates that D10:P50 is a promising system for all-polymer cells. Zhou systematically optimized D10:P50 cells, and a PCE of 2.7% was obtained in the inverted structure ITO/ZnO/D10:P50/MoO<sub>3</sub>/Ag.<sup>220</sup> For the cells fabricated using xylene as the solvent, film morphology having enlarged donor semiconductor/acceptor semiconductor interfacial areas, interpenetrating networks, and enhanced polymer  $\pi$ – $\pi$  stacking were achieved. Such morphology in combination with substantial  $\mu_h$  and  $\mu_e$  resulted in a PCE of 2.7% with a  $J_{sc}$  of 6.28 mA/cm<sup>2</sup>, a  $V_{oc}$  of 0.799 V, and a FF of 53%. The 0.799 V  $V_{oc}$  was larger than that ( $\sim 0.740$  V) from D10:PC<sub>71</sub>BM cells<sup>218</sup> due to the higher lying P50 LUMO compared to the PC<sub>71</sub>BM LUMO.

Poly[2,3-bis(3-octyloxyphenyl)quinoxaline-5,8-diyl-*alt*-thiophene-2,5-diyl] D11 was blended with P50 for all-polymer cells.<sup>221</sup> D11 has a smaller band gap and broader absorption than P3HT. Device performance was found to be highly sensitive to the D11:P50 ratio, and cells with D11:P50 (70:30; w/w) show the best PCE of 4.1% with a  $J_{sc}$  of 8.85 mA/cm<sup>2</sup>, a  $V_{oc}$  of 0.84 V, and a FF of 55%. The high  $J_{sc}$  was attributed to efficient charge generation from both D11 and P50 excitons as well as high and balanced  $\mu_h$  and  $\mu_e$ . The results indicate that P50 is a highly promising acceptor semiconductor for all-polymer solar cells.

A high-mobility n-type semiconductor, P57 (Figure 20) was blended with P3HT. The preliminary OSCs showed PCEs of  $\sim 0.1\%$  due to poor film quality, which was likely induced by strong polymer aggregation.<sup>199</sup> Inserting cyclopentadithiophene between the bithiophene of P50 afforded P74 with a smaller band gap of 1.25 eV in comparison to that (1.45 eV) of P50.<sup>217</sup> Using tetralin as the processing solvent, all-polymer cells containing a P3HT:P74 active layer showed a PCE of 1.1% with a  $J_{sc}$  of 2.43 cm<sup>2</sup>/(V s), a  $V_{oc}$  of 0.63 V, and a remarkable FF of 70%. Selenophene polymers P75 and P76 (Figure 25)

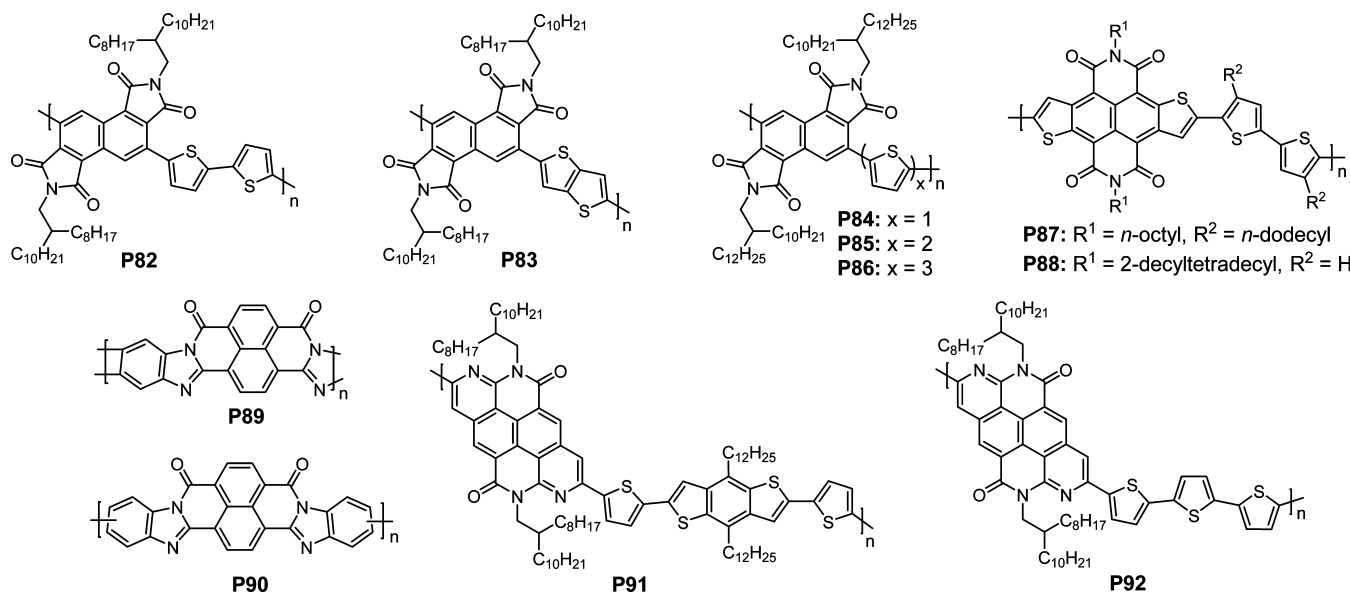


**Figure 26.** Naphthalene diimide isomer and derivative-based polymers for organic thin-film transistors and solar cells.

exhibited smaller band gaps and a higher degree of side chain interdigititation than thiophene polymer P77.<sup>222</sup> OTFT investigation revealed unipolar electron transport with  $\mu_s$ s of  $2 \times 10^{-3}$  and  $7 \times 10^{-3} \text{ cm}^2/(\text{V s})$  for P75 and P76, respectively, which was at least 10 $\times$  higher than that of P77 due to the improved orbital overlap induced by the extended selenium  $\pi$  orbitals. Inverted cells having the structure ITO/ZnO/D12:P77/MoO<sub>3</sub>/Ag showed a PCE of 1.30% with a  $J_{sc}$  of 3.80 mA/cm<sup>2</sup>, a  $V_{oc}$  of 0.61 V, and a FF of 56%. The selenophene polymer P75 showed an improved PCE of 2.96% with a  $J_{sc}$  of 6.53 mA/cm<sup>2</sup>, a  $V_{oc}$  of 0.75 V, and a FF of 60%. The best performance was achieved from D12:P76 cells having short imide chains with a  $J_{sc}$  of 7.78 mA/cm<sup>2</sup>, a  $V_{oc}$  of 0.76 V, a FF of 55%, and a PCE of 3.26%. The performance order was in accordance with their mobilities. Among them, the performance of D12:P76 cells was comparable to that (3.3%) of D12:PCBM cells.<sup>222</sup> Film characterization revealed large-scale phase separation, suggesting that there was room for further PCE improvement of D12:P75 (or P76) cells. Using biselenophene polymer P59 as the acceptor semiconductor, the same group reported an optimal PCE of 0.9% with the OSC structure ITO/PEDOT:PSS/P3HT:P59/LiF/Al.<sup>201</sup> The EQE spectrum showed that ~19% photocurrent was contributed by the solar absorption of P59. Morphological characterization revealed that the performance was mainly limited by microscale phase separation, which suppressed exciton dissociation.

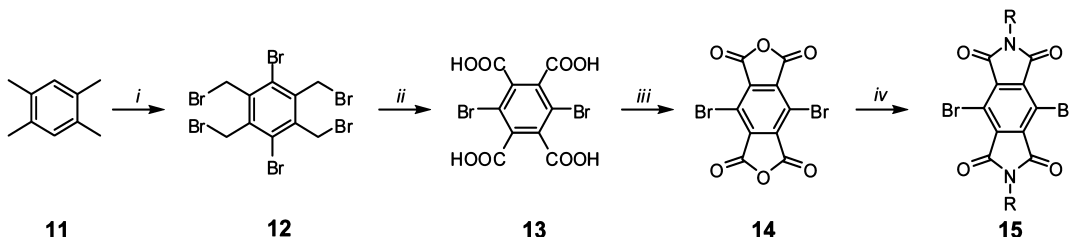
Fluorene copolymer P78 (Figure 25) was synthesized via Suzuki coupling and has a  $M_n$  of 12 kDa with a PDI of 1.59.<sup>223</sup> P78 shows a broader band gap of 2.1 eV and a higher lying LUMO of -3.61 eV than bithiophene polymer P50 due to the greater backbone torsion in P78.<sup>223</sup> The P78 high-lying LUMO results in larger  $V_{oc}$ s of 0.66–0.70 V in P3HT:P78 cells than  $V_{oc}$ s of ~0.5 eV in P3HT:P50 cells. Device optimization using additive DIO leads to improved film morphologies, and the PCE reaches 1.63% with a  $J_{sc}$  of 3.63 mA/cm<sup>2</sup>, a  $V_{oc}$  of 0.68 V, and a FF of 66%. Carbazole-containing P79 was blended with various polymer donor semiconductors, and an optimal PCE of 1.34% was obtained for D10:P79 cells.<sup>224</sup> Inspired by the materials design concept introduced by Li,<sup>164</sup> a PTB7 derivative D13 having conjugated side chain was synthesized. The D13:P79 cells

afforded the best PCE of 3.68% with a  $J_{sc}$  of 7.71 mA/cm<sup>2</sup>, a  $V_{oc}$  of 0.88 V, and a FF of 54% after device optimization.<sup>224</sup> The high  $J_{sc}$  was attributed to the high P79 crystallinity and its good miscibility with D13.

Novel conjugated block polymers P80 and P81 composed of poly(naphthalene diimide) and poly(3-hexylthiophene) were synthesized using quasi-living Grignard metathesis polymerization and Yamamoto coupling.<sup>225</sup> The polymers have  $M_n$  of 19 kDa and polymerization degree (PD) of 56/8 (m/n) for P80 and  $M_n$  of 17 kDa and PD of 36/9 (m/n) for P81. P80 and P81 show broad absorption in the range of 350–850 nm with a band gap of 1.46 eV. OSCs having the structure ITO/PEDOT:PSS/P3HT:P80/Ca/Al show a PCE of 1.20% with a  $J_{sc}$  of 3.28 mA/cm<sup>2</sup>, a  $V_{oc}$  of 0.59 V, and a FF of 62% after annealing at 200 °C. The P3HT:P81 cells show a slightly improved PCE of 1.28% with a  $J_{sc}$  of 4.57%, a  $V_{oc}$  of 0.56 V, and a FF of 50%.<sup>225</sup> The results show that NDI-based fully conjugated copolymers are potentially applicable as acceptor semiconductors for all-polymer solar cells.

### 3.4. Naphthalene Diimide Isomers and Derivatives-Based Polymer Semiconductors for OTFTs and OSCs

In addition to 1,4,5,8-naphthalene diimide, other naphthalene diimide isomers and derivatives were designed for implementation in organic electronics. Gao reported P82 and P83 containing a novel 1,2,5,6-naphthalene diimide (Figure 26).<sup>226</sup> Density functional theory (DFT) computations revealed that the angular-shaped 1,2,5,6-NDI has coplanar structure, but its LUMO/HOMO are elevated by 0.3 eV in comparison to those of 1,4,5,8-NDI, which is likely traced to the limited electron density delocalization of 1,2,5,6-NDI LUMO<sup>227</sup> and the weaker electron-withdrawing ability of the five-membered imide group in 1,2,5,6-NDI.<sup>226</sup> The result indicates that incorporation of 1,2,5,6-NDI into polymers will enable development of a new class of polymers having electrical properties distinct from 1,4,5,8-NDI polymers. In comparison to P50, P82 shows lower solubility due to the reduced steric hindrance between the 1,2,5,6-NDI and the adjacent thiophene. The P82 and P83 band gaps are 1.70 and 1.82 eV, respectively, which are wider than those of the 1,4,5,8-NDI polymer analogues P50 and P55 (Figure 20). The LUMOs of P82 and P83 are -3.72 and -3.60 eV, respectively, which are ~0.2 eV higher than those of P50 and

**Scheme 5.** Synthetic Route to Dibromo PMDI Monomer from Durene<sup>a</sup>

<sup>a</sup>Reagents and conditions: (i) (a)  $\text{Br}_2$ ,  $\text{CCl}_4$ , 54 °C, dark; (b)  $\text{Br}_2$ ,  $\text{CCl}_4$ ,  $h\nu$ , reflux; (ii) 65%  $\text{HNO}_3$ ,  $\text{NaVO}_3$ , reflux; (iii) 205 °C sublimation, vacuum; (iv)  $\text{HOAc}$ , 2-ethylhexyl amine, reflux.

P55. P82 TGBC OTFTs using a poly(perfluorobutenevinyl ether) (CYTOP) dielectric show predominant p-channel transport with the highest  $\mu_h$  of  $0.3 \text{ cm}^2/(\text{V s})$  accompanied by a low  $\mu_e$  of  $10^{-5} \text{ cm}^2/(\text{V s})$  after annealing at 120 °C. The thienothiophene copolymer P83 OTFTs show ambipolarity with a  $\mu_h/\mu_e$  of  $0.02/4 \times 10^{-3} \text{ cm}^2/(\text{V s})$ . Morphological characterization shows that the P82 and P83 films are amorphous. The results indicate that replacement of 1,4,5,8-NDI with 1,2,5,6-NDI promotes polymer hole transport, in good accordance with the FMO level evolution.<sup>226</sup> Although it has p-channel transport, the LUMO of the 1,2,5,6-NDI polymers is sufficiently low in comparison to that of P3HT, which should enable efficient exciton dissociation when the 1,2,5,6-NDI polymer and P3HT are blended. P84–P86 with different numbers of thiophene in the oligothiophenes were synthesized.<sup>228</sup> All-polymer cells having the structure ITO/PE-DOT:PSS/P3HT:polymer/Ca/Al showed moderate PCEs of 0.25–0.32% but with remarkable  $V_{oc}$ s of 0.82–0.94 V when P84, P85, or P86 was used as the acceptor semiconductor. The  $V_{oc}$ s were much larger than those (<0.6 V) of P3HT:1,4,5,8-NDI polymer cells,<sup>214,216</sup> in good accordance with the higher lying 1,2,5,6-NDI polymer LUMOs. The performance of P84–P86-based all-polymer cells was mainly limited by their low  $\mu_e$ s of  $2.15\text{--}6.88 \times 10^{-6} \text{ cm}^2/(\text{V s})$ .<sup>228</sup>

Inspired by the high electron mobility of the NDI polymers<sup>158</sup> and core-extended NDI small molecules,<sup>122</sup> Takimiya et al. designed and synthesized a novel thiophene-fused NDI, naphtho[2,3-*b*:6,7-*b'*]dithiophene diimide.<sup>229</sup> Single-crystal X-ray analysis indicated a high degree of coplanarity of the diimide core with a close  $\pi$ - $\pi$  stacking distance of 3.43 Å. The new diimide was incorporated into polymers to afford P87 and P88 with small band gaps of ~1.2 eV. The LUMO/HOMOs are –4.2/–5.4 and –4.4/–5.6 eV for P87 and P88, respectively. The LUMOs of naphtho[2,3-*b*:6,7-*b'*]dithiophene diimide polymers are comparable to those of NDI polymers.<sup>158</sup> P88 BGTC OTFTs show pronounced ambipolarity with a balanced  $\mu_h/\mu_e$  of  $0.10/0.27 \text{ cm}^2/(\text{V s})$ , and P87 OTFTs exhibit much lower transport with a  $\mu_h$  of  $4 \times 10^{-3} \text{ cm}^2/(\text{V s})$  and no obvious  $\mu_e$ . In comparison to P88, the absence of electron transport in P87 is partially attributed to the electron-donating effect of the dodecyl chain on bithiophene.<sup>229</sup> The high mobility together with the great “chemical flexibility” toward structural modifications indicate that naphtho[2,3-*b*:6,7-*b'*]dithiophene diimide is a versatile and valuable acceptor building block for high-performance polymer semiconductors.

Van Deussen reported a ladder polymer P89 synthesized via polycondensation of 1,2,4,5-tetraaminobenzene and 1,4,5,8-naphthalenetetracarboxylic acid; a semiladder polymer P90 was also synthesized. Both polymers showed high quality and were completely soluble in methanesulfonic acid.<sup>230</sup> Jenekhe first

reported their applications in OTFTs.<sup>231</sup> P89 and P90 have a NDI-like building block in their backbones and show band gaps of 1.80 eV with low-lying LUMOs from –4.0 to –4.4 eV. Due to the ladder-like backbone and strong interchain interaction, P89 and P90 show low solubilities in organic solvents. Using methanesulfonic acid as the processing solvent, P89 OTFTs were fabricated from liquid phase and exhibited a substantial  $\mu_e$  of  $0.1 \text{ cm}^2/(\text{V s})$  with a good  $I_{on}/I_{off}$  of  $10^5$ . The excellent P89 electron mobility was attributed to its low-lying LUMO, high degree of backbone coplanarity, and good crystallinity. Semiladder P90 showed a much lower  $\mu_e$  of  $10^{-6} \text{ cm}^2/(\text{V s})$  due to its twisted backbone. As the first high-performance n-type polymer, implementation of P89 in OTFTs closed the performance gap between p- and n-type polymers. The result demonstrates that NDI derivatives should be excellent building blocks for constructing n-type polymers.

Zhang developed a synthetic strategy to modify NDI at the “shoulder” position, which afforded a new expanded conjugated framework with a planar structure and moderate electron-withdrawing capability.<sup>232</sup> Incorporation of this novel acceptor into polymers afforded P91 and P92.<sup>233</sup> Due to the extended core, P92 shows reduced solubility versus NDI polymer P50. The LUMO/HOMOs are ~–3.60/–5.40 eV for both P91 and P92. In comparison to the LUMOs of NDI polymers, the LUMOs of P91 and P92 are elevated by ~0.30 eV. The P91 and P92 HOMOs are in good alignment with the Fermi level of Au, which leads to efficient hole injection. Using solvent annealing,  $\mu_{hs}$ s of 0.024 and  $0.135 \text{ cm}^2/(\text{V s})$  are obtained for P91 and P92 BGBT OTFTs, respectively.<sup>233</sup> Incorporation of the NDI derivative into P91 and P92 does not enable n-channel transport but leads to good p-channel OTFT stabilities due to their low-lying HOMOs.

### 3.5. Summary

In conclusion, as a highly electron-deficient core, NDI has been successfully incorporated into diverse polymers. In comparison to PDI polymers, NDI polymers can be readily obtained in regioregular pure form. The moderate NDI size and facile alkylation on the imide afford NDI polymers with high  $M_n$ s and good solubilities. The low-lying LUMO leads to facile electron injection, and ordered film morphology results in efficient charge transport. Therefore, NDI polymers show very promising n-channel performance with  $\mu_e$  approaching  $2 \text{ cm}^2/(\text{V s})$ . NDI polymers usually show higher  $\mu_e$ s than PDI polymers due to the high molecular weights, regioregularity, and reduced steric hindrance in NDI polymers. The high electron mobility and good film-forming properties of NDI polymers result in the highest PCE in all-polymer cells. Structure modification and device optimization should enable NDI polymers with further improved device performance.

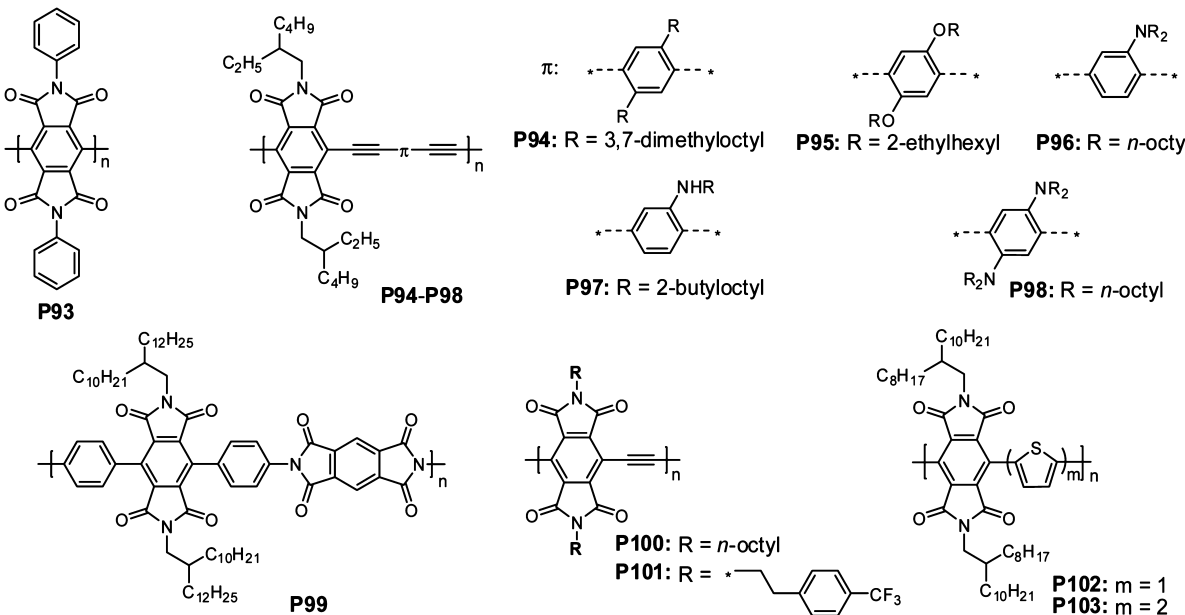


Figure 27. Pyromellitic diimide-based polymer semiconductors.

#### 4. PYROMELLITIC DIIMIDE-BASED POLYMER SEMICONDUCTORS

Perylene diimides and naphthalene diimides have shown great success in creating high-performance n-type polymers, while pyromellitic diimide (PMDI) has been overlooked, which could be partially due to its smallest rylene core and the synthetic challenge of the dibromo PMDI for polymer synthesis. As diimide-functionalized semiconductors, PMDI-based polymers should maintain the low-lying LUMOs and the small PMDI core can afford high  $M_n$  polymers with enhanced solubilities. Recently, Katz et al. demonstrated good OTFT performance with a  $\mu_e$  of  $0.079 \text{ cm}^2/(\text{V s})$  using the simple PMDI small molecules,<sup>115</sup> which encouraged investigation of PMDI polymers for organic electronics.

##### 4.1. Synthesis of Dibrominated Pyromellitic Diimide

The synthetic methodology to 3,6-dibromo PMDI **15** was first reported by Hopff,<sup>234</sup> and the procedure was simplified by combining steps and eliminating unnecessary purification (Scheme 5) by Watson.<sup>205</sup> Starting from durene **11**, 1,4-dibromo-2,3,5,6-tetrakis(bromomethyl)benzene **12** is obtained by consecutive bromination in near quantitative yield in one pot, which is then oxidized by  $\text{HNO}_3$  with catalyst  $\text{NaVO}_3$  to prepare the tetracarboxylic acid **13**. Without purification, the acid **13** is dehydrated via high-temperature vacuum sublimation to afford dianhydride **14** in high purity. Finally, **14** reacts with amines to afford dibromo PMDI **15**. It was found that the imidization in glacial acetic acid can suppress the competing nucleophilic aromatic substitution at the brominated ring positions.<sup>205</sup>

##### 4.2. Pyromellitic Diimide-Based Polymer Semiconductors for OTFTs

The first PMDI polymer is a poly(*p*-phenylene)-type homopolymer **P93** (Figure 27).<sup>235</sup> By comparing polymer and monomer absorption spectra it was found that **P93** is not electronically conjugated along its backbone due to significant backbone torsion induced by the extensive steric/electronic repulsion between adjacent pendant imide groups.<sup>205</sup> Insertion of alkyne between successive phenyl rings could greatly attenuate steric hindrance and planarize polymer backbone. A homologous series

of PMDI-based poly(phenylene ethynylene)s (PPEs)-type conjugated polymers **P94–P98** were synthesized via Sonogashira coupling. The variation of donors leads to tunable band gaps and HOMOs over a wide range, but LUMOs are determined by the PMDI. The strong intermolecular interaction and the low-lying LUMO ( $-3.60 \text{ eV}$ ) of **P94–P98** suggest some promise as n-type semiconductors.

The first PMDI polymer for OTFTs was prepared by Katz through imidization polymerization of a diamine and pyromellitic dianhydride, and the resulting **P99** had a  $M_n$  of  $16.6 \text{ kDa}$  with a PDI of  $1.9$ .<sup>236</sup> **P99** features subunits linked alternately at the 3,6- and *N,N'*-positions. Due to the nonconjugated characteristics, **P99** is transparent in the near UV-vis region and has a wide band gap of  $3.2 \text{ eV}$ . Absorption spectra and differential scanning calorimetry (DSC) data suggest the amorphous nature of **P99** film. The LUMO derived from cyclic voltammetry is  $-3.80 \text{ eV}$ . **P99** BGTC OTFTs using Al source/drain electrodes show a  $\mu_e$  of  $10^{-4} \text{ cm}^2/(\text{V s})$  in vacuum. After being blended with PCBM, a  $\mu_e$  of  $3 \times 10^{-3} \text{ cm}^2/(\text{V s})$  with an  $I_{\text{on}}/I_{\text{off}}$  of  $10^3$  is obtained for **P99:PC<sub>61</sub>BM** blend (1:9, w/w). The mobility can be further increased to  $1.1 \times 10^{-2} \text{ cm}^2/(\text{V s})$  after the OTFT is exposed to a n-type dopant, propylamine. Therefore, it was demonstrated that **P99** is a promising binder material to form organic semiconducting blends.<sup>236</sup> The same group reported PMDI PPEs **P100** and **P101** having different *N*-substituents.<sup>204</sup> The PPEs were synthesized under Stille coupling from dibromo PMDI and bis(tributylstannyl)acetylene and have  $M_n$ s of  $3.8$  and  $5.9 \text{ kDa}$  for **P100** and **P101**, respectively. The LUMOs are  $-3.84$  and  $-3.88 \text{ eV}$  for **P100** and **P101**, respectively. Film characterization indicated that the PPEs are amorphous. TGBC OTFTs using **P100** as the channel material exhibited a moderate  $\mu_e$  of  $2 \times 10^{-4} \text{ cm}^2/(\text{V s})$  with a  $V_t$  of  $55 \text{ V}$  and an  $I_{\text{on}}/I_{\text{off}}$  of  $10^3$  under vacuum. **P101** OTFTs did not show measurable electron mobility. The **P100** mobility was considered high in PPE-type polymers, and the study highlights the good potential of PMDI for constructing simple n-channel semiconductors.

Pei et al. reported a series of PMDI polymers containing thiophene or bithiophene as donors.<sup>237</sup> The polymer band gaps derived from absorption onsets are  $2.84$  and  $2.22 \text{ eV}$  for **P102**

and **P103**, respectively, which are much larger than those of NDI polymer analogues **P52** and **P50** (Figure 20).<sup>179</sup> The broad **P102** and **P103** band gaps are attributed to their limited  $\pi$  conjugation due to the high degree of backbone torsion. **P102** TGBC OTFTs show n-channel transport with a  $\mu_e$  of  $6.23 \times 10^{-4} \text{ cm}^2/(\text{V s})$ , and **P103** TGBC OTFTs exhibit ambipolarity with a  $\mu_e/\mu_h$  of  $2.01 \times 10^{-4}/1.89 \times 10^{-5} \text{ cm}^2/(\text{V s})$ . The n-channel transport of **P102** and **P103** is attributed to their low-lying LUMOs ( $\sim 3.7 \text{ eV}$ ), and their mobilities are limited by the low degree of polymer backbone coplanarity.<sup>237</sup>

#### 4.3. Summary

PMDI as the smallest rylene diimide has been successfully used for synthesizing n-channel polymers. In comparison to PDI and NDI, PMDI imposes greater steric hindrance on neighboring arenes, which limits backbone coplanarity and the crystallinity of the resultant polymers. In order to attenuate the steric hindrance, ethynylene is incorporated into the polymer backbone. Both PMDI-based nonconjugated and conjugated polymers show moderate  $\mu_e$ s in the range of  $10^{-4}-10^{-2} \text{ cm}^2/(\text{V s})$  in OTFTs. The moderate mobility is partially attributed to the limited conjugation of the triple bond in comparison to the double bond or double-bond containing arenes.<sup>110</sup> Structural modification is desired to further enhance the device performance of PMDI-based polymer semiconductors for organic electronics.

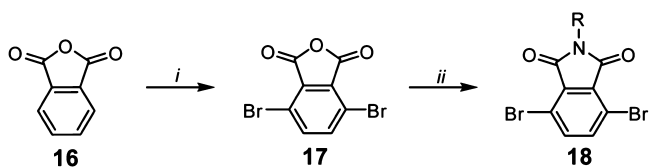
## 5. PHTHALIMIDE-BASED POLYMER SEMICONDUCTORS

Rylene diimide (PDI, NDI, and PMDI)-based polymers have demonstrated superior performance as n-type semiconductors due to their low-lying LUMOs enabled by strong electron-withdrawing diimide groups. Using monoimide-functionalized arenes as the electron acceptor, the resultant polymer LUMOs should not be as low as those of diimide polymer analogues; therefore, n-type characteristics may not prevail. However, the electron-deficient monoimide-functionalized arenes can effectively lower polymer HOMOs through orbital hybridizations.<sup>110</sup> Hence, the resultant polymers should have improved materials stability and device durability. Moreover, low-lying HOMOs can enlarge  $V_{oc}$ s and enhance PCEs in OSCs. Therefore, monoimide-functionalized arenes are highly valued. As a simple monoimide-functionalized arene, phthalimide (PhI) was successfully incorporated into conjugated poly(phenylene ethynylene)s<sup>238</sup> and polyaniline derivatives,<sup>239</sup> but no device performance was reported. Recently, conjugated polymers containing PhI as the electron acceptor and thiophene derivative as the electron donor have shown promising OTFT and OSC performance.

#### 5.1. Synthesis of Dibrominated Phthalimide

The 3,6-dibromophthalimide **18** can be readily prepared using a simple two-step procedure (Scheme 6) from commercial

**Scheme 6. Synthetic Route to Dibrominated Phthalimide<sup>131,240 a</sup>**



<sup>a</sup>Reagent and conditions: (i) Br<sub>2</sub>, I<sub>2</sub>, oleum, 60 °C; (ii) RNH<sub>2</sub>, glacial acetic acid, reflux.

phthalic anhydride **16** following the procedure reported by Wilson in 1941.<sup>240</sup> Anhydride bromination is readily accomplished using bromine in oleum at 60 °C to provide a mixture of monobromo, dibromo, and tribromo derivatives.<sup>240</sup> The desired 3,6-dibrominated anhydride **17** can be separated from the mixture after recrystallization three times in acetic acid. Imidization of **17** with alkyl amines is highly effective in almost quantitative yields (>95%). Unlike in the synthesis of dibromo PDI monomer **3** (Scheme 1) and dibromo NDI monomer **10** (Scheme 4), nucleophilic aromatic substitution of bromine atoms by amines is greatly suppressed due to the less electron-deficient characteristics of the anhydride **17**. The 3,6-dibrominated phthalimides **18** should be attractive electron acceptors for developing polymer semiconductors due to their facile synthesis and ready substitution at the imide nitrogen, allowing effective manipulation of materials solubility, packing, and morphology.

#### 5.2. Phthalimide-Based Polymer Semiconductors for OTFTs

Phthalimide polymers for OTFTs were first reported by Watson and co-workers.<sup>131</sup> Copolymerizing phthalimide with a novel electron donor, 3,3'-didodecyloxy-2,2'-bithiophene, afforded **P104** and **P105** (Figure 28) with high  $M_n$ s of 117 and 207 kDa, respectively, and excellent solubilities. **P105** having linear *n*-dodecyl on the imide has a slightly smaller band gap (1.65 eV) than that (1.72 eV) of **P105** having branched 2-ethylhexyl. The  $\pi-\pi$  stacking distances measured from film XRD are 3.7 and 3.6 Å for **P104** and **P105**, respectively. The small **P104** and **P105** band gaps are likely due to their effective backbone coplanarity induced by the consecutive S···O interactions along the backbone.<sup>55,241</sup> BGBT OTFTs exhibit average  $\mu_h$ s of 0.02 and 0.17 cm<sup>2</sup>/(V s) with  $I_{on}/I_{off}$ s of  $10^4-10^5$  in the saturation regime for **P104** and **P105**, respectively.<sup>131</sup> The high  $\mu_h$ s are in accordance with the close  $\pi-\pi$  stacking, good lamellar ordering, and extensive domain connectivity. Replacing 3,3'-didodecyloxy-2,2'-bithiophene with 4,4'-dialkoxy-5,5'-bithiazole results in **P106** and **P107**, which have a more planar backbone than **P104** and **P105** because of the elimination of repulsive C–H···H–C interactions between phthalimide and thiazole.<sup>210</sup> The higher degree of backbone coplanarity leads to a reduced band gap, enhanced  $\pi-\pi$  stacking, and increased film crystallinity for **P106** and **P107**. The band gaps of **P106** and **P107** are 1.58 and 1.62 eV, respectively, which are ~0.1 eV smaller than those of **P104** and **P105**. The high degree of backbone coplanarity and strong intermolecular interactions result in reduced **P106** and **P107** solubilities. The soluble batches of **P106** and **P107** have  $M_n$ s of 34.6 and 5.2 kDa, respectively. OTFTs show  $\mu_h$ s of 0.13 and 0.06 cm<sup>2</sup>/(V s) for **P106** and **P107**, respectively, which are comparable to or greater than those of thiophene-based polymer analogues **P104** and **P105** having comparable  $M_n$ s.<sup>210</sup> Moreover, the thiazole-based polymers **P106** and **P107** show enhanced OTFT durability due to their low-lying HOMOs. After 6 weeks storage in ambient, **P107** OTFT  $\mu_h$  and  $I_{on}/I_{off}$  remain unchanged while **P105**  $I_{on}/I_{off}$  falls by more than 100 times.<sup>210</sup>

The phthalimide–dithiophene copolymer **P108** was synthesized and showed excellent thermal stability with decomposition temperature ( $T_d$ ) at 5% weight loss above 430 °C.<sup>242</sup> **P108** BGBC OTFTs exhibited a  $\mu_h$  of 0.005 cm<sup>2</sup>/(V s) with an  $I_{on}/I_{off}$  of  $4 \times 10^5$ .  $\mu_h$  is mainly limited by its substantial hole injection barrier (~0.5 eV) and relatively low  $M_n$  (12 kDa).<sup>242</sup> **P109** and **P110** having thiophene or selenophene spacers were synthesized.<sup>243</sup> The lower electronegativity of selenium (versus sulfur) yielded a stronger intramolecular Se···(carbonyl)O attraction

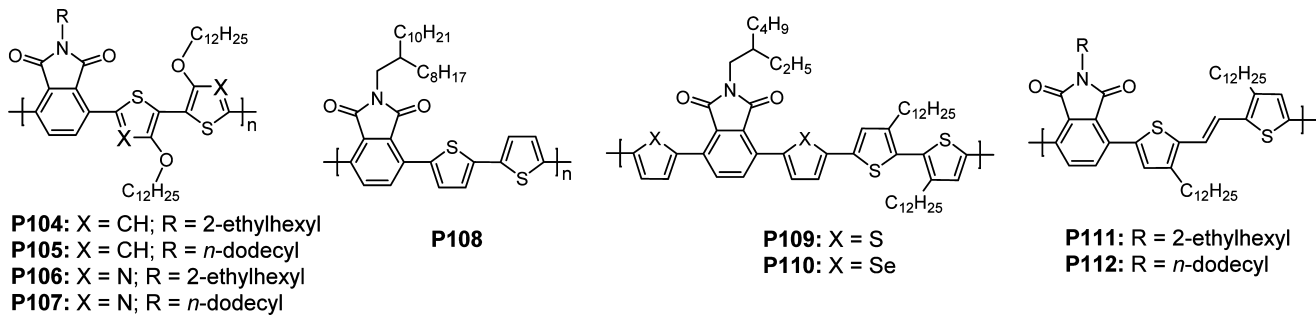
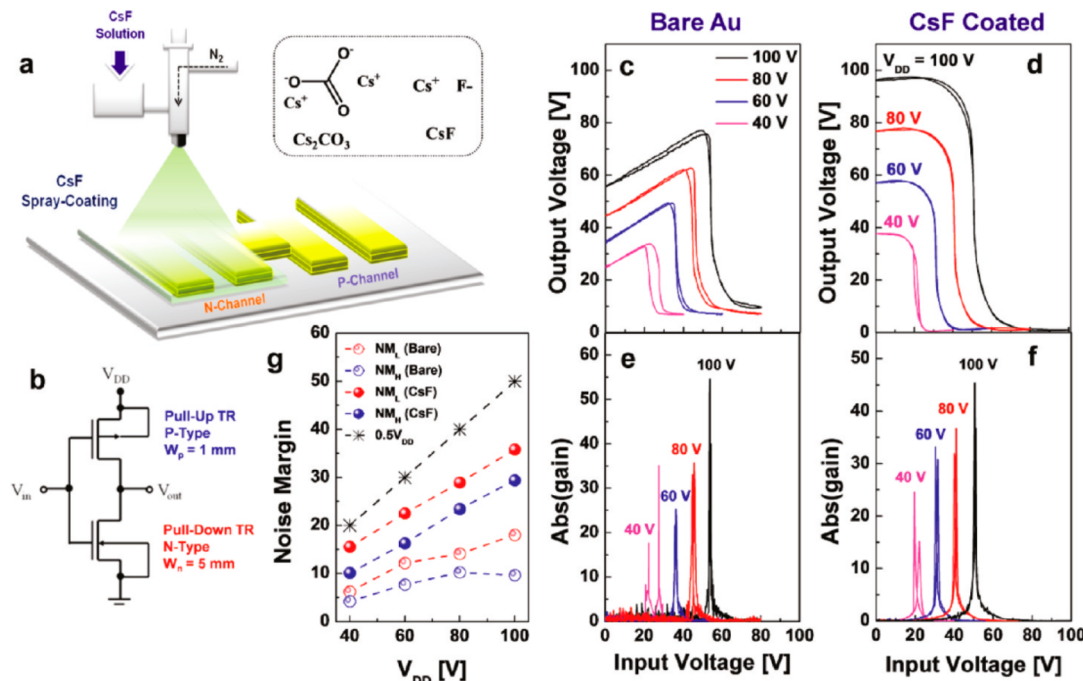


Figure 28. Chemical structures of phthalimide-based polymer semiconductors for OTFTs.

Figure 29. Complementary inverters based on polymer P111 OTFTs. (a) Schematic illustration of the spray-coating process, where  $\text{Cs}_2\text{CO}_3$  and CsF are deposited selectively onto the n-channel transistor region. (b) Circuit configuration of the complementary inverter. Voltage transfer characteristics and corresponding output voltage gains of the inverters: (c, e) Bare Au source/drain electrode and, (d, f) after selective spray-deposited CsF layer. (g) Noise margins of the corresponding inverter with or without the CsF layer only in the n-channel region. Reprinted with permission from ref 37. Copyright 2011 American Chemical Society.

than a S···(carbonyl)O attraction and therefore higher backbone coplanarity of P110 than that of P109, which led to higher ordering in the P110 film. P110 OTFTs showed a  $\mu_h$  of  $3.2 \times 10^{-4} \text{ cm}^2/(\text{V s})$ , while P109 OTFTs were inactive under the condition used for device fabrication and characterization. The low P109  $\mu_h$  was due to the large hole injection barrier ( $\sim 0.7 \text{ eV}$ ) and twisted backbone induced by the head-to-head linkage containing bithiophene.

Kim and co-workers reported P111 and P112 having bithienylene vinylene donors.<sup>244</sup> Introducing vinylene linkers greatly reduced steric hindrance in the dialkyl bithiophene moiety and led to a band gap of 1.85 eV for P111 and P112. Without annealing, TGBG OTFTs fabricated by spin coating P111 chlorobenzene solution showed ambipolarity with a  $\mu_h/\mu_e$  of  $0.18/0.004 \text{ cm}^2/(\text{V s})$ . Annealing at  $200^\circ\text{C}$  led to a  $\mu_h/\mu_e$  of  $0.75/0.03 \text{ cm}^2/(\text{V s})$ . Further annealing at  $250^\circ\text{C}$  resulted in a  $\mu_h/\mu_e$  of  $0.40/0.06 \text{ cm}^2/(\text{V s})$ . The threshold voltages for n- and p-channel operation were typically around  $50$  and  $-40 \text{ V}$ , respectively, due to the substantial charge injection barriers. In comparison to P111, P112 showed inferior performance with an

optimal  $\mu_h/\mu_e$  of  $0.041/0.049 \text{ cm}^2/(\text{V s})$ . The performance was in good agreement with their film microstructure. Complementary inverters having two identical TGBG OTFTs were then fabricated by spin coating P111 and annealing polymer film at  $250^\circ\text{C}$ . The inverters showed "Z"-shaped voltage transfer character and exhibited a voltage gain of  $\sim 40$  at  $V_{dd} = 70 \text{ V}$ . P111 was viable for fabricating large-area OTFT arrays and complementary circuits by a simple bar-coating process, which resulted in enhanced film crystallinity, smoother morphology, and increased mobility versus spin coating.<sup>245</sup> A simple method to tune charge injection and transport in ambipolar OTFTs via engineering electrical contacts was developed by the same group.<sup>37</sup> Inserting a thin  $\text{Cs}_2\text{CO}_3$  or CsF layer between the Au electrode and the polymer via spray coating led to greatly enhanced n-channel performance with a  $\mu_e$  of  $0.3 \text{ cm}^2/(\text{V s})$  but resulted in degraded p-channel performance with a  $\mu_h$  of  $0.04 \text{ cm}^2/(\text{V s})$  for P111 OTFTs.<sup>37,246</sup> After selective deposition of CsF onto the n-channel region, P111-based inverters yielded voltage gains  $>50$  with negligible bias hysteresis and good noise margin as high as  $\sim 75\%$  of  $1/2 V_{DD}$  (Figure 29). A five-stage ring

oscillator with a high oscillation frequency of 12 kHz was fabricated from **P111**.<sup>37,245</sup> The results demonstrated the great potential of phthalimide ambipolar polymers for fabrication of a variety of large-area and cost-effective organic integrated circuits.

### 5.3. Phthalimide-Based Polymer Semiconductors for OSCs

The small band gap (~1.70 eV), good hole mobility, and decent solubility render **P104** and **P105** (Figure 28) as promising donor semiconductors for OSCs. Jeneke and co-workers first reported **P105**-based OSCs and fully investigated the film morphology, charge transport property, and device performance.<sup>247</sup> **P105**:P<sub>71</sub>BM BHJ OSCs showed a PCE of 2.0% with a  $J_{sc}$  of 6.43 mA/cm<sup>2</sup>, a  $V_{oc}$  of 0.56 V, and a FF of 55%. Annealing the blend films at 120 °C led to phase separation at the micrometer scale and thus negligible performance.<sup>247</sup> **P104**:PC<sub>71</sub>BM cells achieved an optimal PCE of 4.1% with a  $V_{oc}$  of 0.54 V,<sup>248</sup> which was improved two-fold over **P105** OSCs. It was found that **P104** performance was highly sensitive to processing additives. Thus, 1,8-octanedithiol addition led to a 10-fold PCE enhancement. Film morphology characterization revealed that 1,8-octanedithiol can effectively inhibit PC<sub>71</sub>BM intercalation into **P104** side chains<sup>107</sup> and reduce phase-segregated polymer and fullerene domains to 15–20 nm (Figure 30). The major limits of **P104** and **P105** performance were the small  $V_{oc}$ s, which are associated with their high-lying HOMOs due to the highly electron-rich dialkoxy bithiophene.

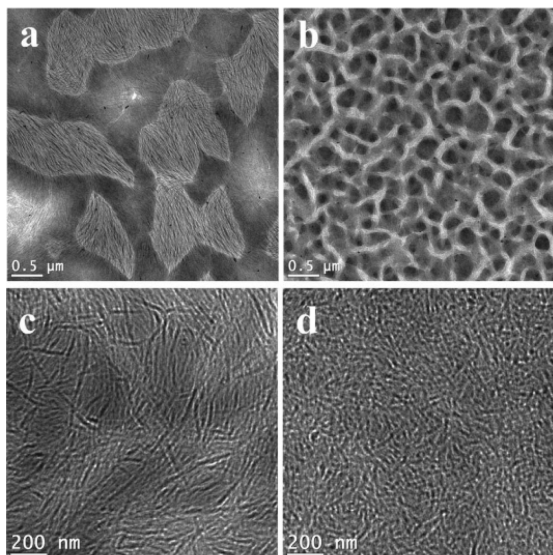


**Figure 30.** TEM images of **P104**:PC<sub>71</sub>BM (1:1) films processed under different conditions: (a) without additive and slow drying; (b) without additive and fast drying; (c) with additive and slow drying; (d) with additive and fast drying. Scale bars are 0.5  $\mu$ m in a and b and 200 nm in c and d. Reprinted with permission from ref 248. Copyright 2012 Wiley-VCH Verlag GmbH & Co. KGaA.

Using fluorene and carbazole as the weak donors and thiophene as the spacer, **P113** and **P114** (Figure 31) were synthesized and used as the donor semiconductors in BHJ OSCs.<sup>249</sup> The cells showed large  $V_{oc}$ s of 0.90 and 0.94 eV for **P113** and **P114**, respectively. However,  $J_{sc}$ s were limited to lower than 5 mA/cm<sup>2</sup> due to their large band gaps (~2.4 eV). Therefore, limited PCEs of 0.47% and 1.40% were obtained for **P113** and **P114** cells, respectively.<sup>249</sup> Next, tetrathiophene was copolymerized with Phi to afford **P115** having a band gap of 1.96 eV. Optimized BHJ OSCs containing **P115**:PC<sub>71</sub>BM active layer

exhibited a moderate PCE of 1.50% due to limited absorption of solar irradiation.<sup>250</sup> As a promising electron donor, dithienosilole<sup>106</sup> was incorporated into Phi polymers, and the resulting **P116** had a band gap of 2.03 eV. A PCE of 0.58% was obtained from **P116**:PC<sub>70</sub>BM cells.<sup>251</sup> By inserting a thiophene spacer, **P117** exhibited a slightly smaller band gap of 1.93 eV than **P116**. **P117** had a  $-5.2$  eV HOMO, which lead to a 0.83 V  $V_{oc}$  in BHJ OSCs. A maximum PCE of 2.1% was obtained from the **P117**:PC<sub>70</sub>BM cells. Dithienopyrrole was next incorporated to reduce polymer band gaps. **P118** and **P119** showed strong absorption in the visible region with band gaps of 2.05 and 1.86 eV, respectively. Inverted OSCs having structure ITO/ZnO/**P118**(or **P119**):PCBM/PEDOT:PSS/Ag exhibited low PCEs (<1%). These materials show amenability for fabricating large-area cells by roll-to-roll slot-die coating, and a PCE of 0.43% was obtained from **P118**-based OSCs.<sup>252</sup>

PhIs with benzodithiophene copolymers were synthesized;<sup>253,254</sup> the resultant **P120**–**P122** have broad band gaps of 2.0–2.10 eV due to the unfavorable quinoidal structure formation. The **P120**–**P122**  $\mu_h$ s measured from OTFTs were in the range of  $10^{-4}$ – $10^{-3}$  cm<sup>2</sup>/(V s). The two-dimensional conjugated **P122** with alkylthienyl-substituted benzodithiophene exhibited a ~10-fold higher  $\mu_h$  than **P121** having an alkoxy-substituted benzodithiophene. BHJ OSCs showed limited PCEs, and the highest PCE of 3.70% was obtained from **P122** with a  $J_{sc}$  of 7.01 cm<sup>2</sup>/(V s), a  $V_{oc}$  of 0.89 eV, and a FF of 59%.<sup>254</sup> The high-mobility **P122** was used as a donor semiconductor for OSCs; the resultant cells having structure ITO/PEDOT:PSS/**P122**:PC<sub>71</sub>BM/Ca/Al exhibited an optimal PCE of 4.14% with a  $J_{sc}$  of 7.32 mA/cm<sup>2</sup>, a  $V_{oc}$  of 0.87 V, and a FF of 65%.<sup>255</sup> The high  $V_{oc}$  was attributed to the low-lying **P122** HOMO ( $-5.2$  eV), but the performance was mainly limited by the wide band gap (1.8 eV) of **P122**, which led to a small  $J_{sc}$ . The performance indicates that **P122**-based cells could be a promising candidate for the front cell in tandem cells owing to its strong visible range absorption and good  $V_{oc}$ .<sup>256</sup>

### 5.4. Summary

The first monoimide-functionalized polymers for OTFT incorporate a phthalimide unit, and these semiconductors exhibit, when compared to the corresponding diimide-functionalized polymers, predominant p-type transport with good mobilities. The unfavored population of the quinoidal form of the phthalimide building block and the greater steric demands when compared to five-membered ring imide/amide units (vide infra) are the major factors preventing phthalimide-based polymers from outperforming in OTFTs and OSCs. However, this materials system represents a stepping stone for development of monoimide-functionalized polymers for organic electronics.

## 6. THIENO[3,4-*c*]PYRROLE-4,6-DIONE-BASED POLYMER SEMICONDUCTORS

As a structural analogue to phthalimide, thieno[3,4-*c*]pyrrole-4,6-dione (TPD)<sup>257</sup> is the obvious next acceptor for creating polymer semiconductors due to its geometry and electronic properties. Compared to the aromatic resonance energy ( $E_{ar}$ ) of benzene (1.56 eV) in phthalimide, thiophene has a greatly reduced  $E_{ar}$  of 1.26 eV. Therefore, TPD polymers should more likely adopt the quinoidal form and therefore achieve lower band gaps than phthalimide polymers.<sup>110</sup> Moreover, the TPD's geometry should impose reduced steric hindrance on neighboring arenes, and intramolecular thielen(S)…carbonyl(O) inter-

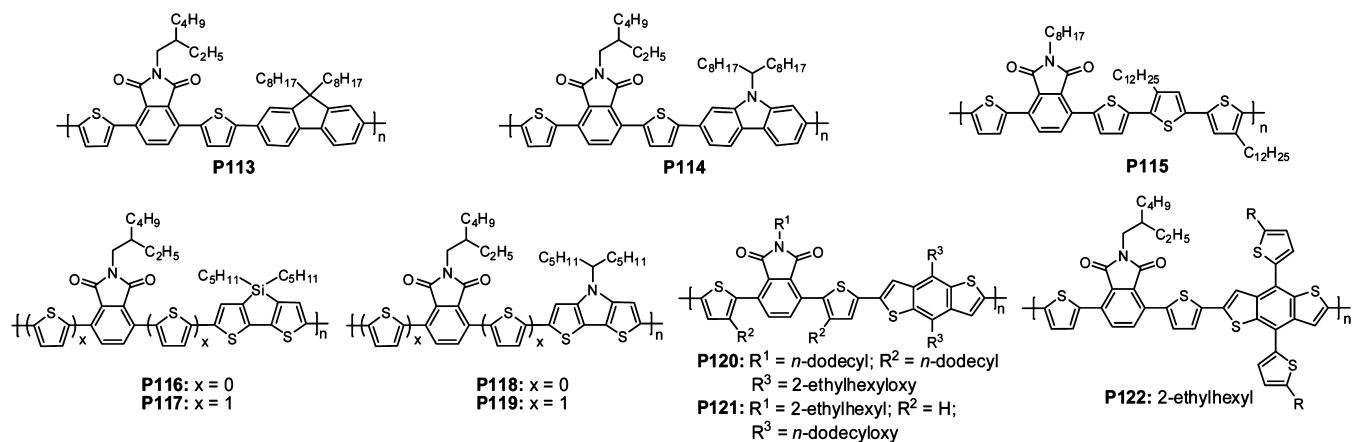
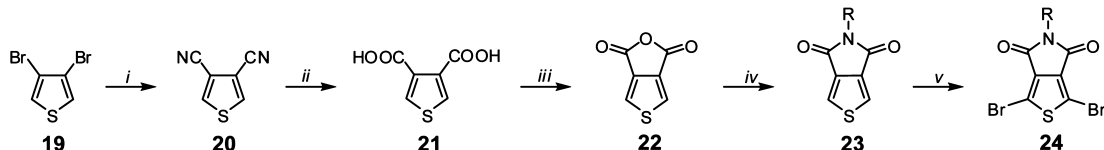


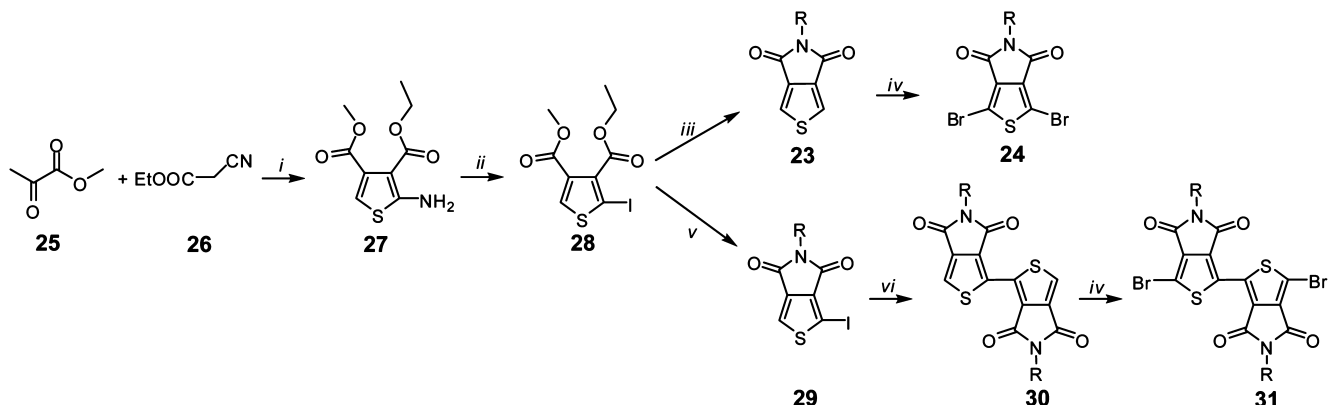
Figure 31. Chemical structures of phthalimide-based polymer semiconductors for OSCs.

Scheme 7. Synthetic Route to Dibrominated Thieno[3,4-*c*]pyrrole-4,6-dione<sup>a</sup>



<sup>a</sup>Reagent and conditions: (i) CuCN, DMF, reflux; (ii) KOH, ethylene glycol, reflux; (iii) Ac<sub>2</sub>O, 140 °C; (iv) (a) RNH<sub>2</sub>, toluene, reflux; (b) SOCl<sub>2</sub>, reflux; (v) NBS, H<sub>2</sub>SO<sub>4</sub>, CF<sub>3</sub>COOH.

Scheme 8. Alternative Synthetic Route to Dibrominated Thieno[3,4-*c*]pyrrole-4,6-dione and Synthetic Route to 1,1'-Dibromo-[3,3'][bi[thieno[3,4-*c*]pyrrol]-4,6,4',6'-tetraone<sup>a</sup>



<sup>a</sup>Reagents and conditions: (i) S<sub>8</sub>, Et<sub>3</sub>N, DMF, 50 °C; (ii) HCl (2 M), NaNO<sub>2</sub>, KI; (iii) neat RNH<sub>2</sub>, 200–280 °C; (iv) NBS, H<sub>2</sub>SO<sub>4</sub>, CF<sub>3</sub>COOH; (v) (a) HCl (2 M), reflux; (b) Ac<sub>2</sub>O; (c) dioxane, DMAP, RNH<sub>2</sub>; (d) Ac<sub>2</sub>O; (vi) Cu, DMF, reflux.

actions are likely to enforce backbone coplanarity.<sup>44</sup> Hence, when appropriate counits are chosen, TPD polymers can possess small band gap, high degrees of coplanarity, and close  $\pi-\pi$  stacking. Alkylation at the imide nitrogen enables access to a large library of polymers with fine-tuned solubility and film microstructure; hence, TPD polymers have recently shown highly promising performance in OTFTs and OSCs.

### 6.1. Synthesis of Dibrominated Thieno[3,4-*c*]pyrrole-4,6-dione and Its Dimer

Sicé first reported unsubstituted thieno[3,4-*c*]pyrrole-4,6-dione by treating thiophene anhydride with ammonia for confirming the hydride structure.<sup>258</sup> In 1970, BASF patented a series of TPD-based synthetic dyes.<sup>259</sup> In 1997, Tour et al. reported a synthetic route to dibromo TPD having an alkyl substituent on the imide group,<sup>257</sup> and a modified procedure was developed by

Björnholm (Scheme 7).<sup>260</sup> Starting from 3,4-dibromothiophene **19**, 3,4-dicyanothiophene **20** is synthesized via a Rosenmund–von Braun reaction with cuprous cyanide, which is then converted to dicarboxylic acid **21** through basic hydrolysis in ethylene glycol. Diacid **21** dehydration in acetic anhydride affords anhydride **22** in high yield, which can be purified by recrystallization in toluene. Imidization for synthesis of **23** is proved to be troublesome under the conditions for the synthesis of phthalimide<sup>131</sup> or naphthalene diimide.<sup>179</sup> A two-step procedure was then developed. After reacting with amine in toluene under reflux, anhydride **22** is converted to 4-alkylcarbamoylthiophene-3-carboxylic acid (structure not shown).<sup>260</sup> The second amide formation to imide does not proceed spontaneously. It was found that SOCl<sub>2</sub>-assisted ring closure affords imide **23** in high yield. The following bromination of the imide affords dibromo TPD **24** with near quantitative

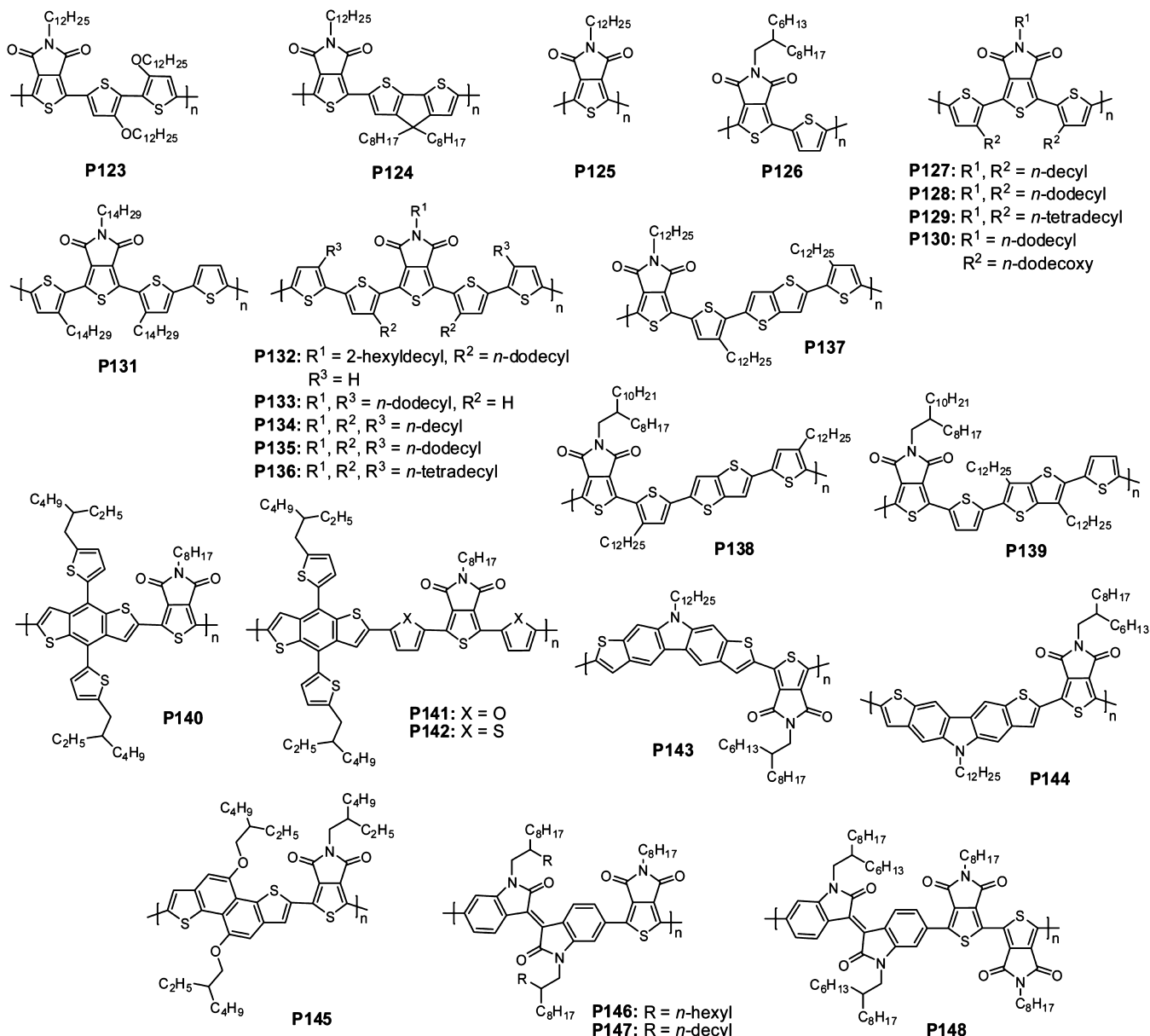


**Figure 32.** Chemical structures of TPD-based polymer semiconductors for OTFTs.

yields. The original procedure for imide synthesis developed by Tour is slightly different,<sup>257</sup> and includes conversion of the dibrominated dicarboxylic acid to the diacyl chloride. Then the diacyl chloride is subjected to imidization by heating the diacyl chloride with amine at 140 °C to afford dibromo TPD 24. Recently, the commercial availability of 3,4-dicarboxylic thiophene 21 makes the synthesis of 24 much easier, which renders TPD polymers particularly suitable for upscale synthesis.

Leclerc et al. developed an alternative pathway to dibromo TPD 24 (Scheme 8).<sup>261</sup> The methyl 2-oxopropanoate 25 and ethyl cyanoacetate 26 undergo a Gewald-type reaction to form 27 with amine at the 2-position and two ester groups at the 3- and 4-positions. Amine 27 can be converted to iodide derivative 28 via a Sandmeyer-type reaction. It was discovered that neat condensation between diester 28 and alkylamine at temperatures above 200 °C affords 23 as the major product, accompanied by iodine elimination. The new methodology eliminates the use of toxic reagents such as thionyl chloride.<sup>261</sup>

Except for the synthesis of the dibromo TPD 24, the iodide diester 28 also enables access to dibromo TPD dimer 31.<sup>132</sup> After hydrolysis under acidic conditions, the ester groups of 28 are converted to acid groups, which is followed by ring closure with amine to form pyrroledione intermediate 29. Ullmann reaction results in TPD dimer 30, which can be readily brominated to afford dibrominated dimer 31. Single-crystal X-ray structure characterization shows that dimer 30 adopts an anticoplanar conformation with strong intramolecular noncovalent (thienyl)-S...(carbonyl)O interactions (Figure 11a). The access to dibrominated TPD dimer 31 expands the TPD polymer family.

## 6.2. Thieno[3,4-c]pyrrole-4,6-dione-Based Polymer Semiconductors for OTFTs

Inspired by the high mobility of phthalimide polymer P105 (Figure 28),<sup>131</sup> the first TPD polymer P123 (Figure 32) for OTFTs was reported by Watson et al., which contains a dialkoxy bithiophene donor.<sup>262</sup> P123 exhibits a reduced band gap of 1.50 eV, which is ~0.2 eV smaller than that of P105 due to the higher

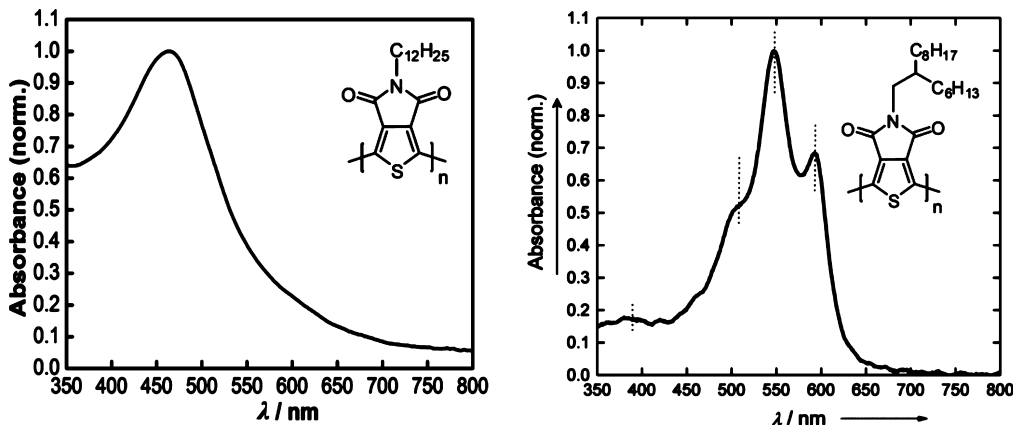


**Figure 33.** Optical absorption spectra of TPD homopolymer **P125** (left) synthesized via Yamamoto coupling (Reprinted with permission from ref 241. Copyright 2011 American Chemical Society.) and the **P125** analogue (right) having 2-hexyldecyl on the imide group synthesized via direct heteroarylation (Reprinted with permission from ref 263. Copyright 2012 Wiley-VCH Verlag GmbH & Co. KGaA.).

degree of population of the quinoidal form in **P123**. However, **P123** shows a much reduced  $\mu_h$  of  $\sim 10^{-3} \text{ cm}^2/(\text{V s})$  versus **P105** in OTFTs. Film characterization by XRD reveals that **P123** has much lower ordering than **P105**. The origin of such lower order in more conjugated **P123** is not well understood. TPD–cyclopentadithiophene copolymer **P124** has a band gap of 1.67 eV and shows a maximal  $\mu_h$  of  $8.9 \times 10^{-3} \text{ cm}^2/(\text{V s})$  with an  $I_{\text{on}}/I_{\text{off}}$  of  $10^5$  in BGBC OTFTs after annealing at  $150^\circ\text{C}$ . The moderate **P124**  $\mu_h$  is in good agreement with its low-order film microstructure as revealed by XRD investigation.

TPD homopolymer **P125** was synthesized via Cu-mediated Ullmann-type polymerization and obtained as a lustrous black solid having a  $M_n$  of 3.3 kDa with a PDI of 1.48.<sup>260</sup> The same polymer synthesized via Ni-mediated Yamamoto coupling showed an increased  $M_n$  of 4.7 kDa with a PDI of 3.80.<sup>241</sup> **P125** film optical absorption shows a featureless profile with a band gap of 2.15 eV (Figure 33),<sup>241</sup> which indicates its limited conjugation, although DFT computation<sup>44</sup> and X-ray diffraction of a single crystal<sup>132</sup> indicate that TPD dimer **30** adopts a coplanar conformation. It is interesting to note that the TPD homopolymer having 2-hexyldecyl on the imide group synthesized via direct heteroarylation<sup>263</sup> shows a smaller band gap of  $\sim 1.97$  eV and structured absorption with a sharper peak and shoulder than polymers synthesized by Ullmann<sup>260</sup> or Yamamoto coupling (Figure 33).<sup>241</sup> OTFTs using **P125** synthesized from Yamamoto coupling as the channel material are inactive due to the unfavorable high-lying LUMO ( $-3.46$  eV) and amorphous film microstructure as revealed by DSC and XRD.

Marks et al. investigated copolymerization reactions of TPD with various oligothiophenes ( $n$ Ts) to afford a series of TPD– $n$ T copolymers **P126**–**P136** for fine tuning solubility, FMO level, and film microstructure. Insertion of thiophene units into the TPD polymer results in greatly reduced band gaps when compared to that of homopolymer **P125**.<sup>241</sup> **P126** bearing a monothiophene has a band gap of 1.74 eV, and its BGTC OTFTs show ambipolarity in vacuum with a  $\mu_e/\mu_h$  of  $1.0 \times 10^{-3}/2.5 \times 10^{-4} \text{ cm}^2/(\text{V s})$ . The **P126** mobilities are limited by the large charge injection barrier and low degree of film ordering. As the oligothiophene conjugation length is extended to bithiophene, terthiophene, and tetrathiophene, the resulting copolymers show enhanced p-type response with  $\mu_h$ s approaching or surpassing  $0.1 \text{ cm}^2/(\text{V s})$ . **P129** having a bithiophene donor and **P131** having a terthiophene donor achieve the highest average  $\mu_h$  of  $0.18 \text{ cm}^2/(\text{V s})$ .

( $\text{V s}$ ) in the series. The maximum  $\mu_h$  of  $\sim 0.6 \text{ cm}^2/(\text{V s})$  is obtained from **P131** after annealing at  $210^\circ\text{C}$ . The  $\mu_h$ s of **P132**, **P134**, **P135**, and **P136** are  $\sim 0.1 \text{ cm}^2/(\text{V s})$ . **P132** and **P133** have tetrathiophene donors but with different alkylation patterns. In comparison to **P135**, deletion of two *n*-dodecyls on the TPD neighboring thiophenes leads to greatly decreased ordering and crystallinity for **P133** and therefore a 10 times lower  $\mu_h$ . In comparison to **P135**, deletion of two *n*-dodecyls on the middle bithiophene of the tetrathiophene in **P132** minimally impacts on the film microstructure. Therefore, **P132** exhibits a  $\mu_h$  of  $9.8 \times 10^{-2} \text{ cm}^2/(\text{V s})$ , slightly lower than that ( $0.14 \text{ cm}^2/(\text{V s})$ ) of **P135**. As compared to **P133**, the greater **P132** crystallinity is likely due to a higher degree of side-chain interdigitation, enabled by the large local free volume between alkyl chain clusters. These results demonstrate the significance of manipulating the alkylation patterns for performance enhancement. It was also found that the optical properties and OTFT performance of tetrathiophene copolymers **P134**–**P136** are insensitive to alkyl chain length. However, bithiophene copolymers **P127**–**P129** show a distinct red-shifted absorption maximum, greatly increased film crystallinity, and enhanced  $\mu_h$  as the chain length increases. TPD incorporation leads to lower lying HOMOs than P3HT by  $>0.24$  eV for **P126**–**P136** except for **P130** in which a strong electron-donating dialkoxy bithiophene is the donor. For polymers with  $\mu_h > 0.1 \text{ cm}^2/(\text{V s})$ , both air and operational stabilities are monitored. OTFTs fabricated from **P129**, **P131**, **P132**, **P135**, and **P136** show negligible performance degradation up to 5 months storage in ambient. Under bias stress, **P131** and **P135** OTFTs show greater performance degradation than **P129** OTFTs. The superior **P129** OTFT stability is attributed to its lowest HOMO, rendering charge carriers least sensitive to trapping.<sup>241</sup>

Li investigated alkyl orientation effects on film microstructure and OTFT performance of **P137**–**P139** having thienothiophene flanked with thiophene as the donors.<sup>264</sup> The donors have a similar repeat unit structure as the high-performance polymer PBT<sup>47</sup> but with varied alkyl orientations. OTFT performance was found to be highly sensitive to the alkylation pattern with  $\mu_h$ s of 0.011, 0.15, and  $1.29 \text{ cm}^2/(\text{V s})$  for **P137**, **P138**, and **P139**, respectively. 2D-GIXD shows that the alkylation patterns have a small impact on the  $\pi$ – $\pi$  stacking distances, which are 3.67, 3.63, and 3.74 Å for **P137**, **P138**, and **P139**, respectively. However, they have a substantial impact on alkyl chain interdigitation and ordering in the lamellar direction. The diffraction features reveal

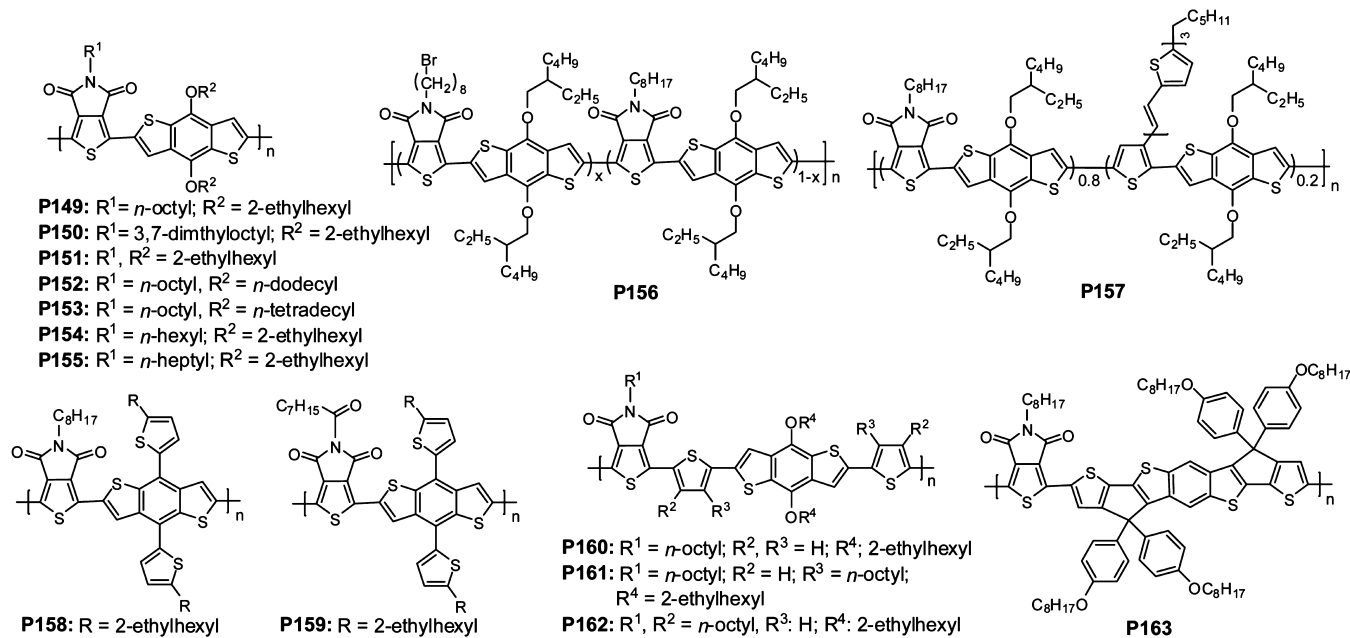


**Figure 34.** Chemical structures of TPD-benzodithiophene copolymers for OSCs.

their layer-by-layer lamellar structure with an edge-on orientation relative to substrate. The interlayer distances separated by alkyl chains are 34.1, 24.66, and 24.31 Å for P137, P138, and P139, respectively. P139 with the largest spacing between the alkyl chain clusters shows the highest interdigititation, while P137 having the smallest space exhibits the least interdigititation.<sup>264</sup> Therefore, the large spacing between the alkyl clusters facilitates side-chain interdigititation. P139 having the greatest interdigititation shows a higher degree of ordering with the 2D-GIXD diffraction peaks progressing to high order. Device stability data indicate that TPD polymers show improved OTFT stability as compared to PBTETT.<sup>47</sup> The studies demonstrate the significance of alkyl chain orientation on the polymer packing model and device performance.<sup>131,264</sup>

Ma studied the effects of bridge units on TPD polymer mobilities.<sup>265</sup> The furan-bridged P141 has a slightly larger band gap (1.88 eV) than P140 (1.85 eV) without a bridge. The thiophene-bridged P142 is insoluble. Therefore, furan-bridged polymer show improved solubility compared to the thiophene-bridged analogues.<sup>266</sup> Theoretical simulation indicates that furan incorporation results in a lower degree of backbone planarity due to the weaker (furyl)O···(carbonyl)O interactions as compared to (thienyl)S···(carbonyl)O interactions, in good accordance with the XRD data. TGBC OTFTs show optimal  $\mu_{\text{h}}$ s of 0.12 and 0.03 cm<sup>2</sup>/(V s) for P140 and P141, respectively. Therefore, furan incorporation leads to a 3-fold smaller  $\mu_{\text{h}}$  for P141, in good agreement with polymer backbone coplanarity and film crystallinity. Dithieno[2,3-*b*:7,6-*b*]carbazole and its isomer dithieno[3,2-*b*:6,7-*b*]carbazole are incorporated into P143 and P144, which show distinctive performance in BGTC OTFTs with  $\mu_{\text{h}}$ s of  $2.9 \times 10^{-3}$  and 0.31 cm<sup>2</sup>/(V s), respectively.<sup>267</sup> P143 has strong backbone curvature, and the film exhibits amorphous character, while P144 shows a sine-wave-shaped backbone and forms ordered films with an edge-on orientation relative to the substrate. P145 containing extended naphtho[1,2-*b*:5,6-*b*']dithiophene donor shows a  $\mu_{\text{h}}$  of 0.07 cm<sup>2</sup>/(V s) with an extremely high  $I_{\text{on}}/I_{\text{off}}$  of  $10^{9-10}$ , which are ascribed to its low-lying HOMO of -5.38 eV.<sup>268</sup>

P146 and P148 having all-acceptor backbone were synthesized. Traditional Suzuki–Miyaura coupling shows low activity or inactivity. Direct (hetero)arylation polymerization<sup>263</sup> afforded P146 and P148 with good  $M_n$ s of 24 and 20 kDa, respectively.<sup>269</sup> Cyclic voltammograms showed low-lying LUMOs of -4.2 eV for both polymers. After annealing at 200 °C, P146 and P148 OTFTs exhibited  $\mu_{\text{e}}$ s of  $2.0 \pm 0.7 \times 10^{-4}$  and  $2.5 \pm 0.7 \times 10^{-3}$  cm<sup>2</sup>/(V s), respectively. Using a TPD dimer instead of TPD led to enhanced electron mobility for P148, which could be attributed to the centrosymmetric characteristics of the TPD dimer.<sup>208</sup> Yang et al. reported P147, which has the same polymer backbone as P146 but a longer solubilizing chain.<sup>270</sup> P147 BGTC OTFTs showed unipolar n-channel performance with a  $\mu_{\text{e}}$  of ~0.01 cm<sup>2</sup>/(V s) after annealing at 150 °C. In comparison to P146, P147 exhibited increased mobility, which was attributed to its higher  $M_n$  (57 kDa) facilitated by the longer branched chains.

### 6.3. Thieno[3,4-*c*]pyrrole-4,6-dione-Based Polymer Semiconductors for OSCs

Application of TPD polymers in OSCs was pioneered by Leclerc.<sup>271</sup> TPD–benzodithiophene copolymer P149 (Figure 34) was synthesized by Stille coupling. Despite the strong TPD electron-withdrawing capability, P149 has a moderate band gap of ~1.8 eV but a low-lying HOMO of -5.56 eV. P149 OSCs having the structure ITO/PEDOT:PSS/P149:PC<sub>71</sub>BM/LiF/Al with a 1.0 cm<sup>2</sup> active area demonstrate a PCE of 5.5% with a high  $V_{\text{oc}}$  of 0.85 V. The seminal work by Leclerc shows the great potential of TPD for constructing high-performance solar cell polymers. Soon after, several groups simultaneously reported TPD–benzodithiophene copolymers having the same or slightly different alkyl chains with PCEs of 4–6.8%.<sup>272–274</sup> Among them, Fréchet et al. reported a series of polymers P149–P151, and an optimized PCE of 6.8% was achieved for P149:PC<sub>61</sub>MB (1:1.5; w:w) cells fabricated from chlorobenzene/DIO (99/1, v/v) solution. It was found that the performance was highly dependent on the TPD solubilizing chain. The linear *n*-octyl chains led to a closer P149 π–π stacking (3.6 Å) than that (3.8 Å) of P151 having 2-ethylhexyl chains (Figure 35).<sup>274</sup> GIXS

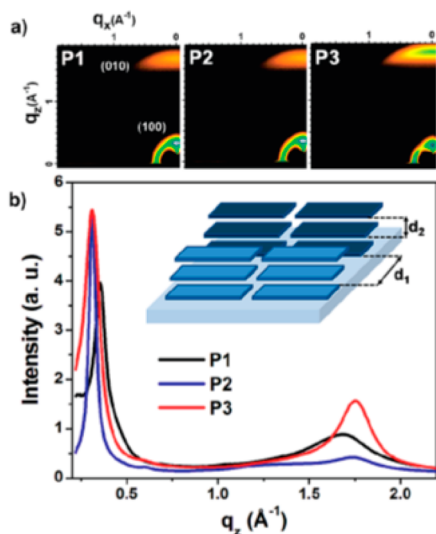


**Figure 35.** (a) Two-dimensional grazing incidence X-ray scattering (GIXS) patterns of films of P149 (P3), P150 (P2), and P151 (P1). (b) Out-of-plane linecuts of GIXS. (Inset) Schematic illustration of the face-on orientation of the polymers with the backbone parallel to the substrate. Lamellar spacing and the  $\pi$ - $\pi$  stacking distance are labeled  $d_1$  and  $d_2$ , respectively. Reprinted with permission from ref 274. Copyright 2010 American Chemical Society.

scattering indicated that 1,8-diiodooctane (DIO) addition greatly promoted film ordering, which resulted in improved PCEs. Further performance optimization led to PCEs of 7.1–7.3% with  $V_{oc}$ s of ~0.95 V using binary processing additives<sup>275</sup> or high  $M_n$  (41 kDa) P149.<sup>276,277</sup>  $V_{oc}$ s approaching 1.1 V were obtained in P149:multiadduct fullerene (ICBA) cells, which was attributed to the large energy offset between the P149 HOMO and the ICBM LUMO. However, the  $J_{sc}$ s, FFs, and PCEs were significantly decreased in P149:ICBM cells due to the slow and inefficient electron transfer from P149 to ICBA.

Further materials structure-device performance correlations were explored by varying the substituents on both the benzodithiophene and TPD units.<sup>139</sup> P152 and P153 having *n*-alkyl substitutions on the benzodithiophene show the absence of a preferential  $\pi$ - $\pi$  stacking orientation, resulting in reduced PCEs of <4.2%. P149, P154, and P155 having branched 2-ethylhexyl on the benzodithiophene and linear *N*-substituents on the TPD unit adopt a preferential face-on orientation relative to the substrate, which benefits charge extraction. Fine tuning the aliphatic carbon number on the linear imide *N*-substituents

delivers a PCE of 8.5% in the optimized P155:PC<sub>71</sub>BM cells,<sup>139</sup> while the optimal PCEs are 7.5% and 6.6% for P149:PC<sub>71</sub>BM and P154:PC<sub>71</sub>BM cells, respectively. Quantitative X-ray analyses are desired to provide insight into the performance variations for P149, P154, and P155 having subtle structural variations. The promising PCE makes P155 one of the best broad band-gap polymers for tandem cells.

P156, a P149 analogue, but having photo-cross-linkable side chains, has also been reported.<sup>278</sup> Introduction of a terminal alkyl-bromine functional group on imide at 16% loading does not detrimentally affect P156 optical properties and device performance in comparison to P149. A 5.6% PCE is obtained for P156:PC<sub>71</sub>BM cells before photo-cross-linking, which is comparable to 5.2% PCE from P149:PC<sub>71</sub>BM cells. However, photo-cross-linking results in a lower initial PCE of 3.3% for P156:PC<sub>71</sub>BM cells. Therefore, photo-cross-linking detrimentally affects polymer device performance. Thermal annealing leads to a sharp PCE drop for both P149 and P156 cells without cross-linking but results in improved PCE for P156 cells with cross-linking. PCEs of the cross-linked P156 cells can be stabilized with a maximum value of 4.6% obtained after 72 h annealing at 150 °C. AFM characterization indicates that photo-cross-linking allows maintenance of the optimal film morphology throughout long-term annealing process. However, thermal annealing dramatically alters film morphology and results in a very rough film with a root-mean-square (RMS) roughness of 35 nm for the non-cross-linked film.<sup>278</sup>

Tajima reported a benzodithiophene–TPD copolymer with a tris(thienylenevinylene) (TTV) conjugated side chain attached to a polymer backbone.<sup>279</sup> Replacement of TPD with TTV containing thiophene afforded P157, in which the ratio between TTV containing thiophene and TPD was 1:4. P157 showed identical absorption onset but enhanced absorption in the range of 400–500 nm when compared to P149, which was attributed to TTV side-chain absorption. P157:PC<sub>70</sub>BM cells showed a PCE of 6.46%, which was increased by 25% in comparison to the PCE (5.14%) of P149:PC<sub>70</sub>BM cells. The performance enhancement was attributed to the improved charge separation at the P157:PC<sub>70</sub>BM interface due to introduction of TTV side chains, but the 10-fold improved hole mobility and morphology changes should not be excluded in the P157:PC<sub>70</sub>BM cell performance enhancement.<sup>279</sup>

Polymers containing conjugated alkylthienyl-substituted benzodithiophene were synthesized for fine tuning FMO levels.<sup>280</sup> P158 had a moderate band gap of 1.85 eV. BHJ OSCs having the structure ITO/PEDOT:PSS/P158:PC<sub>61</sub>BM/

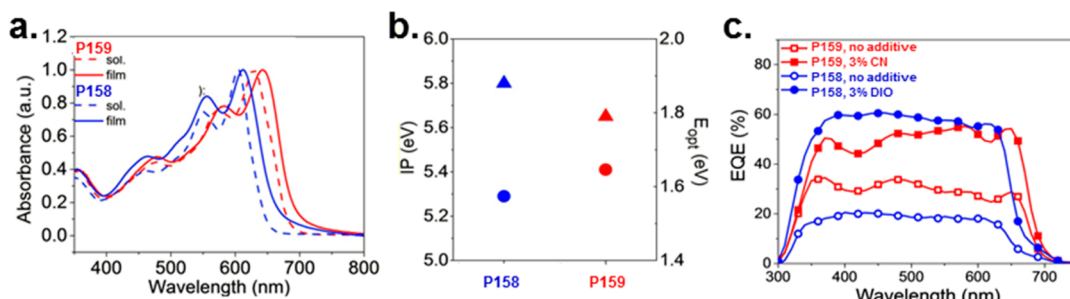


**Figure 36.** (a) Superimposed UV–vis absorption spectra of P158 and P159 in solution and as thin films. (b) Photoelectron spectroscopy-estimated ionization potentials (IP, circles) and optical band gaps ( $E_{\text{opt}}$ , triangles) estimated from the absorption onset of P158 and P159 films. (c) Superimposed external quantum efficiency spectra of optimized P158 and P159 BHJ solar cells. Reprinted with permission from ref 281. Copyright 2014 American Chemical Society.

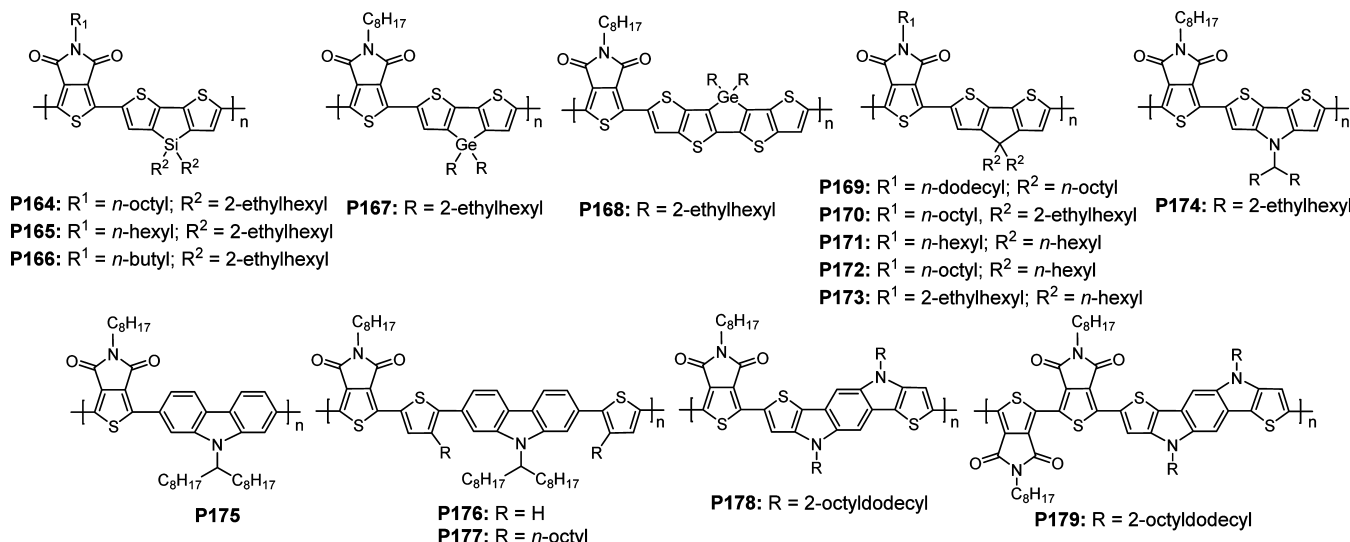


Figure 37. Chemical structures of TPD-based polymer semiconductors for OSCs.

LiF/Al showed a PCE of 6.17% with a  $J_{sc}$  of  $9.79 \text{ mA/cm}^2$ , a  $V_{oc}$  of 1.0 V, and a FF of 63% s. The  $V_{oc}$  of P158 cells was much greater than that (0.90 V) of P149 cells.<sup>280</sup> Replacement of alkoxy with alkylthienyl on the benzodithiophene led to lower lying HOMOs and enlarged  $V_{oc}$ s in OSCs.<sup>274,280</sup>

Beaujuge et al. designed a novel TPD acceptor functionalized with an acyl (or alkoyl) substituent.<sup>281</sup> The N-acylated TPD was readily obtained from dibrominated thiophene anhydride in two steps. The new monomer was copolymerized with thiényl-substituted benzodithiophene to afford P159,<sup>281</sup> and the parent polymer P158<sup>280</sup> was synthesized as a control. By comparing the structures of P158 and P159, the only difference was that the methylene moiety attached to the imide nitrogen in P158 was replaced by a carbonyl group in P159. Single-crystal X-ray diffraction of the new TPD revealed that there was a  $20.6^\circ$  torsion between the carbonyl of the N-acyl group and the TPD plane. It was found that such away backbone torsion was not detrimental to polymer packing. Grazing incidence X-ray scattering revealed that P159 and P158 neat films show comparable scattering patterns. Both polymers assumed a face-on orientation with a  $\pi-\pi$  stacking of 3.65 and 3.68 Å for P159 and P158, respectively. The acylated TPD led to P159 having a smaller band gap of 1.79 eV than that (1.88 eV) of the parent polymer P158 (Figure 36a) accompanied by a lower lying HOMO of  $-5.41 \text{ eV}$  versus that ( $-5.29 \text{ eV}$ ) of P158 (Figure 36b). Solar cells with the structure ITO/PEDOT:PSS/P159(or P158):PC<sub>71</sub>BM/Ca/Al were fabricated to test their photovoltaic performance.<sup>281</sup> The addition of processing additives greatly improved the cell performance. The optimal P159 cells showed a PCE of 6.7% with a  $J_{sc}$  of  $10.6 \text{ cm}^2/(\text{V s})$ , a  $V_{oc}$  of 1.05 V, and a FF of 60%, which outperformed P158 cells having a PCE of 6.5% with a  $J_{sc}$  of  $11.1 \text{ m}^2/(\text{V s})$ , a  $V_{oc}$  of 1.00 V, and a FF of 58%. The external quantum efficiency (EQE) spectra revealed that P159 has a more extended response in the red region than P158 by ca. 50 nm (Figure 36c), which is consistent with their absorption profiles. The improved P159 cell performance was attributed to the larger  $V_{oc}$  enabled by its lower lying HOMO. The result demonstrated that using the acyl side chains is an effective strategy for enhancing OSC performance.<sup>281,282</sup>

Leclerc introduced thiophene bridges between TPD and benzodithiophene units and synthesized a new series of polymers P160–P162 having thiophene bridges functionalized with or

without alkyl substituents.<sup>283</sup> The absorption spectra of P160–P162 are blue shifted when compared to that of P149, indicating that the thiophene bridge gives rise to a twisted dihedral angle around the interannular single bond. Polymers with unsubstituted thiophene or with substituted thiophene bridges (alkyl facing benzodithiophenes) show low device performance. The P160- and P161-based solar cells show PCEs of 0.95% and 0.2%, respectively. The low PCEs of P160 and P161 cells are attributed to poor film morphology. However, P162 having a substituted thiophene (alkyl facing TPD) shows optimized morphology and greatly enhanced PCE up to 3.9%, which is still lower than that (5.2%) of P149 cells.<sup>283</sup> Therefore, introduction of thiophene bridges in the TPD and benzodithiophene copolymers results in decreased backbone conjugation and degraded solar cell performance. P163 bearing a heptacyclic benzodi(cyclopentadithiophene) was also synthesized.<sup>284</sup> In comparison to P160–P162 containing thiophene-flanked benzodithiophene, the heptacyclic benzodi(cyclopentadithiophene) in P163 covalently rigidifies the backbone by fastening the flanking thiophene and thiophene moieties on benzodithiophene using a carbon bridge, which greatly increases backbone coplanarity, strengthens parallel p-orbital interactions, and facilitates charge transport. With the implementation of the forced planarization, P163 exhibits a red-shifted absorption and smaller band gap in comparison to those of P160–P162. OSCs having the structure ITO/PEDOT:PSS/P163:PC<sub>71</sub>BM/Ca/Al show an optimal PCE of 6.1% with a  $J_{sc}$  of  $11.95 \text{ mA/cm}^2$ , a  $V_{oc}$  of 0.85 V, and a FF of 60.4% using *o*-dichlorobenzene/DMSO (95%/5%, v/v) as the processing solvent. The performance is significantly improved in comparison to the PCE of 0.2% for P161 cells. Replacement of PEDOT:PSS with MoO<sub>3</sub> as the hole-transporting layer delivers a further increased PCE of 6.6% with a  $J_{sc}$  of  $12.21 \text{ mA/cm}^2$ , a  $V_{oc}$  of 0.87 V, and a FF of 62.2%. This performance enhancement can be ascribed to the close energy alignment between the MoO<sub>3</sub> work function and the P163 HOMO, which results in better charge extraction.

While the benzodithiophene–TPD copolymers exhibit promising PCEs in OSCs, the  $J_{sc}$ s are limited by their moderate band gaps due to unfavorable population of the quinoidal resonance form induced by the benzodithiophene. As a widely used donor,<sup>285</sup> dithienosilole was copolymerized with TPD to afford P164 (Figure 37) with a  $M_n$  of 28 kDa and excellent

solubility. **P164** has a greatly reduced band gap of 1.73 eV versus **P149** and is accompanied by a deep HOMO ( $-5.57$  eV).<sup>106</sup> Optimized OSCs having the structure ITO/PEDOT:PSS/**P164**:PC<sub>71</sub>BM/bathocuproine/Al show a PCE of 7.3% with a  $J_{sc}$  of 12.2 mA/cm<sup>2</sup>, a  $V_{oc}$  of 0.88 V, and a FF of 68% with 1 cm<sup>2</sup> active area. Thick cells with a 220 nm active layer show a PCE of 6.1% with an improved  $J_{sc}$  of 13.3 cm<sup>2</sup>/(V s) but a reduced FF of 54%. In comparison to **P149**, **P164** performance improvement is attributed to the increased  $J_{sc}$  due to its better absorption of solar irradiation. The 68% FF is in good accordance with the substantial **P164** hole mobility ( $10^{-4}$  cm<sup>2</sup>/(V s)) measured from OTFTs. Fine-tuning materials structure was carried out by modifying TPD alkyl chains in combination with  $M_n$  optimization. As **P164**  $M_n$  was increased from 10 to 18 and 31 kDa, the PCE was improved from 3.0% to 5.2% and 7.5%.<sup>112</sup> The improvement was attributed to  $J_{sc}$  and FF enhancement, which was associated with the increased mobility. The higher  $M_n$  polymer also showed an improved interpenetrating nanoscale morphology for the polymer:PC<sub>71</sub>BM blend. Shortening the TPD alkyl chain in **P164**–**P166** not only led to monotonically decreased solubilities but also resulted in a less ordered film lamellar structure. OSCs showed reduced PCEs of 6.3% and 5.1% for **P165** and **P166**, respectively.

TPD was also copolymerized with dithienogermole to afford **P167**.<sup>105</sup> The long C–Ge bond mitigates steric hindrance between the bulky side chains and the backbone as well as allows for strong interchain  $\pi$ – $\pi$  interactions, which lowers the band gap and promotes charge transport in **P167**. The band gaps are 1.73 and 1.69 eV for **P164** and **P167**, respectively. The **P167** HOMO derived from differential pulse voltammetry (DPV) is  $-5.60$  eV, which is about 50 mV higher than the **P164** HOMO. Therefore, substitution of Si with Ge leads to an elevated HOMO, red-shifted absorption, and a reduced band gap. **P167** inverted cells having the structure ITO/ZnO/**P167**:PC<sub>70</sub>BM/MoO<sub>3</sub>/Ag show a  $J_{sc}$  of 12.6 mA/cm<sup>2</sup>, a  $V_{oc}$  of 0.85 V, a FF of 68%, and a PCE of 7.3%, which outperform **P164** cells having a  $J_{sc}$  of 11.5 mA/cm<sup>2</sup>, a  $V_{oc}$  of 0.89 V, a FF of 65%, and a PCE of 6.6%. The enhanced **P167** performance is mainly attributed to its improved optical absorption. Leclerc reported the same polymer **P167** but with a greatly lower PCE of 4.1% in conventional cells having the structure ITO/PEDOT:PSS/**P167**:PC<sub>71</sub>MB/LiF/Al.<sup>286</sup> The degraded performance is likely due to its lower  $M_n$  of 16.3 kDa because of the difficulty of purifying the distannylated dithienogermole. The high-purity monomer was obtained using preparative GPC in Reynolds's work, which afforded a higher  $M_n$  (48 kDa) and greatly improved PCEs, but the effect of device structure should not be ruled out.<sup>105</sup> The inverted cells were further optimized by incorporating a surface-modified ZnO–poly(vinylpyrrolidone) (PVP) nanocomposite as the electron-transporting layer.<sup>61</sup> UV–ozone treatment of the nanocomposite film resulted in enhanced  $J_{sc}$ s and FFs for **P167** inverted cells compared to those using as-prepared films. Optimal cells were achieved after 10 min UV–ozone treatment to remove PVP polymer at ZnO–PVP nanocomposite surface and showed a remarkable PCE of 8.1% with a  $J_{sc}$  of 14.0 mA/cm<sup>2</sup>, a  $V_{oc}$  of 0.86 V, and a FF of 67.3%. The enhanced performance of ITO/ZnO–PVP nanocomposite/**P167**:PC<sub>71</sub>BM/MoO<sub>3</sub>/Ag cells was attributed to the modified surface composition, which promoted charge collection due to better electronic coupling between the ZnO nanocluster within the nanocomposite and the PC<sub>71</sub>BM in the active layer. **P164** and **P167** were incorporated into inverted cells using a different type of ZnO-colloidal nanoparticles as the electron extraction layer.<sup>287</sup> UVO treatment of ZnO nanoparticle

films can greatly improve  $J_{sc}$ s and FFs by reducing charge recombination at the ZnO/active layer interfaces. The oxygen vacancy concentration was reduced by oxygen penetration in the NPs films; therefore, defects in ZnO nanoparticles were passivated by the UVO treatment. Average PCEs of 7.8% and 8.1% were obtained for **P164** and **P167** cells having the structure ITO/ZnO nonaparticles/polymer:PC<sub>71</sub>BM/MoO<sub>3</sub>/Ag, respectively. **P167** was incorporated into conventional cells using a NiO hole-transporting layer.<sup>288</sup> The OSCs having the structure ITO/NiO/**P167**:PC<sub>71</sub>BM/LiF/Al showed a PCE of 7.8%, which was increased by 15% over cells using a PEDOT:PSS hole-transporting layer. The performance enhancement was mainly attributed to the optical resonance and the homogeneous blend film morphology on the hydrophobic NiO.

By further extending the conjugation length of the donor, Heeney et al. reported **P168** containing the dithienogermolo-dithiophene donor.<sup>289</sup> The polymer showed a band gap of 1.75 eV, which was slightly larger than that of **P167**. The larger **P168** band gap was likely due to the higher degree of electron localization induced by replacement of thiophene with thienothiophene.<sup>39</sup> Without using any processing additive, **P168** conventional cells with the structure ITO/PEDOT:PSS/**P168**:PC<sub>71</sub>BM/Ca/Al showed a promising PCE of 7.2% with a  $J_{sc}$  of 13.85 mA/cm<sup>2</sup>, a  $V_{oc}$  of 0.81 V, and a FF of 64%.

**P169**–**P173** containing carbon-bridged cyclopentadithiophene were synthesized and show moderate PCEs of 3–4%.<sup>262,290</sup> Extensive materials structural modification and device optimization delivered improved PCEs of cyclopentadithiophene–TPD polymers **P171**–**P173**. A maximal PCE of 6.41% with a  $J_{sc}$  of 14.1 mA/cm<sup>2</sup>, a  $V_{oc}$  of 0.75 V, and a FF of 60.7% was obtained from **P172** cells, and **P171** and **P173** showed slightly lower PCEs of ~5.7%.<sup>291</sup> In comparison to the device performance of **P164** and **P167**, the  $V_{oc}$ s of cyclopentadithiophene polymers were lowered by ~0.1 V, which resulted in their lower PCEs. The short C–C bond length between the 3-position carbon of thiophene and the carbon bridge limited the intermolecular packing, which lowered the  $J_{sc}$ s and FFs.

Other fused electron donors such as dithienopyrrole and carbazole were also incorporated into TPD polymers. Polymer **P174** containing dithieno[3,2-*b*:2'3'-*d*]pyrrole has an optical band gap of 1.59 eV but with an elevated HOMO of  $-5.16$  eV due to the strong donor dithienopyrrole.<sup>290</sup> **P174**:PC<sub>71</sub>BM cells showed a moderate PCE of 1.69% with a  $J_{sc}$  of 4.69 mA/cm<sup>2</sup>, a  $V_{oc}$  of 0.76 V, and a FF of 53%. Performance was mainly limited by the low **P174** mobility ( $3.9 \times 10^{-4}$  cm<sup>2</sup>/(V s)) and nonoptimized device fabrication condition. Note that **P174** delivered a high  $V_{oc}$  of 0.76 eV, which was much higher than other dithienopyrrole-containing copolymers. The results demonstrate the strong electron-withdrawing character of TPD, which lowered the polymer HOMO.

The thiophene bridge was introduced to mitigate the steric hindrance and increase the polymer backbone coplanarity for carbazole-based **P176** and **P177** (Figure 37). The weak electron-donor carbazole leads to **P176** having a broad band gap of 2.05 eV with a low-lying HOMO of  $-5.71$  eV.<sup>292</sup> **P176** OSCs show a PCE of 1.82% with a  $J_{sc}$  of 4.72 mA/cm<sup>2</sup>, a  $V_{oc}$  of 1.07 V, and a FF of 36%. **P177** having an alkyl chain on the thiophene bridge shows blue-shifted absorption and an increased band gap of 2.21 eV as compared to **P176**. Therefore, the alkyl chain on the thiophene increases steric hindrance, which adversely impacts the backbone conformation, charge carrier mobility, and film morphology. **P177** cells show a poor PCE of 0.14%. Pyrroloindacenodithiophene, a hybridized donor of carbazole

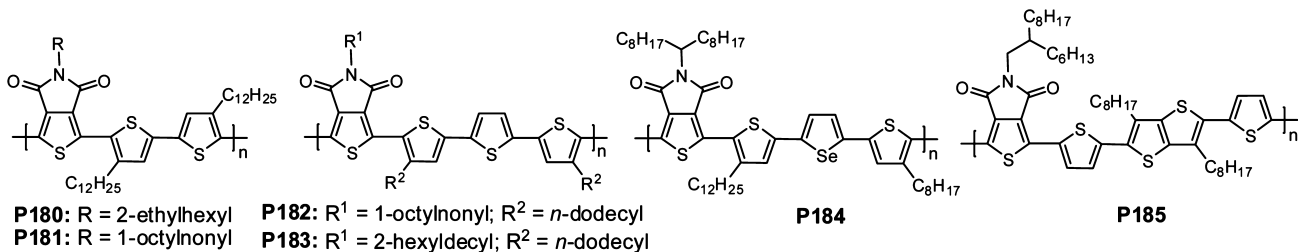


Figure 38. Chemical structures of TPD–oligothiophene polymer semiconductors for OSCs.

and dithienopyrrole, was copolymerized with TPD and the TPD dimer to provide **P178** and **P179**, respectively.<sup>293</sup> The band gaps estimated from absorption onset are 1.7 and 1.6 eV for **P178** and **P179**, respectively. Their HOMOs derived from cyclic voltammetry are −5.10 eV. Therefore, incorporation of pyrroloindacenedithiophene results in significantly smaller band gaps than carbazole-bearing **P176** and **P177**. **P178** OSCs show a PCE of 1.1% with a  $J_{sc}$  of 4.04 mA/cm<sup>2</sup>, a  $V_{oc}$  of 0.58 V, and a FF of 47.8%. For **P179** having TPD dimer acceptor, the OSCs show an enhanced PCE of 2.5% with a  $J_{sc}$  of 4.62 mA/cm<sup>2</sup>, a  $V_{oc}$  of 0.77 V, and a FF of 68.8%. The improved **P179** performance is attributed to its lower HOMO induced by the higher TPD loading in polymer and its high  $M_n$ . AFM characterization reveals that **P179**:PC<sub>71</sub>BM films show a more homogeneous and smoother morphology than **P178**:PC<sub>71</sub>BM films.

Branched 2-ethylhexyl substituents are usually attached to benzodithiophene, dithienosilole, and dithienogermole to achieve the desired polymer solubility due to their fused π systems. However, the branched chains generally lead to a low degree of materials ordering and crystallinity. Oligothiophenes are effective in promoting polymer crystallinity to increase mobility as shown in OTFTs.<sup>241</sup> Due to rotational freedom, the linear alkyl-substituted oligothiophenes can imbue the resultant polymers with good solubility. A tail-to-tail linkage containing bithiophene was copolymerized with TPD using a Stille protocol to afford **P180** (Figure 38), which showed a high degree of crystallinity as revealed by DSC and XRD.<sup>294</sup> The high **P180** crystallinity delivered a sizable  $\mu_h$  of 10<sup>−4</sup> cm<sup>2</sup>/(V s) in both neat and blend films as measured in the SCLC regime. Without processing additives, **P180**:PC<sub>61</sub>BM cells showed a promising PCE of 4.7% with a  $J_{sc}$  of 8.02 mA/cm<sup>2</sup>, a  $V_{oc}$  of 0.95 V, and a FF of 62%. Device optimization led to a greatly improved **P180**:PC<sub>71</sub>BM cell PCE of 7.3% with a  $J_{sc}$  of 13.1 mA/cm<sup>2</sup>, a  $V_{oc}$  of 0.92 V, and a FF of 61%, which was attributed to the enhanced film crystallinity, removal of grain boundaries, and nanoscale phase separation induced by solvent additives.<sup>98</sup> As an analogue to **P180** having 1-octylnonyl substitution on TPD, **P181** was synthesized via direct heteroarylation polycondensation using *trans*-di(μ-acetato)bis[*o*-(*di*-*o*-tolyl-phosphino)-benzyl]dipalladium(II) and tris(*o*-methoxyphenyl)phosphine as the catalyst.<sup>295</sup> **P181** had a high  $M_n$  of 50 kDa and PDI of 2.0 with excellent solubility. **P181** OTFT hole mobility is on the order of 10<sup>−5</sup> cm<sup>2</sup>/(V s), 2 orders of magnitude lower than that of **P128** (Figure 32) having an *n*-dodecyl chain on the imide group.<sup>241</sup> **P181**:PC<sub>70</sub>BM cells showed a PCE of 1.90%, which is significantly lower than that (7.3%) of **P180**:PC<sub>71</sub>BM cells. The performance is in good accordance with their mobilities, and the result highlights the significance of fine tuning the solubilizing chains.

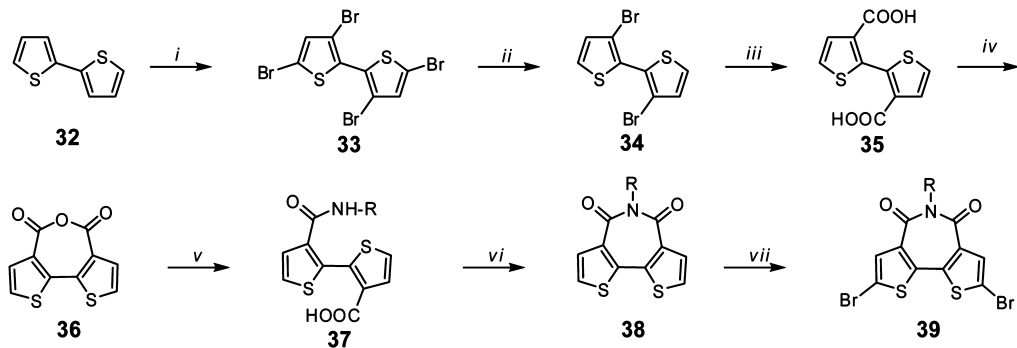
**P182** containing an alkylated terthiophene was synthesized by direct heteroarylation polycondensation.<sup>295</sup> The polymer had a

high  $M_n$  of 41 kDa and a low-lying HOMO of −5.66 eV. **P182** OSCs having the structure ITO/PEDOT:PSS/**P182**:PC<sub>70</sub>BM/TiO<sub>x</sub>/Al showed a  $J_{sc}$  of 10.51 mA/cm<sup>2</sup>, a  $V_{oc}$  of 0.92 V, a FF of 63%, and a PCE of 6.1% when fabricated using 3% 1-chloronaphthalene as the processing additive. **P182** exhibited superior performance to **P181**, although both had identical absorption in the film state. OTFT characterization showed that **P182** had a  $\mu_h$  of 0.013 cm<sup>2</sup>/(V s), which was 3 orders of magnitude higher than that of **P181**. The increased **P182**  $\mu_h$  was attributed to better side-chain interdigitation induced by the wide side-chain spacings.<sup>241,295</sup>

TPD–terthiophene copolymers with the optimized 2-hexyldecyl chain on TPD were designed and synthesized by Marks et al.<sup>62</sup> **P183** shows more structured and red-shifted absorption than **P182**, indicating stronger intermolecular interactions and a higher degree of ordering. Inverted OSCs having the structure ITO/ZnO/**P183**:PC<sub>71</sub>BM/MoO<sub>x</sub>/Ag show a promising PCE of 7.90% with a  $V_{oc}$  of 0.795 V, a  $J_{sc}$  of 12.5 mA/cm<sup>2</sup>, and an unprecedented FF of 79.6%. Therefore, using a polymer having enhanced intermolecular interactions and adopting an inverted structure, **P183** cells show greatly improved performance versus **P182** cells through  $J_{sc}$  and FF enhancement. The remarkable FFs are mainly attributed to the substantial charge carrier mobility, highly ordered and π-face-on oriented microstructures with close π–π interplane spacings, ordered bicontinuous networks, and vertical phase gradation.<sup>62</sup> Such film properties greatly suppress charge recombination and lead to efficient charge sweep out and therefore, an unprecedented FF. Achievement of a FF of ~80% heralds a bright future of organic solar cells.<sup>88</sup>

Replacing the central thiophene of the terthiophene unit in **P182** with selenophene affords selenophene-containing **P184**,<sup>296</sup> which shows greatly red-shifted absorption.<sup>295</sup> The **P184** HOMO measured from cyclic voltammetry is −5.49 eV, which is ∼0.1 eV higher than that of **P182**. **P184** BHJ OSCs with an optimized active layer thickness of ∼95 nm show a PCE of 5.80% with a  $J_{sc}$  of 10.74 mA/cm<sup>2</sup>, a  $V_{oc}$  of 0.88 eV, and a FF of 62%. As compared to **P182**, **P184** shows a slightly reduced  $V_{oc}$  which is in accordance with the HOMO ordering. It is interesting to note that the optimal **P184** performance is achieved without using a processing additive, and the cells fabricated without an additive exhibit enhanced device stability compared to cells fabricated with an additive.<sup>296</sup>

**P185** containing the rigid and coplanar 2,5-di(thiophen-2-yl)thieno[2,3-*b*]thiophene unit was designed for achieving high crystallinity. DSC data showed that **P185** has a significant transition, and XRD scan revealed that **P185** has sharp and strong diffractions up to the third order with a close π–π stacking distance of 3.7 Å. The optimal **P185**:PC<sub>71</sub>BM (1:1, w/w) cells exhibited a PCE of 5.1% with a  $J_{sc}$  of 8.99 mA cm<sup>−2</sup>, a  $V_{oc}$  of 0.85 V, and a FF of 67%.<sup>297</sup> The high FF was ascribed to the high **P185** hole mobility. Moreover, **P185** showed great potentials for

Scheme 9. Synthetic Route to Dibrominated Bithiophene Imide<sup>a</sup>

<sup>a</sup>Reagent and conditions: (i)  $\text{Br}_2$ ,  $\text{CHCl}_3$ ,  $\text{HOAc}$ , reflux; (ii)  $\text{Zn}$ ,  $\text{CH}_3\text{CH}_2\text{OH}$ ,  $\text{H}_2\text{O}$ ,  $\text{HOAc}$ ,  $\text{HCl}$ , reflux; (iii) (a)  $n\text{-BuLi}$ ,  $\text{Et}_2\text{O}$ ,  $-78^\circ\text{C}$ ; (b)  $\text{CO}_2$ ,  $-78^\circ\text{C}$ ; (c)  $\text{HCl}$ ; (iv)  $\text{Ac}_2\text{O}$ , reflux; (v)  $\text{RNH}_2$ ,  $\text{DCM}$ , reflux; (vi)  $\text{SOCl}_2$ , reflux; (vii)  $\text{Br}_2$ ,  $\text{FeCl}_3$ ,  $\text{DCM}$ .

hybrid cells using CdSe tetrapods as the acceptor semiconductor. Annealing the device having the structure ITO/PEDOT:PSS/P185:CdSe tetrapod (1:9; w/w)/Al at  $130^\circ\text{C}$  led to a tripled PCE of 2.9% with a  $J_{\text{sc}}$  of  $7.26 \text{ mA/cm}^2$ , a  $V_{\text{ooc}}$  of  $0.88 \text{ V}$ , and a  $FF$  of 46% compared to as-prepared cells with a  $J_{\text{sc}}$  of  $3.16 \text{ mA/cm}^2$ , a  $V_{\text{ooc}}$  of  $0.89 \text{ V}$ , and a  $FF$  of 36%. The performance enhancement was ascribed to the removal of the pyridine ligands from the CdSe surfaces, which induced denser morphologies and resulted in more efficient charge generation and collection.<sup>298</sup>

#### 6.4. Summary

During the last few of years numerous TPD-based polymers have been developed and have exhibited promising device performance. Due to the space limitation, we are unable to discuss the chemistry and device properties for all recent TPD polymers in details. However, we have shown that TPD has been copolymerized with oligothiophenes, and the resulting polymers exhibit  $\mu_{\text{h,s}} > 1.0 \text{ cm}^2/(\text{V s})$  with excellent OTFT stability. The TPD carbonyl group can promote a high degree of polymer backbone coplanarity through intramolecular (thienyl)S... (carbonyl)O interactions, and the resulting polymers show ordered film microstructures, which rationalizes the substantial charge carrier mobility. When copolymerized with commonly used electron donors such as benzodithiophene, dithienosilole-(germole), and terthiophene, the TPD-based polymers exhibit PCEs > 8% and an unprecedented fill factor approaching 80% in solution-processed BHJ solar cells. Thus, facile synthetic access to TPD, the low-lying HOMO enabling large  $V_{\text{ooc}}$  and stable hole transport in ambient, and the high charge carrier mobility render TPD as one of the most promising building blocks for synthesizing polymers for organic optoelectronic applications.

## 7. BITHIOPHENE IMIDE-BASED POLYMER SEMICONDUCTORS

Bithiophene imide (BTI) was designed and synthesized by Marks et al. in 2008 in order to mitigate the backbone torsion existing in TPD-based semiconductors.<sup>130</sup> On the basis of the computation from Pomerantz,<sup>44</sup> TPD dimers have  $>20^\circ$  torsional angle which should be detrimental to charge transport.<sup>130</sup> Moving the imide to the center of the bithiophene could greatly attenuate steric hindrance; therefore, backbone coplanarity would be increased.<sup>130</sup> Presynthesis computations were carried out to predict the optimized geometry, FMO levels, and orbital electron density contours of BTI and its derivatives.<sup>130</sup> The results revealed that the intrinsic properties of BTI were in good agreement with those required for efficient electron

transport. The design and synthesis of dibrominated BTI enabled development of a new family of polymer semiconductors with good device performance.

### 7.1. Synthesis of Dibrominated Bithiophene Imide

Bithiophene 32 is tetrabrominated (Scheme 9) using  $\text{Br}_2$  under reflux in the mixture of chloroform and acetic acid to give 3,5,3',5'-tetrabromo-2,2'-bithiophene 33, which can be selectively debrominated with  $\text{Zn}$  powder in acetic acid to afford 3,3'-dibromo-2,2'-bithiophene 34.<sup>130</sup> Lithiation of 34 followed by quenching the resultant dilithium salt with dry  $\text{CO}_2$  affords 3,3'-dicarboxylate-2,2'-bithiophene (structure not shown). The dicarboxylic acid 35 is obtained as an off-white solid via acidification of the dicarboxylate, which can be used without further purification. The dehydration of 35 in acetic anhydride under reflux provides high-purity anhydride 36 as yellow needle-like crystals. The synthetic route to the anhydride is highly efficient with an overall yield greater than 70% from the 2,2'-bithiophene.<sup>130</sup> The imide 38 is first synthesized under a one-step imide condensation using seven-membered anhydride 36 with primary alkyl amines in molten imidazole. The protocol requires high reaction temperatures ( $>200^\circ\text{C}$ ) and extended reaction period over 12 h, which leads to  $<5\%$  yields when sterically encumbered amines are used, accompanied by imide decomposition to the corresponding diamide. Imidization also shows limited success in refluxing propionic acid<sup>299</sup> and by removing water via azeotropic distillation. The challenge of imidization of the novel anhydride 36 is likely associated with its seven-membered structure. Effective imidization is implemented under microwave irradiation in toluene at  $220^\circ\text{C}$  with a catalytic amount of 4-(dimethylamino)pyridine to afford imide 38 in moderate yields of 30–70%, depending on the *N*-functionalization. Branched amines usually afford imides in lower yield ( $\sim 30\%$ ) than linear amines ( $\sim 70\%$ ).<sup>130</sup> A modified two-step procedure (Scheme 9) can greatly improve the imidization yield. Slow addition of an amine solution in dichloromethane to an anhydride 36 solution in dichloromethane under reflux over an extended period ( $\sim 2$  h) affords a carbamoyl intermediate 37, which can be purified by flash column chromatography to remove the unreacted starting materials. The subsequent thionyl chloride-assisted imidization successfully converts carbamoyl intermediate 37 to bithiophene imide 38 in high yield, typically with a two-step overall yield  $>80\%$ , even for very sterically encumbered amines. The subsequent dibromination of 38 using  $\text{Br}_2$  with a catalytic amount of ferric chloride affords the dibromo BTI 39 in near quantitative yield ( $>95\%$ ). Therefore, the modified synthetic route to dibromo BTI 32 is highly efficient,

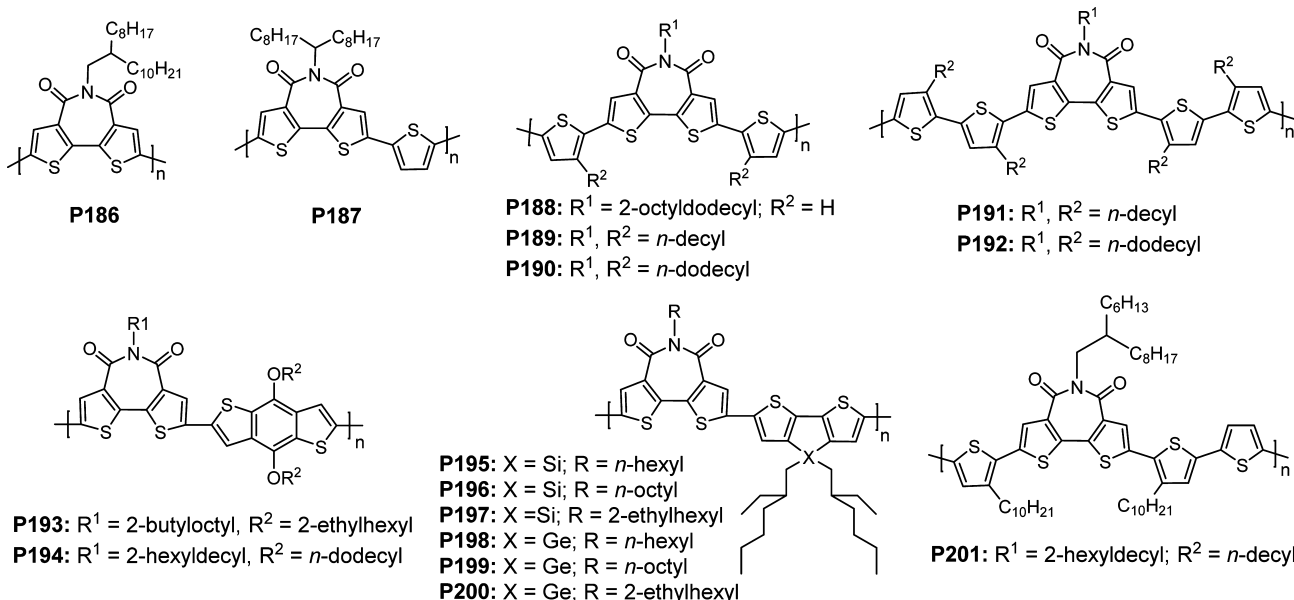


**Figure 39.** Chemical structures of bithiophene imide-based polymers for OTFTs and OSCs.

with a typical overall yield greater than 50%.<sup>50</sup> The crystal structure of imide 38 derivative *N*-hexyl-2,2':5',2":5",2"-quaterthiophene-4',3"-dicarboximide (structure not shown) reveals that the dithiophene imide moiety has a coplanar structure, close intermolecular  $\pi$ - $\pi$  stacking distance of 3.43 Å, and favorable solubilizing substituent orientations.<sup>130</sup> These properties indicate that bithiophene imide is a promising building block for polymer semiconductors.

## 7.2. Bithiophene Imide-Based Polymer Semiconductors for OTFTs and OSCs

The BTI homopolymer **P186** (Figure 39) having a branched 2-octyldodecyl substituent on the imide group was first synthesized by Ni-mediated Yamamoto polycondensation in DMF at 60 °C and had a small  $M_n$  of 3.6 kDa with a PDI of 2.2.<sup>130</sup> Polymer analogues with smaller branched chains or straight chains showed reduced solubilities, which limit materials processing and device applications. **P186** BGTC OTFTs with Au source/drain showed a promising  $\mu_e$  of 0.01 cm<sup>2</sup>/(V s) and a high  $I_{on}/I_{off}$  of 10<sup>7</sup> in vacuum but with a substantial  $V_t$  of >70 V, which was attributed to the substantial energy barrier between the **P186** LUMO and the work function of the Au electrode.<sup>130</sup> XRD diffraction of polymer film revealed that **P186** has a highly crystalline microstructure with the Bragg diffraction peaks progressing to the fifth order after annealing at 240 °C.<sup>130</sup> Polymerization at 80 °C in DMF and using chloroform as the Soxhlet extraction solvent after hexane afforded **P186** having an increased  $M_n$  of 7.2 kDa with a PDI of 1.98.<sup>50</sup> Polymerization at 80 °C using DMF and toluene as solvents led to insoluble **P186**. These results highlight the significance of optimizing polymerization conditions to balance  $M_n$  and materials processability. **P186** having a  $M_n$  of 7.2 kDa showed a  $\mu_e$  of 0.038 cm<sup>2</sup>/(V s) in BGTC OTFTs, which was 3 times higher than that of **P186** having a  $M_n$  of 3.6 kDa. XRD and AFM data showed that the high  $M_n$  **P186** yielded far more crystalline films and better-defined grains with reduced grain boundaries.<sup>50</sup> TGBC OTFTs with Au source/drain and polyolefin–polyacrylate dielectric<sup>197</sup> afforded an improved  $\mu_e$  of ~0.2 cm<sup>2</sup>/(V s) with an  $I_{on}/I_{off}$  of 10<sup>5</sup> using high  $M_n$  **P186** as the channel material. The ~0.2 cm<sup>2</sup>/(V s)  $\mu_e$  was among the highest for n-channel polymers at that time.<sup>17,123</sup>

However, the **P186** OTFTs cannot operate in ambient due to the high-lying LUMO of ~−3.50 eV.<sup>41</sup>

Although homopolymer **P186** does not yield air-stable n-channel OTFTs, BTI incorporation into donor–acceptor copolymers should lower their HOMOs for air-stable p-channel OTFTs.<sup>300</sup> BTI copolymer **P188** containing unsubstituted bithiophene had a limited  $M_n$  of 1.8 kDa with a PDI of 1.4, which corresponds to ~4 repeating units (~16 thiophene rings) in the backbone.<sup>130</sup> The low  $M_n$  was due to the low density of solubilizing chains and the fused BTI structure. Despite the low  $M_n$ , **P188** showed a crystalline film microstructure and morphology as revealed by DSC, XRD, and AFM. **P188** OTFTs exhibited p-channel transport with a  $\mu_h$  of ~0.01 cm<sup>2</sup>/(V s) and a remarkable  $I_{on}/I_{off}$  of 10<sup>7</sup>.<sup>130</sup> The promising  $\mu_h$  from low  $M_n$  **P188** encouraged development of BTI polymers having higher  $M_n$  and better solubility. By introducing oligothiophenes having varied thiophene numbers and strategically manipulated alkylation patterns a series of BTI and oligothiophene (nT) copolymers with improved solubility and higher  $M_n$  was synthesized. BTI and monothiophene copolymer **P187** had a  $M_n$  of 5.5 kDa with an acceptable solubility of >5 mg/mL when swallow-tail-like 1-octylnonyl was attached to the imide. **P189** and **P190** containing tail-to-tail dialkyl bithiophene achieved greatly enhanced solubility and >3 times higher  $M_n$ s than **P188**.<sup>301</sup> As the oligothiophene units were further extended to alkylated tetrathiophene, **P191** and **P192** became extremely soluble due to the high volume fraction of alkyl chains. The HOMOs derived from cyclic voltammetry were −5.55, −5.45, −5.44, −5.40, and −5.38 eV for **P187**, **P189**, **P190**, **P191**, and **P192**, respectively.<sup>50</sup> Therefore, as the numbers of thiophenes increased, the polymer HOMO moved upward. **P187** containing monothiophene showed ambipolarity with balanced  $\mu_h$  and  $\mu_e$  of ~5 × 10<sup>−4</sup> cm<sup>2</sup>/(V s). **P190** and **P192** having bithiophene and tetrathiophene donors showed  $\mu_h$  of 1.7 × 10<sup>−3</sup> and 1.6 × 10<sup>−2</sup> cm<sup>2</sup>/(V s) in BGTC OTFTs, respectively. In comparison to **P190** and **P192**, **P189** and **P191** with shorter alkyl chains showed reduced  $\mu_h$ s. Device optimization employing TGBC structures resulted in an improved  $\mu_h$  of ~0.1 cm<sup>2</sup>/(V s) for **P192**. Therefore, increasing the conjugation length of the oligothiophene led to lower n-channel performance but

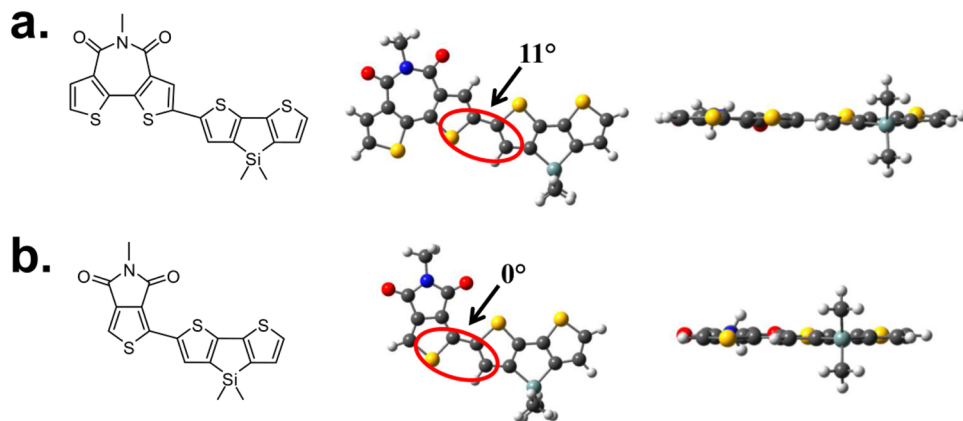


**Figure 40.** Chemical structures and optimized geometries for the polymer repeat units of (a) **P196** and (b) **P164**. Calculations are carried out at the DFT//B3LYP/6-31G\*\* level; dihedral angles between the planes of donor block and acceptor block are indicated by red circles. Alkyl substituents are replaced here by methyl groups to simplify the calculations. Reprinted with permission from ref 55. Copyright 2012 American Chemical Society.

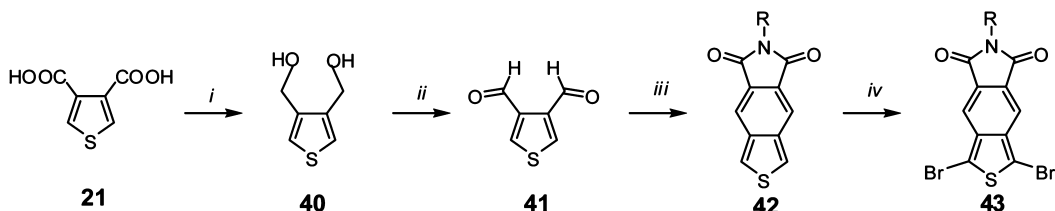
improved p-channel response, which was in good agreement with their FMO evolution. Microstructure investigation revealed that alkylated thiophenes can promote crystallinity. **P191** and **P192** having alkylated tetrathiophenes showed the greatest ordering and crystallinity. BTI incorporation improved p-channel performance durability of copolymers; **P189–P192** OTFTs showed minimal changes of  $\mu_h$ ,  $I_{on}/I_{off}$  ratio, and threshold voltage when the OTFTs were stored in ambient up to 9 months.<sup>50</sup> Because of their sizable and balanced mobilities and good materials solubilities, **P186** and **P192** were chosen for complementary inverters by monolithic integration of p- and n-channel OTFTs. The inkjet-printed inverters showed a high voltage gain of ~40 at  $V_{DD} = -100$  V with negligible bias hysteresis. Studies showed effective tuning of charge carrier polarity and mobility magnitude by altering donors, and the results demonstrated the great potential of BTI polymers for printable electronic devices.

The promising charge transport, low-lying HOMO, and good solubility of BTI polymers underscore their potential for OSCs. Thus, **P193** and **P194** (Figure 39) containing benzodithiophene were synthesized with  $M_n$ s of 21.8 and 34.0 kDa, respectively.<sup>108</sup> The band gaps derived from absorption onset are ~1.93 eV with HOMOs of −5.58 and −5.63 eV for **P193** and **P194**, respectively. Inverted BHJ solar cells having the structure ITO/ZnO/polymer:PC<sub>71</sub>BM/MoO<sub>x</sub>/Ag show PCEs of 4.39% and 5.50% for optimized **P193** and **P194** devices, respectively. The promising performance of these BTI polymers is mainly attributed to their large  $V_{oc}$ s with the largest one approaching 1.0 V, which is in good agreement with their low-lying HOMOs. **P194** having linear *n*-dodecyl groups on the benzodithiophene shows increased PCE versus **P193** having branched 2-ethylhexyl, in accordance with the  $\mu_h$ s measured in the OTFT and SCLC regimes. The higher **P194**  $\mu_h$  results in its greater  $J_{sc}$  and higher FF. The bottleneck for the BTI–benzodithiophene polymer OSCs appears to be the large band gaps (~1.93 eV) associated with unfavorable population of the quinoidal form, which limits exciton formation and  $J_{sc}$ s. The low polymer HOMO and inverted cell structure deliver improved device stability. The PCEs retain 50% of their original value after the cells are stored in ambient under continuous illuminations at 80 °C for 600 h.

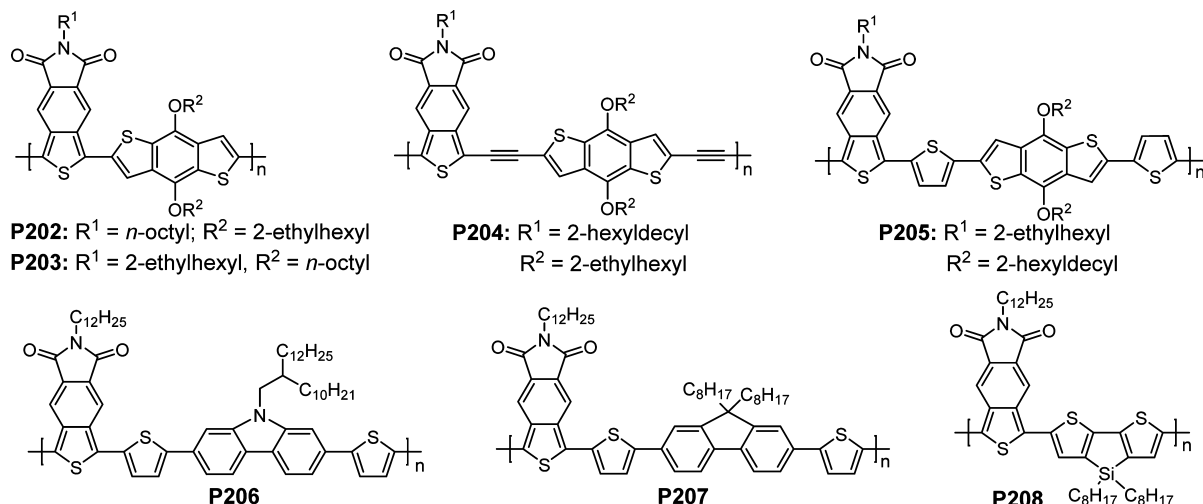
In comparison to the benzodithiophene-based **P193** and **P194**, **P195–P200** containing dithienosilole<sup>106,112</sup> or dithieno-germole<sup>105</sup> show reduced band gaps of ~1.75 eV, and the HOMOs measured from cyclic voltammetry are in the range

from −5.38 to −5.45 eV.<sup>55</sup> The bithiophene bridge progression  $R_2Si \rightarrow R_2Ge$  has minimal impact on the polymer band gaps, but it leads to destabilized HOMOs by ~0.05 eV for **P198–P200**.<sup>105</sup> Film microstructure characterization by GIWAXS indicates that the dithienosilole polymers **P195–P197** exhibit more ordered packing both in lamellar and  $\pi$ – $\pi$  stacking than the dithieno-germole polymer analogues **P198–P200**. **P195**, **P196**, **P198**, and **P199** with linear *n*-hexyl or *n*-octyl N-substituents afford more compact microstructures than **P197** and **P200** bearing branched 2-ethylhexyl, and therefore enhanced mobility. The  $\mu_h$ s measured in the OTFT regime are ~10<sup>−4</sup> cm<sup>2</sup>/(V s) for **P195–P200** with the mobilities of the dithienosilole polymers being slightly higher than those of the dithieno-germole polymers. The moderate  $\mu_h$  is due to the low degree of ordering revealed by DSC and XRD. Inverted OSCs having the structure ITO/ZnO/polymer:PC<sub>71</sub>BM/MoO<sub>x</sub>/Ag show promising performance with PCEs typically >4% and  $V_{oc}$ s ≥ 0.75 eV. Optimal performance is obtained from **P196** with a  $J_{sc}$  of 12.81 mA/cm<sup>2</sup>, a  $V_{oc}$  of 0.803 V, a FF of 62.3%, and a PCE of 6.41%. The dithienosilole polymers **P195–P197** show greater  $V_{oc}$ s and enhanced PCEs than dithieno-germole polymers **P198–P200**, in good agreement with their HOMO order, film microstructure, and charge carrier mobility. However, the  $M_n$  effect should not be ruled out. The dithieno-germole polymers have smaller  $M_n$ s than the dithienosilole polymers due to the difficulty of purifying distannylated dithieno-germole monomer.<sup>105,302</sup> **P164** (Figure 37) was synthesized as the control for better understanding the structure–property–device performance correlations of BTI polymers.<sup>55</sup> It was found that TPD polymer **P164** has a high degree of backbone coplanarity induced by the intramolecular (thienyl)S···(carbonyl)O interaction (Figure 40), which leads to a smaller band gap, better absorption in the red region, a higher degree of lamellar ordering, and enhanced charge transport than bithiophene imide polymer **P196**. However, the slight backbone torsion (~10° dihedral angle between BTI and dithienosilole or dithieno-germole, Figure 40) in BTI polymer affords useful solubilities. Under optimized conditions, **P196** cells exhibit ~1 mA/cm<sup>2</sup> larger  $J_{sc}$  than **P164** cells, which is attributed to the more ordered and closer  $\pi$ – $\pi$  stacking (3.5 Å) of **P196**. The improved **P164** PCE is mainly attributed to the larger  $V_{oc}$  due to its higher imide density in the TPD polymer than that in the BTI polymer.

**P195–P200** OSC performance is mainly limited by their moderate FFs (47–62%), which are associated with their low  $\mu_h$ s.

**Scheme 10.** Synthetic Route to the Dibrominated Thienoisooindoledione<sup>a</sup>

<sup>a</sup>Reagents and conditions: (i) (a) Oxalyl chloride, ClCH<sub>2</sub>CH<sub>2</sub>Cl; (b) LiAlH<sub>4</sub>, THF; (ii) pyridinium chlorochromate, DCM; (iii) maleimide, DBU, tri-*n*-butylphosphine, DCM; (iv) NBS, CHCl<sub>3</sub>, HOAc.

**Figure 41.** Chemical structures of thienoisooindoledione-based polymer semiconductors for OSCs.

OTFT studies have revealed that BTI–oligothiophene copolymers P188–P192 show  $\mu_{hs}$ s of 0.01–0.1 cm<sup>2</sup>/s. P201 containing terthiophene donor was synthesized, and UV–vis absorption spectra, DCS, and XRD indicated that P201 has a high degree of ordering.<sup>62</sup> In spite of its moderate band gap of 1.82 eV, P201 inverted cells having the structure ITO/ZnO/P201:PC<sub>71</sub>BM/MoO<sub>x</sub>/Ag exhibited a PCE of 8.66%. The superior performance was attributed to the large  $V_{oc}$  of 0.859 V and the exceptional FF of 77.8%. It is interesting to compare the performance between the BTI polymer P201 and the TPD polymer counterpart P183 (Figure 38). The absence of a planarizing (thienyl)S···(carbonyl)O interaction in P201 led to the greater backbone torsion, which resulted in its lower lying HOMO and larger  $V_{oc}$ .<sup>303</sup> However, the absence of a S···O interaction in P201 led to its lower degree of ordering and smaller hole mobility. GIWAXS investigation of polymer:PC<sub>71</sub>BM films showed that the TPD polymer P183 adopted complete  $\pi$ -face-on orientation on ZnO substrate, while P201 showed predominant  $\pi$ -face-on orientation with a face-on:edge-on ratio of 14, which accounted for the smaller FF of BTI polymer P201 cells than TPD polymer P183 cells.<sup>62</sup>

### 7.3. Summary

In conclusion, as a structural analogue to TPD, the BTI unit having the imide centered on the bithiophene eliminates the intramolecular (thienyl)S···(carbonyl)O interactions, which profoundly impacts polymer properties and device performance. The absence of S···O interactions imbues BTI polymers with slightly larger backbone torsion and a lower degree of order as compared to TPD polymers. Hence, BTI copolymers usually exhibit lower  $\mu_{hs}$ s than TPD polymer analogues. However,

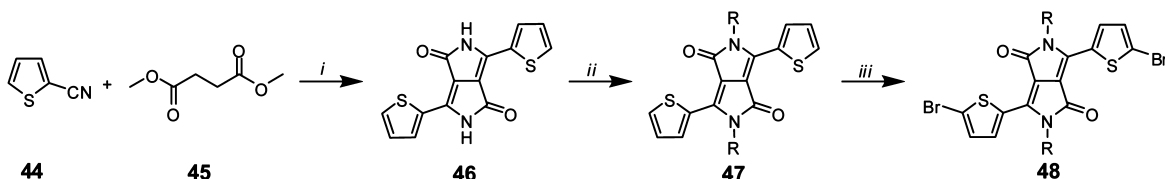
substantial  $\mu_{cs}$ s of >0.2 cm<sup>2</sup>/(V s) are obtained for the BTI homopolymer. The backbone torsion in the BTI polymers can favorably enhance polymer solubility and lower polymer HOMO, which leads to larger  $V_{oc}s$  in OSCs.<sup>303</sup> Promising PCEs of 8.7% are obtained from BTI polymers and are associated with large  $V_{oc}s$  and FFs. The results demonstrate the great potential of BTI for creating high-performance polymer semiconductors. Furthermore, investigation of BTI polymers enables establishment of materials structure–property–device performance correlations. The results from BTI and TPD polymers offer guides to design new materials for performance improvements.

## 8. THIEENOISOINDOLEDIONE-BASED POLYMER SEMICONDUCTORS

Thienoisooindoledione (TID), an acceptor having an isoindoledione fused to the C<sub>3</sub>–C<sub>4</sub> bond of the thiophene, has a greater tendency to form a quinoidal structure than TPD since the fused benzene moiety has a higher aromatic resonance energy than that of thiophene.<sup>110</sup> Therefore, in the aromaticity competition, the benzene would likely adopt an aromatic form, which induces the thiophene to be dearomatized and enhances quinoidal character.<sup>110</sup> The quinoidal structure of TID semiconductors will be stabilized by a gain in the aromatic resonance energy of isoindoledione unit, which should enhance certain electronic and device characteristics.

### 8.1. Synthesis of Dibrominated Thienoisooindoledione

The TID unit was designed by Wudl for developing low-bandgap polymers.<sup>304</sup> The eight-step synthetic route to dibrominated TID 43 is rather tedious,<sup>304</sup> and a simplified procedure was

**Scheme 11. Synthetic Route to Diketopyrrolopyrrole and Dibrominated Diketopyrrolopyrrole<sup>a</sup>**

<sup>a</sup>Reagents and conditions: (i) diisopropylsuccinate,  $t\text{-C}_5\text{H}_{11}\text{ONa}$ , *tert*-amyl alcohol, 120 °C; (ii) alkyl bromide,  $\text{K}_2\text{CO}_3$ , DMF, 130 °C; (iii)  $\text{Br}_2$ ,  $\text{CHCl}_3$ , room temperature.

developed by Olson et al. (Scheme 10).<sup>305</sup> The commercial thiophene-3,4-dicarboxylic acid **21** is reduced by  $\text{LiBH}_4$  to form a diol **40**, which is subjected to oxidation using pyridinium chlorochromate to provide thiophene-3,4-dicarbaldehyde **41**. The subsequent one-pot Wittig olefination and Knoevenagel condensation<sup>306</sup> between the dicarbaldehyde and *N*-alkylmaleimide proceed smoothly to provide TID **42** when catalyzed by tributylphosphine. The TID can be readily brominated with *N*-bromosuccinimide to offer dibrominated TID **43**, which enables synthesis of a family of TID-based polymers.

## 8.2. Thienoisoindoledione-Based Polymer Semiconductors for OSCs

**P202** (Figure 41) bearing benzodithiophene was specifically designed for OSCs.<sup>305</sup> The donor–acceptor backbone motif and stabilized quinoidal structure by a gain in the aromatic resonance energy of TID enable effective tuning of the polymer band gap and HOMO. The polymer was synthesized via Stille coupling and had a  $M_n$  of 40.3 kDa with a PDI of 2.5. The **P202** band gap was 1.43 eV, which was substantially smaller than that (1.83 eV) of TPD polymer **P149** (Figure 34). The smaller **P202** band gap reflected its enhanced quinoidal structure stabilization. The HOMO derived from cyclic voltammetry was −5.37 eV, comparable to that (−5.39 eV) of **P149**. **P202:PC<sub>61</sub>BM** BHJ solar cells showed an optimized PCE of 2.1% with a  $J_{sc}$  of 5.0 mA/cm<sup>2</sup>, a good  $V_{oc}$  of 0.792 V, and an FF of 52%.<sup>305</sup> The PCE was less than one-half of that of the **P149** control cells having a PCE of 4.8% with a  $J_{sc}$  of 8.0 mA/cm<sup>2</sup>, a  $V_{oc}$  of 0.888 V, and a FF of 67%. The much smaller  $J_{sc}$  and FF of the **P202** cells were mainly attributed to its large backbone torsion induced by the steric hindrance created by the hydrogen atom on the isoindole unit of TID and the neighboring BDT unit,<sup>305</sup> while in **P149** the intramolecular S···O interactions promoted backbone coplanarity. The twisted **P202** backbone was in good accordance with its featureless absorption and amorphous film microstructure. Moreover, the sufficiently deep **P202** LUMO relative to that of PCBM could lead to insufficient exciton dissociation and hence limit the  $J_{sc}$  and FF.<sup>111</sup> Frechét and co-workers reported the same polymer and achieved a comparable PCE of 2.88% with a  $J_{sc}$  of 7.70 mA/cm<sup>2</sup>, a  $V_{oc}$  of 0.71 V, and a FF of 53%.<sup>307</sup> Structural modification by tuning the side chains on the TID and BDT units led to slightly improved **P203** OSC performance with a  $J_{sc}$  of 7.05 mA/cm<sup>2</sup>, a  $V_{oc}$  of 0.78 V, a FF of 55%, and a PCE of 3.01%.<sup>307</sup>

To attenuate the steric hindrance between TID and neighboring arenes, an ethynylene linkage was introduced into polymer,<sup>205</sup> and the resulting **P204** showed a higher degree of backbone coplanarity and a lower lying HOMO when compared to the polymer without an ethynylene linkage.<sup>308</sup> Despite the promising characteristics of **P204**, no photovoltaic performance was reported. Thiophene bridges were introduced into TID and a benzodithiophene copolymer **P205** for achieving more extended conjugation, and the TPD polymer counterpart was

synthesized as a reference material.<sup>309</sup> Optical and electrochemical measurements showed that **P205** had a band gap of 1.53 eV and a LUMO/HOMO of −3.78/−5.40 eV, while the TPD polymer counterpart had a larger band gap of 1.80 eV and LUMO/HOMO of −3.70/−5.52 eV. Therefore, replacement of TPD with TID lowered the **P205** LUMO, elevated its HOMO, and consequently reduced its band gap. OSCs having the structure ITO/PEDOT:PSS/**P205:PC<sub>61</sub>BM/Ca/Al** showed a PCE of 3.12% under AM 1.5G conditions, which was greatly improved in comparison to the PCE of 0.92% from the TPD polymer counterpart. Carbazole and fluorene were incorporated into **P206** and **P207**, respectively. BHJ OSCs showed low PCEs of 0.5% and 1.6% for **P206** and **P207**, respectively. The low PCEs were partially due to their large band gaps. **P208** bearing a TID acceptor and a dithienosilole donor had a small band gap of 1.33 eV with a LUMO/HOMO of −3.91/−5.26 eV. However, the **P208:PC<sub>61</sub>BM** cells showed a poor PCE of 0.33%, which was likely limited by the polymer backbone torsion and too deep LUMO.<sup>310</sup>

## 8.3. Summary

The strong electron-withdrawing capability and favorable quinoidal structure of TID enable the resulting polymers with narrow band gaps and low-lying HOMO/LUMOs. However, to date, TID-based polymers typically show lower PCEs than their TPD polymer counterparts. The low-lying polymer LUMOs prevent efficient exciton dissociation when blended with PCBM, which limits the solar cell performance. The hydrogen atom on the isoindole moiety of TID imposes significant steric hindrance on the neighboring arenes, which is detrimental for film crystallinity and charge transport. Therefore, the TID-based polymers reported to date only show moderate PCEs in OSCs and very limited OTFT performance.

## 9. DIKETOPYRROLOPYRROLE-BASED POLYMER SEMICONDUCTORS

As described previously, imide-functionalized arenes are promising for creating high-performance polymer semiconductors. As structural analogues, amide (or lactam)-functionalized arenes could inherit the advantages of imide-functionalized arenes partially if not completely. Among various amide-functionalized arenes, 2,5-dihydro-pyrrolo[3,4-*c*]pyrrole-1,4-dione (DPP) has gained a great amount of attention recently. DPP was originally designed as a high-quality pigment for paints, plastics, and inks.<sup>311–313</sup> The first DPP polymer was reported for photorefractive application by Yu and co-workers in 1993.<sup>314</sup> However, DPP had been largely overlooked by the community until Janssen et al. reported the first DPP-based polymers for solar cells in 2008.<sup>315</sup> The unique properties of DPP render it a promising building block for polymer semiconductors with excellent performance in OTFTs and OSCs. There are several recent reviews covering DPP polymers for organic elec-

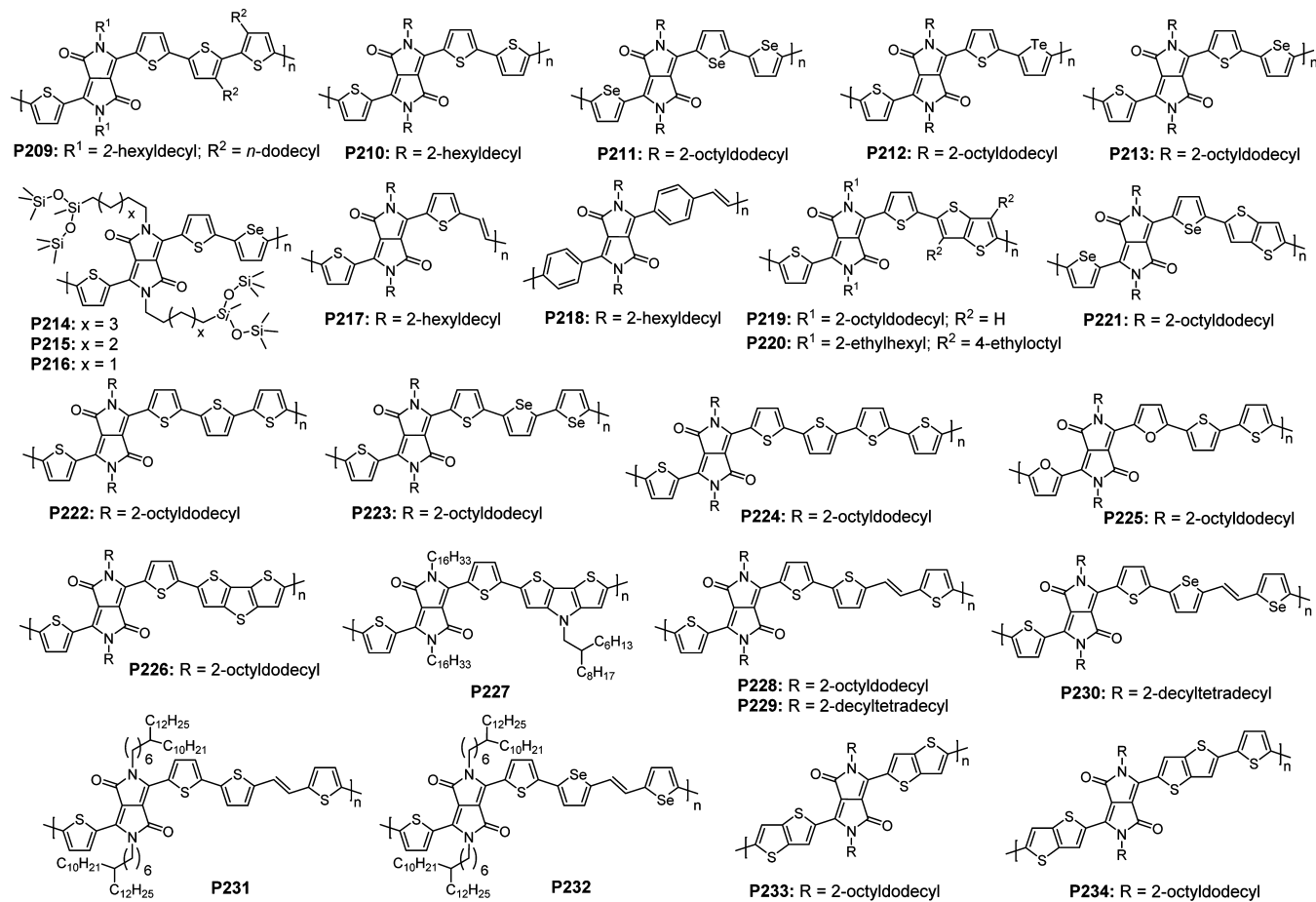


**Figure 42.** Diketopyrrolopyrrole-based polymers for OTFTs.

tronics.<sup>48,316,317</sup> Due to space limitations, this section mainly focuses on recent advances in DPP polymers with substantial OTFT and OSC performance. However, a few DPP polymers with lower performance are also included for better understanding the structure–property correlations.

### 9.1. Synthesis of Dibrominated Diketopyrrolopyrrole

The synthesis of dibrominated thiophene-flanked DPP is straightforward and involves a three-step procedure (Scheme 11). Thionyl carbonitrile **44** reacts with succinic acid ester **45** under the condition established by Rochat et al. to afford a thiophene-flanked diketopyrrolopyrrole **46**.<sup>318</sup> Alkylation can be readily accomplished by reacting **46** with an alkyl bromide under basic conditions to afford DPP **47** with the desired solubilities. The subsequent bromination using  $\text{Br}_2$  in chloroform provides the dibrominated DPP monomers **48**. On the basis of this procedure, various five- and six-membered arenes flanked DPP monomers are synthesized from aryl or heteroaryl carbonitriles. These arenes include furan, selenophene, thiazole, thieno[3,2-*b*]thiophene, benzene, and pyridine.<sup>313,316</sup> The synthesis of DPPs flanked with various arenes enables development of DPP polymers with widely tunable optoelectronic properties and self-assemblies. Recently, the commercial availability of the dibrominated DPP greatly promoted applications of DPP polymers in organic electronics.

### 9.2. Diketopyrrolopyrrole-Based Polymer Semiconductors for OTFTs

The first DPP polymer for OTFTs was reported by Winnewisser.<sup>319</sup> DPP and tetrathiophene copolymer **P209**

(Figure 42) was synthesized via Yamamoto coupling. Although **P209** contains a head–head bithiophene linkage, it shows a narrow band gap of 1.5 eV with a LUMO/HOMO of  $-4.0\text{--}5.5$  eV. The narrow band gap and low-lying LUMO/HOMO are attributed to the strong DPP electron-withdrawing capability. **P209** BGTC OTFTs show ambipolarity with a  $\mu_h/\mu_e$  of 0.1/0.09  $\text{cm}^2/(\text{V s})$  in  $\text{N}_2$ . The mobilities are the highest for ambipolar polymers. The ambipolarity can be obtained in various device structures (bottom-gate, top-gate, bottom-contact, and top-contact) using different dielectrics ( $\text{SiO}_2$ , PVP, and PMMA) and electrodes (Au and Ba), which is attributed to its appropriate FMOs.<sup>196</sup> **P209** transistors exhibit near-infrared light emission when integrated into light-emitting field-effect transistors.<sup>319</sup> Note that head–head linkage-containing polymers usually show low mobility ( $<10^{-2}\text{ cm}^2/(\text{V s})$ ).<sup>39,40</sup> The substantial **P209** mobilities demonstrate the great potential of DPP for creating high-mobility polymers.

DPP–monothiophene copolymer **P210** was synthesized from the dibromo DPP and 2,5-thiophenebis(boronic ester) via Suzuki coupling and has a band gap of 1.30 eV,<sup>320</sup> which is much smaller than that of **P209** due to the elimination of the head–head linkage. **P210** OTFTs show pronounced ambipolar transport with a balanced  $\mu_h/\mu_e$  of 0.04/0.01  $\text{cm}^2/(\text{V s})$  in vacuum. It is interesting to note that **P210** mobilities are almost independent of  $M_n$ s. The high and balanced  $\mu_h$  and  $\mu_e$  of **P210** deliver a voltage gain of 30 when it is incorporated into complementary inverters.<sup>320</sup> Replacing all thiophenes in **P210** with selenophenes leads to **P211**, which has a band gap of 1.18 eV.<sup>321</sup> The smaller **P211** band gap is attributed to the stabilizing

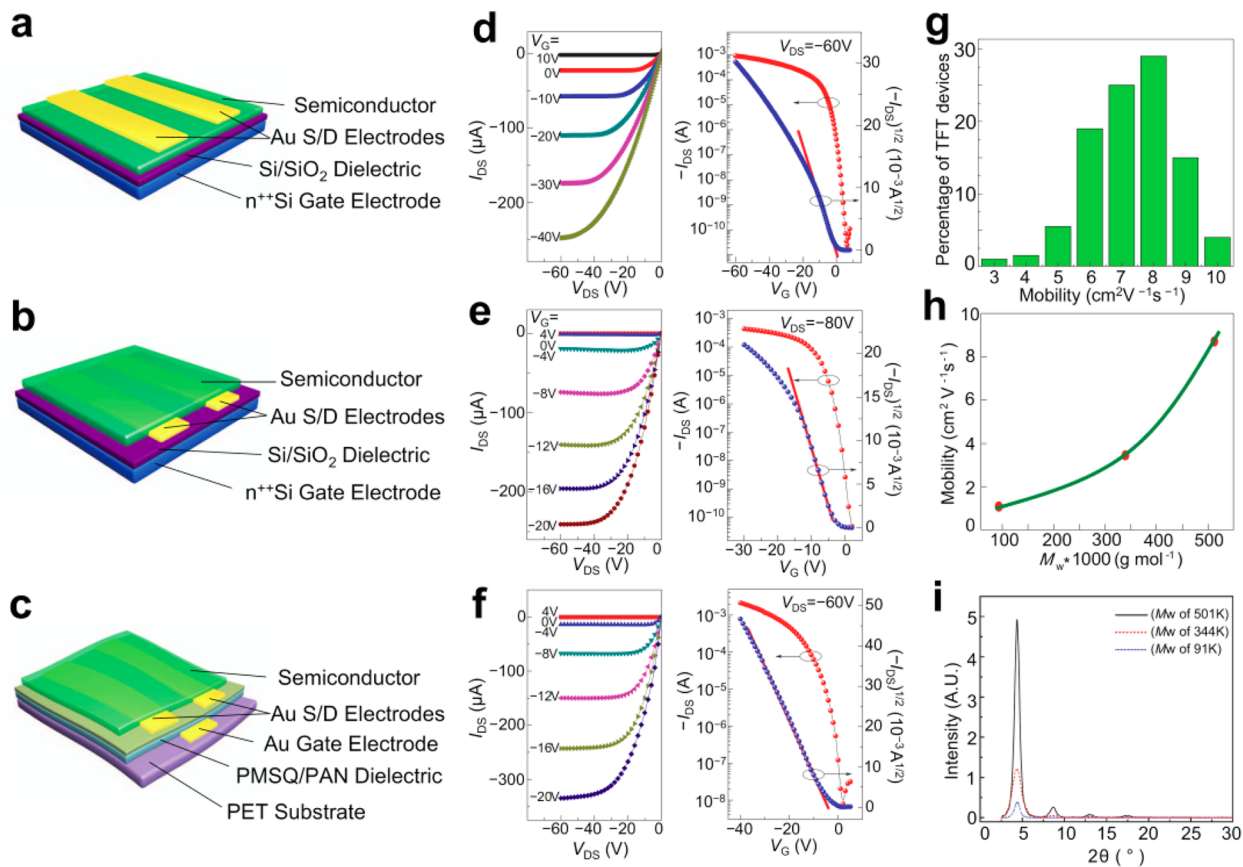


**Figure 43.** Illustration of P219 OTFTs and their characteristics in ambient conditions: (a and b) schematic BGTC and BGBC devices on a Si wafer, respectively, and (c) schematic BGBC device on flexible PET substrate. (d, e, and f) Respective output and transfer characteristics of devices a, b and c. The mobility distribution for over 200 devices of a and b is summarized in g. The dependence of the average saturated mobility of five representative devices on the semiconductor weight-average molecular weight ( $M_w$ ) is depicted in h. Increased crystallinity of a thin film (~100 nm) of semiconductor P219 as a function of increasing  $M_w$  is evident in the intensity of XRD diffractions as shown in i. Reprinted with permission from ref 328. Copyright 2012, Rights Managed by Nature Publishing Group.

effect of selenophene on the polymer LUMO. **P211** BGTC OTFTs demonstrate balanced  $\mu_h$  and  $\mu_e$  of  $0.1 \text{ cm}^2/(\text{V s})$ . In comparison to the thiophene-based **P210**, the improved **P211** mobilities are attributed to the more facile electron injection due to its lower lying LUMO. These results suggest that incorporation of the larger and more polarizable Se into the polymer backbone promotes electron transport.<sup>321</sup> **P212** containing a thiophene-flanked DPP acceptor and a tellurophene donor shows a smaller band gap (1.25 eV) than **P210**.<sup>322</sup> The smaller **P212** band gap is due to the more electron-rich character of the Te atom as compared to the S atom, which elevates the **P212** HOMO to  $-5.13 \text{ eV}$  in comparison to the  $-5.38 \text{ eV}$  HOMO of thiophene-based polymer **P210**. The smaller energy barrier between **P212** HOMO and Au electrode work function results in more facile hole injection, which leads to an enhanced **P212**  $\mu_h$  of  $1.47 \text{ cm}^2/(\text{V s})$  in comparison to **P210**  $\mu_h$  of  $0.62 \text{ cm}^2/(\text{V s})$  in the optimized OTFTs.

Siloxane-terminated side chains can greatly improve polymer mobilities due to the closer  $\pi-\pi$  stacking and larger crystallite coherence lengths.<sup>323</sup> Inspired by this discovery of Bao, Yang et al. reported a novel polymer **P214** containing dithienyl-DPP and selenophene with hybrid siloxane-solubilizing groups on the DPP nitrogen, and **P213** with alkyl chains was synthesized as the reference polymer.<sup>324</sup> Stille coupling provided a readily soluble **P214** with a  $M_n$  of 20 kDa and a PDI of 4.93 measured by GPC at 150 °C. Replacement of an alkyl chain with a siloxane chain has a

minimal impact on the polymer band gap; however, such structural modification elevates both the **P214** HOMO and LUMO by  $\sim 0.15 \text{ eV}$ . X-ray diffraction patterns reveal that **P214** has an ordered microstructure with a closer  $\pi-\pi$  stacking distance of 3.6 Å than the ~3.8 Å  $\pi-\pi$  stacking of **P213**. AFM characterization reveals that **P214** has larger and more structured granular domains with better domain connectivity than **P213**. BGTC OTFTs are fabricated using the solution-shearing method to investigate the charge transport of **P213** and **P214**. The alkyl polymer **P213** shows ambipolarity with a  $\mu_h/\mu_e$  of  $2.53/0.43 \text{ cm}^2/(\text{V s})$  under N<sub>2</sub>, and the siloxane polymer **P214** exhibits an extraordinarily high  $\mu_h/\mu_e$  of  $3.97/2.20 \text{ cm}^2/(\text{V s})$ . The superior **P214** charge transport can be attributed to its stronger interchain interactions and formation of larger and better connected domains through incorporation of siloxane-solubilizing groups. The same group systematically investigated the effect of the alkyl spacer chain length on charge transport in **P214–P216** containing siloxane-terminated side chains. It was found that the ambipolar transport can be further enhanced by optimizing the branching position of the hybrid side chains.<sup>328</sup> Using the solution-shearing OTFT fabrication method, an unprecedented ambipolar performance with a  $\mu_h/\mu_e$  of  $8.84/4.34 \text{ cm}^2/(\text{V s})$  is obtained from **P215**. **P216** OTFTs show a  $\mu_h/\mu_e$  of  $6.16/3.07 \text{ cm}^2/(\text{V s})$ , respectively. **P215** and **P216** having shorter chains exhibit improved charge transport characteristics than **P214** due to the denser molecular packing in **P215** and **P216**.

**P216.** The slightly lower mobility of **P216** is likely due to its reduced solubility and formation of smaller fibrils as compared to those of **P215**.<sup>138</sup>

Jenekhe et al. introduced vinylene into thiophene-flanked DPP to afford **P217**.<sup>325</sup> Replacement of thiophene with vinylene resulted in **P217** with a band gap of 1.22 eV, which is smaller than that of **P210**. The XRD pattern revealed that **P217** film has an ordered lamellar structure with a  $\pi-\pi$  stacking distance of 3.92 Å. **P217** showed promising ambipolarity with a  $\mu_h/\mu_e$  of 0.2/0.03 cm<sup>2</sup>/(V s), respectively, in BCBG OTFTs having Au source/drain with a 2 nm chromium adhesive layer. Integration of the ambipolar OTFTs into complementary-like inverters led to a good voltage gain of 15–27 with sharp switching character in the logic circuits. A phenyl-flanked DPP-based polymer analogue **P218** was synthesized and showed a band gap of 2.00 eV, which is ~0.80 eV larger than that of thiophene-flanked DPP polymer **P217** due to its low degree backbone coplanarity induced by the significant steric hindrance between the flanking phenyl and DPP.<sup>325</sup> Such backbone torsion led to the amorphous **P218** film microstructure and hence a negligible  $\mu_h$  of  $4.9 \times 10^{-7}$  cm<sup>2</sup>/(V s). The results demonstrate that thiophene-flanked DPP is a superior acceptor to phenyl-flanked DPP for promoting charge transport.

**P219** containing a thieno[3,2-*b*]thiophene donor was synthesized<sup>326,327</sup> and has a narrow band gap of 1.23 eV with a low-lying LUMO of –4.02 eV.<sup>326</sup> Film microstructure characterization showed that the polymer chain predominantly adopts an edge-on lamellar packing motif with a  $\pi-\pi$  stacking distance of 3.71 Å. **P219** charge transport properties were characterized by fabricating BGTC OTFTs on OTS-modified SiO<sub>2</sub>/Si substrates. The  $\mu_{hs}$ s extracted from the saturation regime of the transfer curves are in the range of 0.40–0.72 cm<sup>2</sup>/(V s) for the OTFTs without annealing. OTFTs annealed at 200 °C lead to greatly enhanced  $\mu_{hs}$ s of 0.88–0.94 cm<sup>2</sup>/(V s) with  $I_{on}/I_{off}$ s of 10<sup>6</sup>. The high mobility is attributed to the close  $\pi-\pi$  stacking and large-area intermolecular overlapping induced by the fused DPP and thienothiophene moieties, which result in an efficient channel for charge hopping. Weak electron transport characteristics with a very low on current of 60 nA is also observed in the n-channel operation mode, which indicates that **P219** is predominantly a hole-transporting material. Ong and co-workers systematically optimized the reaction conditions to achieve high  $M_n$  **P219** by varying the polymerization solvents, catalyst systems, and reaction temperatures. It was found that polymerizations in chlorobenzene and using a tri(dibenzylideneacetone)-dipalladium/tri(*o*-tolyl)phosphine catalyst at 130 °C provided **P219** with a high  $M_n$  of 110 kDa measured by high-temperature GPC at 160 °C using 1,2,4-trichlorobenzene eluent.<sup>328</sup> **P219** shows a very close  $\pi-\pi$  stacking distance of ~3.40 Å as revealed by grazing incidence X-ray diffraction and high-resolution transmission electron microscopy (TEM). Out-of-plane X-ray diffraction indicates that the high  $M_n$  **P219** has a higher degree of crystallinity compared to the low  $M_n$  batch. **P219** BGBC OTFTs show extraordinary  $\mu_{hs}$ s of 5.4–10.5 cm<sup>2</sup>/(V s) and remarkable  $I_{on}/I_{off}$ s of 10<sup>6–8</sup> for the spin-coated devices. Under various fabrication conditions and device structures,  $\mu_{hs}$ s of 1.5–10 cm<sup>2</sup>/(V s) can be routinely obtained (Figure 43). Among them, inkjet-printed BGTC OTFTs show  $\mu_{hs}$ s of 1.5–3.5 cm<sup>2</sup>/(V s) with an  $I_{on}/I_{off}$  of 10<sup>5–6</sup>. It was found that the high  $M_n$  is central to achieving extremely high  $\mu_{hs}$  (Figure 43h). Moreover, **P219** OTFTs show negligible  $\mu_h$  and  $I_{on}/I_{off}$  changes when stored in ambient without encapsulation for 56 weeks, which is attributed to its low-lying HOMO of –5.2 eV and compact film

morphology. These results represent a significant achievement for propelling the technological transition of printed electronics from the laboratory to the marketplace.

Careful device optimization led to ambipolar transport with balanced  $\mu_h$  and  $\mu_e$ , both exceeding 1 cm<sup>2</sup>/(V s), for **P219** OTFTs.<sup>327</sup> It was found that Au source/drain electrode treatment greatly affected its work function and hence the charge injection and measured mobility. **P219** OTFTs using oxygen plasma-cleaned Au electrodes showed a  $\mu_h/\mu_e$  of 0.93/0.29 cm<sup>2</sup>/(V s) with good  $I_{on}/I_{off}$ s of 10<sup>5–6</sup>,<sup>327</sup> while OTFTs using solvent-cleaned Au electrodes exhibited a  $\mu_h/\mu_e$  of 1.36/1.56 cm<sup>2</sup>/(V s) with  $I_{on}/I_{off}$ s of 10<sup>5–6</sup>. UV photoelectron spectroscopy measurements revealed that the solvent-cleaned Au had a work function of 4.7–4.9 eV, while the oxygen-plasma-cleaned Au had a work function of 5.0–5.5 eV. Therefore, the electron injection barrier in OTFTs employing solvent-cleaned Au electrodes was reduced as compared to that in OTFTs employing oxygen-plasma-cleaned Au electrodes, which delivered a greatly enhanced  $\mu_e$  of 1.56 cm<sup>2</sup>/(V s) in OTFTs employing solvent-cleaned electrodes.<sup>327</sup>

Janssen and co-workers reported copolymer **P220** containing alkylated thienothiophenes.<sup>329</sup> Alkylation of thienothiophenes leads to blue-shifted absorption and a larger band gap in comparison to those of **P219**, which indicates decreased conjugation of **P220**. OTFTs using **P220** as the channel semiconductor show ambipolarity with a  $\mu_h/\mu_e$  of  $1 \times 10^{-2}/2 \times 10^{-3}$  cm<sup>2</sup>/(V s)<sup>329</sup> which is several times lower than those (0.03/0.009 cm<sup>2</sup>/(V s),  $\mu_h/\mu_e$ ) of the polymer counterpart without alkyl chains on the thienothiophene. Therefore, alkyl installation on the thienothiophene is detrimental to charge transport.<sup>329</sup> Selenophene substitution for thiophene has been demonstrated as an effective strategy for enhancing OTFT performance.<sup>321</sup> Following this strategy, **P221** containing a selenophene-flanked DPP was synthesized and had a small band gap of 1.21 eV.<sup>321</sup> **P221** BGTC OTFTs showed a peak  $\mu_h/\mu_e$  of 1.1/0.15 cm<sup>2</sup>/(V s). Although the exact comparison was complicated by the materials quality, fabrication conditions, and device structure, it was apparent that incorporating selenophene into DPP polymers led to an enhanced  $\mu_e$  as compared to the thiophene polymer analogue.<sup>321,328</sup>

**P222** bearing a bithiophene donor was synthesized by Stille coupling with a high  $M_n$  of 106 kDa and exhibited good solubilities.<sup>330</sup> A band gap of 1.2 eV was measured from the optical absorption onset of the polymer film. The XRD pattern revealed that the film crystallinity increased gradually as the annealing temperature was increased from room temperature to 200 °C. The  $\pi-\pi$  stacking distance of 3.75 Å, derived from two-dimensional transmission XRD measurements, was slightly larger than that (3.71 Å) of thienothiophene polymer **P219**.<sup>326</sup> BGTC OTFTs incorporating unannealed **P222** as the channel material showed a  $\mu_h$  of 0.89 cm<sup>2</sup>/(V s) with a high  $I_{on}/I_{off}$  of 10<sup>7</sup> and a  $V_t$  of –2.6 V. The OTFTs annealed at 100 °C exhibited a higher  $\mu_h$  of 0.97 cm<sup>2</sup>/(V s).<sup>330</sup> No further improvement was observed as the temperature was increased beyond 100 °C (up to 200 °C), although higher crystallinity was observed. AFM characterization revealed that the unannealed **P222** film showed reduced structural defects, which compensated for lower crystallinity. The combined effects resulted in comparable mobilities for the OTFTs fabricated before and after annealing. It is potentially useful to achieve such high mobility without annealing, which should be compatible for high-throughput manufacturing of cost-effective OTFT arrays and circuits.<sup>330</sup> **P223** bearing biselenophene was synthesized and had a  $M_n$  of 19

kDa, and **P222** with a  $M_n$  of 59 kDa was synthesized as control.<sup>331</sup> Polymer absorption spectra revealed that **P223** has a 35 nm bathochromic shift relative to **P222**, and the band gaps are 1.39 and 1.32 eV for **P222** and **P223**, respectively. The smaller **P223** band gap was mainly due to the more electron-rich nature of Se and stronger intermolecular interactions. The XRD patterns indicated that the selenophene-containing **P223** is more crystalline than the thiophene-containing **P222**. **P223** BGTC OTFTs showed typical p-channel performance with a  $\mu_h$  of  $1.5 \text{ cm}^2/(\text{V s})$ , which was higher than that of optimized **P222** OTFTs, even if **P223** had a much smaller  $M_n$ . The enhanced **P223** mobility was attributed to its slightly denser chain packing and higher crystallinity. This study demonstrates that replacing thiophene with selenophene could be an effective strategy for mobility enhancement.

Incorporating extended  $\beta$ -unsubstituted quinqueithiophene into DPP polymers resulted in polymer **P224**.<sup>332</sup> DeLongchamp and co-workers found that as the side-chain density decreases, the DPP polymers show preferential edge-on orientation.<sup>36</sup> Therefore, incorporation of unsubstituted quinqueithiophene will promote the **P224** edge-on orientation. **P224** was prepared via Stille coupling and had a high  $M_n$  of 44 kDa.<sup>332</sup> The unsubstituted quinqueithiophene lowers polymer solubility, and **P224** was only soluble in chlorinated solvents at elevated temperatures. Incorporation of quinqueithiophene increased the distance of the bulky side chains along the polymer backbone and diminishes the steric hindrance, and hence, **P224** shows an ordered lamellar structure with a closer  $\pi-\pi$  stacking distance of 3.65 Å than that (3.76 Å) of **P222**. **P224** BGTC OTFTs showed a  $\mu_h$  of  $1.08 \text{ cm}^2/(\text{V s})$  with an  $I_{\text{on}}/I_{\text{off}}$  of  $10^5$  without annealing. After annealing at  $200^\circ\text{C}$  in air, the OTFTs achieved a  $\mu_h$  of  $3.46 \text{ cm}^2/(\text{V s})$  with an exceptional  $I_{\text{on}}/I_{\text{off}}$  of  $10^8$ .

The furan-flanked DPP was coupled with bithiophene to afford **P225**, which has a band gap of 1.41 eV.<sup>333</sup> The band gap was larger than that (1.24 eV) of the thiophene-flanked DPP polymer **P222**. Therefore, introduction of furan into DPP polymer broadened its band gap, accompanied by a lower **P225** HOMO of  $-5.32 \text{ eV}$  than that ( $-5.20 \text{ eV}$ ) of **P222**. Film characterization by XRD revealed that **P225** is less crystalline than **P222**. Despite the big hole injection barrier, less ordered film microstructure, and without preferential edge-on orientation, **P225** showed a high  $\mu_h$  up to  $1.54 \text{ cm}^2/(\text{V s})$  with an  $I_{\text{on}}/I_{\text{off}}$  of  $10^6$  in BGTC OTFTs under  $\text{N}_2$ . The promising **P225** charge transport was partially attributed to the strong intermolecular interactions and well-interconnected film morphology, which facilitated charge hopping between the distinct domains.

**P226** comprised of a thiophene-flanked DPP and dithieno[3,2-*b*:2',3'-*d*]thiophene was synthesized and had a small band gap of 1.22 eV with a LUMO/HOMO of  $-3.80/-5.19 \text{ eV}$ .<sup>334</sup> The **P226** film showed a crystalline microstructure and readily formed a layered structure with edge-on stacking on the substrate owing to the extended and planar structure of both DPP and dithieno[3,2-*b*:2',3'-*d*]thiophene and their strong intermolecular interaction. BGTC OTFTs showed  $\mu_h$ s of 0.60 and  $0.75 \text{ cm}^2/(\text{V s})$  for the as-spun and annealed films at  $250^\circ\text{C}$ , respectively. The **P226**  $\mu_h$  was highest for dithieno[3,2-*b*:2',3'-*d*]thiophene-based polymers,<sup>335</sup> manifesting the great potential of the DPP building block to facilitate charge transport.

Dithieno[3,2-*b*:2',3'-*d*]pyrrole<sup>336</sup> was polymerized with thiophene-flanked DPP to afford **P227**, which had a narrow band gap of 1.15 eV with a HOMO of  $-5.20 \text{ eV}$ .<sup>337</sup> **P227** BGBC OTFTs showed an average  $\mu_h$  of  $0.29 \pm 0.05 \text{ cm}^2/(\text{V s})$  with an  $I_{\text{on}}/I_{\text{off}}$  of  $10^{3-4}$  under an argon stream. The moderate  $I_{\text{on}}/I_{\text{off}}$  was due to

the highly electron-rich characteristics of dithienopyrrole. Grazing incidence wide-angle X-ray scattering patterns showed that the **P227** film has pronounced Bragg peaks up to fifth order with a  $\pi-\pi$  stacking distance of 3.70 Å, which indicates the presence of highly ordered lamellar sheets. AFM images showed that **P227** films did not have nanofibrillar morphology. The nonfibrillar morphology with smaller grain boundaries should benefit in achieving highly reproducible device performance.

**P228** and **P229** containing 2-(2-(thiophen-2-yl)vinyl)-thiophene were designed to extend the conjugation and promote intermolecular stacking. Upon Stille coupling, **P228** and **P229** were obtained with  $M_n$ s of 70 and 74 kDa, respectively, and a narrow PDI of  $\sim 2.5$ .<sup>338</sup> BGBC OTFTs with Au source/drain were fabricated to investigate charge transport. After polymer deposition, poly(methyl methacrylate) (PMMA) was spin-coated onto the semiconductor for encapsulation. It was found that encapsulation has little effect on mobilities but increases  $I_{\text{on}}/I_{\text{off}}$ s. The saturated  $\mu_h$ s for OTFTs with PMMA encapsulation were  $2.0-4.5$  and  $4.0-8.2 \text{ cm}^2/\text{s}$  for **P228** and **P229**, respectively.<sup>338</sup> Due to their low-lying HOMOs ( $\sim -5.30 \text{ eV}$ ), **P228** and **P229** OTFTs showed high  $I_{\text{on}}/I_{\text{off}}$ s of  $10^{5-7}$ . X-ray scattering patterns of the polymer films revealed a high degree of ordering with close  $\pi-\pi$  stacking distances of 3.72 and 3.66 Å for **P228** and **P229**, respectively. Moreover, these polymers exhibit a predominant edge-on orientation relative to Si/SiO<sub>2</sub> substrates. The smaller **P229**  $\pi-\pi$  stacking and better domain connectivity were factors contributing to its higher mobility. The low-lying HOMO led to good environmental and operation stability of **P229** OTFTs having a PMMA encapsulation layer. Moreover, **P229**-based flexible inverters were fabricated by spin-coating, and the inverters showed high voltage gains of 35–64 with clear response for switching between logic 1 and logic 0 with a very small hysteresis.

Replacement of thiophene with selenophene can induce stronger intermolecular interactions, leading to denser packing and hence increased mobility.<sup>339</sup> Incorporating selenophene vinylene selenophene into a DPP polymer affords **P230**.<sup>340</sup> The polymer shows reduced solubilities and red-shifted absorption versus **P229**, which indicates stronger **P230** interchain interactions. X-ray diffraction analysis demonstrates that selenophene-containing **P230** has slightly denser packing than **P229**. **P230** BGTC OTFTs show a  $\mu_h$  as high as  $4.97 \text{ cm}^2/(\text{V s})$  (average  $4.37 \text{ cm}^2/(\text{V s})$ ) with an  $I_{\text{on}}/I_{\text{off}}$  of  $1.55 \times 10^7$ . Hole mobility is substantially higher than that ( $2.77 \text{ cm}^2/(\text{V s})$ ) of **P229**.<sup>340</sup> Hence, replacement of thiophene with selenophene greatly improves charge transport due to the stronger intermolecular interaction of the selenophene units.

Side-chain engineering leads to **P231** and **P232** having longer alkyl spacers between the polymer backbone and the branching points, and **P229** and **P230** with branching points on the second position were synthesized for comparison.<sup>135</sup> Moving the branching point away from the backbone in **P231** and **P232** increases the  $\pi$  conjugation versus **P229** and **P230** as revealed by the optical absorption spectra. XRD characterization shows that **P231** and **P232** have close  $\pi-\pi$  stacking distances of 3.62 and 3.58 Å, respectively. BGTC OTFTs are fabricated on OTS- or CYTOP-modified SiO<sub>2</sub>/Si substrate to investigate polymer charge transport. **P231** and **P232** having branching positions away from the backbone show 2–3 times higher  $\mu_h$ s than **P229** and **P230** having the branching position on the second carbon. An unprecedented  $\mu_h$  of  $12.04 \text{ cm}^2/(\text{V s})$  is obtained from **P232** on the OTS/SiO<sub>2</sub> substrate after annealing at  $200^\circ\text{C}$ . Thiophene polymer **P231** shows a slightly lower maximum  $\mu_h$  of  $10.54 \text{ cm}^2/$

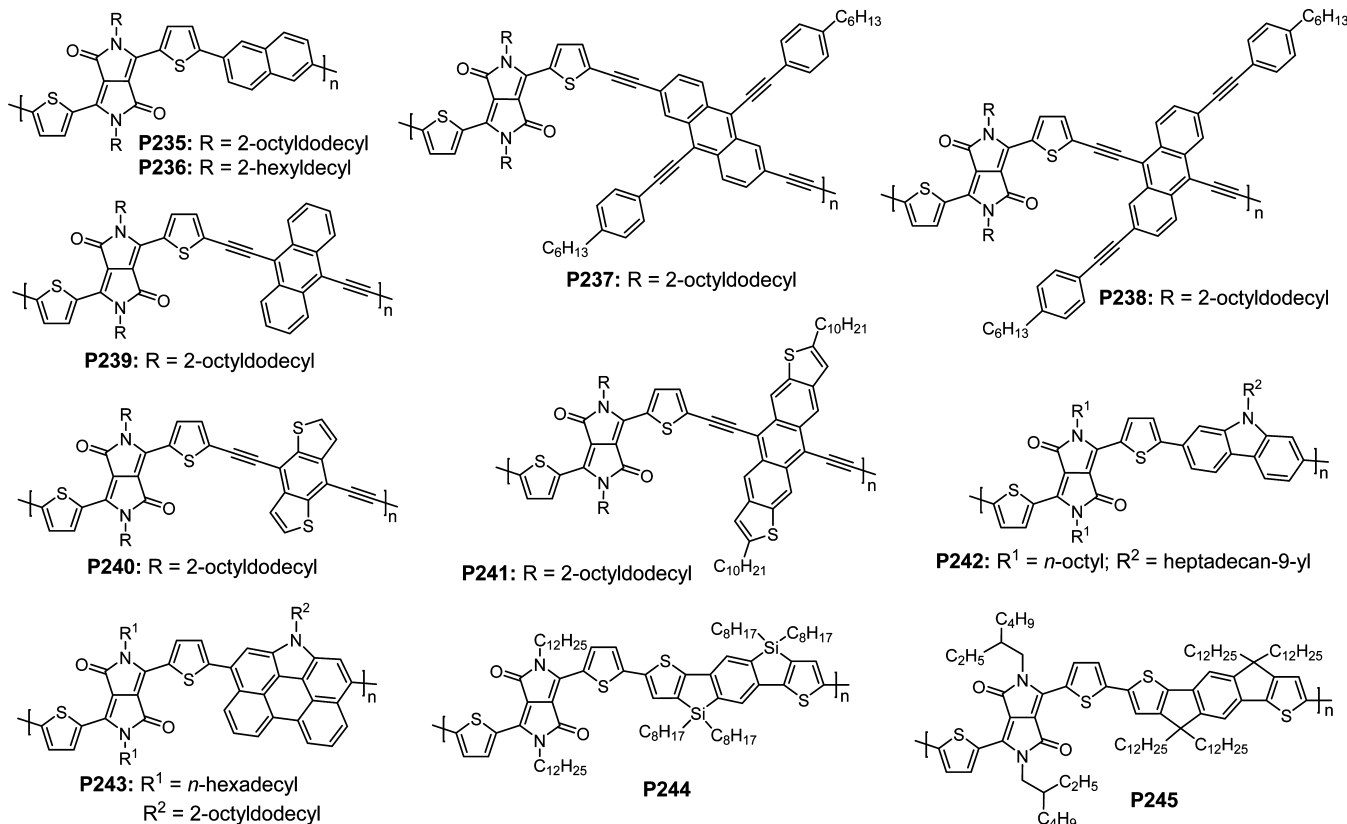


**Figure 44.** Diketopyrrolopyrrole-based polymer semiconductors for OTFTs.

(V s). The enhanced mobilities of P231 and P232 are in good agreement with their extended conjugation, high-degree ordering, close  $\pi$ - $\pi$  stacking, and edge-on orientation on the substrate as revealed by photophysical and structural characterization. These results demonstrate that using a highly conductive polymer backbone and engineering branching position leads to polymers with unprecedented mobilities.

Thieno[3,2-*b*]thiophene is a widely used building block for organic semiconductors.<sup>39,47</sup> Thus, the thienothiophene-flanked DPP monomer was designed, which enabled synthesis of polymers having DPP connected to fused heterocycles. P233 and P234 (Figure 42) were synthesized according to the Stille coupling protocol. Due to the high content of fused  $\pi$  systems in the backbone, P233 and P234 were poorly soluble and had moderate  $M_n$ s of 16 and 14 kDa, respectively, but the solubilities were sufficient for device fabrication.<sup>341</sup> P233 and P234 TGBC OTFTs using a PMMA dielectric show pronounced ambipolarity. For P233 OTFTs, a  $\mu_h$  of 0.037 cm<sup>2</sup>/(V s) and a  $\mu_e$  of 0.30 cm<sup>2</sup>/(V s) in the saturation regime were obtained, while for P234 OTFTs  $\mu_h$  was greatly increased to 1.42 cm<sup>2</sup>/(V s), accompanied by a decreased  $\mu_e$  of 0.063 cm<sup>2</sup>/(V s). The mobility evolution from P233 to P234 was due to the diluted DPP content and increased thiophene loadings in P234 as compared to P233. For n-channel operation, P233 and P234 OTFTs show high  $V_t$ s of 42 and 56 V, respectively, which were attributed to their high-lying LUMOs of -3.76 and -3.68 eV, respectively.<sup>341</sup>

As the number of the electron-donating aromatic cycles and/or the electron-donating capability of the donor units increases, the resulting polymers P222–P232 having extended electron donors show predominant hole transport accompanied by suppressed electron mobility. Hole mobilities greater than 10 cm<sup>2</sup>/(V s) are obtained routinely in these polymers, while for

DPP polymers containing fewer electron-donating aromatic cycles the resulting polymers P210–P217 (except P212) show considerably lower hole mobilities accompanied by enhanced electron mobilities and hence pronounced ambipolarity in OTFTs. Replacement of thiophene with selenophene not only promotes n-channel performance but also increases the magnitude of mobility, which is attributed to the stabilized LUMOs and stronger interchain interactions in the selenophene-containing polymers.

Donor–acceptor polymer P235 (Figure 44) containing naphthalene was synthesized via Suzuki coupling. The polymer had a  $M_n$  of 64 kDa with a narrow PDI of 1.43 and showed good solubility in common organic solvents.<sup>342</sup> The band gap calculated from the absorption onset of P235 film is 1.50 eV, which is wider than that (1.23 eV) of the thienothiophene-based polymer analogue P219 (Figure 42).<sup>326</sup> Film microstructure characterization indicated that P235 had a high degree of ordering with a  $\pi$ - $\pi$  stacking distance of 3.82 Å, which was larger than that (3.71 Å) of P219. After thermal annealing of P235 films at 120 °C the BGTC OTFTs showed a  $\mu_h$  of 0.65 cm<sup>2</sup>/(V s) with an  $I_{on}/I_{off}$  of 10<sup>5</sup> and a  $V_t$  of -22 V.<sup>342</sup> The P235 performance was lower than that of thienothiophene-based P219 due to the less conjugated characteristics and larger  $\pi$ - $\pi$  stacking distance of P235. In dual-gate (BGTC/BGBC) OTFTs, P235 showed a higher  $\mu_h$  of 0.98 cm<sup>2</sup>/(V s) with a greater  $I_{on}/I_{off}$  of 2 × 10<sup>7</sup>. The improved performance in the dual-gate OTFTs was attributed to the reduced contact resistance and enhanced charge injection. Kim et al. further modified the naphthalene and DPP copolymers and optimized their device performance.<sup>343</sup> It was found that P235 carrying a longer branched 2-octyldodecyl had a higher degree of crystallinity and closer packing as compared to P236 containing 2-hexyldecyl, which resulted in improved P235

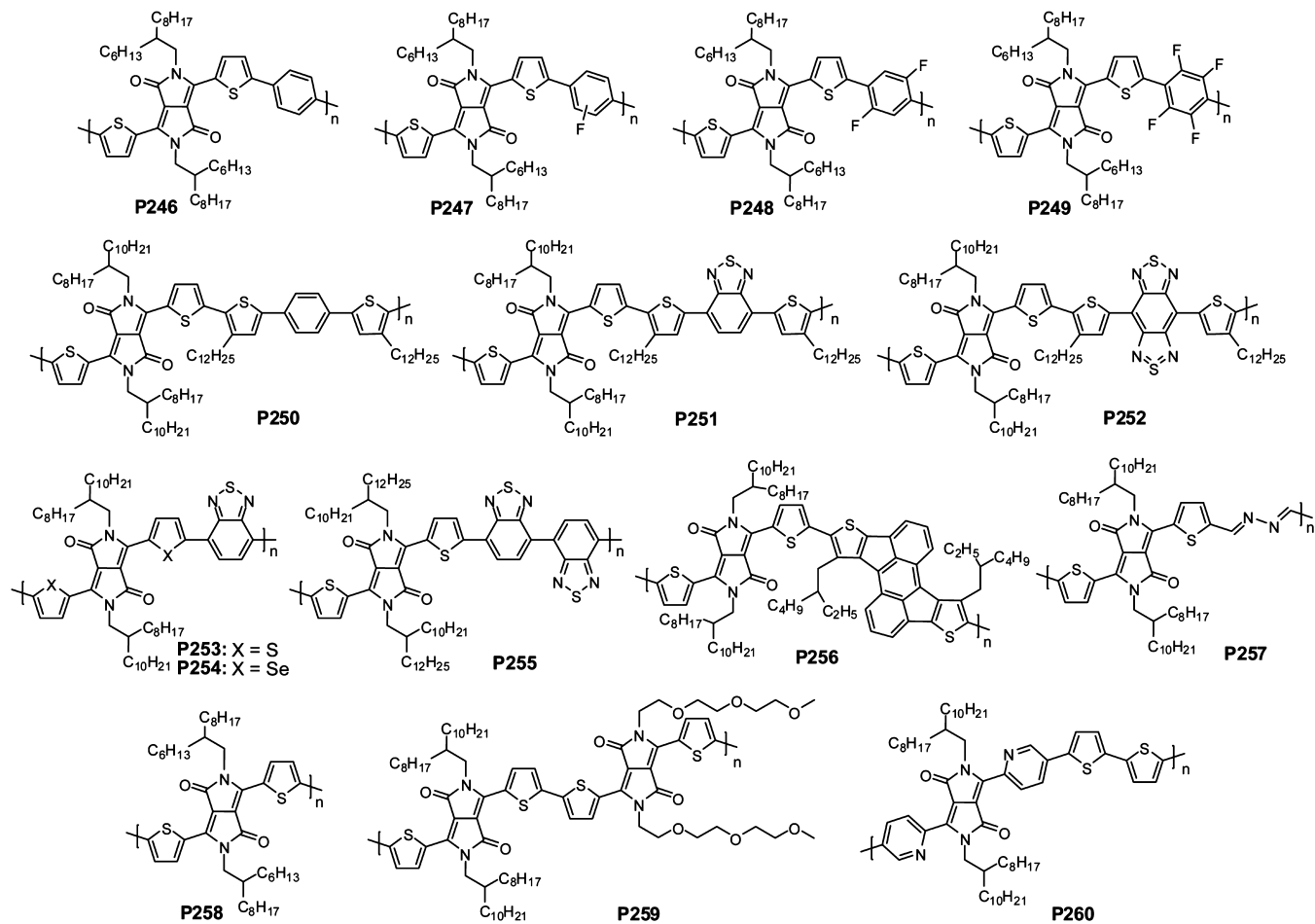


**Figure 45.** Diketopyrrolopyrrole-based polymer semiconductors for OTFTs.

performance. BGTC OTFTs exhibited pronounced ambipolar transport for P235 and P236. The highest  $\mu_h$  and  $\mu_e$  were 1.3 and  $\sim 0.1 \text{ cm}^2/(\text{V s})$ , respectively, for P235 OTFTs after annealing at  $150^\circ\text{C}$ , while P236 OTFTs showed smaller  $\mu_h$  and  $\mu_e$  of 0.11 and  $\sim 0.1 \text{ cm}^2/(\text{V s})$ , respectively. The OTFT performance evolution is in good accordance with the film microstructures and morphologies.

As a symmetric and  $\pi$ -extended donor, anthracene was incorporated into DPP polymers for improved  $\pi$ -orbital overlapping,<sup>344,345</sup> and the ethynylene group was introduced between thiophene-flanked DPP and anthracene to attenuate steric hindrance.<sup>205</sup> P237 and P238 were synthesized via Sonogashira coupling and showed good solubilities in various organic solvents. Incorporation of anthracene led to polymers with wide band gaps. P237 and P238 had band gaps of 1.63 and 1.44 eV, respectively, and low-lying HOMOs of  $\sim -5.5 \text{ eV}$ .<sup>345</sup> On the basis of the polymer band gaps, linking anthracene at the 9,10-positions in P238 achieves a higher degree of conjugation than at the 2,6-positions in P237. Film microstructure characterization revealed the amorphous characteristics of P237 and P238. BGTC OTFTs showed  $\mu_h$ s of 0.026 and  $0.12 \text{ cm}^2/(\text{V s})$  for P237 and P238, respectively, after annealing at  $120^\circ\text{C}$ . The higher P238  $\mu_h$  was in good agreement with its smaller band gap as compared to that of P237.<sup>345</sup> Elimination of 4-(hexylphenyl)ethynyl groups on anthracene afforded P239 with enhanced crystallinity. P240 bearing benzo[1,2-*b*:4,5-*b'*]dithiophene in an orthogonal fashion was synthesized for comparison.<sup>344</sup> UV-vis absorption spectra showed that P239

has an absorption maximum at longer wavelength with a smaller band gap than P240, even if benzodithiophene is known as a stronger donor. Wide-angle X-ray diffraction patterns reveal the crystalline characteristics of P239 and P240. In comparison to P238, the higher degree of P239 crystallinity led to its improved hole mobilities. P239 BGTC OTFTs showed an average  $\mu_h$  of  $1.46 \text{ cm}^2/(\text{V s})$ , which was  $>10$  times higher than that of P238. In comparison to P239, P240 showed a slightly lower  $\mu_h$  of  $0.82 \text{ cm}^2/(\text{V s})$  due to its lower degree of edge-on chain orientation as revealed by GIXRD. By incorporating a larger anthradithiophene, Bao and co-workers developed P241. The polymer exhibited distinct ordered film microstructure and P241 OTFTs showed a  $\mu_h$  of  $0.12 \text{ cm}^2/(\text{V s})$ ,<sup>346</sup> which was substantially higher than other anthradithiophene-containing polymers.<sup>347</sup>

A ladder-type phenanthro[1,10,9,8-*c,d,e,f,g*]carbazole with extended  $\pi$  conjugation along the vertical orientation of the carbazole was incorporated into DPP polymers.<sup>348</sup> UV-vis spectra of P243 were greatly red shifted, and a smaller band gap was obtained when compared to those of carbazole-bearing P242.<sup>349</sup> P243 BGTC OTFTs showed  $\mu_h$ s of  $0.13\text{--}0.30 \text{ cm}^2/(\text{V s})$ ,<sup>348</sup> which was 10 times higher than that ( $0.02 \text{ cm}^2/(\text{V s})$ ) of P242.<sup>349</sup> The higher P243 mobility was attributed to the strong  $\pi\text{-}\pi$  stacking facilitated by the  $\pi$ -extended phenanthro[1,10,9,8-*c,d,e,f,g*]carbazole. The results showed that extension of the  $\pi$  conjugation along the vertical orientation of polymer backbone was an effective strategy to improve charge transport.

Ashraf et al. synthesized P244 bearing a  $\pi$ -extended planar silaindacenodithiophene.<sup>350</sup> The presence of silole in the

conjugated backbone should induce mixing of the  $\sigma^*$  orbital of the silylene and the  $\pi^*$  orbital of the conjugated moiety.<sup>351</sup> Therefore, the LUMOs of silole-based conjugated polymers will be stabilized, which should facilitate electron injection and transport. **P244** TGBC OTFTs using a PMMA dielectric show pronounced ambipolar transport with a  $\mu_h/\mu_e$  of  $0.4/0.1\text{ cm}^2/(\text{V s})$  after the polymer film is annealed at  $320^\circ\text{C}$ . In comparison to **P244**, **P245** containing indacenodithiophene showed unipolar hole transport with a  $\mu_h$  of  $0.065\text{ cm}^2/(\text{V s})$ .<sup>352</sup> From **P245** to **P244**, the appearance of n-channel performance in **P244** reflects the silole effect on LUMO stabilization. The lower **P245**  $\mu_h$  is likely due to the shorter bond length of the (thienyl)carbon–(bridging)carbon bond as compared to that of (thienyl)carbon–(bridging)silicon, which brings the bulky side chains on the bridging carbon closer to the polymer backbone and hence creates greater steric hindrance and increases the  $\pi$ – $\pi$  stacking distance.

Acceptor units have been copolymerized with DPP to enable all-acceptor polymers. A series of DPP polymers **P247**–**P249** (Figure 45) bearing varied fluorine numbers (1, 2, and 4 fluorine atoms) on the phenyl count were synthesized mostly via Suzuki coupling, and fluorine-free polymer analogue **P246** was also synthesized.<sup>35</sup> Increasing the fluorine number on phenyl gradually lowers the polymer LUMOs and HOMOs. The HOMOs measured by CV are  $-5.36$ ,  $-5.45$ ,  $-5.57$ , and  $-5.65\text{ eV}$  for **P246**, **P247**, **P248**, and **P249**, respectively. Dipole moment calculation indicates that the tetrafluorinated phenyl is an even stronger acceptor than DPP, which leads to the lowest lying LUMO of  $-4.18\text{ eV}$  for **P249**. **P246** and **P247** BGTC OTFTs with Au source/drain show balanced ambipolarity with  $\mu_s$ s and  $\mu_h$ s of  $0.2$ – $0.3\text{ cm}^2/(\text{V s})$ , while **P248** and **P249** OTFTs show predominant n-type ambipolarity. After thermal annealing, **P249** exhibits the highest  $\mu_e$  of  $2.36\text{ cm}^2/(\text{V s})$  with a one order of magnitude lower  $\mu_h$  of  $0.23\text{ cm}^2/(\text{V s})$ . Due to its low-lying LUMO, **P249** shows excellent OTFT stabilities. After 7 months storage in ambient, the  $\mu_e$  is slightly decreased from  $2.36$  to  $1.88\text{ cm}^2/(\text{V s})$ . Film characterization indicates that **P249** adopts both edge-on and face-on orientations on the substrate with high crystallinity and a long coherence length. Such orientation may promote three-dimensional charge transport and hence high mobility. The result demonstrates how fluorination effects promote electron mobility.

Wudl et al. reported a family of DPP polymers containing various acceptors via modulating the phenyl unit with varied numbers of thiadiazole.<sup>353</sup> Thiadiazole incorporation gradually reduces the polymer band gaps and lowers their LUMOs. Hence, the band gaps are  $1.5$ ,  $1.35$ , and  $0.65\text{ eV}$  and the LUMOs are  $-3.2$ ,  $-3.4$ , and  $-3.9\text{ eV}$  for **P250**, **P251**, and **P252**, respectively.<sup>353</sup> BGBT transistors with Au source/drain electrodes were fabricated. Due to the high-lying LUMO, **P250** exhibits unipolar p-type transport with a  $\mu_h$  of  $0.24\text{ cm}^2/(\text{V s})$  in a  $\text{N}_2$ -purged glovebox. **P251** shows predominant p-type transport with a  $\mu_h$  of  $0.17\text{ cm}^2/(\text{V s})$  accompanied by slight electron injection. **P252** OTFTs show pronounced and balanced ambipolar transport with an average  $\mu_h/\mu_e$  of  $0.89/0.99\text{ cm}^2/(\text{V s})$ . The high **P252**  $\mu_e$  is associated with its low-lying LUMO enabled by the strong electron-withdrawing benzobisthiadiazole unit. The enhanced **P252**  $\mu_h$  is attributed to the strong interchain interaction induced by the stronger interchain donor–acceptor interactions and intermolecular S···N contacts from benzobisthiadiazole.<sup>353</sup>

Dodabalapur et al. reported **P253** containing DPP and benzothiadiazole as the acceptors. The polymer was synthesized

via Suzuki coupling with a  $M_n$  of  $42\text{ kDa}$  and a small PDI of  $1.42$ . **P253** has a HOMO of  $-5.2\text{ eV}$ , a LUMO of  $-4.0\text{ eV}$ , and a band gap of  $1.2\text{ eV}$ .<sup>354</sup> After annealing at  $200^\circ\text{C}$ , **P253** BGTC OTFTs exhibit ambipolarity with a balanced  $\mu_h/\mu_e$  of  $0.35/0.4\text{ cm}^2/(\text{V s})$ , respectively.<sup>354</sup> Two dimensional XRD reveals a highly ordered lamellar packing motif with an edge-on orientation and a close  $\pi$ – $\pi$  stacking of  $3.73\text{ \AA}$  for **P253** films. In comparison to **P251**, deletion of electron-rich alkyl thiophenes flanked to benzothiadiazole promotes n-channel transport for **P253**, which is in good accordance with the FMO evolution. It was found that substitution of thiophene with selenophene can improve charge transport<sup>331,355</sup> and lower polymer LUMOs.<sup>356</sup> Replacement of the thiophene with selenophene affords **P254**, and **P253** is synthesized for comparison.<sup>339</sup> The new selenophene polymer **P254** shows a smaller optical band gap of  $1.05\text{ eV}$  than that ( $1.20\text{ eV}$ ) of **P253**. Cyclic voltammetry measurements reveal that selenophene substitution results in HOMO and LUMO lowering by  $0.1$  and  $0.07\text{ eV}$ , respectively, in **P254**. **P254** TGBC OTFTs show ambipolar performance with a saturated  $\mu_h/\mu_e$  of  $0.46/0.84\text{ cm}^2/(\text{V s})$ . The extracted  $\mu_h/\mu_e$  of **P253** are  $0.33/0.57\text{ cm}^2/(\text{V s})$ , similar to the value reported by Dodabalapur.<sup>354</sup> Therefore, incorporating larger and more polarizable selenium increases **P254** charge transport, which stems from the lowered LUMO and enhanced interchain interactions of the selenophene polymer. **P254** is subsequently used for fabrication of CMOS-like inverters and ring oscillators. The inverters show a voltage gain of  $40$  with a switching point close to  $V_{DD/2}$ , and the three-stage ring-oscillator exhibits a maximum oscillation frequency of  $182\text{ kHz}$  at a relatively low  $V_{DD} = 50\text{ V}$ .<sup>339</sup>

Highly electron-deficient bisbenzothiadiazole was incorporated into **P255**, which was synthesized by Suzuki coupling and had a  $M_n$  of  $57\text{ kDa}$  and a PDI of  $3.5$ .<sup>357</sup> Most DPP polymers reported in the literature showed either p-channel or ambipolar transport. **P255** was designed for improving electron transport to afford n-channel characteristics. Bisbenzothiadiazole incorporation led to a lower lying **P255** LUMO of  $\sim -3.8\text{ eV}$ , comparable to the highly electron-depleted rylene diimide polymers. **P255** BGTC OTFTs were fabricated by spin-coating semiconductor onto the polypropylene-*co*-1-butene-modified  $\text{SiO}_2/\text{Si}$  substrate having minimized hydroxyl groups, which act as electron traps.<sup>38</sup> The OTFTs demonstrated predominant electron transport with a  $\mu_e/\mu_h$  of  $1.3 \times 10^{-3}/6.5 \times 10^{-4}\text{ cm}^2/(\text{V s})$ . Moderate mobilities were attributed to the twisted polymer backbone caused by the bisbenzothiadiazole as revealed by theoretical calculation and the UV–vis absorption spectrum. The deviation from backbone coplanarity led to poorly defined and amorphous **P255** film microstructure.

A polycyclic  $\pi$ -extended acceptor, emeraldicene,<sup>358</sup> was incorporated into **P256** (Figure 45), which has a narrow band gap of  $1.0\text{ eV}$ .<sup>359</sup> The **P256** LUMO and HOMO energies derived from cyclic voltammetry are  $-3.50$  and  $-4.65\text{ eV}$ , respectively. XRD data show an ordered and crystalline microstructure for **P256** films with a  $\pi$ – $\pi$  stacking distance of  $4.03\text{ \AA}$ . **P256** BGBT OTFTs with Au source/drain electrodes show an optimized ambipolar transport with a high and balanced  $\mu_h/\mu_e$  of  $0.29/0.25\text{ cm}^2/(\text{V s})$  after annealing at  $320^\circ\text{C}$ , which is in accordance with its highest crystallinity achieved at this temperature.

A novel all-acceptor conjugated polyazine-containing DPP was synthesized by reacting a dialdehyde-functionalized DPP with equimolar hydrazine monohydrate via condensation polymerization.<sup>360</sup> The azine linkage,  $\text{C}=\text{N}-\text{N}=\text{C}$ , is isoelectronic with the diene but is electron deficient. The resulting **P257** has a high

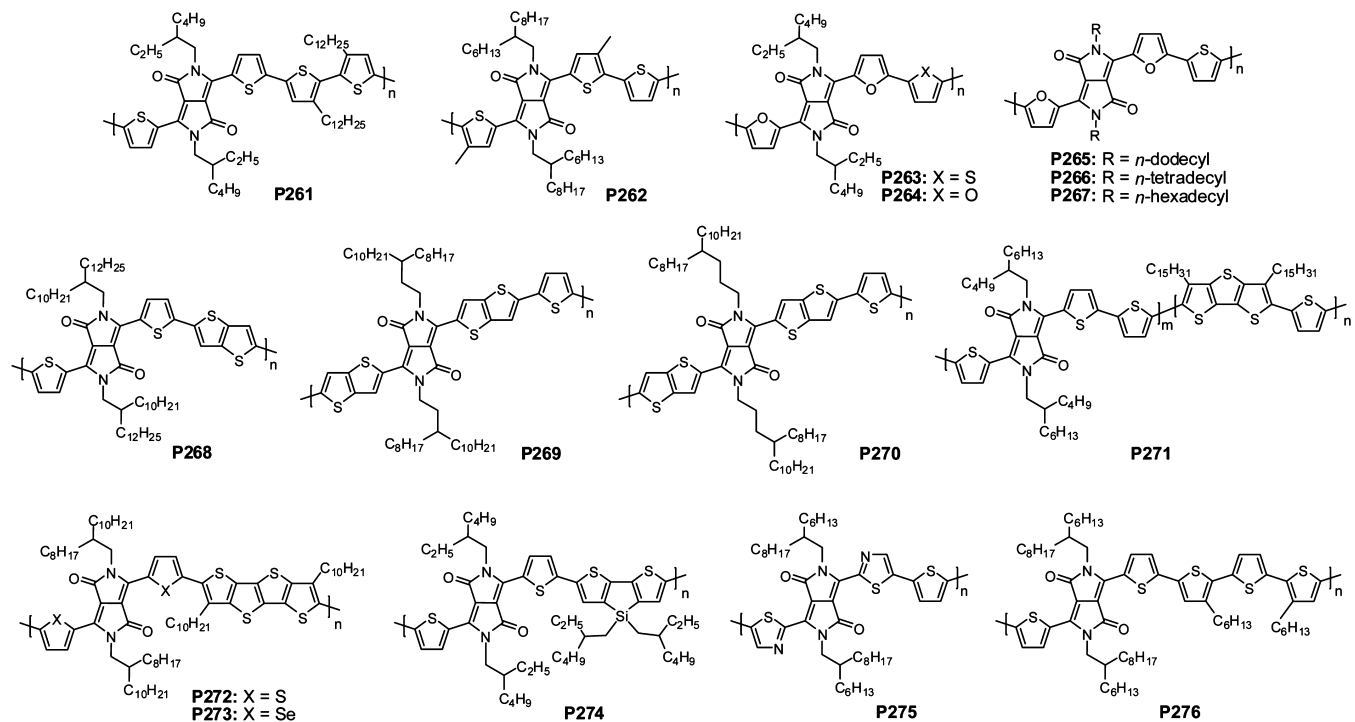


**Figure 46.** Diketopyrrolopyrrole and thiophene derivative-based polymers for organic solar cells.

$M_n$  of 102 kDa measured by GPC at 140 °C and shows good solubility in common organic solvents. The P257 band gap calculated from the absorption cutoff is 1.43 eV, which is larger than those of thiophene–DPP polymer P210 and vinyl–DPP polymer P217 (Figure 42). The P257 LUMO and HOMO derived from cyclic voltammetry are –4.24 and –5.67 eV, respectively. P257 was evaluated as a channel material in TGBC OTFTs using a CYTOP dielectric and Au source/drain electrodes. The OTFTs show ambipolarity with a  $\mu_h/\mu_e$  of 0.36/0.41 cm<sup>2</sup>/(V s) after annealing at 200 °C. The high mobility is attributed to the ordered P257 film microstructure. The result demonstrates that the azine is a promising electron-withdrawing unit for lowering polymer LUMOs to enhance electron transport.

In comparison to DPP–benzothiadiazole copolymer P253, a DPP–DPP polymer was designed for better materials solubility since solubilizing alkyl groups can be installed on every DPP unit. Yamamoto coupling of the dibrominated thiophene-flanked DPPs afforded homopolymer P258 (Figure 45).<sup>361,362</sup> The polymer has a narrow band gap of ~1.2 eV. The LUMO and HOMO are found to lie at –4.2 and –5.4 eV, which should facilitate electron and hole injection from Au electrodes, respectively. When used as an active layer, P258 exhibits balanced ambipolar transport with a  $\mu_h/\mu_e$  of 0.024/0.056 cm<sup>2</sup>/(V s).<sup>362</sup> Morphological studies show poor crystallinity and random chain orientation of the P258 films, likely due to the steric hindrance induced by the bulky side chains on the consecutive DPP repeating units. The side chains are engineered to allow optimized polymer packing and promote formation of crystalline domains.<sup>363,364</sup> Triethylene glycol and alkyl chains are alternatively attached to DPP units to induce spontaneous chain crystallization and maintain good solubility. P259 is synthesized via Suzuki coupling and has a  $M_n$  of 67 kDa with a PDI of 4.66.<sup>365</sup> The optical band gap from film absorption onset is 1.2 eV. GIXRD shows that P259 adopts a highly ordered lamellae structure with the lamellae parallel to the substrate. Moreover,

the polymer has a close  $\pi$ – $\pi$  stacking distance of 3.6 Å. P259 BGBC OTFTs with Au source/drain show balanced  $\mu_h$  and  $\mu_e$  of ~0.01 cm<sup>2</sup>/(V s), similar to the values from P258 OTFTs. Interestingly, TGBC OTFTs with Al source/drain electrodes and a CYTOP dielectric show strictly unipolar n-channel transport with a  $\mu_e$  of 3 cm<sup>2</sup>/(V s). The greatly improved  $\mu_e$  in top-gate OTFTs is attributed to the more facile electron injection from low work function Al and formation of a high-quality P258/CYTOP interface. The result shows an effective materials design strategy by coupling acceptor with acceptor to afford high-performance n-channel polymers.<sup>365</sup>

Most of the high-mobility DPP polymers feature a monomeric unit with a DPP core capped with two five-membered heteroarenes, such as thiophene, furan, or selenophene. The electron-rich character of these heteroarenes offsets the electron deficiency of DPP, which can elevate the polymer LUMOs. When six-membered benzene is used, the resulting DPP-based building block shows a substantial dihedral angle between benzene and DPP,<sup>366</sup> which degrades the polymer mobility. Therefore, a very low mobility of  $4.9 \times 10^{-7}$  cm<sup>2</sup>/(V s) was obtained from P218 (Figure 42). Li et al. introduced 2-pyridinyl-capped DPP<sup>367</sup> to alleviate the steric incumbrance of six-membered rings, and the resulting P260 shows a high degree of backbone coplanarity as revealed by DFT computation and the XRD pattern of the polymer film.<sup>368</sup> P260 has a low-lying LUMO/HOMO of –4.33/–5.69 eV enabled by the electron-withdrawing DPP and pyridine. P260 TGBC OTFTs using a CYTOP dielectric exhibited n-channel dominating ambipolar performance with an average  $\mu_e/\mu_h$  of 4.54/2.20 cm<sup>2</sup>/(V s). The best device showed a  $\mu_e/\mu_h$  of 6.30/2.78 cm<sup>2</sup>/(V s). The excellent electron transport of P260 was attributed to the low-lying polymer LUMO and the high degree of polymer film crystallinity with a close  $\pi$ – $\pi$  stacking distance of 3.6 Å. The results demonstrate that the pyridinyl-capped DPP is a highly promising building block for organic semiconductors for OTFT applications.

### 9.3. Diketopyrrolopyrrole-Based Polymer Semiconductors for OSCs

Janssen et al. first reported the DPP–quaterthiophene copolymer **P261** for OSCs (Figure 46),<sup>315</sup> which had the same backbone as the first OTFT DPP polymer **P209** (Figure 42) but with a shorter 2-ethylhexyl on DPP.<sup>319</sup> When compared to **P209**, **P261** showed strong aggregation.<sup>315</sup> OSCs using a **P261**:PC<sub>70</sub>BM active layer achieved an optimal PCE of 4.0% with a  $J_{sc}$  of  $11.3 \text{ cm}^2/(\text{V s})$ , a  $V_{oc}$  of 0.61 V, and a FF of 58%. The cells showed broad spectral response in the range of 400–900 nm with the highest EQE of ~45%. The same group investigated the high-performance ambipolar **P210** (Figure 42) for OSCs.<sup>320</sup> Addition of a small amount (100 mg/mL) of DIO to the **P210**:PC<sub>70</sub>BM chloroform solution was found to greatly improve PCEs, mainly by boosting  $J_{sc}$ s. The best OSCs with **P210**:PC<sub>70</sub>BM in a 1:2 weight ratio showed a  $J_{sc}$  of  $11.8 \text{ mA/cm}^2$ , a  $V_{oc}$  of 0.65 V, a FF of 60%, and a PCE of 4.7%. In comparison to quaterthiophene-based polymer **P261**, the terthiophene-bearing **P210** showed a greater  $V_{oc}$ .

As a weak donor, the methyl group was installed on the thiophene flanked to DPP to afford polymer **P262**. The methyl groups have a minimal impact on the **P262** band gap, which is identical to that (1.30 eV) of **P210**.<sup>369</sup> Single-junction OSCs having the structure ITO/PEDOT:PSS/**P262**:PC<sub>70</sub>BM/LiF/Al show a PCE of 6.8% with a  $J_{sc}$  of  $16.9 \text{ mA/cm}^2$ , a  $V_{oc}$  of 0.59 V, and a FF of 68%. The  $V_{oc}$  of **P262** cells is smaller than that (0.66 V) of **P210** cells, which is in good agreement with their HOMOs. Replacement of LiF with poly[(9,9-bis(3'-(*N,N*-dimethylamino)propyl)-2,7-fluorene)-*alt*-2,7-(9,9-diethylfluorene)] polyelectrolyte leads to an improved PCE of 7.0%, which is attributed to the enhanced  $J_{sc}$  of  $17.8 \text{ mA/cm}^2$ . The small band gap and high performance of **P262** lead to promising tandem and triple-junction polymer:fullerene cells with PCEs of 8.9% and 9.6%, respectively, when appropriate complementary absorber materials are used.<sup>369</sup>

Fréchet and co-workers found that furan-flanked DPP polymers possess enhanced solubilities versus the thiophene-flanked DPP polymer analogues, which was attributed to the greater backbone curvature in furan-flanked DPP polymers.<sup>370</sup> **P263** and **P264** were synthesized and showed good solubilities and high  $M_n$ s, while the **P210** analogue (Figure 42) having 2-ethylhexyl on the DPP moiety was insoluble.<sup>266</sup> Band gaps were 1.41 and 1.35 eV for **P263** and **P264**, respectively, which were wider than that (1.30 eV) of **P210**. **P263** cells having the structure ITO/PEDOT:PSS/**P263**:PC<sub>71</sub>BM/LiF/Al show a PCE of 5.0% with a  $J_{sc}$  of  $11.2 \text{ mA/cm}^2$ , a  $V_{oc}$  of 0.74 V, and a FF of 60% when using chlorobenzene containing 9% of 1-chloronaphthalene as the processing solvent. 1-Chloronaphthalene addition led to a more optimal, intermixed, phase-segregated active layer with good polymer crystallinity.<sup>371</sup> In comparison to **P210** cells,<sup>320</sup> the improved **P263** cell performance was mainly attributed to its enlarged  $V_{oc}$  due to its lower lying HOMO. In comparison to **P263**, **P264** showed a reduced PCE of 3.8% in the same structure after optimization, which could be attributed to its lower  $M_n$  (29 kDa) versus that (66 kDa) of **P263**.<sup>266</sup> Further fine tuning of the polymer structure afforded **P265**–**P267** having straight chains on DPP.<sup>372</sup> Due to the improved solubilities of furan polymers, solution processability was retained for these *n*-alkyl-substituted polymers. PCEs of 5.2%, 6.5%, and 6.2% were obtained for **P265**, **P266**, and **P267** BHJ cells, respectively. The lower **P265** performance was related to its reduced solubility, and the highest PCE of **P266** was attributed to the good combination of polymer solubility and

miscibility with PC<sub>71</sub>BM to achieve optimal morphology. In comparison to **P263** having branched chains, **P265**–**P267** showed a closer  $\pi$ – $\pi$  stacking of 3.6 Å and higher crystallinity, which led to higher  $J_{sc}$ s, FFs, and PCEs.<sup>372</sup>

DPP polymer containing thienothiophene has achieved  $\mu_h s > 1 \text{ cm}^2/(\text{V s})$  in OTFTs, but the corresponding solar cells show moderate performance with PCEs of <2%, which is likely limited by the low polymer  $M_n$  and unsatisfactory solubility.<sup>329</sup> Side-chain engineering affords **P268** with improved solubility and a substantial  $M_n$  of 447 kDa measured by GPC at 80 °C. **P268** BHJ OSCs having a 220 nm **P268**:PC<sub>70</sub>BM active layer show a promising PCE of 6.9% with a  $J_{sc}$  of  $14.8 \text{ mA/cm}^2$ , a  $V_{oc}$  of 0.66 V, and a FF of 70%. As the film thickness is varied, the solar cells show decreased PCEs but the fill factors remain high. For cells having a 300 nm active layer, the FF is still higher than 60%, and the highest FF of 74% is achieved from a 140 nm or thinner active layer. The high FFs and promising PCEs are mainly attributed to the suppressed bimolecular recombination as the result of high charge carrier mobility and optimal film morphology.<sup>89,97</sup>

High-mobility thienothiophene-flanked DDP polymers **P233** and **P234** (Figure 42) were blended with PC<sub>71</sub>BM.<sup>341</sup> The resulting cells showed comparable  $V_{oc}$ s of 0.57 V. **P234** cells achieved a remarkable  $J_{sc}$  of  $15.0 \text{ mA/cm}^2$ , which is much higher than that ( $8.9 \text{ mA/cm}^2$ ) of **P233** cells, although **P234** showed greatly blue-shifted absorption. The improved **P234**  $J_{sc}$  was attributed to the more favorable film morphology and higher lying LUMO, which enabled more efficient exciton dissociation at polymer/PC<sub>71</sub>BM interfaces.<sup>341</sup> The lower lying **P233** LUMO resulted in more pronounced electron mobility than **P234** in OTFTs. Side-chain engineering via moving the branching point away from the backbone can promote polymer packing and increase charge carrier mobility.<sup>122,373</sup> By following this strategy, **P269** and **P270** were synthesized. Among **P234**, **P269**, and **P270**, **P270** having the longest alkyl chain was most soluble and achieved the highest  $M_n$  of 80 kDa, and **P269** showed improved solubility and a higher  $M_n$  than **P234**.<sup>374</sup> UV–vis absorption spectra revealed that **P269** and **P270** had red-shifted absorption maxima accompanied by more structured profiles than **P234**. BHJ OSCs exhibited promising performance for polymers with engineered side chains. **P269** cells achieved a PCE of 7.3% with a  $J_{sc}$  of  $18.6 \text{ mA/cm}^2$ , a  $V_{oc}$  of 0.61 V, and a FF of 64% without using processing additives; **P270** cells showed a PCE of 6.9% with a  $J_{sc}$  of  $18.7 \text{ mA/cm}^2$ , a  $V_{oc}$  of 0.60 V, and a FF of 62%. The PCEs of **P269** and **P270** cells were >1% higher than that (5.9%) of **P234** cells fabricated under optimized conditions mainly due to the  $J_{sc}$  enhancement.<sup>374</sup> Film characterization showed that **P269** and **P270** having larger branching point distances exhibited increased crystallinity than **P234** in blend films, which led to increased **P269** and **P270** hole mobilities. The improved mobilities result in more efficient charge extraction and hence higher  $J_{sc}$ s in **P269** and **P270** OSCs. The result demonstrated the effectiveness of the engineering branching point for performance improvement.

**P226** (Figure 42) bearing dithienothiophene was incorporated into solar cells having the structure ITO/PEDOT:PSS/**P226**:PC<sub>71</sub>BM (1:1.5)/LiF/Al; the best average PCE of 6.05% with a high  $J_{sc}$  of  $13.7 \text{ mA/cm}^2$ , a  $V_{oc}$  of 0.66 V, and a FF of 66.1% was achieved from cells cast from a mixed solvent of chloroform, dichlorobenzene, and 2.5 vol % of DIO.<sup>334</sup> The promising performance was attributed to the nanoscale phase separation with an interconnected network and a high  $\mu_h$  of  $5.33 \times 10^{-3} \text{ cm}^2/(\text{V s})$  measured by SCLC. A DPP-based random donor–acceptor copolymer **P271** was synthesized via Stille coupling. The DPP was linked with 3,5-dialkylthienothiophene using the

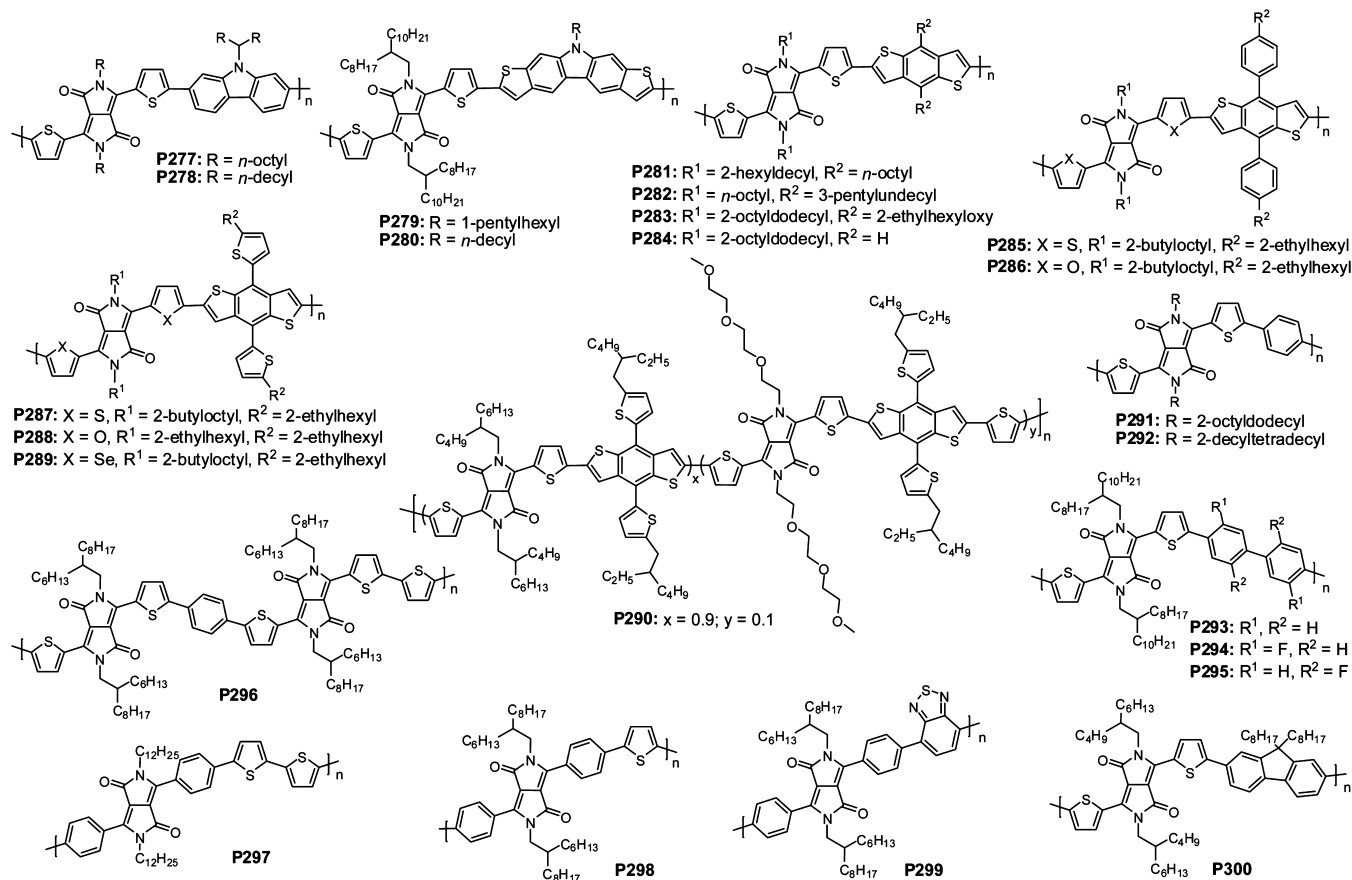


**Figure 47.** Diketopyrrolopyrrole and benzene derivative copolymers for organic solar cells.

thiophene bridge. The combination of DPP with dithienothiophene led to **P271** with wide absorption and a band gap of 1.37 eV. OSCs having the structure ITO/PEDOT:PSS/**P271**:PC<sub>71</sub>BM/Ca/Ag achieved a promising PCE of 5.02% with a  $J_{sc}$  of 12.76 mA/cm<sup>2</sup>, a  $V_{oc}$  of 0.584 V, and a FF of 67.27%. The promising PCE from a random polymer indicated the effectiveness of using DPP for creating polymers for high-performance OSCs.<sup>375</sup> To further extend the thiophene conjugation, **P272** bearing a tetrathienoacene unit was synthesized. In order to achieve enough solubility, two alkyl chains were installed on the tetrathienoacene.<sup>376</sup> **P272** BHJ OSCs showed a PCE of 4.55% with a  $J_{sc}$  of 11.76 cm<sup>2</sup>/(V s), a  $V_{oc}$  of 0.60 V, and a FF of 64%. As noted above, replacement of thiophene with selenophene can lower the polymer band gap and promote intermolecular interaction. **P273** having a selenophene bridge shows a slightly smaller band gap of 1.28 eV than that (1.30 eV) of **P272**. The smaller band gap in combination with the more ordered packing and higher hole mobility leads to **P273** cells with an enhanced PCE of 5.68%. The performance enhancement is mainly attributed to the greatly increased  $J_{sc}$  of 15.62 cm<sup>2</sup>/(V s).<sup>376</sup>

Dithienosilole-containing **P274** was also synthesized and had a small band gap of 1.29 eV with a high-lying HOMO of -5.04 eV.<sup>377</sup> However, the **P274** BHJ OSCs having the structure ITO/PEDOT:PSS/**P274**:PC<sub>70</sub>BM (1:2 wt %)/Ca/Al showed an unsatisfactory PCE of 2.10% with a  $J_{sc}$  of 7.5 mA/cm<sup>2</sup>, a  $V_{oc}$  of 0.55 V, and a FF of 50.8%. The performance was mainly limited by its small  $J_{sc}$  and moderate  $V_{oc}$  due to its high-lying HOMO.

Janssen and co-workers designed and synthesized a thiazole-capped DPP-based polymer **P275**,<sup>378</sup> introduction of thiazole

led to **P275** with a low-lying LUMO of -4.00 eV and a small band gap of 1.44 eV, which was 0.3 eV lower than that of **P210** (Figure 42). **P275** showed n-channel performance in OTFTs with a  $\mu_e$  of 0.13 cm<sup>2</sup>/(V s). The low-lying LUMO, good electron mobility, and near-infrared absorption made **P275** a good acceptor semiconductor in all-polymer OSCs. When **P276** was used as the donor semiconductor, which has a higher lying LUMO of -3.63 eV, the resultant ITO/ZnO/**P275**:**P276**/MoO<sub>3</sub>/Ag inverted cells showed an optimized PCE of 2.9% with a  $J_{sc}$  of 6.9 mA/cm, a  $V_{oc}$  of 0.81 V, and a FF of 51%.<sup>378</sup> From a molecular structure perspective, both donor semiconductor and acceptor semiconductor are very similar. The results demonstrate that DPP polymers can operate as a donor semiconductor or acceptor semiconductor by varying the counit in the polymer backbone.

Carbazole is a promising electron donor for high-performance solar cell polymers.<sup>379</sup> Hence, **P277** (Figure 47) was synthesized for BHJ OSCs,<sup>349</sup> and showed a narrow band gap of 1.57 eV, a low-lying HOMO of -5.44 eV, and a good  $\mu_h$  of 0.02 cm<sup>2</sup>/(V s). These characteristics indicated that **P277** should be a good candidate for OSCs. However, the fabricated cells showed an unsatisfactory PCE of 1.6%, which was mainly limited by the unoptimized film morphology.<sup>349</sup> The morphology can be greatly improved using a processing additive<sup>21</sup> and modifying polymer side chains.<sup>372</sup> Using 2 vol % 1-chloronaphthalene processing additive, **P277**:PC<sub>70</sub>BM BHJ OSCs showed improved film morphology featuring interpenetrating networks and hence an increased PCE of 3.28%.<sup>380</sup> UV absorption spectra showed that **P278** having longer solubilizing chains had a clearer vibronic shoulder and red-shifted absorption in comparison to those of

**P277**, suggesting more ordered stacking and stronger intermolecular interactions of **P278**. **P278:PC<sub>70</sub>BM** cells using a TiO<sub>x</sub> functional interlayer between the photoactive layer and the Al electrode exhibited the highest PCE of 3.80% with a *J<sub>sc</sub>* of 9.10 mA/cm<sup>2</sup>, a *V<sub>oc</sub>* of 0.77 V, and a *FF* of 55%. Such performance was achieved without using a processing additive, and additive addition led to degraded performance.<sup>380</sup> As compared to carbazole, dithieno[2,3-*b*:7,6-*b*]carbazole has reduced steric hindrance and more extended  $\pi$  conjugation, and the dithienocarbazole polymers exhibit good mobility.<sup>267</sup> DPP polymers bearing dithienocarbazole were synthesized for OSCs. The resulting **P279** and **P280** have band gaps of  $\sim$ 1.3 eV and HOMOs of  $-$ 5.1 eV.<sup>381</sup> The band gaps of dithienocarbazole polymers were smaller than that (1.57 eV) of the carbazole polymer analogues **P277** and **P278** due to the reduced steric hindrance and extended conjugation. Without using processing additives, BHJ OSCs having the structure ITO/PEDOT:PSS(40 nm)/polymer:PC<sub>71</sub>BM(90 nm)/LiF(1 nm)/Al(100 nm) showed a PCE of 5.9% with a *J<sub>sc</sub>* of 13.4 mA/cm<sup>2</sup>, a *V<sub>oc</sub>* of 0.72 V, and a *FF* of 62% for **P280** cells and a PCE of 1.1% with a *J<sub>sc</sub>* of 2.51 mA/cm<sup>2</sup>, a *V<sub>oc</sub>* of 0.68 V, and a *FF* of 65% for **P279** cells. The alkyl chains on dithienocarbazole have a profound impact on polymer:PC<sub>71</sub>BM film morphology. **P279** containing branched chains shows severe phase separation with domain sizes  $>$  100 nm, while **P280** bearing straight chains has fine phase separation with domain sizes  $<$  15 nm. The nanoscale phase separation and enhanced mobility of **P280:PC<sub>71</sub>BM** blend contribute to its greatly improved PCEs.<sup>381</sup>

DPP polymers containing benzodithiophene were synthesized with linear and branched alkyl chains installed on the benzodithiophene and DPP.<sup>382</sup> The resulting **P281** and **P282** show band gaps of 1.45 and 1.36 eV, respectively. XRD characterization of **P281** and **P282** films reveals crystalline patterns with diffractions up to third order accompanied by a  $\pi$ - $\pi$  stacking distance of  $\sim$ 4 Å. **P281** OSCs having the structure ITO/PEDOT:PSS/**P281:PC<sub>71</sub>BM/LiF/Al** showed a PCE of 4.1% with a *J<sub>sc</sub>* of 9.4 mA/cm<sup>2</sup>, a *V<sub>oc</sub>* of 0.71 V, and a *FF* of 61% fabricated from dichlorobenzene solution containing 2.5 vol % DIO. **P282** cells show much degraded PCE of 1.4%, which was attributed to a particular interaction at the polymer:PC<sub>71</sub>BM interface.<sup>382,383</sup> The straight alkyl on **P282** DPP leads to a greater degree of back transfer of electrons from fullerene to the polymer DPP moiety; therefore, bimolecular recombination is exacerbated in **P282** cells, which lowers the PCEs.<sup>382</sup> As a strong electron-donor group, alkoxy can elevate polymer HOMOs and hence decrease *V<sub>oc</sub>*.<sup>210</sup> By removing alkoxy on benzodithiophene, Jo and co-workers reported **P284**, which had a red-shifted absorption maximum and a greatly lowered HOMO of  $-$ 5.46 eV in comparison to those of **P283** having 2-ethylhexyloxy on the benzodithiophene.<sup>384</sup> The red-shifted **P284** absorption indicates its enhanced backbone coplanarity. **P284** cells showed a PCE of 5.16% with a *J<sub>sc</sub>* of 10.49 mA/cm<sup>2</sup>, a *V<sub>oc</sub>* of 0.82 V, and a *FF* of 60%. In comparison to **P283**, **P284** exhibited a 0.2 V larger *V<sub>oc</sub>* as the result of the removal of the alkoxy group on benzodithiophene. The red-shifted absorption together with its greater hole mobility increased the **P284** *J<sub>sc</sub>*. The enlarged *V<sub>oc</sub>* and increased *J<sub>sc</sub>* led to a higher PCE (5.16%) for **P284** cells versus that (2.24%) of **P283** cells.<sup>384</sup>

Further materials modification focused on side-chain engineering, and alkylthienyl and alkylphenyl<sup>385</sup> groups were installed on the benzodithiophene. A furan moiety was introduced as a bridge between the DPP and benzodithiophene in place of thiophene. Yang and co-workers reported a series of

polymers **P285**–**P288**.<sup>386</sup> UV-vis absorption spectra indicated that furan introduction leads to slightly enlarged polymer band gaps for **P286** and **P288** as compared to those of thiophene-flanked polymers **P285** and **P287**. The low-band-gap polymers **P285**–**P288** have small absorption overlaps with wide-band-gap P3HT. The absorption spectra of the DPP polymer and P3HT cover the solar spectra from 350 to 850 nm complimentarily, which indicates that they are promising materials for tandem cells. Replacement of alkyl with an alkylthienyl or alkylphenyl group results in greatly improved performance of **P285**–**P288** versus **P281** and **P283**. The optimal PCEs of single-layer OSCs having the structure ITO/PEDOT:PSS/polymer:PC<sub>71</sub>BM/Ca/Al were 6.2%, 3.3%, 6.6%, and 5.8% for **P285**, **P286**, **P287**, and **P288**, respectively. Among the four polymers, three of them afforded PCEs around 6%. Their superior performance was attributed to their low-lying HOMOs, broad photoresponse, high charge carrier mobilities, and optimized film morphology. These polymers were then incorporated into inverted tandem cells having the structure ITO/ZnO(30 nm)/P3HT:IC<sub>60</sub>BM-(150 nm)/PEDOT:PSS(30 nm)/ZnO(30 nm)/polymer:PC<sub>71</sub>BM(100 nm)/MoO<sub>3</sub>(5 nm)/Ag. The best cells showed PCEs of 8.5%, 8.8%, and 8.3% for **P285**, **P287**, and **P288**, respectively.<sup>386</sup> Among these, the **P287** tandem cells exhibited a certified PCE of 8.62% by the National Renewable Energy Laboratory.<sup>59</sup> All tandem cells showed large *V<sub>oc</sub>*s of  $\sim$ 1.6 V, which were equal to the sum of those of the individual front and rear cells. In addition to the high PCEs, the tandem cells showed good device durability. After encapsulation for 30 days, the cells (stored in a glovebox) maintained  $>$ 95% of their original values. Further structural modification afforded a selenophene-containing **P289**. Replacing thiophene with selenophene led to **P289** with a band gap of 1.38 eV, which was smaller than that (1.46 eV) of thiophene-containing analogue **P287**.<sup>387</sup> The smaller band gap and better mobility of **P289** resulted in its improved PCE of 7.2% with a *J<sub>sc</sub>* of 16.8 mA/cm<sup>2</sup>, a *V<sub>oc</sub>* of 0.69 V, and a *FF* of 62% in single-layer cells. In comparison to **P287**, **P289** showed low absorptivity in the visible region (400–650 nm) and high absorptivity in the near-IR (650–900 nm) and UV region (<400 nm), which rendered **P289** as a very promising candidate for tandem cells and visibly transparent cells. **P289** inverted tandem cells showed a PCE of 9.5% with a *J<sub>sc</sub>* of 9.44 mA/cm<sup>2</sup>, a *V<sub>oc</sub>* of 1.52 V, and a *FF* of 66.3%, and the visibly transparent cells exhibited a PCE of 4.5% with a *J<sub>sc</sub>* of 11.5 mA/cm<sup>2</sup>, a *V<sub>oc</sub>* of 0.72 V, and a *FF* of 55%. The improved **P289** performance indicates that selenophene substitution is an effective strategy to enhance OSC performance. The results demonstrate the great success of DPP low-band-gap polymers for high-performance tandem cells.<sup>386,387</sup>

By replacing the alkyl on DPP with triethylene glycol, Yang and co-workers reported a new triple-component random copolymer.<sup>388</sup> The resulting **P290** showed slightly red-shifted absorption in comparison to the parent **P287** (*x* = 1, *y* = 0). **P290** BHJ OSCs having the structure ITO/PEDOT:PSS/**P290:PC<sub>71</sub>BM/Ca/Al** showed a PCE of 7.0%, which was 10% higher than the PCE (6.2%) of the parent polymer **P287**. The performance enhancement was attributed to a more ordered polymer domain and favorable blend film morphology as triethylene glycol was installed on **P290**. As the loading of triethylene glycol-functionalized DPP was further increased, the PCE decreased. For the polymer containing 50% triethylene glycol-functionalized DPP (*x* = 0.5, *y* = 0.5), the solar cells showed a PCE of 3.2%. Performance degradation was attributed to the strong polymer aggregation, which led to detrimental

phase separation. The study showed that solar cell performance can be boosted by introducing stack-inducing agents at precise controlled loadings.

By replacing thiophene with benzene in the polymer backbone, **P246** (Figure 45) shows an enlarged band gap of 1.53 eV and lower lying HOMO of −5.35 eV in comparison to those of **P210** (Figure 42).<sup>389</sup> Under simulated AM1.5G conditions, the optimal **P246**:PC<sub>70</sub>BM cells show a  $J_{sc}$  of 10.3 cm<sup>2</sup>/(V s), a  $V_{oc}$  of 0.80 V, a FF of 65%, and a PCE of 5.5%. The external quantum efficiency (EQE) is over 40% in the range of 440–770 nm. In comparison to **P210**, **P246** shows a greatly enhanced  $V_{oc}$  and increased FF. The improved  $V_{oc}$  is attributed to the lower **P246** HOMO due to the lower electron-donating ability of benzene versus thiophene. The increased FF is likely related to the higher lying **P246** LUMO, which may suppress geminate charge recombination.<sup>111</sup> Janssen and co-workers systematically investigated a series of DPP- and phenylene-containing polymers **P246**, **P291**, and **P292** by varying DPP solubilizing chains.<sup>390</sup> As the chains become larger, the polymers show improved solubilities from **P246** to **P291** and to **P292**. Conventional cells having the structure ITO/PEDOT:PSS/polymer:PC<sub>70</sub>BM/LiF/Al show PCEs of 7.4%, 5.7%, and 3.2% when using **P246**, **P291**, and **P292** as the donor semiconductor, respectively. The performance is in good agreement with the width of polymer fibers in the polymer:PC<sub>70</sub>BM blend. **P246** having the shortest side chains shows the narrowest polymer fiber width of 9 nm in blend film, which leads to efficient exciton dissociation, and hence has the greatest PCE in the series. Heeger and co-worker optimized the device performance of **P291**-based cells. By employing inverted structure, **P291** OSCs having the structure ITO/ZnO/CPE/**P291**:PC<sub>70</sub>BM/MoO<sub>x</sub>/Ag show a PCE of 7.04% with a  $J_{sc}$  of 14.5 mA/cm<sup>2</sup>, a  $V_{oc}$  of 0.78 V, and a FF of 62% under optimized condition, in which CPE is a fluorene-based conjugated polyelectrolyte.<sup>391</sup> The performance of **P291** inverted cells is substantially higher than that of conventional cells,<sup>390</sup> which is mainly attributed to the improved electron transport and interfacial contact between the active layer and the ITO electrode in inverted cells.

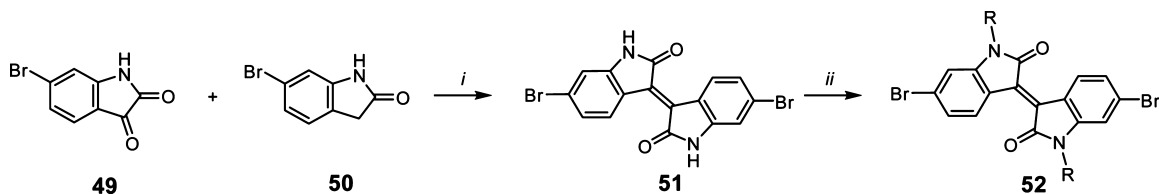
High hole mobility, wide absorption in the UV-vis-NIR region, and appropriate FMOs of naphthalene-containing **P235** (Figure 44) render it a promising donor semiconductor for OSCs. BHJ cells having the structure ITO/PEDOT:PSS/**P235**:PC<sub>71</sub>BM/Al show a PCE of 4.7% with a  $J_{sc}$  of 11.8 mA/cm<sup>2</sup>, a  $V_{oc}$  of 0.76 V, and a FF of 52%.<sup>342</sup> In comparison to  $V_{oc}$ s of other DPP polymers, the **P235**  $V_{oc}$  is quite high due to its low-lying HOMO enabled by incorporation of weak donor, naphthalene. **P293** bearing a biphenyl unit was synthesized and shows a broad band gap of 1.63 eV,<sup>392</sup> which is much larger than those (1.25–1.55 eV) of typical DPP-thiophene derivative copolymers due to the weaker electron-donating character of biphenyl. **P293** conventional cells show a PCE of 5.7% with a  $J_{sc}$  of 11.5 mA/cm<sup>2</sup>, a  $V_{oc}$  of 0.80 V, and a FF of 63%. The high  $V_{oc}$  is in accordance with the **P293** low-lying HOMO (−5.39 eV). The good  $J_{sc}$  and FF are attributed to the high  $\mu_h$  of 0.03 cm<sup>2</sup>/(V s). Fluorine atoms were next introduced to the polymer backbone to afford **P294** and **P295**. In comparison to **P293**, **P294** having fluorine on the 3,3'-position of the biphenyl group exhibits a reduced band gap of 1.59 eV, while **P295** having fluorine on the 2,2'-position has a wider band gap of 1.70 eV due to its high degree of backbone torsion. **P294** BHJ OSCs show a PCE of 3.7% with a  $J_{sc}$  of 6.7 mA/cm<sup>2</sup>, a  $V_{oc}$  of 0.89 V, and a FF of 62%, and **P295** cells exhibit a PCE of 4.1% with a  $J_{sc}$  of 7.7 mA/cm<sup>2</sup>, a  $V_{oc}$  of 0.93 V, and a FF of 56%.<sup>392</sup> Installation of fluorine on

biphenyl increases the  $V_{oc}$ s but decreases  $J_{sc}$ s and FFs for **P294** and **P295** cells, likely related to the degraded charge transport. The **P293** OSC performance is greater than that of a fused biphenyl, i.e., the naphthalene-based polymer **P235**. The results demonstrate that incorporation of a nonplanar biphenyl into the DPP polymer is not necessarily detrimental to solar cell performance.<sup>392</sup>

Janssen and co-workers reported a regular alternating D<sub>1</sub>—A—D<sub>2</sub>—A terpolymer for fine tuning of the polymer FMO levels. **P296** contains DPP acceptor alternating with an electron-rich terthiophene and a thiophene–phenylene–thiophene segment in a regular fashion.<sup>140</sup> It was found that using a slightly decreased palladium catalyst loading and a higher triphenylphosphine to palladium ligand ratio (PPh<sub>3</sub>/Pd of 2:1) can greatly increase the polymer  $M_n$ s because the higher ligand ratio serves to prevent palladium catalyst decomposition. Moreover, addition of DMF to the polymerization media can accelerate the reaction and increase the polymer  $M_n$ . Polymerization under optimal condition affords previously reported **P210** (Figure 42) and **P246** (Figure 45) with much higher  $M_n$ s of 147 and 72 kDa, respectively. The improved  $M_n$ s lead to greatly improved PCEs of 7.1% and 7.4% for **P210** and **P246** OSCs, respectively.<sup>140</sup> The PCEs are substantially higher than their previously reported values,<sup>320,389</sup> which highlights the significance of increasing polymer  $M_n$ s. Under optimized polymerization conditions, **P296** shows a  $M_n$  of 42 kDa with a PDI of 3.68. Optoelectrical characterization reveals that the **P296** optical absorption and electronic structure is better described by the average of the two parent copolymers **P210** and **P246** rather than by their sum. The optical band gap of **P296** is 1.43 eV, which is near the gap for maximum efficiency in OSCs.<sup>88</sup> **P296** OSCs show a superior PCE of 8.0% with a  $J_{sc}$  of 15.9 mA/cm<sup>2</sup>, a  $V_{oc}$  of 0.75 V, and a FF of 67%. Hence, the new terpolymer **P296** outperforms its parent polymers **P210** and **P246**.<sup>140</sup> The study shows the feasibility of combining repeating units of high-performance polymers in a regular fashion to form new terpolymers with fine tailored optoelectronic properties for performance enhancement in OSCs.<sup>140</sup>

Benzene-flanked DPP was incorporated into **P297**, which has a band gap of 1.9 eV with a LUMO/HOMO of −3.5/−5.4 eV.<sup>393</sup> In comparison to the thiophene polymer analogue **P222**, **P297** has a larger band gap, which was attributed to the less electron-rich characteristics of benzene and the greater backbone torsion of **P297**.<sup>366</sup> **P297** BHJ OSCs having the structure ITO/PEDOT:PSS/**P297**:PCBM/LiF/Al show a PCE of 1.67% with a  $J_{sc}$  of 7.8 mA/cm<sup>2</sup> and a  $V_{oc}$  of 0.58 V. The unsatisfactory performance was due to its large band gap and low mobility induced by poor backbone coplanarity.<sup>393</sup> Jo and co-workers designed and synthesized a novel pyridine-capped DPP and bithiophene copolymer **P260** (Figure 45).<sup>367</sup> Pyridine incorporation led to the small **P260** band gap of 1.71 eV and a low-lying HOMO (−5.77 eV) due to its geometry and electron deficiency. BHJ solar cells having the structure ITO/PEDOT:PSS/**P260**:PC<sub>71</sub>BM/Ca/Al showed a promising PCE of 4.88% with a  $J_{sc}$  of 7.96 mA/cm<sup>2</sup>, a  $V_{oc}$  of 0.92 V, and a FF of 65.8%. In comparison to **P297** cell performance, the enhanced **P260** cell performance was attributed to its lower lying HOMO, smaller band gap, and increased hole mobility of **P260** versus those of **P297**,<sup>367</sup> which suggests that the pyridine-capped DPP is a promising building block for high-performance solar cell polymers.

The n-channel transport of DPP polymers indicates their potential for use as acceptor semiconductors in OSCs.<sup>394</sup> Cyclic

Scheme 12. Synthetic Route to the Dibrominated Isoindigo Derivatives<sup>a</sup>

<sup>a</sup>Reagents and conditions: (i) AcOH/HCl, reflux; (ii) RBr, K<sub>2</sub>CO<sub>3</sub>, DMF.

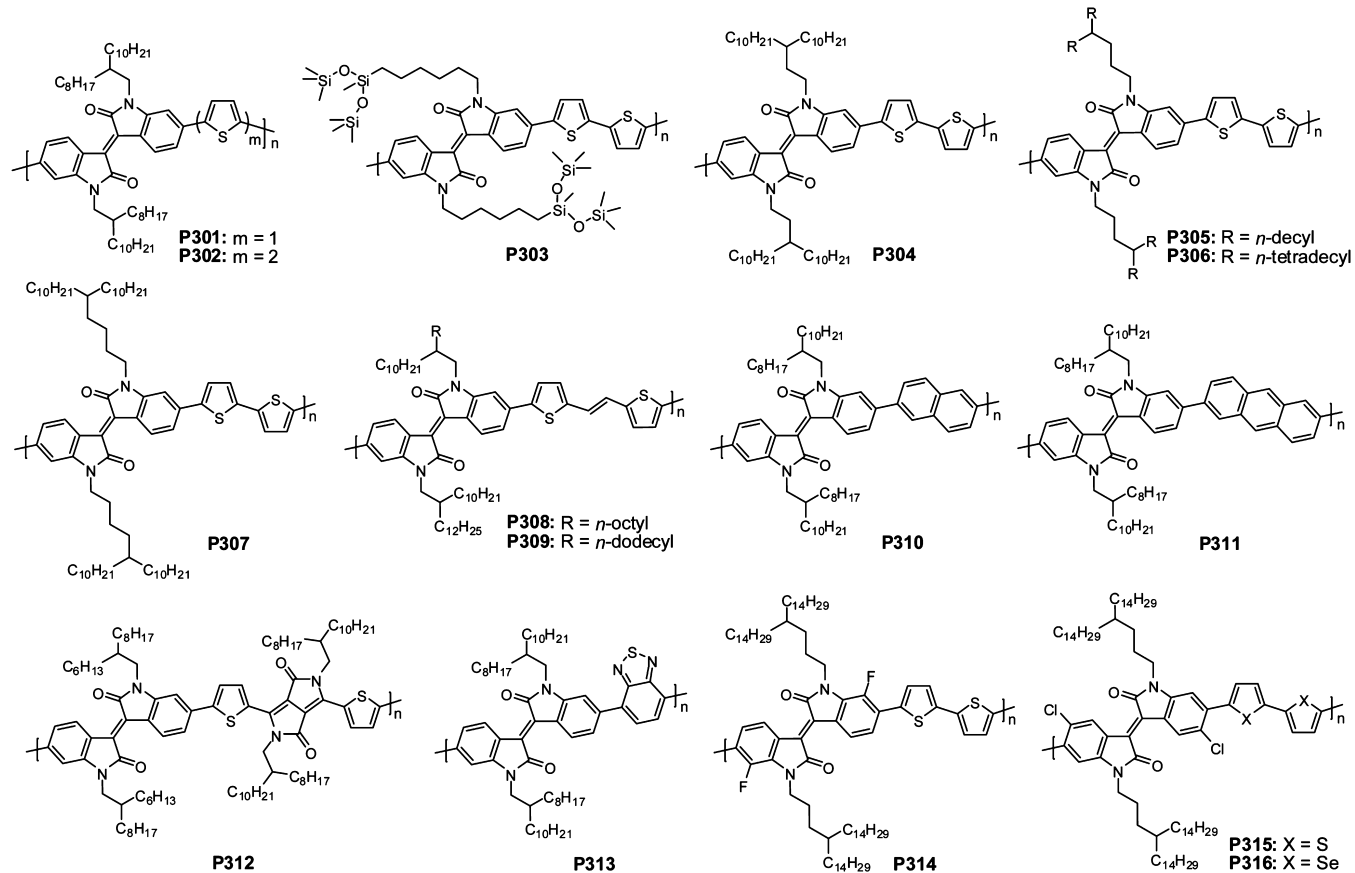


Figure 48. Isoindigo-based polymer semiconductors for OTFTs.

voltammetry shows that P297 has a LUMO of  $-3.5$  eV, which is  $0.4$  eV lower than that of p-type P3HT.<sup>393</sup> The combination of P3HT:P297 shows some degree of photoluminescence quenching, which indicates charge transfer from P3HT to P297.<sup>393</sup> SCLC measurements reveal that P297 has a  $\mu_e$  of  $4.7 \times 10^{-5}$  cm<sup>2</sup>/(V s). BHJ all-polymer cells having the structure ITO/PEDOT:PSS/P3HT:P297/LiF/Al show a moderate PCE of 0.84% with a  $J_{sc}$  of  $2.6$  mA/cm<sup>2</sup> and a  $V_{oc}$  of  $0.92$  V. When combined with PCBM, the P297:PCBM cells show a PCE of 1.67%.<sup>393</sup> The result demonstrates that P297 can be used as either a donor or acceptor semiconductor, depending on the choice of another component, which is in good agreement with its FMOs and ambipolar transport characteristics.<sup>393</sup> Other phenyl-flanked DPP-based polymers P298 and P299 are incorporated into solar cells as acceptor semiconductors.<sup>394</sup> The BHJ OSCs having the structure ITO/PEDOT:PSS/P3HT:P298 (or P299)/Ca/Al exhibit high  $V_{oc}$ s of  $0.9$  V but unsatisfactory PCEs of  $0.11$ – $0.14$ %. The photoinduced absorption spectra indicate limited charge transfer from P3HT to P298 (or P299), which leads to small  $J_{sc}$ s. When thiophene-

flanked DPP and fluorene copolymer P300 is blended with P3HT, the resulting OSCs show a slightly improved PCE of 0.37%.<sup>394</sup> Photoinduced absorption spectra show that free charge carriers recombine to the triplet state, which limits performance. By applying a reverse electric field, the P3HT:P300 photocurrent can be greatly increased due to the suppressed charge recombination. The low electron mobility and inefficient generation of long-lived free charge carriers are the main factors limiting P298–P300 OSC performance. Further performance enhancement may be possibly realized by modifying DPP polymer structures to lower their LUMOs and increase their electron mobilities for their use as acceptor semiconductors in BHJ solar cells.

#### 9.4. Summary

Since the first report of a DPP polymer for OTFTs in 2008, DPP has been one of the most studied acceptor building blocks in organic electronics. DPP polymers usually exhibit substantial charge transport, and the charge carrier polarity can be tuned from p- to ambipolar to n-type by varying the counit in the

polymer backbone. Among them, p-type transport with record hole mobilities  $> 10 \text{ cm}^2/(\text{V s})$  and ambipolar transport with electron and hole mobilities  $> 8$  and  $4 \text{ cm}^2/(\text{V s})$ , respectively, are achieved in OTFTs. These transport characteristics demonstrate that organic polymer semiconductors can achieve mobilities comparable to those of polycrystalline silicon or other inorganic semiconductors. Furthermore, DPP is particularly suitable for constructing all-acceptor polymers, and electron mobilities approaching  $3.0 \text{ cm}^2/(\text{V s})$  have been demonstrated. The promising charge transport characteristics of DPP polymers are attributed to the unique combination of several structural and electronic characteristics in a single entity. The strong electron-withdrawing DPP leads to the resulting polymers with narrow band gaps. When an appropriate donor is chosen, the resultant polymers can achieve fine-tuned band gaps and FMOs. Several DPP polymers have shown promising solar cell performance with PCEs  $> 7\%$ . Further research on DPP polymers should aim at improving OTFT stability and enhancing the power conversion efficiency of OSCs.

## 10. ISOINDIGO-BASED POLYMER SEMICONDUCTORS

Isoindigo, a structural isomer of indigo, was used as a dye in industry a long time ago,<sup>395</sup> and the unique structure of isoindigo imparts several desirable attributes for organic electronics. Since there is a lactam ring in conjunction with an extended  $\pi$  system throughout the bis-oxindole framework, isoindigo should be an excellent acceptor for creating polymer semiconductors due to its strong electron-withdrawing capability, good solubility, and high degree of coplanarity.<sup>222,396</sup> Isoindigo was first introduced by Ciba. Its incorporation into organic semiconductors was pioneered by Reynolds in 2010,<sup>397</sup> and the isoindigo-based small molecules show promising PCEs as donor semiconductors in OSCs. The pioneering work of Reynolds inspires the community to exploit isoindigo (IID) for constructing organic semiconductors, and the resultant materials have advanced the device performance in OTFTs and OSCs.<sup>398</sup>

### 10.1. Synthesis of Dibrominated Isoindigo

The synthetic route to dibrominated isoindigo (IID) is depicted in Scheme 12.<sup>397</sup> Commercial 6-bromoisoindole **49** and 6-bromooxindole **50** are subjected to acid-catalyzed aldol condensation and dehydration in acetic acid under argon to afford 6,6'-dibromoisoindigo **51** in almost quantitative yield. The compound shows limited solubility in organic solvents due to the extended  $\pi$ -core and hydrogen bonding. The subsequent *N*-alkylation affords soluble 6,6'-dibromoisoindigo derivative **52** in good yield under basic conditions using alkyl bromide. Compound **52** possesses sufficient reactivity toward Pd-mediated coupling reactions and hence enables access of a variety of isoindigo-based semiconductors for OTFTs and OSCs.

### 10.2. Isoindigo-Based Polymer Semiconductors for OTFTs

Pei and co-workers synthesized IID copolymers **P301** and **P302** (Figure 48) bearing thiophene and bithiophene donors, respectively, and first investigated their OTFT performance.<sup>172</sup> Introduction of long and branched 2-octyldodecyl groups on IID afforded good solubilities and decent  $M_n$ s of 19.8 and 87.9 kDa for **P301** and **P302**, respectively. The IID electron deficiency lowered the polymer HOMOs to  $-5.8$  and  $-5.7$  eV for **P301** and **P302**, respectively. BGTC OTFTs were fabricated to investigate their charge transport. A  $\mu_h$  of  $0.019 \text{ cm}^2/(\text{V s})$  was obtained for **P301**, which is much lower than that ( $0.79 \text{ cm}^2/(\text{V s})$ ) of **P302**. The higher **P302**  $\mu_h$  was attributed to its greater  $M_n$  and more ordered microstructure. In addition to high mobility, **P302**

OTFTs showed a high  $I_{on}/I_{off}$  ( $10^7$ ) and excellent device air stability, which were ascribed to its low-lying HOMO.

IID and bithiophene copolymer **P303** bearing unconventional siloxane-terminated chains was designed to move the branching point away from the polymer backbone to promote intermolecular  $\pi-\pi$  interactions.<sup>323</sup> The novel hybrid solubilizing side chains lead to a short  $\pi-\pi$  stacking distance of  $3.58 \text{ \AA}$  and result in mixed molecular orientations and larger crystallite coherence length as compared to those of **P302** having common aliphatic side chains. The close **P303** intermolecular interaction slightly elevates its HOMO to  $-5.20$  eV in comparison to that ( $-5.38$  eV) of **P302** as measured by photoelectron spectroscopy. **P303** OTFTs show a  $\mu_h$  of  $2.0 \pm 0.49 \text{ cm}^2/(\text{V s})$  after annealing at  $150^\circ\text{C}$ , which is significantly higher than that of **P302**.<sup>172</sup> GIXRD characterization shows that **P303** adopts both edge-on and face-on orientations relative to the substrate. Such microstructure results in a 3D conduction channel, which can increase charge carrier mobilities.<sup>399</sup> The study shows that the side chains not only are useful to achieve desired materials solubility but also play an important role in controlling intermolecular interactions and supramolecular self-assembly.<sup>363</sup>

Pei and co-workers investigated the influence of the alkyl chain branching position on the hole mobilities of IID and bithiophene copolymers **P304**, **P305**, and **P307**.<sup>373</sup> It was found that moving the branching point away from the backbone led to a noticeable elevation of the polymer HOMOs. The  $\mu_h$ s measured from BGTC OTFTs were  $0.28$ ,  $2.98$ , and  $1.44 \text{ cm}^2/(\text{V s})$  for **P304**, **P305**, and **P307**, respectively. The improved **P305** and **P307**  $\mu_h$ s were ascribed to their closer  $\pi-\pi$  stacking distances of  $3.57 \text{ \AA}$  and more ordered microstructure as revealed by 2D-GIXRD patterns of the polymer films. The results demonstrate that a subtle change of alkyl chains can result in dramatically improved mobility.<sup>122,373</sup> IID and di(thienyl)ethylene copolymers **P308** and **P309** with different IID chains were also synthesized.<sup>400</sup> Thermal annealing of **P309** films at  $230^\circ\text{C}$  led to a pronounced  $\mu_h$  of  $2.20 \text{ cm}^2/(\text{V s})$  in BGTC OTFTs in ambient, while the **P308** OTFTs showed a  $\mu_h$  of  $0.38 \text{ cm}^2/(\text{V s})$ . **P309** having 2-decyldodecyl tethered to the IID unit showed greatly higher  $\mu_h$  than **P308** having a 2-octydecyl chain. The enhanced **P309**  $\mu_h$  was attributed to its high degree of edge-on orientation of polymer backbones and dense crystallite connectivity on the OTS-modified  $\text{SiO}_2/\text{Si}$  substrate.<sup>400</sup>

In comparison to thiophene derivatives, benzene derivatives are less electron rich and more likely to maintain their aromatic character.<sup>110</sup> Naphthalene and anthracene were next incorporated into IID polymers for lowering the HOMOs. **P310** and **P311** were synthesized via Suzuki coupling and had optical band gaps of  $1.80$  and  $1.75$  eV, respectively. The HOMOs measured by photoelectron spectroscopy in air were  $-5.66$  and  $-5.53$  eV for **P310** and **P311**, respectively. **P310** BGTC OTFTs exhibited a  $\mu_h$  of  $0.003 \text{ cm}^2/(\text{V s})$ , and **P311** OTFTs showed an improved  $\mu_h$  of  $0.13 \text{ cm}^2/(\text{V s})$  in air.<sup>401</sup> Their moderate  $\mu_h$ s were due to the substantial hole injection barriers between the electrode Fermi levels and the polymer HOMOs. Additionally, the distortion caused by the steric hindrance between isoindigo and six-membered naphthalene/anthracene units lowered the polymer backbone coplanarity, increased the intermolecular  $\pi-\pi$  stacking distance, decreased film crystallinity, and hence lowered charge carrier mobility.<sup>401</sup>

By copolymerizing IID with various donors, the resulting polymers usually show predominant p-channel performance. For the realization of n-channel or ambipolar transport, IID polymer LUMOs should be further lowered to minimize electron

injection barriers and stabilize injected electrons. IID-based all-acceptor polymers **P146**, **P147**, **P148** (Figure 32), **P312**, and **P313** (Figure 48) containing TPD, the TPD dimer, DPP, and benzothiadiazole (BT) as the counits, respectively, are synthesized via direct (hetero)arylation polymerization or Suzuki–Miyaura coupling.<sup>269,402</sup> Due to the all-acceptor backbone makeup, **P146**, **P147**, **P148**, and **P312** OTFTs exhibit n-channel transport with moderate  $\mu_e$ s of  $2.0 \pm 0.7 \times 10^{-4}$ ,  $0.01$ ,  $2.5 \pm 0.7 \times 10^{-3}$ , and  $1.6 \pm 0.6 \times 10^{-4} \text{ cm}^2/(\text{V s})$ , respectively.<sup>269</sup> A IID–benzothiadiazole acceptor–acceptor polymer is synthesized via Suzuki coupling; the resultant **P313** shows unipolar n-channel operation with a substantial  $\mu_e$  up to  $0.22 \text{ cm}^2/(\text{V s})$  and a high  $I_{\text{on}}/I_{\text{off}}$  of  $10^7$  in BGTC OTFTs.<sup>270</sup> In comparison to **P147**, **P313** shows higher degrees of crystallinity and larger domains with better connectivity, which lead to enhanced **P313** mobility. The result demonstrates the effectiveness of an acceptor–acceptor strategy for designing high-mobility n-type polymers.

Furthermore, 7,7'-fluorinated isoindigo was designed and synthesized to increase core electron affinity.<sup>403</sup> It was found that IID fluorination not only lowered the polymer LUMOs but also greatly affected polymer interchain interactions.<sup>403</sup> The F···H interactions led to a decreased dihedral angle between IID and neighboring thiophene; therefore, introduction of fluorine afforded **P314** with a more planar backbone, in good accordance with its optical absorption features. The LUMO of **P314** was  $-3.88 \text{ eV}$ , which was  $0.18 \text{ eV}$  lower than that of **P306** without fluorine. **P314** TGBC OTFTs with CYTOP dielectric showed a  $\mu_h/\mu_e$  of  $1.41/0.38 \text{ cm}^2/(\text{V s})$  in air after annealing at optimized  $180^\circ\text{C}$ . The mobilities were among the highest for ambipolar OTFTs fabricated and characterized in ambient. The non-fluorinated **P306** showed comparable  $\mu_h$ s but with substantially reduced  $\mu_e$ s of  $10^{-3}$ – $10^{-2} \text{ cm}^2/(\text{V s})$  for OTFTs fabricated in ambient.<sup>403</sup> Hence, IID fluorination substantially improved polymer ambient n-channel performance. Microstructure investigations showed that IID fluorination did not alter polymer lamellar and  $\pi$ – $\pi$  stacking but promoted the fluorinated **P314** to adopt an edge-on orientation with a higher degree of ordering, while **P306** adopted a face-on orientation.<sup>403</sup>

The promising **P314** performance spurred development of other halogenated IID building blocks. Thus, 5,5'-dichloroisooindigo was synthesized, and the resulting polymer **P315** had a slightly smaller band gap of  $1.53 \text{ eV}$  and a lowered LUMO/HOMO of  $-3.86$ – $-5.64 \text{ eV}$  versus **P306**.<sup>404</sup> **P315** TGBC OTFTs showed balanced ambipolar transport with a  $\mu_h/\mu_e$  of  $0.54/0.48 \text{ cm}^2/(\text{V s})$  in air. Therefore, introduction of chlorine increases electron mobility and device stability. The chloroisooindigo polymer **P316** bearing a diselenophene showed a further improved  $\mu_h/\mu_e$  of the  $0.81/0.66 \text{ cm}^2/(\text{V s})$ . 2D-GIXD characterization of polymer films revealed that **P315** adopts both edge-on and face-on orientations, while **P316** only adopts an edge-on orientation.<sup>404</sup> Complementary inverters fabricated from **P315** and **P316** exhibited sharp signal switching with high voltage gains of 46 and 48, respectively. The results showed that chlorination is an effective strategy to modulate polymer properties for performance improvement.<sup>404</sup>

### 10.3. Isoindigo-Based Polymer Semiconductors for OSCs

The small band-gap, lower lying HOMO, and good charge transport of IID polymers support their potential as donor semiconductors for OSCs. By copolymerizing IID with fused benzene derivative donors, fluorene, carbazole, and benzodithiophene, **P317**–**P319** (Figure 49) were synthesized via Stille or Suzuki coupling.<sup>405,406</sup> The polymer films show broad

absorption in the wavelength range from 300 to 800 nm, and the optical band gaps are  $1.79$ ,  $1.67$ , and  $1.54 \text{ eV}$  for **P317**, **P318**, and **P319**, respectively. The narrow band gap of the weak electron-donor carbazole-bearing **P318** indicates the strong IID electron-withdrawing ability and high degree of electron delocalization of IID polymers. OSCs fabricated from **P317**–**P319** show unsatisfactory PCEs of  $0.02$ – $1.91\%$ , which are attributed to the low polymer  $\mu_h$ s and poor polymer:PCBM film quality. When thienyl-substituted benzodithiophene is incorporated into polymers, and the product **P320** has a band gap of  $1.56 \text{ eV}$  and low-lying HOMO of  $-5.71 \text{ eV}$ .<sup>407</sup> In comparison to **P319**, **P320** displays a lower HOMO and better optical absorption with a red-shifted absorption profile and a higher molar extinction coefficient, attributed to the additional conjugation in the thienyl-substituted BDT. OSCs with  $100 \text{ nm}$  **P320**: $\text{PC}_{61}\text{BM}$  cast from chloroform solution exhibit a PCE of  $4.02\%$  with a  $J_{\text{sc}}$  of  $8.55 \text{ mA}/\text{cm}^2$ , a  $V_{\text{oc}}$  of  $0.94 \text{ V}$ , and a  $FF$  of  $50\%$ . It is remarkable that polymer having a  $1.50 \text{ eV}$  band gap can achieve a high  $V_{\text{oc}}$  of  $0.94 \text{ eV}$ , which reaches the limit of the theoretical value according to the empirical formula  $eV_{\text{oc}} = E_g - 0.6 \text{ eV}$ .<sup>408</sup> The result indicates that the IID polymer LUMO is sufficiently low to minimize  $V_{\text{oc}}$  loss during exciton dissociation.

When thiophene bridges are incorporated into IID and benzodithiophene copolymers, the resulting **P321** shows greatly improved performance in comparison to **P319**. The highest PCE of  $4.22\%$  with a  $J_{\text{sc}}$  of  $7.87 \text{ mA}/\text{cm}^2$ , a  $V_{\text{oc}}$  of  $0.79 \text{ V}$ , and a  $FF$  of  $68\%$  is obtained from **P321**: $\text{PC}_{61}\text{BM}$  cells.<sup>409</sup> In contrast, **P322** containing a 3-octylthiophene bridge shows inferior performance with a PCE of  $1.39\%$ . The degraded performance of **P322** with an alkylated thiophene is attributed to its higher degree of backbone torsion as revealed by UV-vis absorption spectra and DFT computations.<sup>409</sup> Structural modifications via side-chain tuning lead to **P323** and **P324**.<sup>410</sup> Introduction of a methyl on the thiophene bridge would be expected to give a slightly twisted backbone, which should thus increase  $V_{\text{oc}}$ .<sup>62,303</sup> Meanwhile, a beneficial intermolecular stacking might be retained, which will not hinder charge transport. **P323** OSCs having the structure ITO/PEDOT:PSS/**P323**: $\text{PC}_{71}\text{BM}/\text{LiF}/\text{Al}$  show a PCE of  $4.98\%$  with a  $J_{\text{sc}}$  of  $10.70 \text{ mA}/\text{cm}^2$ , a  $V_{\text{oc}}$  of  $0.73 \text{ V}$ , and a  $FF$  of  $64\%$ . In comparison to **P321** and **P322**, **P323** shows improved PCE, which indicates that methyl introduction is an effective strategy to improve solar cell performance. **P324** bearing alkylated benzodithiophene shows a PCE of  $5.36\%$  with a  $J_{\text{sc}}$  of  $10.20 \text{ mA}/\text{cm}^2$ , a  $V_{\text{oc}}$  of  $0.80 \text{ V}$ , and a  $FF$  of  $65\%$  when blended with  $\text{PC}_{61}\text{BM}$ .<sup>410</sup> In comparison to **P323**, **P324** shows a greater  $V_{\text{oc}}$  due to the less electron-donating tendency of the alkyl in **P324** versus the alkoxy in **P323** on benzodithiophene. Thiophene was next introduced between the IID and thienyl-substituted benzodithiophene to afford **P325**. The **P325** cells having the structure ITO/PEDT:PSS/**P325**: $\text{PC}_{71}\text{BM}/\text{Ca}/\text{Al}$  exhibit a PCE of  $4.76\%$  with a  $J_{\text{sc}}$  of  $8.95 \text{ mA}/\text{cm}^2$ , a  $V_{\text{oc}}$  of  $0.88 \text{ V}$ , and a  $FF$  of  $60\%$ . In comparison to the **P320** cell, introduction of a thiophene bridge slightly improves **P325** performance.<sup>411</sup> Fluorinated IID has shown great effectiveness in lowering polymer FMOs and promoting OTFT mobility.<sup>403</sup> Replacement of IID with fluorinated IID affords **P326**, which has a smaller band gap ( $1.58 \text{ eV}$ ) and a lower lying HOMO ( $-5.64 \text{ eV}$ ) than **P325**.<sup>411</sup> The **P326**: $\text{PC}_{71}\text{BM}$  cells show a PCE of  $5.52\%$  with a  $J_{\text{sc}}$  of  $9.62 \text{ mA}/\text{cm}^2$ , a  $V_{\text{oc}}$  of  $0.94 \text{ V}$ , and a  $FF$  of  $61\%$ . When incorporated into inverted cells having the structure ITO/ZnO/PNFB<sub>x</sub>/P326: $\text{PC}_{71}\text{BM}/\text{MoO}_3/\text{Ag}$ , the resultant OSCs show a greatly improved PCE of  $7.04\%$  with a  $J_{\text{sc}}$  of  $11.30 \text{ mA}/\text{cm}^2$ , a  $V_{\text{oc}}$  of  $0.92 \text{ V}$ , and a  $FF$  of  $68\%$ .<sup>411</sup> The promising PCE of **P326** cells

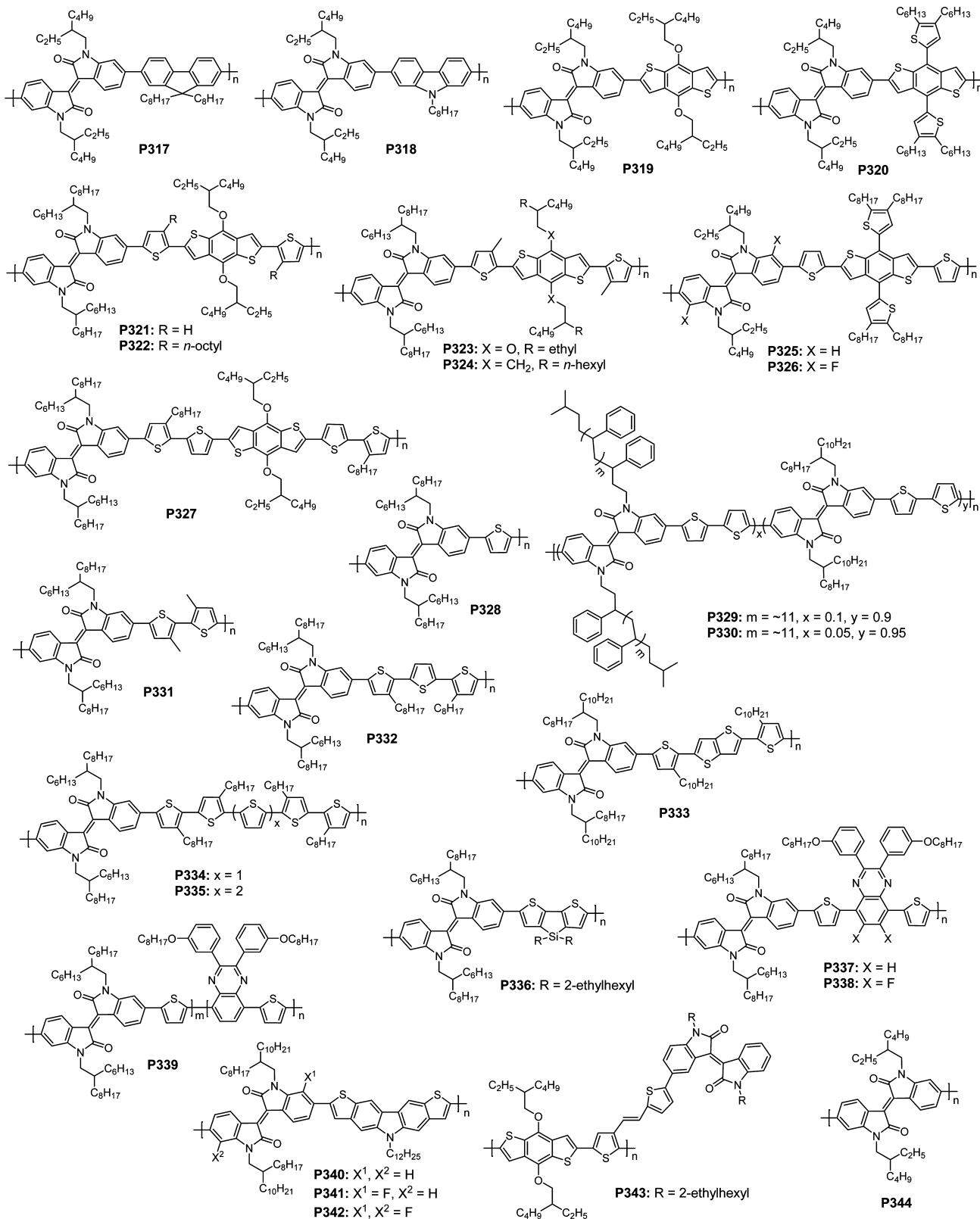


**Figure 49.** Isoindigo-based polymer semiconductors for organic solar cells.

indicates that fluorinated IID is an attractive acceptor for solar cell polymers. By introducing a bithiophene spacer, Wang prepared polymer P327.<sup>412</sup> The fabricated BHJ OSCs showed a PCE of 7.31% with a  $V_{oc}$  of 0.72 V, a  $J_{sc}$  of 14.96 mA/cm<sup>2</sup>, and a FF of 68%. The P327 performance is greater than that of

polymers without thiophene or with monothiophene or terthiophene as the result of efficient charge formation, transport, and collection. These studies demonstrate the significance of using an optimal thiophene number as the spacer to enhance performance.

The performance of carbazole-, benzodithiophene-, or fluorene-containing IID polymers is mainly limited by their low mobilities. Oligothiophenes are known to be excellent donors for constructing high-mobility polymers.<sup>172,241</sup> Andersson et al. developed an IID and monothiophene copolymer **P328** (Figure 49), which is easily synthesized via three steps in an excellent overall yield of 68%.<sup>413</sup> **P328** has a band gap of 1.6 eV and a low-lying HOMO of -5.85 eV. **P328** OSCs having the structure glass/ITO/PEDOT:PSS/**P328**:PC<sub>71</sub>BM/LiF/Al show a PCE of 3% with a high  $V_{oc}$  of 0.89 V, a  $J_{sc}$  of 5.4 mA/cm<sup>2</sup>, and a FF of 63% when the active layer is processed from *o*-dichlorobenzene containing 2.5 wt % DIO.<sup>413</sup> The high-mobility IID and bithiophene copolymers **P302** and **P303** (Figure 48) are then blended with PCBM.<sup>414</sup> Without a processing additive, only moderate PCEs of 0.5% and 1.6% are obtained for the **P302**:PC<sub>71</sub>BM and **P303**:PC<sub>71</sub>BM cells, respectively. The enhanced **P303** performance is due to its higher fraction of polymer crystallites assuming face-on orientation. Incorporation of the processing additive DIO into the blend solution from which the active layers are spin cast leads to improved PCEs of 5.2% and 3.4% for **P302** and **P303** cells, respectively. The performance enhancement is larger for the **P302** cells due to the dramatically reduced domain size and reorientation of the polymer crystallites to a largely face-on arrangement. The lower PCE of siloxy-terminated **P303** is traced to the large-scale aggregation induced by the closer polymer backbones and therefore increased self-interaction.<sup>414</sup>

Bao et al. synthesized a novel IID random polymer **P329** incorporating polystyrene side chains via random polymerization.<sup>173</sup> In comparison to **P302**, **P329** showed improved materials processability without affecting the polymer optoelectronic properties when the molar percentage ( $x$ ) of polystyrene-containing repeating units was  $\leq 0.1$ . **P329** OSCs showed a PCE of 7% with a  $V_{oc}$  of 0.96 V, which was greater than the PCE (6.5%) of **P302** cells fabricated under optimized condition. The **P329** performance enhancement was attributed to its higher molecular weight ( $M_n = 341$  kDa) and better solubility. Incorporation of polystyrene also led to improved synthetic batch-to-batch reproducibility, which should result in reduced performance variation. As the polystyrene loading increases, the **P329** analogues having  $x = 0.33$  or 1 showed degraded PCEs due to the lower absorption coefficients, limited exciton dissociation, and poor charge transport.<sup>173</sup> Incorporation of polystyrene side chains offers a new approach to achieve enhanced polymer solubility without sacrificing the polymer optoelectrical properties and device performance.

The IID and 3,3'-dimethylbithiophene copolymer **P331** shows a red-shifted absorption and smaller band gap than IID and bithiophene copolymer **P302**.<sup>172,323,410</sup> The results indicate that introduction of head–head linkages into the polymer backbone does not necessarily lead to a higher degree of backbone torsion.<sup>415–417</sup> However, the **P331** cells show an unsatisfactory PCE of 1.64%, which is attributed to the low polymer  $\mu_h$  of  $7.4 \times 10^{-5}$  cm<sup>2</sup>/(V s) as measured by SCLC, and suboptimal phase segregation with large and poorly defined domains.<sup>410</sup> When high-mobility IID and thienylenevinylene copolymer **P309** is incorporated into OSCs, they exhibit a PCE of 7.09% with a  $J_{sc}$  of 13.2 cm<sup>2</sup>/(V s), a  $V_{oc}$  of 0.91 V, and a FF of 59%.<sup>418</sup> It is remarkable that a low-band-gap **P309** (1.61 eV) can achieve such a high  $V_{oc}$  (0.91 eV), which indicates its excellent FMO alignments. In comparison to that of bithiophene polymer **P302**, the enhanced **P309** performance is attributed to the more

efficient absorption in the high-energy region and the greater mobility due its more planar conformation.

By further modifying the polymer structure, Andersson and Wang reported an IID polymer with PCE approaching 7% in BHJ OSCs.<sup>419,420</sup> Terthiophene was copolymerized with IID, and the resultant **P332** (Figure 49) showed broad absorption in the visible region with a band gap of 1.50 eV, which was close to the ideal value for OSCs. Optimal device performance was obtained from OSCs having the structure ITO/PEDOT:PSS/**P332**:PC<sub>71</sub>BM/LiF/Al. Cells containing a 90 nm **P332**:PC<sub>71</sub>BM (1:1.5) layer showed a PCE of 6.3% with a  $J_{sc}$  of 13.1 mA/cm<sup>2</sup>, a  $V_{oc}$  of 0.70 V, and a decent FF of 69%. The PCE was among the highest for a polymer having a band gap as low as 1.5 eV.<sup>419</sup> As the **P332**  $M_n$  was increased from 43 to 100 kDa, the **P332**:PC<sub>71</sub>BM cells showed an increased PCE of 6.9%.<sup>420</sup> By incorporating IID into the highly crystalline polymer PBT<sub>TT</sub>,<sup>47</sup> Ong reported a new polymer **P333**.<sup>421</sup> Incorporation of IID greatly reduced the band gap to 1.49 eV and lowered the HOMO to -5.34 eV. OSCs having the structure ITO/PEDOT:PSS (40 nm)/**P333**:PC<sub>71</sub>BM (85 nm)/PCP-EP (4 nm)/Al (100 nm) were used to investigate the photovoltaic performance in which an alcohol-soluble conjugated polymer PCP-EP was used as the interlayer between the active layer and the cathode. An optimal PCE of 4.69% with a  $J_{sc}$  of 9.34 mA/cm<sup>2</sup>, a  $V_{oc}$  of 0.77, and a FF of 65.2% was obtained from **P333**:PC<sub>71</sub>BM (1/1.5; w/w) cells. The good FF was attributed to the high  $\mu_h$  of  $1.9 \times 10^{-4}$  cm<sup>2</sup>/(V s) measured by SCLC from a hole-only device. Further increasing the thiophene numbers in the oligothiophene donors afforded **P334** and **P335**, and the resultant BHJ cells showed PCEs of 5.26% and 4.65% for **P334** and **P335**, respectively. In comparison to **P332**, **P334** and **P335** exhibited smaller  $V_{oc}$ s of ~0.65 V due to their higher lying HOMOs and smaller  $J_{sc}$ s traced to their coarse film morphology with large polymer domains in the blends.<sup>420</sup>

As an excellent building block for constructing high-performance polymers,<sup>55,105</sup> dithienosilole was incorporated into **P336**, which exhibited promising characteristics such as a narrow band gap of 1.54 eV and low-lying LUMO/HOMO of -3.95/-5.55 eV.<sup>422</sup> **P336** conventional cells showed a PCE of 2.62% with a  $J_{sc}$  of 8.26 mA/cm<sup>2</sup>, a  $V_{oc}$  of 0.76 V, and a FF of 42%. Under the same processing conditions, **P336** inverted cells achieved an improved PCE of 4.01% with a  $J_{sc}$  of 10.49 mA/cm<sup>2</sup>, a  $V_{oc}$  of 0.77 V, and a FF of 50%. Performance enhancement in inverted cells was likely attributed to the improved charge extraction at electrodes enabled by the favored vertical phase gradation in the BJH film.<sup>62,79,80</sup>

Andersson et al. reported two new alternating donor–acceptor (D–A<sub>1</sub>–D–A<sub>2</sub>) copolymers **P337** and **P338** (Figure 49) containing IID and quinoxaline acceptors and investigated the effects of quinoxaline fluorination on device performance.<sup>423</sup> Fluorination of quinoxaline caused a slightly blue-shifted absorption for **P338** in comparison to that of **P337**. The HOMO of **P338** was 0.1 eV lower than that of **P337**. **P337** BHJ OSCs with the structure ITO/PEDOT:PSS/**P337**:PC<sub>61</sub>BM/Ca/Al showed a PCE of 4.82% with a  $J_{sc}$  of 11.40 mA/cm<sup>2</sup>, a  $V_{oc}$  of 0.82 V, and a FF of 52%. **P338** cells exhibited a PCE of 6.32% with a  $J_{sc}$  of 12.58 mA/cm<sup>2</sup>, a  $V_{oc}$  of 0.93 V, and a FF of 54%. In comparison to **P337**, the improved **P338** performance was attributed to the greater  $V_{oc}$  associated with the lower lying HOMO and improved **P338**:PC<sub>61</sub>BM film morphology.<sup>423</sup> Regiorandom **P339** was synthesized, and the resulting **P339**:PC<sub>61</sub>BM cells showed a lower PCE of 4.37% in comparison to that (4.82%) of alternating copolymer **P337**,<sup>424</sup> each of which

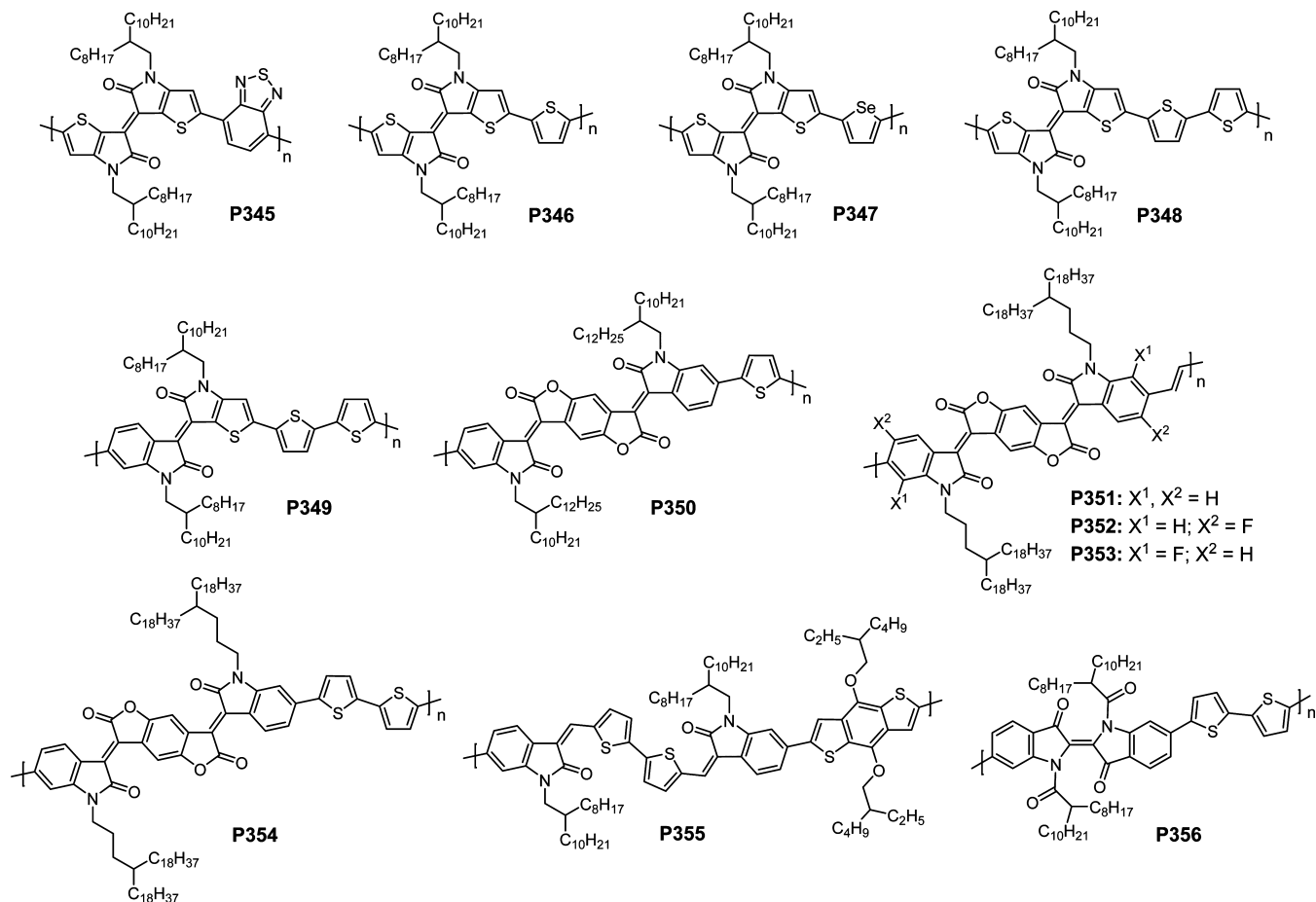


**Figure 50.** Isoindigo derivatives-based polymer semiconductors for OTFTs and OSCs.

contains the same amount of an electron-rich moiety and two electron-deficient chromophores. The lower performance of the regiorandom P337 was likely due to its unfavorable  $\pi$ - $\pi$  stacking of the polymer backbone, which may limit charge transport.<sup>424</sup>

Geng et al. synthesized a series of IID polymers P340–P342 (Figure 49) containing the novel dithieno[3,2-*b*;6,7-*b*]carbazole donor.<sup>141</sup> IID was functionalized with a different number of fluorine atoms ( $n = 0$ –2) for fine tuning polymer FMOs. P340, P341, and P342 had  $M_n$ s of 40, 85, and 108 kDa, respectively, as measured by GPC at 150 °C; hence, the fluorinated IID favors polymerization. The band gaps derived from absorption onsets were 1.61, 1.59, and 1.59 eV for P340, P341, and P342, respectively.<sup>141</sup> Fluorine incorporation on IID gradually lowers the polymer FMOs; the LUMO/HOMOs derived from cyclic voltammetry are –3.54/–5.22, –3.67/–5.30, and –3.74/–5.36 eV for P340, P341, and P342, respectively. Film characterization revealed their amorphous characteristics, however all P340–P342 showed highly promising and comparable PCEs of 7.1–7.2% in conventional OSCs.<sup>141</sup> As expected, the  $V_{oc}$ s were decreased from 0.86 V for P342 cells, to 0.82 V for P341 cells, and to 0.79 V for P340 cells, but P340 cells showed the highest  $J_{sc}$  of 14.6 mA/cm<sup>2</sup> as compared to those (12.6 and 12.3 mA/cm<sup>2</sup>) of the P341 and P342 cells, respectively. The lower  $J_{sc}$ s of P341 and P342 cells were attributed to the lower contribution of PC<sub>71</sub>BM absorption as revealed by the EQE spectra. Device optimization by employing the inverted structure ITO/ZnO/polymer:PC<sub>71</sub>BM/MoO<sub>3</sub>/Al led to improved performance with PCEs of 8.2%, 7.9%, and 7.6% for P340, P341, and P342 cells, respectively.<sup>141</sup> Performance enhancement is mainly the result of

the improved FFs attributed to more efficient charge collection and lower degrees of charge recombination in inverted cells.<sup>62,80</sup>

The novel benzodithiophene-based P343 (Figure 49) having an all-donor backbone makeup but containing an isoindigo acceptor as the side chains was synthesized.<sup>425</sup> Attachment of IID to the polymer backbone via a 2-vinylthiophenyl linkage led to a smaller band gap (1.83 eV) and enhanced optical absorption in the red region in comparison to those of the polymer counterpart without IID side chains.<sup>426</sup> The P343:PC<sub>61</sub>BM conventional cells exhibited an optimal PCE of 5.25% with a  $J_{sc}$  of 12.65 mA/cm<sup>2</sup>, a  $V_{oc}$  of 0.80 V, and a FF of 52%, which was substantially higher than the PCE of 1.60% from the polymer counterpart without the IID-2-vinylthiophenyl substituent. Inverted cells showed a further improved PCE of 6.51% with a  $J_{sc}$  of 15.07 mA/cm<sup>2</sup>, a  $V_{oc}$  of 0.82 V, and a FF of 53%. It is remarkable that a polymer having a 1.83 eV band gap can achieve a  $J_{sc} > 15$  mA/cm<sup>2</sup>, which is likely attributed to the high P343  $\mu_h$  ( $2.5 \times 10^{-3}$  cm<sup>2</sup>/(V s)). The results indicate that polymer backbone functionalization with IID-containing side chains is an effective strategy for performance improvement.

In addition to functioning as donor semiconductors, IID polymers can be used as acceptor semiconductors in all-polymer solar cells. Thus the IID homopolymer P344 was synthesized via Suzuki polycondensation, and showed broad absorption throughout the visible spectrum with an optical band gap of 1.70 eV.<sup>427</sup> The LUMO derived from electrochemistry was –3.84 eV, and the P344 spectroelectrochemistry showed stable negative charge generation, which indicated its n-type character. All-polymer cells using a P3HT:P344 active layer showed a PCE

of 0.47% with a  $J_{sc}$  of 1.91 mA/cm<sup>2</sup>, a  $V_{oc}$  of 0.62 V, and a  $FF$  of 41%. The performance was limited by the coarse phase segregation of hundreds of nanometers. The preliminary solar cell results were encouraging; more extensive morphology control should greatly reduce the current scale of phase-segregated regions to 10–20 nm scale.

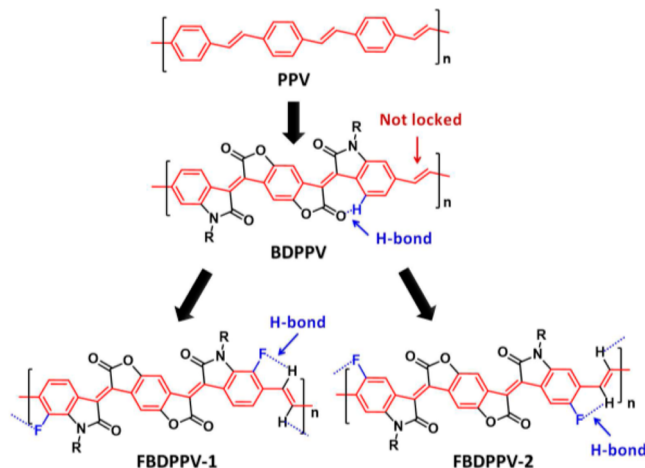
#### 10.4. Isoindigo Derivatives-Based Polymer Semiconductors for OTFTs and OSCs

The promising device performance of IID polymers has encouraged their structural modifications for the performance enhancement. McCulloch et al. reported an approach to replace the outer phenyl of IID with thiophene to afford a new acceptor, thienoisoindigo.<sup>428</sup> The thienoisoindigo geometry should lead to reduced steric demands in comparison to isoindigo. By copolymerizing it with benzothiadiazole, the new all-acceptor P345 (Figure 50) was synthesized and showed an ultralow band gap of 0.92 eV, which indicated a high degree of backbone coplanarity. P345 TGBC OTFTs showed pronounced ambipolarity with a balanced  $\mu_e/\mu_h$  of 0.14/0.16 cm<sup>2</sup>/(V s). The good P345 charge transport was attributed to the well-delocalized HOMO and LUMO electron density and a high degree of crystallinity with a close  $\pi-\pi$  stacking distance (3.6 Å) in P345 films.<sup>428</sup> By copolymerizing thienoisoindigo with thiophene and selenophene derivatives, Yang reported a series of thienoisoindigo polymers P346–P348, which showed narrow band gaps of 0.91, 0.89, and 0.97 eV for P346, P347, and P348, respectively. The low band gaps of P346–P348 were attributed to the strong electron-accepting capability of thienoisoindigo and high degree of polymer backbone coplanarity promoted by the sulfur–oxygen contacts.<sup>429</sup> BGTC OTFTs using Au source/drain were fabricated; P346, P347, and P348 showed unipolar p-channel transport with  $\mu_{hs}$  of 0.15, 0.059, and 0.16 cm<sup>2</sup>/(V s), respectively. When using Al source/drain, P346, P347, and P348 showed ambipolarity with  $\mu_e/\mu_{hs}$  of 0.015/0.12, 0.0082/0.043, and 0.006/0.16 cm<sup>2</sup>/(V s), respectively.<sup>429</sup> The results indicate the potential of thienoisoindigo for enabling high-mobility polymers.

Substituting one benzene of IID with a thiophene in P348 affords P349, which shows a broader band gap (1.37 eV) than that (1.12 eV) of P348 due to reduced backbone coplanarity.<sup>430</sup> P349 BGTC OTFTs show p-channel transport with a  $\mu_h$  of  $4.7 \times 10^{-2}$  cm<sup>2</sup>/(V s), while isoindigo polymer P302 (Figure 48) and thienoisoindigo polymer P348 OTFTs show greater  $\mu_{hs}$  of 0.46 and 0.29 cm<sup>2</sup>/(V s) under optimized conditions, respectively. Therefore, the mobilities here do not correlate with polymer backbone coplanarity. The regiorandom P349 shows lower  $\mu_h$  than the regiosymmetric P302 and P348. Hence, it appears that regiosymmetry rather than backbone coplanarity plays a more significant role in promoting polymer charge carrier mobilities. P349 cells having the structure ITO/PEDOT:PSS/polymer:PC<sub>7.1</sub>BM/LiF/Al were fabricated and show a PCE of 3.2% with a  $J_{sc}$  of 10.40 mA/cm<sup>2</sup>, a  $V_{oc}$  of 0.54 V, and a  $FF$  of 57%, while P302 and P348 cells show much lower PCEs of 1.6% and 0.4%, respectively. The improved P349 cell performance could be attributed to its greater degree of  $\pi$ -face-on orientation of the polymer.<sup>430</sup> These results indicate that the IID derivative having one thiophene substituted by benzene could be a more promising building block for constructing polymers for solar cells than IID and thienoisoindigo.

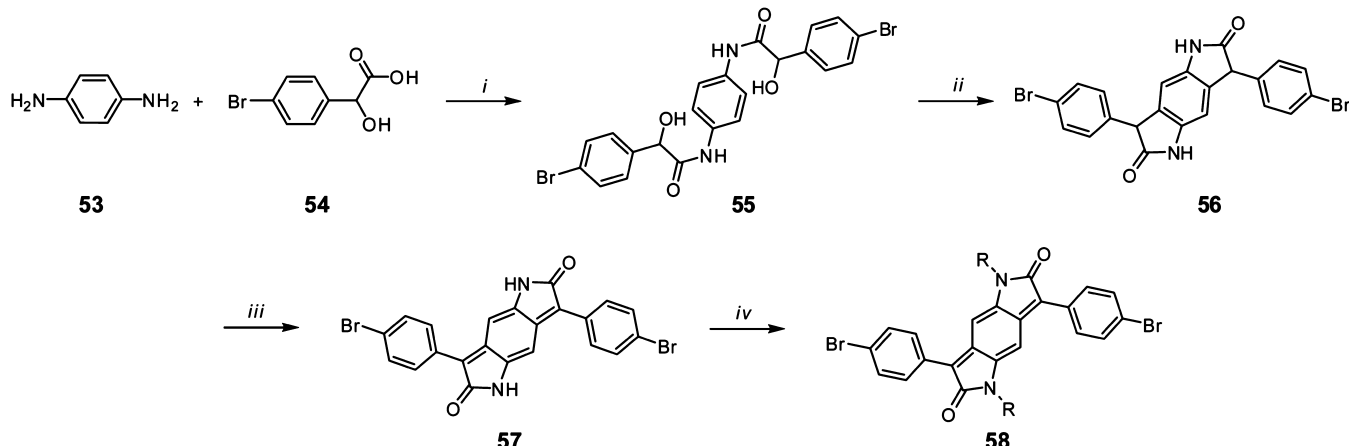
Li reported 3,7-bis(2-oxoindolin-3-ylidene)benzo[1,2-*b*:4,5-*b'*]difuran-2,6(3H,7H)-dione (IBDF) as a new acceptor for the synthesis of the donor–acceptor polymer P350 (Figure 50).<sup>431</sup>

The IBDF is a large fused aromatic arene with an electron-deficient lactone in the central core coupled with lactams on the outer oxoindoline. DFT computations reveal that IBDF is more electron deficient than DPP and IID. The IBDF and thiophene copolymer P350 has a narrow band gap of 1.36 eV with a low-lying LUMO/HOMO of −4.11/−5.79 eV. P350 BGBC OTFTs show unipolar n-type transport with a  $\mu_e$  of  $5.4 \times 10^{-3}$  cm<sup>2</sup>/(V s) in air when the device is encapsulated with PMMA. Without PMMA encapsulation, P350 BGBC OTFTs show ambipolarity with a  $\mu_h/\mu_e$  of  $1.0 \times 10^{-2}/8.2 \times 10^{-3}$  cm<sup>2</sup>/(V s) in ambient. The transition mechanism from n-type to ambipolarity when the unencapsulated device is exposed to air is not understood.<sup>431</sup> Pei and co-workers synthesized IBDF-based polymer P351 with engineered side chains. The polymer has a poly(*p*-phenylenevinylene)-like backbone and shows a small band gap of 1.42 eV with a low-lying LUMO of −4.10 eV.<sup>432</sup> The narrow band gap is attributed to a high degree of polymer backbone coplanarity promoted by extensive intramolecular hydrogen bonding and conformation locking (Figure 51). P351 TGBC OTFTs using a



**Figure 51.** Design strategy for “conformation-locked” PPV-based conjugated polymers via intramolecular hydrogen bond, P351 (BDPPV), P353 (FBDPPV-1), and P352 (FBDPPV-2). Reprinted with permission from ref 137. Copyright 2014 American Chemical Society.

CYTOP dielectric show a high  $\mu_e$  of 1.1 cm<sup>2</sup>/(V s) in ambient with good device stability. The high  $\mu_e$  is attributed to the low-lying LUMO and good lamellar edge-on packing with a close  $\pi-\pi$  stacking (3.55 Å) of P351.<sup>432</sup> The P351 mobility is 4 orders of magnitude higher than those of typical poly(*p*-phenylenevinylene)s, which is traced to the locked backbone conformation and low-lying LUMO of P351.<sup>432</sup> Using the centrosymmetric bithiophene donor and 4-octadecyldocosyl as the solubilizing chain, the same group synthesized P354, which has a band gap of 1.31 eV and a low-lying HOMO/LUMO of −5.66/−4.35 eV estimated from photoelectron spectroscopy and the optical band gap.<sup>433</sup> P354 TGBC OTFTs show clear n-type transport with a high  $\mu_e$  of 1.74 cm<sup>2</sup>/(V s) when the devices are fabricated in a glovebox and characterized in ambient. The high P354  $\mu_e$  is attributed to the high degree of crystallinity with a close  $\pi-\pi$  stacking distance (3.55 Å) in the polymer film. When P354 OTFTs are fabricated and characterized in ambient, a  $\mu_h$  up to 0.47 cm<sup>2</sup>/(V s) is obtained with a slightly decreased  $\mu_e$  of 1.45 cm<sup>2</sup>/(V s). The enhanced  $\mu_h$  for the OTFTs fabricated in ambient is mainly attributed to oxygen doping of the polymer film. The results demonstrate the great potential of the isoindigo

Scheme 13. Synthetic Route to the Dibrominated Phenyl-Flanked Benzodipyrrolidone<sup>a</sup>

<sup>a</sup>Reagents and conditions: (i) chlorobenzene, reflux; (ii)  $\text{H}_2\text{SO}_4$ , room temperature; (iii)  $\text{K}_2\text{S}_2\text{O}_8$ ,  $\text{NaOH}$  (aq),  $\text{EtOH}$ ; (iv)  $\text{RI}$  (or  $\text{RBr}$ ),  $t\text{-BuOK}$ ,  $\text{DMF}$ ,  $80^\circ\text{C}$ .

derivative, IBDF, for constructing high-mobility n-type polymers.<sup>433</sup>

By introducing fluorine atoms on IBDF, Pei et al. synthesized two new polymers P352 and P353 via microwave-assisted Stille coupling.<sup>137</sup> In comparison to the LUMO ( $-4.1\text{ eV}$ ) of P351, IBDF fluorination effectively lowers the LUMOs of P352 and P353 to  $\sim -4.3\text{ eV}$ , which are among the lowest for polymer semiconductors. It was found that fluorination not only enables the low-lying LUMO but also greatly promotes polymer packing. The P352 and P353 backbones are fully locked due to the intramolecular hydrogen bond enabled by the carbonyl group and the fluorine atom, while only two-thirds of the P351 backbone is locked by a carbonyl-induced hydrogen bond (Figure S1). P352 and P353 show a close interchain  $\pi-\pi$  stacking of  $3.42\text{ \AA}$ , which is smaller than that ( $3.45\text{ \AA}$ ) of P351. P352 and P353 TGBC OTFTs showed typical n-channel performance with the highest  $\mu_{\text{e}}$ s of  $0.81$  and  $1.70\text{ cm}^2/(\text{V s})$  in ambient, respectively. The  $\mu_{\text{e}}$  of P353 is greater than that ( $1.10\text{ cm}^2/(\text{V s})$ ) of P351.<sup>137,432</sup> In comparison to P351 and P353, P352 showed lower performance, which was attributed to its different molecular conformation and supramolecular organization, but further investigations are desired to explore the origin of the performance differences.<sup>137</sup> OTFT stability studies showed that fluorinated IBDF polymers P352 and P353 have significantly enhanced air stability versus nonfluorinated polymer P351 after storage in air for 30 days. The electron mobility and device stability of P353 are among the highest for n-type polymers.<sup>136,137</sup>

Another expanded isoindigo unit was synthesized and incorporated into polymers to afford P355.<sup>434</sup> This isoindigo derivative featuring a divinylbithiophene conjugated bridge was designed to avoid the steric repulsion between the protons on the phenyls and the carbonyl oxygens on the oxindoles in isoindigo. The new monomer and the resulting polymer were expected to achieve a high degree of coplanarity enabled by the intramolecular interaction between the carbonyl oxygen of the oxindole and the sulfur of thiophene. P355 showed a  $M_n$  of  $43.5\text{ kDa}$  with good solubilities in organic solvents. The optical band gap of P355 was  $1.71\text{ eV}$ , which is larger than that ( $1.54\text{ eV}$ ) of isoindigo polymer homologue P319.<sup>405</sup> BHJ solar cells with the structure ITO/ZnO/P355:PC<sub>61</sub>BM/MoO<sub>3</sub>/Ag achieved an optimized PCE of  $6.41\%$  with a  $J_{\text{sc}}$  of  $11.71\text{ mA/cm}^2$ , a  $V_{\text{oc}}$  of

$0.77\text{ V}$ , and a  $FF$  of  $71\%$ . The result shows versatility of oxindole as a basic building block for constructing expanded isoindigo derivatives.

Indigo, an excellent organic semiconductor for OTFTs,<sup>435</sup> was first incorporated into polymers by Li and co-workers.<sup>436</sup> Unlike isoindigo, indigo does not have a lactam structure. Indigo alkylation on nitrogen using alkyl bromide was troublesome, and only led to the monoalkylated product. However, indigo acylation was readily accomplished, which resulted in the acylated indigo with amide functionalities. The indigo and bithiophene copolymer P356 was synthesized under Stille coupling. In comparison to the isoindigo polymer P302, P356 shows greatly blue-shifted absorption and an enlarged band gap, which were mainly attributed to the significant backbone distortion induced by acylation because the acyls are very close to the carbonyls of neighboring indol-3-ones. The backbone torsion led to limited film crystallinity, which resulted in a low  $\mu_{\text{e}}$  of  $1.1 \times 10^{-3}\text{ cm}^2/(\text{V s})$  for P356 TGBC OTFTs. In comparison to hole-dominant P302, P356 shows electron-dominating performance due to the low-lying P356 LUMO/HOMO of  $-4.02/-5.78\text{ eV}$  enabled by the highly electron-deficient indigo and the additional electron-withdrawing acyl on nitrogen.

## 10.5. Summary

Isoindigo is an emerging building block for organic electronics and it can be readily synthesized in high yields. Its incorporation into polymers leads to a class of semiconductors which exhibit a low-lying HOMO, a high degree of backbone coplanarity, and substantial crystallinity. OTFTs fabricated from IID-based donor–acceptor copolymers show hole mobilities  $> 3.0\text{ cm}^2/(\text{V s})$ . Facile functionalization of the IID core leads to novel fluorinated and chlorinated IID acceptors. The resulting polymers exhibit pronounced and balanced  $\mu_{\text{h}}/\mu_{\text{e}}$  in OTFTs in parallel with excellent device stability in ambient. Further structural modifications lead to n-channel IID derivative-based polymers with  $\mu_{\text{e}}$  approaching  $2\text{ cm}^2/(\text{V s})$  and good OTFT stability. OSCs fabricated from IID polymers show promising performance with PCEs  $> 8.0\%$ . It is remarkable that IID polymers can achieve narrow band gaps ( $1.5\text{ eV}$ ) and high  $V_{\text{oc}}$ s of  $> 0.9\text{ eV}$  simultaneously, which corroborates the sufficiently low LUMOs of these polymers. On the basis of energetic considerations, IID polymers possess ideal band gaps and

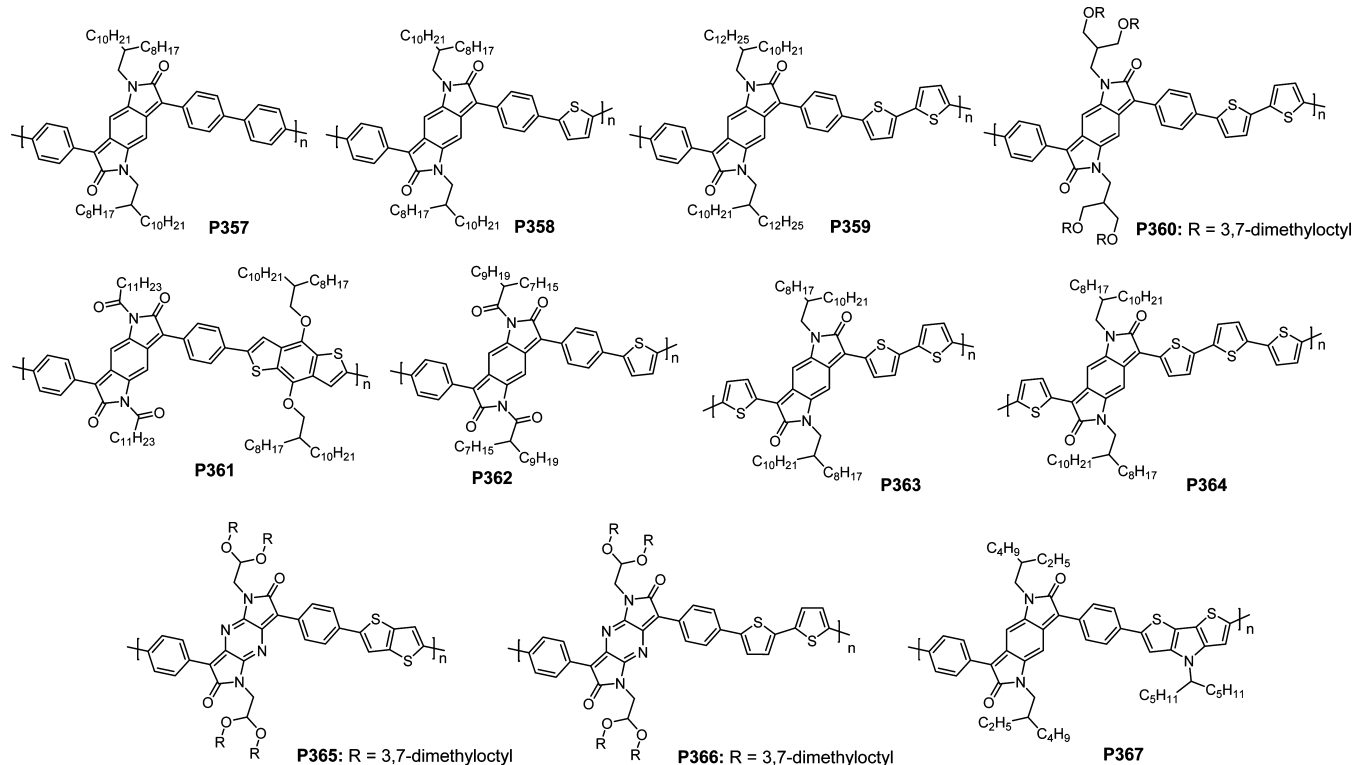


**Figure 52.** Benzodipyrrolidone-based polymers for OTFTs and OSCs. As structural analogues, dipyrrolo[2,3-*b*:2',3'-*e*]pyrazine-2,6(1*H*,5*H*)-dione-based polymers P365 and P366 are also included.

FMOs for OSCs; thus, further film morphology optimization and device engineering should deliver even greater PCEs.

## 11. BENZODIPYRROLIDONE-BASED POLYMER SEMICONDUCTORS

Continuing on the theme of developing building blocks based on dye chemistry, another bisamide (or bislactam) acceptor, benzodipyrrolidone (BDP), was developed for organic electronics. The chromophore was originally prepared as disperse dyes in the mid-1970s owing to its brilliant color and excellent photochemical stability.<sup>437</sup> Benzodipyrrolidone can be viewed as an “extended” DPP by fusing two pyrrolinones to cyclohexa-1,4-diene, which should provide stronger intermolecular interactions and larger  $\pi$ - $\pi$  overlapping. Moreover, the quinodimethane moiety in benzodipyrrolidone, in analogy to the tetracyanoquinodimethane (TCNQ), is expected to exhibit extensive  $\pi$ - $\pi$  stacking. On the basis of the molecular geometry and electronic structure, benzodipyrrolidone should be a promising building block for organic electronics. The benzodipyrrolidone-based polymer semiconductors were developed recently and show encouraging performance in both OTFTs and OSCs.

### 11.1. Synthesis of Dibrominated Benzodipyrrolidone

The synthetic route to the dibrominated phenyl-flanked benzodipyrrolidone (BDPDP) is outlined in Scheme 13.<sup>437,438</sup> *p*-Phenylenediamine 53 is condensed with 4-bromomandelic acid 54 to afford amide 55 in good yields, typically >80%. The subsequent ring-closure reaction is completed in concentrated H<sub>2</sub>SO<sub>4</sub> to afford 56, which is then oxidized by potassium persulfate<sup>438</sup> or hydrogen peroxide<sup>439</sup> to produce compound 57. Finally, alkylation with an alkyl bromide or iodide is readily accomplished in the presence of potassium *tert*-butoxide or potassium carbonate and provides dibrominated monomer 58, which is similar to the one for preparation of the alkylated DPP

counterpart.<sup>326</sup> The single crystal of the nonbrominated benzodipyrrolidone derivative confirms that the benzodipyrrolidone core is fully coplanar, and the alternating bond length pattern of the core verifies its quinodimethane structure, which should ensure a high degree of conjugation and electron delocalization of the resulting polymers.<sup>110,438</sup>

### 11.2. Benzodipyrrolidone-Based Polymer Semiconductors for OTFTs and OSCs

Wudl et al. first reported BDPDP-based polymer semiconductors for OTFTs.<sup>438</sup> P357 and P358 (Figure 52) were synthesized via Suzuki coupling, and showed good solubilities in organic solvents. The P357 and P358 band gaps derived from the absorption onsets were 1.90 and 1.68 eV, respectively, which indicate that BDPDP should be an effective acceptor for constructing narrow band-gap polymers. In comparison to P357, P358 has a smaller band gap due to the stronger electron-donating thiophene and the higher degree of backbone coplanarity. BGBC OTFTs were fabricated to investigate their charge transport properties. P357 showed pronounced n-channel performance with a  $\mu_e$  of  $2.4 \times 10^{-3}$  cm<sup>2</sup>/(V s) after annealing at 240 °C. P358 exhibited ambipolarity with a  $\mu_h/\mu_e$  of  $3.5 \times 10^{-3}/6.4 \times 10^{-3}$  cm<sup>2</sup>/(V s). The moderate  $\mu_s$ s of P357 and P358 could be partially attributed to their high-lying LUMOs of –3.35 and –3.50 eV, respectively, which led to a substantial electron injection barrier. Janssen reported the same polymer P358 but having greatly improved OTFT performance with a  $\mu_h/\mu_e$  of 0.21/0.18 cm<sup>2</sup>/(V s).<sup>440</sup> The improved charge transport is attributed to the greater polymer  $M_n$  and the staggered TGBC structure, which led to reduced contact resistance as compared to the BGBC structure.<sup>50,441</sup>

By incorporating the stronger bithiophene donor, P359 was synthesized to suppress electron transport. In comparison to the DPP polymer analogue having the same solubilizing chain, P359

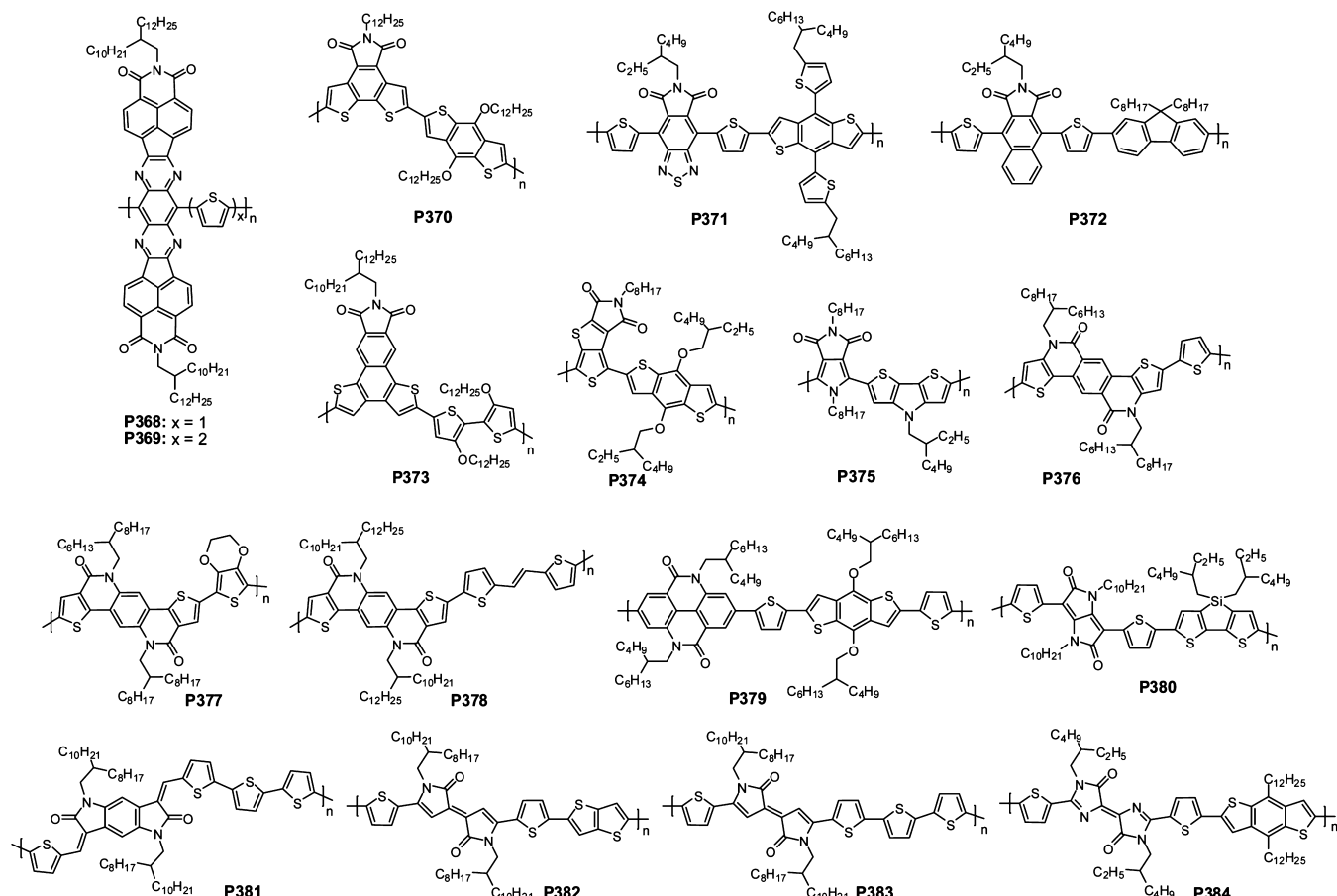


**Figure 53.** Polymer semiconductors containing imide- or amide-functionalized arenes as electron-acceptor units. These polymers show limited device performance or their performance has not been fully investigated.

showed a smaller  $M_n$  with reduced solubility due to its more extended benzodipyrrolidone core. P359 TGBT OTFTs exhibit an optimal  $\mu_h$  of  $0.018 \text{ cm}^2/(\text{V s})$  after annealing at  $120^\circ\text{C}$  for 5 min.<sup>439</sup> The study showed that increasing the thiophene number in donors can convert n-type or ambipolar transport of benzodipyrrolidone polymer to unipolar p-type transport with substantial hole mobility. Attaching a highly branched acetal-type side chain, 2,2-bis((3,7-dimethyloctyl)oxy)ethyl, on benzodipyrrolidone afforded P360, which showed better solubility and a higher  $M_n$  than P359. Moreover, P360 exhibited a  $\sim 15 \text{ nm}$  red-shifted absorption and a smaller band gap than P359 due to the stronger interchain interactions enhanced by the acetal side chains in P360.<sup>439</sup> In comparison to P359, P360 showed an improved  $\mu_h$  of  $0.026 \text{ cm}^2/(\text{V s})$  with an  $I_{\text{on}}/I_{\text{off}}$  of  $10^{5-6}$  in TGBC OTFTs. The result indicates that an acetal-type side chain could be an excellent solubilizing group for polymer semiconductors.

Zhang et al. reported a novel strategy to effectively lower benzodipyrrolidone polymer LUMOs via N-acylation.<sup>442</sup> Benzodipyrrolidone acylation was implemented by reacting benzodipyrrolidone with acyl chloride in the presence of 4-dimethylaminopyridine in THF; the subsequent polymerization afforded P361 and P362. In fact, after the N-acylation of the lactam the imide group is formed. Therefore, P361 and P362 are more like imide-containing polymers. The N-acylated polymers P361 and P362 showed a  $\sim 40 \text{ nm}$  red-shifted absorption in comparison to the N-alkylated polymer counterparts. Moreover, N-acylation lowered the polymer LUMOs by  $\sim 0.3 \text{ eV}$ , and P361 and P362 showed LUMOs of  $-3.84$  and  $-3.90 \text{ eV}$ , respectively.

P362 BGTC OTFTs with Au source/drain electrodes exhibited a  $\mu_e$  of  $0.012 \text{ cm}^2/(\text{V s})$ , which was substantially higher than that ( $5.34 \times 10^{-4} \text{ cm}^2/(\text{V s})$ ) of the N-alkylated counterpart P358.<sup>442</sup> Therefore, N-acylation effectively lowers the polymer LUMOs and enhances n-channel performance in OTFTs. This study demonstrated that N-acylation offers an effective strategy for tuning organic semiconductor FMOs and improving n-channel transport.<sup>442</sup>

For P357–P362, the BDP is flanked with phenyls, which leads to a  $38^\circ$  dihedral angle between the phenyl ring and the benzodipyrrolidone core as revealed by X-ray diffraction of a BDPDP single crystal.<sup>438</sup> McCulloch developed a new thiophene-flanked benzodipyrrolidone (BDPDT).<sup>443</sup> P363 and P364 (Figure 52) containing thiophene and bithiophene donors were synthesized and showed narrow band gaps of  $1.03$  and  $1.17 \text{ eV}$ , respectively. The small P363 and P364 band gaps are in good accordance with the high degree of backbone coplanarity of thiophene-flanked benzodipyrrolidone polymers. As compared to the P364 band gap, the smaller P363 band gap is likely attributable to its far higher  $M_n$ . The HOMO/LUMOs of P363 and P364 were  $-5.3/-4.2 \text{ eV}$ , which allows efficient hole and electron injection from a single Au electrode. TGBC OTFTs showed clear ambipolarity with balanced  $\mu_h/\mu_e$ s of  $0.21/0.1$  and  $0.08/0.01 \text{ cm}^2/(\text{V s})$  for P363 and P364, respectively, in parallel with a good current  $I_{\text{on}}/I_{\text{off}}$  of  $10^{4-5}$ .<sup>443</sup> The lower P364 mobilities were likely limited by its smaller  $M_n$ . In comparison to BDPDP-based P358 and P359, BDPDT-based P363 and P364 showed greatly improved charge transport, which were attributed

to the higher degree of BDPDT polymer backbone coplanarity as revealed by the single-crystal structure of dithienylbenzodipyrrolidone.<sup>444</sup>

Facchetti et al. synthesized a new benzodipyrrolidone analogue building block, dipyrrolo[2,3-*b*:2',3'-*e*]pyrazine-2,6-(1H,5H)-dione (PzDP), which shows stronger electron-accepting capability than benzodipyrrolidone.<sup>445</sup> The resulting P365 and P366 have small band gaps of 1.32 and 1.28 eV and low-lying HOMO/LUMOs of  $-5.49/-4.17$  and  $-5.59/-4.31$  eV, respectively.<sup>445</sup> These polymers were incorporated into BGBC OTFTs, which exhibited ambipolar behavior with  $\mu_h/\mu_e$ s of 0.053/0.021 and 0.066/0.0062 cm<sup>2</sup>/(V s) for P365 and P366, respectively.<sup>445</sup> It is interesting to note that P365 and P366 OTFTs have unusually high  $I_{on}/I_{off}$ s of  $10^{5-6}$  with low off-currents of  $10^{-10}-10^{-12}$  A as ambipolar organic semiconductors, which is associated with their low-lying HOMOs induced by the strong electron-withdrawing dipyrrolo[2,3-*b*:2',3'-*e*]pyrazine-2,6-(1H,5H)-dione. The high  $I_{on}/I_{off}$  and low off-current will be advantageous for OTFT applications since they provide sharp switching and lower energy consumption.

The good mobilities and low-lying HOMOs indicate that benzodipyrrolidone polymers should be promising donor semiconductors for OSCs. BDPDP and dithienopyrrole copolymer P367 was also synthesized, and has a small band gap of 1.39 eV and LUMO/HOMO of  $-3.83/-5.27$  eV.<sup>446</sup> OSCs having the structure ITO/PEDOT:PSS/P367:PCBM/LiF/Al showed an optimal PCE of 2.6% with a  $J_{sc}$  of 7.87 mA/cm<sup>2</sup>, a  $V_{oc}$  of 0.74 V, a FF of 44.6%.<sup>446</sup> It is interesting to note that the dithienopyrrole-based narrow band gap (1.39 eV) polymer can achieve a high  $V_{oc}$  of 0.74 V, which can be traced to the strong electron-withdrawing benzodipyrrolidone.  $J_{sc}$  and FF are likely limited by the low P367 hole mobility of  $2.0 \times 10^{-5}$  cm<sup>2</sup>/(V s) measured by SCLC and its low-lying LUMO, which prevents efficient exciton dissociation.

### 11.3. Summary

Benzodipyrrolidone, a new electron acceptor, was successfully synthesized and incorporated into several polymers. The resulting polymer semiconductors show broad absorption, small band gaps, and appropriate FMO levels. Despite the limited number of benzodipyrrolidone polymers developed to date, promising charge transport and power conversion efficiencies have been demonstrated in OTFTs and OSCs, respectively. As a new class of polymer semiconductors, there is great room for further structural modifications of benzodipyrrolidone polymers, such as varying comonomer units, changing flanked arenes, and engineering solubilizing chains. New materials development together with morphology optimization and device engineering will enhance device performance for benzodipyrrolidone-based polymers.

## 12. OTHER IMIDE/AMIDE-FUNCTIONALIZED POLYMER SEMICONDUCTORS

The polymers discussed above have shown the most promising performance in both OTFTs and OSCs, which has inspired synthetic chemists to develop other imide- or amide-functionalized arenes for constructing organic semiconductors with tailored optoelectronic and physical properties for performance advancement and exploration of structure–property–device performance correlations. Figure 53 shows several imide- and amide-functionalized polymer semiconductors which exhibit limited device performance or for which their performance has not been fully investigated.

Jenekhe designed and synthesized a novel 11-ring polycyclic electron-accepting chromophore, *N,N'*-bis(2-decyltetradecyl)-tetraazabenzodifluoranthene diimide (BFI).<sup>120</sup> The chromophore has a 2.0 nm long  $\pi$ -conjugated framework and shows a high degree of coplanarity, low-lying LUMO, and strong intermolecular interactions.<sup>120</sup> Incorporation of BFI into the polymer backbone affords two new polymers P368 and P369 (Figure 53) with well-defined lateral  $\pi$ -electron delocalization in addition to the backbone  $\pi$  conjugation.<sup>447</sup> The band gaps are 1.29 and 0.94 eV, and the LUMOs measured by cyclic voltammetry are  $-3.80$  and  $-3.74$  eV for P368 and P369, respectively. P368 BGTC OTFTs using Ag source/drain show a  $\mu_e$  of 0.30 cm<sup>2</sup>/(V s) with an  $I_{on}/I_{off}$  of  $10^{5-6}$  for the devices fabricated and characterized in ambient. The good electron mobility is attributed to the low-lying LUMO and well-ordered film morphology of P368. P369 OTFTs show a lower  $\mu_e$  of 0.09 cm<sup>2</sup>/(V s) due to its smaller  $M_n$ . Integration of n-channel P368 OTFTs into complementary inverters with suitable p-channel OTFTs leads to ideal switching behavior with a high voltage gain of 107.<sup>447</sup>

A new fused electron acceptor dithieno[3,2-*f*:2',3'-*h*]-phthalimide was designed and synthesized, and its copolymerization with benzodithiophene provided P370,<sup>448</sup> which has a band gap of 2.11 eV with a LUMO/HOMO of  $-2.78/-5.55$  eV. The broad band gap indicates limited polymer  $\pi$  conjugation due to the unfavorable population of the quinoidal structure. Without optimization, P370:PC<sub>61</sub>BM BHJ OSCs showed a PCE of 0.30% with a  $J_{sc}$  of 1.42 mA/cm<sup>2</sup>, a  $V_{oc}$  of 0.50 V, and a FF of 42.4%. The unsatisfactory performance was traced to the inefficient absorption and low hole mobility of P370.

Another phthalimide derivative, 2,1,3-benzothiadiazole-5,6-dicarboxylic imide,<sup>449</sup> was synthesized and incorporated into a polymer backbone. The resulting P371 showed broad absorption in the visible region with a band gap of 1.55 eV. Introduction of the strong electron-withdrawing 2,1,3-benzothiadiazole-5,6-dicarboxylic imide lowered the P371 HOMO to  $-5.51$  eV. P371:PC<sub>71</sub>BM BHJ OSCs with a conventional structure showed a promising PCE of 5.19% with a  $J_{sc}$  of 11.59 mA/cm<sup>2</sup>, a  $V_{oc}$  of 0.91 V, and a FF of 49.2%. The results demonstrate the great potential of 2,1,3-benzothiadiazole-5,6-dicarboxylic imide for creating high-performance solar cell materials.<sup>449</sup> Benzo[*f*]-isoindole-1,3-dione was designed and incorporated into polyfluorene to afford P372. The UV-vis absorption spectra showed that P372 had a wide band gap of 2.41 eV and a high-lying LUMO of  $-2.88$  eV. The result indicates that benzo[*f*]-isoindole-1,3-dione is a weak acceptor, and the benzo[*f*]-isoindole-1,3-dione polymer has limited  $\pi$  conjugation, which limits the PCEs of benzo[*f*]-isoindole-1,3-dione and DPP-based copolymer semiconductors to  $\sim 1\%$ .<sup>450</sup>

Peng et al. reported polymers containing imide-functionalized naphthodithiophene acceptor and dialkoxy bithiophene donor.<sup>451</sup> In comparison to phthalimide polymer P105 (Figure 28), the band gap (1.85 eV) of P373 is significantly larger, which is attributed to the lower electron deficiency and/or a lower degree of the quinoidal form of imide-functionalized naphthodithiophene (versus that of phthalimide). BHJ OSCs having the structure ITO/PEDOT:PSS/P373:PC<sub>71</sub>BM/Ca/Al show a moderate PCE of 2.45% with a  $J_{sc}$  of 7.26 mA/cm<sup>2</sup>, a  $V_{oc}$  of 0.60 V, and a FF of 56%. The performance is mainly limited by the broad band gap and high-lying HOMO of P373 due to the weak electron-withdrawing imide-functionalized naphthodithiophene.

Inspired by the promising device performance of TPD polymers, Kwon synthesized 2,7-dithia-5-azacyclopenta[*a*]-

pentalene-4,6-dione, a TPD derivative having a more extended  $\pi$  conjugation.<sup>452</sup> The dione was copolymerized with benzodithiophene to afford P374, which has a narrow band gap of 1.31 eV with broad absorption in the range of 550–900 nm. The P374 band gap is significantly smaller than that (~1.80 eV) of TPD polymer analogue P149 (Figure 34), which is attributed to the favored formation of the quinoidal structure promoted by the thieno[3,4-*b*]thiophene<sup>33,218</sup> in P374. Incorporation of 2,7-dithia-5-azacyclopenta[*a*]pentalene-4,6-dione leads to the low-lying P374 LUMO/HOMO of −4.06/−5.37 eV. P374:PC<sub>70</sub>BM BHJ OSCs show a promising PCE of 5.3% with a  $J_{sc}$  of 13.5 mA/cm<sup>2</sup>, a  $V_{oc}$  of 0.72 V, and a FF of 54%.<sup>452</sup>

A structurally novel pyrrole-based imide-functionalized electron acceptor, 2,5-diocytpyrrolo[3,4-*c*]pyrrole-1,3-(2H,5H)-dione (DPPD), was synthesized and incorporated into polymers.<sup>453</sup> The resulting P375 has a band gap of 1.89 eV with a LUMO/HOMO of −3.35/−5.24 eV. The band gap is much greater than that (1.59 eV) of the structurally similar TPD–dithienopyrrole polymer analogue P174 (Figure 37), which indicates the lower electron-accepting capability of 2,5-diocytpyrrolo[3,4-*c*]pyrrole-1,3(2H,5H)-dione versus TPD. Preliminary P375:PC<sub>71</sub>BM OSCs show a PCE of 1.64% with a  $J_{sc}$  of 6.24 mA/cm<sup>2</sup>, a  $V_{oc}$  of 0.56 V, and a FF of 46%. The wide band gap and high-lying HOMO of P375 indicate that DPPD is not as strong an electron acceptor as TPD due to the intrinsic electron-rich character of pyrrole.

Thieno[2',3':5,6]pyrido[3,4-*g*]thieno[3,2-*c*]isoquinoline-5,11(4H,10H)-dione, a pentacyclic aromatic bislactam, was designed and synthesized for creating low-band-gap polymers for OSC applications.<sup>454</sup> Two electron-withdrawing lactam groups imbued the resultant polymer P376 with a low-lying HOMO of −5.42 eV. The band gap estimated from the absorption onset was 1.86 eV. P376 OSCs with the conventional structure ITO/PEDOT:PSS/P376:PC<sub>71</sub>BM/Ca/Al afforded a PCE of 7.21% with a  $J_{sc}$  of 12.47 mA/cm<sup>2</sup>, a  $V_{oc}$  of 0.92 V, and a FF of 62.8%. It was found that the processing additive DIO played a crucial role in promoting nanoscale phase separation. Under the same optimized condition for conventional cells, inverted cells with the structure ITO/ZnO/P376:PC<sub>71</sub>BM/MoO<sub>3</sub>/Ag showed a superior PCE of 7.80% with a  $J_{sc}$  of 13.69 mA/cm<sup>2</sup>, a  $V_{oc}$  of 0.87 V, and a FF of 65.6%. The good P376 performance was attributed to its low-lying HOMO and substantial hole mobility ( $1.07 \times 10^{-3}$  cm<sup>2</sup>/(V s)). The P376 OSC performance was mainly limited by its moderate band gap. Further structural modification should lower the polymer band gaps for better absorption.

Thieno[2',3':4,5]pyrido[2,3-*g*]thieno[3,2-*c*]quinoline-4,10-(SH,11H)-dione, a fused bislactam having the carbonyl group connected to thiophene, was also synthesized to afford polymer P377.<sup>455</sup> The polymer was obtained via palladium-catalyzed direct arylation and had a  $M_n$  of 8.2 kDa with a PDI of 2.3. The band gap derived from the absorption onset was 1.78 eV. P377 BGTC OTFTs showed p-type performance with an average  $\mu_h$  of  $5 \times 10^{-5}$  cm<sup>2</sup>/(V s). Film characterization indicated that P377 had limited crystallinity. Pei and co-workers reported an efficient synthetic route to the bislactam via Beckmann rearrangement.<sup>456</sup> The monomer was synthesized from the diketone in two steps under mild condition. The bislactam was incorporated into a polymer to afford P378 through Stille coupling, and showed a high degree of crystallinity with an edge-on lamellar packing and a close  $\pi$ – $\pi$  stacking distance of 3.57 Å in film. P378 BGTC OTFTs exhibited typical hole transport characteristics with a  $\mu_h$  of 0.58 cm<sup>2</sup>/(V s) after annealing at 200 °C.<sup>456</sup> The results

showed that by changing the carbonyl group tethering fashion, two amide-functionalized arenes, thieno[2',3':5,6]pyrido[3,4-*g*]thieno[3,2-*c*]isoquinoline-5,11(4H,10H)-dione<sup>454</sup> and thieno[2',3':4,5]pyrido[2,3-*g*]thieno[3,2-*c*]quinoline-4,10-(SH,11H)-dione,<sup>455</sup> were developed, and both are good electron acceptors for creating polymer semiconductors.

Huang et al. designed and synthesized a novel pyrido[2,3,4-*lmn*]phenanthridine-5,10-dione by fusing two benzenes with two six-membered lactam rings.<sup>457</sup> The pyrido[2,3,4,5-*lmn*]-phenanthridine-5,10-dione copolymerizing with benzodithiophene and using thiophene bridge afforded P379, which has a broad band gap of 2.13 eV and low-lying HOMO of −5.41 eV. P379-based conventional solar cells showed a moderate PCE of 3.47%. Device optimization led to an improved PCE of 4.54% with a  $J_{sc}$  of 8.19 mA/cm<sup>2</sup>, a  $V_{oc}$  of 0.92 V, and a FF of 60.2% in inverted cells. The PCE is the highest for a polymer donor semiconductor with a band gap greater than 2.1 eV.<sup>457</sup> The wide band gap and efficient PCE of P379 indicate that pyrido[2,3,4-*lmn*]phenanthridine-5,10-dione is a promising building block for constructing broad band-gap polymers for tandem cells.

Diketopyrrolo[3,4-*c*]pyrrole (DPP)-based polymers have shown great success in organic electronics. The DPP utility and versatility have inspired the search for related chromophores. Structural modification afforded its isomer, diketopyrrolo[3,2-*b*]-pyrrole (isoDPP).<sup>458–460</sup> DFT computation and X-ray diffraction of a single crystal showed that the isoDPP is highly planar with a close intermolecular distance, which is comparable to those of DPP-based analogues. The isoDPP and dithienosilole copolymer P380 (Figure 53) was synthesized via Stille coupling and had a band gap of 1.59 eV.<sup>461</sup> The P380 band gap was larger than that (1.29 eV) of DPP and dithienosilole polymer analogue P274 (Figure 46), but the HOMO (−5.51 eV) of P380 was much lower than that (−5.04 eV) of conventional DPP polymer,<sup>377</sup> which was in good accordance with the DFT computations. The lower P380 HOMO was due to the particularly strong localization of the FMOs of the isoDPP derivative. P380 BGTC OTFTs showed a  $\mu_h$  of 0.03 cm<sup>2</sup>/(V s) with a high  $I_{on}/I_{off}$  of  $10^7$  after the polymer film was dried at 120 °C for 5 min. P380 was then used as the donor semiconductor in BHJ solar cells having the structure ITO/PEDOT:PSS/P380:PC<sub>71</sub>BM/LiF/Al. The optimized cells showed a PCE of 5.1% with a  $J_{sc}$  of 10.28 mA/cm<sup>2</sup>, a  $V_{oc}$  of 0.76 V, and a FF of 65%. The  $V_{oc}$  of P380 cells was 0.21 V larger than that (0.55 V) of DPP-based polymer analogue P274 (Figure 46) as a result of the deeper P380 HOMO. The results validate the potential of isoDPP semiconductors for optoelectronic device applications, and optimization of isoDPP polymer structures should further improve their performance.

Dihydropyrroloindoledione,<sup>462</sup> a structure analogous to diketopyrrolopyrrole and benzodipyrrolidone, has a vinyl linkage in the acceptor, which can reduce the steric hindrance along and between polymer chains. The dihydropyrroloindoledione polymer P381 shows a broad absorption coupled with a narrow band gap of ~1.6 eV and has a LUMO/HOMO of −3.7/−5.3 eV. P381 TGBC OTFTs exhibit ambipolarity with a  $\mu_h/\mu_e$  of 0.09/0.04 cm<sup>2</sup>/(V s) under N<sub>2</sub>, and the P381-based solar cells show a moderate PCE of 2.1% but with an encouraging  $V_{oc}$  of 0.75 V. Solar cell performance is likely limited by the inefficient charge transfer from P381 to fullerene due to their small LUMO offset.

Bipyrrolylidene-2,2'(1H,1'H)-dione,<sup>463</sup> a derivative of a Pechmann dye,<sup>464</sup> has a planar structure with a bisamide as the electron-withdrawing moiety. Its incorporation into polymers

**Table 1.** Molecular Weights, Optical and Electrochemical Properties, and Organic Thin-Film Transistor Performance of Representative Imide- and Amide-Functionalized Polymer Semiconductors

polymer	$M_n$ (kDa)	$E_g^{\text{opt}}$ (eV)	$E_{\text{LUMO}}/E_{\text{HOMO}}$ (eV)	device structure	source/drain electrode	$\mu_h$ ( $\text{cm}^2/(\text{V s})$ )	$\mu_e$ ( $\text{cm}^2/(\text{V s})$ )	ref
P1	10	1.5	-3.9/-5.9	BGTC	Al		0.013	156
P1	10	1.5	-3.9/-5.9	TGBC	Au		0.06	157
P2	11	1.65	-3.96/-5.61	BGTC	Au		$2 \times 10^{-3}$	158
P28	11	1.86	-3.70/-5.56	TGBC	Au	0.04	0.30	175
P37	31	NA	-3.90/NA	BGBC	Au		$1.2 \times 10^{-3}$	183
P50	50	1.45	-3.91/-5.36	TGBC	Au		0.45–0.85	197
P53	153	1.37	-3.76/-5.13	BGTC	Au		0.076	198
P58	19	1.4	-4.0/-5.4	BGTC	Au		0.2	200
P66	18	2.11	-3.78/-5.89	BGTC	Au		0.056	207
P73	24	1.42	-3.90/-5.62	TGBC	Au	0.3	1.57	212
P73	70	1.42	-4.00/-5.42	TGBC	Au/Cs <sub>2</sub> CO <sub>3</sub>		1.8	136
P82	74	1.70	-3.72/-5.78	TGBC	Au	0.3	$10^{-5}$	226
P88	27	1.2	-4.4/-5.6	BGTC	Au	0.1	0.27	229
P89	82	1.8	-4.0/NA	BGBC	Au		0.1	231
P100	4	2.57	-3.84/-6.41	TGBC	Au		$2 \times 10^{-4}$	204
P102	12	2.84	-3.65/-6.13	TGBC	Au		$6.2 \times 10^{-4}$	237
P105	208	1.65	NA/-5.14	BGBC	Au	0.17		131
P111	19	1.85	-3.39/-5.24	TGBC	Au	0.4	0.06	244
P125	5	2.15	-3.27/-5.73	BGTC	Au		inactive	241
P139	16	1.8	NA/-5.05	BGTC	Au	1.29		264
P186	7	2.02	-3.47/-6.28	TGBC	Au		0.19	50
P192	13	1.83	-3.55/-5.38	TGBC	Au	0.07		50
P209	28	1.5	-4.0/-5.5	BGTC	Ba	0.1	0.09	319
P210	54	1.3	-3.61/-5.17	BGBC	Au	0.04	0.01	320
P211	70	1.08	-4.02/-5.20	BGTC	Au	0.1	0.1	321
P213	18	1.2	-3.82/-5.07	BGTC	Au	2.53	0.43	324
P214	20	1.2	-3.65/-4.91	BGTC	Au	3.97	2.20	324
P215	23	1.24	-3.49/-5.10	BGTC	Au	8.84	4.34	138
P219	110	1.23	-3.5/-5.2	BGBC	Au	10.5		328
P225	130	1.41	-3.91/-5.32	BGTC	Au	1.54		333
P232	36	1.2	NA/-5.27	BGTC	Au	12.04		135
P246	17	1.50	-3.56/-5.36	BGTC	Au	0.34	0.23	35
P249	16	1.47	-3.64/-5.65	BGTC	Au	0.23	2.36	35
P250	21	1.5	-3.2/-4.7	BGBC	Au	0.24		353
P252	9	0.65	-3.9/-4.55	BGBC	Au	0.89	0.99	353
P259	67	1.2	-3.88/-5.38	BGBC	Au	0.01	0.01	365
P259	67	1.2	-3.88/-5.38	TGBC	Al		3	365
P260	26.3	1.65	-4.33/-5.69	TGBC	Au	2.78	6.30	368
P303	138	1.61	-3.58/-5.20	BGTC	Au	2.0		323
P309	99	1.65	-3.65/-5.54	BGTC	Au	2.2		400
P313	25	1.7	-3.64/-5.70	BGTC	Au		0.22	270
P314	76	1.5	-3.88/-5.46	TGBC	Au	1.48	0.38	403
P316	59	1.51	-3.84/-5.57	TGBC	Au	0.81	0.66	404
P351	38	1.42	-4.10/-6.12	TGBC	Au		1.1	432
P352	54	1.39	-4.30/-6.22	TGBC	Au		0.81	137
P353	66	1.46	-4.26/-6.19	TGBC	Au		1.70	137
P354	77	1.31	-4.35/-5.66	TGBC	Au		1.74	433
P358	14	1.68	-3.96/-5.68	BGBC	Au	0.21	0.18	440
P362	23	1.5	-3.90/-5.62	BGTC	Au		0.012	442
P363	34	1.03	-4.24/-5.27	TGBC	Au	0.21	0.1	443
P365	29	1.32	-4.17/-5.49	BGBC	Au	0.05	0.02	445
P368	48	1.29	-3.80/-5.45	BGTC	Ag		0.3	447
P382	7.2	1.1	-3.7/-5.0	BGBC	Au	1.24	0.82	465

afforded P382 and P383 having band gaps of 1.1 and 1.2 eV, respectively.<sup>465</sup> The LUMO/HOMOs derived from cyclic voltammetry were -3.7/-5.0 and -3.6/-5.0 eV for P382 and P383, respectively. After annealing at 200 °C, P382 BGBC OTFTs showed ambipolarity with a  $\mu_h/\mu_e$  of 1.24/0.82  $\text{cm}^2/(\text{V s})$

s) in N<sub>2</sub>, and P383 OTFTs only exhibited p-type transport with a  $\mu_h$  up to 1.37  $\text{cm}^2/(\text{V s})$  after annealing at 120 °C. Their substantial mobilities were attributed to the good film crystallinity.<sup>465</sup> Going from P382 to P383, the disappearance of n-type performance of P383 was due to its elevated LUMO. A

**Table 2.** Molecular Weights, Optical and Electrochemical Properties, and Organic Solar Cell Performance of Representative Imide- and Amide-Functionalized Polymer Semiconductors

polymer	$M_n$ (kDa)	$E_g^{\text{opt}}$ (eV)	$E_{\text{LUMO}}/E_{\text{HOMO}}$ (eV)	device structure <sup>a</sup>	active layer	$J_{\text{sc}}$ (mA/cm <sup>2</sup> )	$V_{\text{oc}}$ (V)	FF	PCE (%)	ref
P1	10	1.5	-3.9/-5.9	C	D1:P1	4.2	0.63	0.39	1	156
P1	10	1.5	-3.9/-5.9	C	D3:P1	8.88	0.752	0.515	3.45	166
P14	20.5	1.80	-3.80/-5.60	I	P330:P14	8.77	1.04	0.46	4.21	171
P17	15	1.68	-3.8/-5.5	I	P3HT:P17	7.65	0.55	0.52	2.17	80
P25	12	1.77	-3.66/-5.83	C	D5:P25	6.35	0.70	0.50	2.23	170
P31	10	1.78	-3.51/-5.70	C	D8:P31	2.14	0.92	0.426	0.84	180
P36	11	2.2	NA	C	P36	0.012	0.97	0.25	0.01	128
P42	1.5	1.58	-3.77/-5.60	C	P3HT:P42	2.16	1.24	0.46	1.23	187
P45	14	1.95	NA	C	P45	2.57	0.51	0.37	0.49	189
P50	26	1.45	-4.35/-5.80	C	P3HT:P50	3.77	0.56	0.65	1.4	217
P50	178	1.45	-4.30/-5.90	C	D11:P50	8.85	0.84	0.55	4.1	221
P76	26	1.7	-4.0/-5.7	I	D12:P76	7.78	0.76	0.55	3.26	222
P79	16	2.1	-3.68/-5.71	C	D13:P79	7.71	0.88	0.54	3.68	224
P81	17	1.46	-4.22/-5.60	C	P3HT:P81	4.57	0.56	0.50	1.28	225
P104	117	1.72	NA/-5.1	C	P104:PC <sub>71</sub> BM	12.5	0.54	0.61	4.09	248
P122	16	2.07	-3.07/-5.57	C	P122:PC <sub>71</sub> BM	7.01	0.89	0.59	3.7	254
P149	13	1.8	-3.75/-5.56	C	P149:PC <sub>71</sub> BM	9.81	0.85	0.66	5.5	271
P155	32	1.8	NA	C	P155:PC <sub>71</sub> BM	12.6	0.97	0.70	8.5	139
P156	30	1.8	NA	C	P156:PC <sub>71</sub> BM	11.7	0.73	0.66	5.6	278
P158	16	1.88	-3.41/-5.29	C	P158:PC <sub>71</sub> BM	11.1	1.00	0.58	6.5	281
P159	21	1.79	-3.62/-5.41	C	P159:PC <sub>71</sub> BM	10.6	1.05	0.60	6.7	281
P164	28	1.73	-3.88/-5.57	C	P164:PC <sub>71</sub> BM	12.2	0.88	0.68	7.3	106
P167	48	1.69	-3.5/-5.6	I	P167:PC <sub>70</sub> BM	12.6	0.85	0.68	7.3	105
P167	48	1.69	-3.5/-5.6	I	P167:PC <sub>70</sub> BM	14.0	0.86	0.67	8.1	61
P168	12	1.75	-3.66/-5.68	C	P168:PC <sub>70</sub> BM	13.85	0.81	0.64	7.2	289
P180	10	1.82	-3.10/-5.56	C	P180:PC <sub>70</sub> BM	13.1	0.92	0.61	7.3	98
P182	41	1.8	-3.86/-5.66	C	P182:PC <sub>70</sub> BM	10.51	0.92	0.63	6.1	295
P183	40	1.82	-3.73/-5.55	I	P183:PC <sub>71</sub> BM	12.5	0.795	0.796	7.9	62
P196	30	1.75	-3.68/-5.43	I	P196:PC <sub>71</sub> BM	12.81	0.803	0.623	6.41	55
P201	31	1.81	-3.77/-5.58	I	P201:PC <sub>71</sub> BM	12.9	0.859	0.778	8.66	62
P203	40	1.51	-3.63/-5.63	C	P203:PC <sub>61</sub> BM	7.05	0.78	0.55	3.01	307
P261	20	1.4	-3.4/-5.1	C	P261:PC <sub>70</sub> BM	11.3	0.61	0.58	4.0	315
P262	110	1.3	NA	C	P262:PC <sub>70</sub> BM	17.8	0.6	0.66	7.0	369
P266	58	1.4	NA/-5.2	C	P266:PC <sub>70</sub> BM	14.8	0.65	0.64	6.5	372
P268	447	1.35	-3.68/-5.10	C	P268:PC <sub>70</sub> BM	14.8	0.66	0.70	6.9	97
P269	45	1.4	-3.7/-5.1	C	P269:PC <sub>70</sub> BM	18.6	0.61	0.64	7.3	374
P275	93	1.44	-4.00/-5.63	I	P276:P275	6.9	0.81	0.51	2.9	378
P276	NA	1.30	-3.63/-5.23	I	P276:P275	6.9	0.81	0.51	2.9	378
P289	38	1.38	-3.70/-5.25	C	P289:PC <sub>70</sub> BM	16.8	0.69	0.62	7.2	387
P296	42	1.43	-3.73/-	C	P296:PC <sub>70</sub> BM	15.9	0.75	0.67	8.0	140
P297	12	1.9	-3.5/-5.4	C	P297:PCBM	7.8	0.58	NA	1.67	393
P297	12	1.9	-3.5/-5.4	C	P3HT:P297	2.6	0.92	NA	0.84	394
P302	135	1.62	-3.77/-5.38	C	P302:PC <sub>71</sub> BM	10.31	0.905	0.60	5.2	414
P303	138	1.61	-3.58/-5.20	C	P303:PC <sub>71</sub> BM	NA	NA	NA	3.4	414
P309	106	1.61	-3.61/-5.54	C	P309:PC <sub>61</sub> BM	13.2	0.91	0.59	7.09	418
P326	37	1.58	-3.98/-5.64	I	P326:PC <sub>71</sub> BM	11.30	0.92	0.68	7.04	411
P327	55	1.57	-3.95/-5.62	C	P327:PC <sub>71</sub> BM	14.96	0.72	0.68	7.31	412
P329	132	NA	NA/-5.36	I	P329:PC <sub>61</sub> BM	11.6	0.96	0.63	7.0	173
P332	10	1.5	-3.97/-5.69	C	P332:PC <sub>71</sub> BM	14.63	0.72	0.66	6.9	420
P338	58	1.58	-3.97/-5.97	C	P338:PC <sub>61</sub> BM	12.58	0.93	0.54	6.32	423
P340	40	1.61	-3.54/-5.22	I	P340:PC <sub>71</sub> BM	15.2	0.78	0.69	8.2	141
P341	85	1.59	-3.67/-5.30	I	P341:PC <sub>71</sub> BM	12.9	0.84	0.73	7.9	141
P342	108	1.59	-3.74/-5.36	I	P342:PC <sub>71</sub> BM	12.4	0.87	0.70	7.6	141
P344	29	1.70	-3.84/-5.54	C	P3HT:P344	1.91	0.62	0.41	0.47	427
P349	56	1.37	-3.84/-5.54	C	P349:PC <sub>71</sub> BM	10.4	0.54	0.57	3.20	430
P367	29	1.39	-3.83/-5.27	C	P367:PCBM	7.87	0.74	0.446	2.6	446
P370	12	2.11	-2.78/-5.55	C	P370:PC <sub>61</sub> BM	1.42	0.5	0.424	0.3	448
P371	29	1.55	-3.76/-5.51	C	P371:PC <sub>71</sub> BM	11.59	0.91	0.492	5.19	449
P374	56	1.31	-4.06/-5.37	C	P374:PC <sub>70</sub> BM	13.5	0.72	0.54	5.3	452
P376	29	1.86	-2.77/-5.42	I	P376:PC <sub>71</sub> BM	13.69	0.87	0.656	7.80	454

Table 2. continued

polymer	$M_n$ (kDa)	$E_g^{\text{opt}}$ (eV)	$E_{\text{LUMO}}/E_{\text{HOMO}}$ (eV)	device structure <sup>a</sup>	active layer	$J_{\text{sc}}$ (mA/cm <sup>2</sup> )	$V_{\text{oc}}$ (V)	FF	PCE (%)	ref
P379	32	2.13	-3.28/-5.41	I	P378:PC <sub>71</sub> BM	8.19	0.92	0.602	4.54	457
P380	31	1.59	-3.52/-5.51	C	P379:PC <sub>71</sub> BM	10.28	0.76	0.65	5.1	461

<sup>a</sup>C stands for conventional structure; I stands for inverted structure.

new amide-functionalized acceptor, (*E*)-[4,4'-biimidazolylidene]-5,5'(1*H*,1'*H*)-dione (BID), was incorporated into P384, which shows a broad absorption with a small band gap of 1.48 eV.<sup>466</sup> The P384 LUMO/HOMO were -3.75/-5.23 eV as measured from cyclic voltammetry. BGBC OTFTs were fabricated to investigate the charge transport, and P384 showed p-channel performance with a  $\mu_h$  of  $6.6 \times 10^{-3}$  cm<sup>2</sup>/(V s), which was much lower than those of bipyrrrolidene-2,2'(1*H*,1'*H*)-dione-based polymers P382 and P383.<sup>463,465</sup> The moderate P384 mobility was due to the low degree of ordering of polymer film, which was partially associated with the low polymer  $M_n$  (6.3 kDa). Despite the moderate OTFT performance, the low-lying LUMO/HOMO and small band gap of P384 indicate that (*E*)-[4,4'-biimidazolylidene]-5,5'(1*H*,1'*H*)-dione is a promising acceptor for organic semiconductors.

The promising device performance of imide- and amide-functionalized polymers has encouraged organic synthetic chemists to design and synthesize new imide- and amide-functionalized arenes and incorporate them into polymer semiconductors. Following this strategy, a large number of such building blocks have been developed, and some of the resulting polymer semiconductors (Figure 53) have shown very promising OTFT and OSC performance. Since most polymers built from these arenes are in the early stage of development, further structural modifications should lead to improved device performance. On the other hand, these novel building blocks deserve deep investigation for exploration of the structure–property–device performance correlations. Such correlation will guide materials synthetic chemists to design new polymer semiconductors with precisely tuned optoelectronic properties for performance improvement.

### 13. CONCLUSIONS AND OUTLOOK

As emerging polymer semiconductors for organic electronics, imide- and amide-functionalized polymers have achieved the most encouraging device performance to date in OTFTs (Table 1) and OSCs (Table 2). As the p-channel semiconductors in OTFTs, diketopyrrolopyrrole-based polymers have shown hole mobilities greater than 10 cm<sup>2</sup>/(V s) with high  $I_{\text{on}}/I_{\text{off}}$  of 10<sup>7–8</sup>. These mobilities are the highest obtained for solution-processed polymer transistors. The high electron deficiency of the DPP unit enables polymer OTFTs with excellent device durability in ambient, which is essential for commercially relevant electronic devices. As n-channel semiconductors, the naphthalene diimide (NDI)-based polymers exhibit electron mobility approaching 2 cm<sup>2</sup>/(V s); the design and development of NDI polymers greatly close the performance gap between p- and n-channel polymer semiconductors. Very promising ambipolar charge transport with balanced hole and electron mobilities is obtained from several isoindigo- and DPP-based polymer semiconductors. The polymers show record ambipolar transport with hole and electron mobilities greater than 8 and 4 cm<sup>2</sup>/(V s) in ambient, respectively. Integration of these high-performance OTFTs affords a voltage gain of 155 in inverters and an oscillation frequency of 182 kHz in ring oscillators. As the donor semiconductors in solution-processable bulk heterojunction

solar cells, several imide- or amide-functionalized polymers have routinely achieved power conversion efficiencies greater than 8% (Table 2). An unprecedented fill factor approaching 80% is also obtained from the high-mobility thienopyrroledione (TPD) polymer. As the acceptor semiconductors, NDI polymers have shown power conversion efficiency of 6.4% in all-polymer solar cells, which is the highest in this category cell. The device performance demonstrates the unique status of imide- and amide-functionalized polymers in organic optoelectronics.

With extensive research and accumulated understanding, the unique physical and optoelectronic properties of imide- and amide-functionalized polymers have been explored and elucidated. Investigation of the polymer structure–property correlations affords insights into the device performance variations of the polymers constructed from different imide- or amide-functionalized arenes. In comparison to monoimide- or amide-functionalized polymers, rylene diimide polymers tend to show n-channel or n-channel predominant transport due to the strong electron-withdrawing capability of the diimide groups. As compared to perylene diimide (PDI) polymers, naphthalene diimide (NDI) polymers usually show superior device performance. The PDI imposes greater steric hindrance on the neighboring arenes than does the NDI due to the sterically congested bay region of PDI, which leads to a high degree of backbone torsion, low degree of  $\pi$  conjugation, and amorphous film microstructure for PDI polymer semiconductors. Furthermore, it is more challenging to obtain a regioregularly pure form for PDI polymers than for NDI polymers. The amorphous film microstructures and regioirregularity of PDI polymers lead to their lower electron mobilities than those of NDI polymers in OTFTs. The lower electron mobility of PDI polymers results in smaller power conversion efficiencies than NDI polymers when they are used as the acceptor semiconductors in OSCs. On the other hand, the extended PDI  $\pi$  core imbues nonconjugated PDI polymers with interesting OTFT and OSC performance, which is attributed to the effective intermolecular  $\pi$ -orbital overlap. In comparison to the PDI polymers, the pyromellitic diimide (PMDI) polymers show lower performance due to their severely twisted polymer backbones.

Monoimide-functionalized phthalimide polymers show promising p-channel performance in OTFTs. Their applications in OSCs are mainly limited by their broad band gaps due to the unfavored population of the quinoidal form. In order to promote the quinoidal form, the benzene in phthalimide is replaced with thiophene to afford a monoimide-functionalized arene, thienopyrroledione (TPD). Incorporation of TPD into the polymer backbone leads to a variety of polymers with substantial hole mobilities. The carbonyl groups on phthalimide and TPD can function as conformation “locks” by promoting intramolecular (thienyl)S···(carbonyl)O interactions. Therefore, the phthalimide and TPD-based polymers show a high degree of backbone coplanarity and good film crystallinity. In comparison to the phthalimide polymers, TPD polymers usually show superior performance in both OTFTs and OSCs, which is attributed to the less sterically hindered thiophene ring in TPD versus the benzene ring in phthalimide. The strong electron-withdrawing

capability of TPD enables TPD polymers with excellent power conversion efficiencies via open-circuit voltage enhancement, and the  $V_{oc}$ s of TPD polymer OSCs can reach 1 V without sacrificing the short-circuit currents. Bithiophene imide (BTI) featuring an imide group on the center of the bithiophene results in the disappearance of intramolecular (thienyl)S···(carbonyl)O contacts. Therefore, the BTI polymers show a slightly higher degree of backbone torsion and hence a lower degree of crystallinity and degraded charge transport as compared to the TPD polymer homologues. However, the backbone torsion is beneficial to polymer solubility and open-circuit voltage in OSCs for BTI polymers. When an appropriate donor is chosen, the BTI polymers can exhibit more promising power conversion efficiencies than TPD polymers. Thienoisooindoledione (TID), another imide-functionalized arene, is highly efficient for constructing low-band-gap polymers due to the stabilized quinoidal form of the polymer. However, the hydrogen atom on the isoindole moiety of TID imposes a significant steric hindrance on neighboring arenes, which is detrimental for film crystallinity and charge transport. Therefore, the TID-based polymers show the lowest charge carrier transport among the four families of monoimide-functionalized polymer semiconductors discussed here.

Amide (or lactam)-functionalized polymers show the most promising p-channel performance in OTFTs, which is attributed to their precisely tuned electrical properties and high degree of polymer film crystallinity. The carbonyl groups on amides can function as conformation “locks” to achieve a high degree of polymer backbone coplanarity and highly crystalline film morphology. A hole mobility exceeding  $10 \text{ cm}^2/(\text{V s})$  has been achieved from DPP polymer semiconductors, which is even beyond those of amorphous silicon-based transistors. Such high OTFT mobilities are surprising and certainly more exploration is needed to understand their origin. In comparison to the monoimide-functionalized polymer semiconductors, the higher mobility of amide-functionalized polymers can be attributed to their ultrahigh polymer molecular weight and centrosymmetric geometry. Two solubilizing chains can be installed on the amide-functionalized arenes, which offer amide polymers with better solubility and higher  $M_n$  than monoimide-functionalized polymers, in which only one solubilizing chain can be attached to the monoimide-functionalized arenes. In comparison to the axisymmetric monoimide-functionalized arenes, amide-functionalized arenes have a centrosymmetric geometry, which can lead to more compact and ordered film microstructures and higher charge carrier mobility for DPP and IID polymers. Furthermore, the DPP- and IID-based polymers may have more appropriately lying HOMOs, which could lead to more efficient hole injection than monoimide-functionalized p-channel polymer semiconductors.

Between DPP- and IID-based polymers the DPP polymers exhibit higher hole mobilities than IID polymers. The enhanced hole mobility of DPP polymers could be attributed to their higher lying HOMOs, which corroborate well with the smaller  $V_{oc}$ s of DPP polymers in OSCs as compared to those of IID polymer homologues having the same donor counits (Table 2). Furthermore, the IID polymers are a class of polymer semiconductors which have attracted attention only in the past 4 years. The community has witnessed the dramatic mobility improvement for IID polymers recently. As the polymer structures are further optimized, we believe that the charge carrier mobilities of IID polymers will approach those of DPP polymers. The IID polymers have lower lying HOMOs than

DPP polymers; hence, the IID polymers usually show greater  $V_{oc}$ s than DPP polymer homologues in OSCs. The  $V_{oc}$ s of IID polymers are comparable to those of TPD polymer homologues. As high-performance donor semiconductors, TPD, IID, and DPP polymers have achieved comparable performance in OSCs with PCEs of 8–9%. Among the three families of amide-functionalized arenes, DPP-, IID-, and BDP-based polymers, BDP polymers show the poorest performance, which could be partially related to their curved polymer backbones, which should deteriorate polymer packing. However, the effects of the included quinodimethane moiety on the optoelectronic property and charge transport of BDP polymers should not be excluded.

Many of the imide- and amide-functionalized arenes used for organic electronics have historical origins as molecules for dyes and pigments, and their incorporation into organic semiconductors has led to such prominent performance only within the last couple of years. Development of new imide- and amide-functionalized arenes with precisely tailored physical and optoelectronic properties is highly desired, and the availability of such arenes will allow a new paradigm to take form. Structural modifications and modern synthetic methodologies generate new imide- and amide-functionalized arenes. By copolymerizing these arenes with appropriate electron donors and engineering the side chains, we believe that the device performance can be further improved. In the course of new materials development, specific attention should be devoted to enhance the OTFT stability and further improve the PCEs of OSCs to reach the threshold for real-world application.

Imide- and amide-functionalized polymers have shown substantial electron mobility, and their incorporation into all-polymer solar cells has resulted in PCEs greater 6%. All-polymer solar cells are unexplored when compared to other types of OSCs; achieving such performance is especially encouraging and deserves further investigations. We believe there is a great room for performance improvement for all-polymer solar cells when the appropriate donor semiconductor and acceptor semiconductor are paired and optimal film morphology is achieved.

Some materials structure–property–device performance correlations have been firmly established, but there is much room for further investigations in terms of fundamental materials development, materials optoelectronic structure, film morphology optimization, and their application in advanced optoelectronic devices and circuitries. The macroscopic device performance of the polymer semiconductors is not only dependent on the materials integrated into the device but also highly related to the materials processing condition and the device structure. There are many factors affecting the device performance parameters. Combined research efforts of organic synthetic chemists, materials scientists, and device engineers will deliver more exciting OTFT and OSC performance using emerging imide- and amide-functionalized polymer semiconductors.

## AUTHOR INFORMATION

### Corresponding Authors

\*E-mail: guo.xg@sustc.edu.cn  
\*E-mail: a-faccetti@northwestern.edu.  
\*E-mail: t-marks@northwestern.edu.

### Notes

The authors declare no competing financial interest.

## Biographies



Xugang Guo is currently Associate Professor of Materials Science and Engineering at the South University of Science and Technology of China (SUSTC). He received his B.S. and M.S. degrees in Chemistry from Lanzhou University under the supervision of Professor Zhengyin Yang in 1999 and 2002, respectively. He joined Mark D. Watson's group at the University of Kentucky in 2006 and obtained his Ph.D. degree in Chemistry in 2009. From 2009 to 2012 he carried out his postdoctoral training with Professor Tobin J. Marks and Professor Antonio Facchetti at Northwestern University and came to SUSTC immediately thereafter.



Antonio Facchetti obtained his Laurea degree in Chemistry cum laude and Ph.D. degree in Chemical Sciences from the University of Milan under the supervision of Professor Giorgio A. Pagani. He then carried out postdoctoral research at the University of California—Berkeley with Professor Andrew Streitwieser and at Northwestern University with Professor Tobin J. Marks. In 2002, he joined Northwestern University, where he is currently an Adjunct Professor of Chemistry. He is a cofounder and currently the Chief Scientific Officer of Polyera Corporation. He has published about 300 research articles and holds 150 patents. His research interests include organic semiconductors and dielectrics for thin-film transistors, conducting polymers, molecular electronics, organic second- and third-order nonlinear optical materials, and organic photovoltaics.



Tobin J. Marks is the Vladimir N. Ipatieff Professor of Chemistry and Professor of Materials Science and Engineering at Northwestern University. He received his B.S. degree from the University of Maryland (1966) and Ph.D. degree from MIT (1971) and came to Northwestern immediately thereafter. He is a fellow of the American Academy of Arts and Sciences (1993), a member of the U.S. National Academy of Sciences (1993), a member of the National Academy of Engineering (2012), a member of the German National Academy of Sciences (2005), a member of the India National Academy of Sciences (2011), a fellow of the Materials Research Society (2009), a fellow of the Royal Society of Chemistry (2005), a honorary fellow of the Chemical Research Society of India (2009), and a honorary member of the Israel Chemical Society (2012). Among other recognitions, he was awarded the National Medal of Science (2005), the Spanish Principe de Asturias Prize for Scientific Research (2008), the Von Hippel Award of the Materials Research Society (2009), the Dreyfus Prize in the Chemical Sciences (2011), and the U.S. National Academy of Sciences Award in the Chemical Sciences (2012).

## ACKNOWLEDGMENTS

X.G. acknowledges financial support from the SUSTC start-up fund. T.J.M. and A.F. are thankful for financial support from ANSER Center, an Energy Frontier Research Center funded by the U.S. Department of Energy, Office of Science, and Office of Basic Energy Sciences (award no. DE-SC0001059), Polyera Corporation, and AFOSR (FA9550-11-1-0142).

## REFERENCES

- (1) Forrest, S. R. *Nature* **2004**, *428*, 911.
- (2) Arias, A. C.; MacKenzie, J. D.; McCulloch, I.; Rivnay, J.; Salleo, A. *Chem. Rev.* **2010**, *110*, 3.
- (3) Sekitani, T.; Zschieschang, U.; Klauk, H.; Someya, T. *Nat. Mater.* **2010**, *9*, 1015.
- (4) Krebs, F. C.; Gevorgyan, S. A.; Alstrup, J. *J. Mater. Chem.* **2009**, *19*, 5442.
- (5) Krebs, F. C. *Sol. Energy Mater. Sol. Cells* **2009**, *93*, 394.
- (6) White, M. S.; Kaltenbrunner, M.; Glowacki, E. D.; Gutnichenko, K.; Kettlgruber, G.; Graz, I.; Aazou, S.; Ulbricht, C.; Egbe, D. A. M.; Miron, M. C.; Major, Z.; Scharber, M. C.; Sekitani, T.; Someya, T.; Bauer, S.; Sariciftci, N. S. *Nat. Photonics* **2013**, *7*, 811.
- (7) Nomura, K.; Ohta, H.; Takagi, A.; Kamiya, T.; Hirano, M.; Hosono, H. *Nature* **2004**, *432*, 488.
- (8) Hoeben, F. J. M.; Jonkheijm, P.; Meijer, E. W.; Schenning, A. P. H. *J. Chem. Rev.* **2005**, *105*, 1491.
- (9) Mas-Torrent, M.; Rovira, C. *Chem. Rev.* **2011**, *111*, 4833.
- (10) Coropceanu, V.; Cornil, J.; da Silva Filho, D. A.; Olivier, Y.; Silbey, R.; Brédas, J.-L. *Chem. Rev.* **2007**, *107*, 926.
- (11) Germs, W. C.; Guo, K.; Janssen, R. A. J.; Kemerink, M. *Phys. Rev. Lett.* **2012**, *109*, 016601.

- (12) Xie, W.; Willa, K.; Wu, Y.; Häusermann, R.; Takimiya, K.; Batlogg, B.; Frisbie, C. D. *Adv. Mater.* **2013**, *25*, 3478.
- (13) Minder, N. A.; Ono, S.; Chen, Z.; Facchetti, A.; Morpurgo, A. F. *Adv. Mater.* **2012**, *24*, 503.
- (14) Forrest, S. R.; Thompson, M. E. *Chem. Rev.* **2007**, *107*, 923.
- (15) Kaltenbrunner, M.; Sekitani, T.; Reeder, J.; Yokota, T.; Kuribara, K.; Tokuhara, T.; Drack, M.; Schwodiauer, R.; Graz, I.; Bauer-Gogonea, S.; Bauer, S.; Someya, T. *Nature* **2013**, *499*, 458.
- (16) Zhong, C.; Duan, C.; Huang, F.; Wu, H.; Cao, Y. *Chem. Mater.* **2010**, *23*, 326.
- (17) Facchetti, A. *Chem. Mater.* **2010**, *23*, 733.
- (18) Boudreault, P.-L. T.; Najari, A.; Leclerc, M. *Chem. Mater.* **2010**, *23*, 456.
- (19) Beaujuge, P. M.; Reynolds, J. R. *Chem. Rev.* **2010**, *110*, 268.
- (20) Thomas, S. W.; Joly, G. D.; Swager, T. M. *Chem. Rev.* **2007**, *107*, 1339.
- (21) Peet, J.; Kim, J. Y.; Coates, N. E.; Ma, W. L.; Moses, D.; Heeger, A. J.; Bazan, G. C. *Nat. Mater.* **2007**, *6*, 497.
- (22) He, Z.; Zhong, C.; Su, S.; Xu, M.; Wu, H.; Cao, Y. *Nat. Photonics* **2012**, *6*, 591.
- (23) Kagan, C. R.; Andry, P. *Thin-Film Transistors*; Marcel Dekker: New York, 2003.
- (24) Murphy, A. R.; Fréchet, J. M. J. *Chem. Rev.* **2007**, *107*, 1066.
- (25) Luzio, A.; Musumeci, C.; Newman, C. R.; Facchetti, A.; Marks, T. J.; Pignataro, B. *Chem. Mater.* **2011**, *23*, 1061.
- (26) Li, Y.; Wu, Y.; Ong, B. S. *J. Am. Chem. Soc.* **2005**, *127*, 3266.
- (27) Allard, S.; Forster, M.; Souharce, B.; Thiem, H.; Scherf, U. *Angew. Chem., Int. Ed.* **2008**, *47*, 4070.
- (28) Newman, C. R.; Frisbie, C. D.; da Silva Filho, D. A.; Brédas, J.-L.; Ewbank, P. C.; Mann, K. R. *Chem. Mater.* **2004**, *16*, 4436.
- (29) Dimitrakopoulos, C. D.; Malenfant, P. R. L. *Adv. Mater.* **2002**, *14*, 99.
- (30) Zaumseil, J.; Sirringhaus, H. *Chem. Rev.* **2007**, *107*, 1296.
- (31) Wu, Z.; Yang, T.; Ong, B. S.; Liang, Y.; Guo, X. *Org. Photon. Photovoltaics* **2014**, *2*, 19.
- (32) Coughlin, J. E.; Henson, Z. B.; Welch, G. C.; Bazan, G. C. *Acc. Chem. Res.* **2014**, *47*, 257.
- (33) Liang, Y.; Yu, L. *Acc. Chem. Res.* **2010**, *43*, 1227.
- (34) Diao, Y.; Tee, B. C. K.; Giri, G.; Xu, J.; Kim, D. H.; Becerril, H. A.; Stoltzenberg, R. M.; Lee, T. H.; Xue, G.; Mannsfeld, S. C. B.; Bao, Z. *Nat. Mater.* **2013**, *12*, 665.
- (35) Park, J. H.; Jung, E. H.; Jung, J. W.; Jo, W. H. *Adv. Mater.* **2013**, *25*, 2583.
- (36) Zhang, X.; Richter, L. J.; DeLongchamp, D. M.; Kline, R. J.; Hammond, M. R.; McCulloch, I.; Heeney, M.; Ashraf, R. S.; Smith, J. N.; Anthopoulos, T. D.; Schroeder, B.; Geerts, Y. H.; Fischer, D. A.; Toney, M. F. *J. Am. Chem. Soc.* **2011**, *133*, 15073.
- (37) Baeg, K.-J.; Kim, J.; Khim, D.; Caironi, M.; Kim, D.-Y.; You, I.-K.; Quinn, J. R.; Facchetti, A.; Noh, Y.-Y. *ACS Appl. Mater. Interfaces* **2011**, *3*, 3205.
- (38) Chua, L.-L.; Zaumseil, J.; Chang, J.-F.; Ou, E. C. W.; Ho, P. K. H.; Sirringhaus, H.; Friend, R. H. *Nature* **2005**, *434*, 194.
- (39) McCulloch, I.; Heeney, M.; Chabinyc, M. L.; DeLongchamp, D.; Kline, R. J.; Cölle, M.; Duffy, W.; Fischer, D.; Gundlach, D.; Hamadani, B.; Hamilton, R.; Richter, L.; Salleo, A.; Shkunov, M.; Sparrowe, D.; Tierney, S.; Zhang, W. *Adv. Mater.* **2009**, *21*, 1091.
- (40) Osaka, I.; McCullough, R. D. *Acc. Chem. Res.* **2008**, *41*, 1202.
- (41) Jones, B. A.; Facchetti, A.; Wasielewski, M. R.; Marks, T. J. *J. Am. Chem. Soc.* **2007**, *129*, 15259.
- (42) Chang, J.; Ye, Q.; Huang, K.-W.; Zhang, J.; Chen, Z.-K.; Wu, J.; Chi, C. *Org. Lett.* **2012**, *14*, 2964.
- (43) Brédas, J. L.; Street, G. B.; Themans, B.; Andre, J. M. *J. Chem. Phys.* **1985**, *83*, 1323.
- (44) Pomerantz, M. *Tetrahedron Lett.* **2003**, *44*, 1563.
- (45) Jackson, N. E.; Savoie, B. M.; Kohlstedt, K. L.; Olvera de la Cruz, M.; Schatz, G. C.; Chen, L. X.; Ratner, M. A. *J. Am. Chem. Soc.* **2013**, *135*, 10475.
- (46) Anthony, J. E. *Chem. Rev.* **2006**, *106*, 5028.
- (47) McCulloch, I.; Heeney, M.; Bailey, C.; Genevicius, K.; MacDonald, I.; Shkunov, M.; Sparrowe, D.; Tierney, S.; Wagner, R.; Zhang, W.; Chabinyc, M. L.; Kline, R. J.; McGehee, M. D.; Toney, M. F. *Nat. Mater.* **2006**, *5*, 328.
- (48) Nielsen, C. B.; Turbiez, M.; McCulloch, I. *Adv. Mater.* **2013**, *25*, 1859.
- (49) Kline, R. J.; McGehee, M. D.; Kadnikova, E. N.; Liu, J.; Fréchet, J. M. J. *Adv. Mater.* **2003**, *15*, 1519.
- (50) Guo, X.; Ortiz, R. P.; Zheng, Y.; Hu, Y.; Noh, Y.-Y.; Baeg, K.-J.; Facchetti, A.; Marks, T. J. *J. Am. Chem. Soc.* **2011**, *133*, 1405.
- (51) Park, J. H.; Jung, E. H.; Jung, J. W.; Jo, W. H. *Adv. Mater.* **2013**, *25*, 2583.
- (52) McCullough, R. D.; Tristram-Nagle, S.; Williams, S. P.; Lowe, R. D.; Jayaraman, M. *J. Am. Chem. Soc.* **1993**, *115*, 4910.
- (53) Ong, B. S.; Wu, Y.; Liu, P.; Gardner, S. *J. Am. Chem. Soc.* **2004**, *126*, 3378.
- (54) Tsao, H. N.; Cho, D. M.; Park, I.; Hansen, M. R.; Mavrinskiy, A.; Yoon, D. Y.; Graf, R.; Pisula, W.; Spiess, H. W.; Müllen, K. *J. Am. Chem. Soc.* **2011**, *133*, 2605.
- (55) Guo, X.; Zhou, N.; Lou, S. J.; Hennek, J. W.; Ortiz, R. P.; Butler, M. R.; Boudreault, P.-L. T.; Strzalka, J.; Morin, P.-O.; Leclerc, M.; López Navarrete, J. T.; Ratner, M. A.; Chen, L. X.; Chang, R. P. H.; Facchetti, A.; Marks, T. J. *J. Am. Chem. Soc.* **2012**, *134*, 18427.
- (56) Cheng, Y.-J.; Yang, S.-H.; Hsu, C.-S. *Chem. Rev.* **2009**, *109*, 5868.
- (57) Peet, J.; Heeger, A. J.; Bazan, G. C. *Acc. Chem. Res.* **2009**, *42*, 1700.
- (58) Green, M. A.; Emery, K.; Hishikawa, Y.; Warta, W.; Dunlop, E. D. *Prog. Photovoltaics: Res. Appl.* **2013**, *21*, 827.
- (59) Dou, L.; You, J.; Yang, J.; Chen, C.-C.; He, Y.; Murase, S.; Moriarty, T.; Emery, K.; Li, G.; Yang, Y. *Nat. Photonics* **2012**, *6*, 180.
- (60) Li, G.; Zhu, R.; Yang, Y. *Nat. Photonics* **2012**, *6*, 153.
- (61) Small, C. E.; Chen, S.; Subbiah, J.; Amb, C. M.; Tsang, S.-W.; Lai, T.-H.; Reynolds, J. R.; So, F. *Nat. Photonics* **2012**, *6*, 115.
- (62) Guo, X.; Zhou, N.; Lou, S. J.; Smith, J.; Tice, D. B.; Hennek, J. W.; Ortiz, R. P.; Navarrete, J. T. L.; Li, S.; Strzalka, J.; Chen, L. X.; Chang, R. P. H.; Facchetti, A.; Marks, T. J. *Nat. Photonics* **2013**, *7*, 825.
- (63) Kearns, D.; Calvin, M. *J. Chem. Phys.* **1958**, *29*, 950.
- (64) Tang, C. W. *Appl. Phys. Lett.* **1986**, *48*, 183.
- (65) Zhou, H.; Yang, L.; You, W. *Macromolecules* **2012**, *45*, 607.
- (66) Zimmerman, J. D.; Xiao, X.; Renshaw, C. K.; Wang, S.; Diev, V. V.; Thompson, M. E.; Forrest, S. R. *Nano Lett.* **2012**, *12*, 4366.
- (67) Lin, Y.; Ma, L.; Li, Y.; Liu, Y.; Zhu, D.; Zhan, X. *Adv. Energy Mater.* **2014**, DOI: 10.1002/aenm.201300626.
- (68) Hirade, M.; Adachi, C. *Appl. Phys. Lett.* **2011**, *99*, 153302.
- (69) Wagner, J.; Gruber, M.; Hinderhofer, A.; Wilke, A.; Bröker, B.; Frisch, J.; Amsalem, P.; Vollmer, A.; Opitz, A.; Koch, N.; Schreiber, F.; Brüttling, W. *Adv. Funct. Mater.* **2010**, *20*, 4295.
- (70) Yu, G.; Gao, J.; Hummelen, J. C.; Wudl, F.; Heeger, A. J. *Science* **1995**, *270*, 1789.
- (71) Halls, J. J. M.; Walsh, C. A.; Greenham, N. C.; Marseglia, E. A.; Friend, R. H.; Moratti, S. C.; Holmes, A. B. *Nature* **1995**, *376*, 498.
- (72) Park, S. H.; Roy, A.; Beaupre, S.; Cho, S.; Coates, N.; Moon, J. S.; Moses, D.; Leclerc, M.; Lee, K.; Heeger, A. J. *Nat. Photonics* **2009**, *3*, 297.
- (73) Coakley, K. M.; McGehee, M. D. *Chem. Mater.* **2004**, *16*, 4533.
- (74) Günes, S.; Neugebauer, H.; Sariciftci, N. S. *Chem. Rev.* **2007**, *107*, 1324.
- (75) Xiao, Z.; Yuan, Y.; Yang, B.; VanDerslice, J.; Chen, J.; Dyck, O.; Duscher, G.; Huang, J. *Adv. Mater.* **2014**, *26*, 3068.
- (76) Campoy-Quiles, M.; Ferenczi, T.; Agostinelli, T.; Etchegoin, P. G.; Kim, Y.; Anthopoulos, T. D.; Stavrinou, P. N.; Bradley, D. D. C.; Nelson, J. *Nat. Mater.* **2008**, *7*, 158.
- (77) Xu, Z.; Chen, L.-M.; Yang, G.; Huang, C.-H.; Hou, J.; Wu, Y.; Li, G.; Hsu, C.-S.; Yang, Y. *Adv. Funct. Mater.* **2009**, *19*, 1227.
- (78) Wei, Q.; Tajima, K.; Tong, Y.; Ye, S.; Hashimoto, K. *J. Am. Chem. Soc.* **2009**, *131*, 17597.
- (79) Kim, J. S.; Lee, Y.; Lee, J. H.; Park, J. H.; Kim, J. K.; Cho, K. *Adv. Mater.* **2010**, *22*, 1355.
- (80) Zhou, Y.; Yan, Q.; Zheng, Y.-Q.; Wang, J.-Y.; Zhao, D.; Pei, J. J. *Mater. Chem. A* **2013**, *1*, 6609.

- (81) Wang, H.; Gomez, E. D.; Kim, J.; Guan, Z.; Jaye, C.; Fischer, D. A.; Kahn, A.; Loo, Y.-L. *Chem. Mater.* **2011**, *23*, 2020.
- (82) Kim, M.; Kim, J.-H.; Choi, H. H.; Park, J. H.; Jo, S. B.; Sim, M.; Kim, J. S.; Jinnai, H.; Park, Y. D.; Cho, K. *Adv. Energy Mater.* **2014**, *4*, DOI 10.1002/aenm.201300612.
- (83) Coakley, K. M.; Liu, Y.; McGehee, M. D.; Frindell, K. L.; Stucky, G. D. *Adv. Funct. Mater.* **2003**, *13*, 301.
- (84) Greene, L. E.; Law, M.; Yuhas, B. D.; Yang, P. *J. Phys. Chem. C* **2007**, *111*, 18451.
- (85) Hochbaum, A. I.; Yang, P. *Chem. Rev.* **2009**, *110*, 527.
- (86) Thompson, B. C.; Fréchet, J. M. J. *Angew. Chem., Int. Ed.* **2008**, *47*, 58.
- (87) Sariciftci, N. S.; Smilowitz, L.; Heeger, A. J.; Wudl, F. *Science* **1992**, *258*, 1474.
- (88) Scharber, M. C.; Mühlbacher, D.; Koppe, M.; Denk, P.; Waldauf, C.; Heeger, A. J.; Brabec, C. J. *Adv. Mater.* **2006**, *18*, 789.
- (89) Kippelen, B.; Brédas, J.-L. *Energy Environ. Sci.* **2009**, *2*, 251.
- (90) Brabec, C. J.; Cravino, A.; Meissner, D.; Sariciftci, N. S.; Fromherz, T.; Rispens, M. T.; Sanchez, L.; Hummelen, J. C. *Adv. Funct. Mater.* **2001**, *11*, 374.
- (91) Malliaras, G. G.; Salem, J. R.; Brock, P. J.; Scott, J. C. *J. Appl. Phys.* **1998**, *84*, 1583.
- (92) Liu, J.; Shi, Y.; Yang, Y. *Adv. Funct. Mater.* **2001**, *11*, 420.
- (93) McNeill, C. R.; Halls, J. J. M.; Wilson, R.; Whiting, G. L.; Berkebile, S.; Ramsey, M. G.; Friend, R. H.; Greenham, N. C. *Adv. Funct. Mater.* **2008**, *18*, 2309.
- (94) Tada, A.; Geng, Y.; Wei, Q.; Hashimoto, K.; Tajima, K. *Nat. Mater.* **2011**, *10*, 450.
- (95) Ma, W.; Yang, C.; Gong, X.; Lee, K.; Heeger, A. J. *Adv. Funct. Mater.* **2005**, *15*, 1617.
- (96) Li, G.; Shrotriya, V.; Huang, J.; Yao, Y.; Moriarty, T.; Emery, K.; Yang, Y. *Nat. Mater.* **2005**, *4*, 864.
- (97) Li, W.; Hendriks, K. H.; Roelofs, W. S. C.; Kim, Y.; Wienk, M. M.; Janssen, R. A. J. *Adv. Mater.* **2013**, *25*, 3182.
- (98) Su, M.-S.; Kuo, C.-Y.; Yuan, M.-C.; Jeng, U. S.; Su, C.-J.; Wei, K.-H. *Adv. Mater.* **2011**, *23*, 3315.
- (99) Jiang, J.-M.; Yuan, M.-C.; Dinakaran, K.; Hariharan, A.; Wei, K.-H. *J. Mater. Chem. A* **2013**, *1*, 4415.
- (100) Guo, X.; Marks, T. J. *Proc. SPIE* **2013**, 8622, 86220K.
- (101) Yang, T.; Wang, M.; Duan, C.; Hu, X.; Huang, L.; Peng, J.; Huang, F.; Gong, X. *Energy Environ. Sci.* **2012**, *5*, 8208.
- (102) Servaites, J. D.; Ratner, M. A.; Marks, T. J. *Energ Environ. Sci.* **2011**, *4*, 4410.
- (103) DeLongchamp, D. M.; Kline, R. J.; Herzing, A. *Energ Environ. Sci.* **2012**, *5*, 5980.
- (104) Clarke, T. M.; Rodovsky, D. B.; Herzing, A. A.; Peet, J.; Dennler, G.; DeLongchamp, D.; Lungenschmied, C.; Mozer, A. J. *Adv. Energy Mater.* **2011**, *1*, 1062.
- (105) Amb, C. M.; Chen, S.; Graham, K. R.; Subbiah, J.; Small, C. E.; So, F.; Reynolds, J. R. *J. Am. Chem. Soc.* **2011**, *133*, 10062.
- (106) Chu, T.-Y.; Lu, J.; Beaupré, S.; Zhang, Y.; Pouliot, J.-R.; Wakim, S.; Zhou, J.; Leclerc, M.; Li, Z.; Ding, J.; Tao, Y. *J. Am. Chem. Soc.* **2011**, *133*, 4250.
- (107) Cates, N. C.; Gysel, R.; Beiley, Z.; Miller, C. E.; Toney, M. F.; Heeney, M.; McCulloch, I.; McGehee, M. D. *Nano Lett.* **2009**, *9*, 4153.
- (108) Zhou, N.; Guo, X.; Ortiz, R. P.; Li, S.; Zhang, S.; Chang, R. P. H.; Facchetti, A.; Marks, T. J. *Adv. Mater.* **2012**, *24*, 2242.
- (109) Woo, C. H.; Thompson, B. C.; Kim, B. J.; Toney, M. F.; Fréchet, J. M. J. *J. Am. Chem. Soc.* **2008**, *130*, 16324.
- (110) Roncali, J. *Chem. Rev.* **1997**, *97*, 173.
- (111) Dimitrov, S. D.; Bakulin, A. A.; Nielsen, C. B.; Schroeder, B. C.; Du, J.; Bronstein, H.; McCulloch, I.; Friend, R. H.; Durrant, J. R. *J. Am. Chem. Soc.* **2012**, *134*, 18189.
- (112) Chu, T.-Y.; Lu, J.; Beaupré, S.; Zhang, Y.; Pouliot, J.-R.; Zhou, J.; Najari, A.; Leclerc, M.; Tao, Y. *Adv. Funct. Mater.* **2012**, *22*, 2345.
- (113) Leong, W. L.; Welch, G. C.; Kaake, L. G.; Takacs, C. J.; Sun, Y.; Bazan, G. C.; Heeger, A. J. *Chem. Sci.* **2012**, *3*, 2103.
- (114) Horowitz, G.; Kouki, F.; Spearman, P.; Fichou, D.; Nogues, C.; Pan, X.; Garnier, F. *Adv. Mater.* **1996**, *8*, 242.
- (115) Zheng, Q.; Huang, J.; Sarjeant, A.; Katz, H. E. *J. Am. Chem. Soc.* **2008**, *130*, 14410.
- (116) Wang, Z.; Kim, C.; Facchetti, A.; Marks, T. J. *J. Am. Chem. Soc.* **2007**, *129*, 13362.
- (117) Katz, H. E.; Lovinger, A. J.; Johnson, J.; Kloc, C.; Siegrist, T.; Li, W.; Lin, Y. Y.; Dodabalapur, A. *Nature* **2000**, *404*, 478.
- (118) Schmidt, R.; Oh, J. H.; Sun, Y.-S.; Deppisch, M.; Krause, A.-M.; Radacki, K.; Braunschweig, H.; Könenmann, M.; Erk, P.; Bao, Z.; Würthner, F. *J. Am. Chem. Soc.* **2009**, *131*, 6215.
- (119) Durso, M.; Gentili, D.; Bettini, C.; Zanelli, A.; Cavallini, M.; De Angelis, F.; Grazia Lobello, M.; Biondo, V.; Muccini, M.; Capelli, R.; Melucci, M. *Chem. Commun.* **2013**, *49*, 4298.
- (120) Li, H.; Kim, F. S.; Ren, G.; Hollenbeck, E. C.; Subramaniyan, S.; Jenekhe, S. A. *Angew. Chem., Int. Ed.* **2013**, *52*, 5513.
- (121) Jones, B. A.; Facchetti, A.; Marks, T. J.; Wasielewski, M. R. *Chem. Mater.* **2007**, *19*, 2703.
- (122) Zhang, F.; Hu, Y.; Schuetzfort, T.; Di, C.-A.; Gao, X.; McNeill, C. R.; Thomsen, L.; Mannsfeld, S. C. B.; Yuan, W.; Sirringhaus, H.; Zhu, D. *J. Am. Chem. Soc.* **2013**, *135*, 2338.
- (123) Zhan, X.; Facchetti, A.; Barlow, S.; Marks, T. J.; Ratner, M. A.; Wasielewski, M. R.; Marder, S. R. *Adv. Mater.* **2011**, *23*, 268.
- (124) Anthony, J. E.; Facchetti, A.; Heeney, M.; Marder, S. R.; Zhan, X. *Adv. Mater.* **2010**, *22*, 3876.
- (125) Jung, B. J.; Tremblay, N. J.; Yeh, M.-L.; Katz, H. E. *Chem. Mater.* **2010**, *23*, 568.
- (126) Anthony, J. E. *Chem. Mater.* **2010**, *23*, 583.
- (127) Zhao, Y.; Guo, Y.; Liu, Y. *Adv. Mater.* **2013**, *25*, 5372.
- (128) Neuteboom, E. E.; Meskers, S. C. J.; van Hal, P. A.; van Duren, J. K. J.; Meijer, E. W.; Janssen, R. A. J.; Dupin, H.; Pourtois, G.; Cornil, J.; Lazzaroni, R.; Brédas, J.-L.; Beljon, D. *J. Am. Chem. Soc.* **2003**, *125*, 8625.
- (129) Carsten, B.; He, F.; Son, H. J.; Xu, T.; Yu, L. *Chem. Rev.* **2011**, *111*, 1493.
- (130) Letizia, J. A.; Salata, M. R.; Tribout, C. M.; Facchetti, A.; Ratner, M. A.; Marks, T. J. *J. Am. Chem. Soc.* **2008**, *130*, 9679.
- (131) Guo, X.; Kim, F. S.; Jenekhe, S. A.; Watson, M. D. *J. Am. Chem. Soc.* **2009**, *131*, 7206.
- (132) Berrouard, P.; Grenier, F. O.; Pouliot, J.-R. M.; Gagnon, E.; Tessier, C.; Leclerc, M. *Org. Lett.* **2010**, *13*, 38.
- (133) Qiao, Y.; Guo, Y.; Yu, C.; Zhang, F.; Xu, W.; Liu, Y.; Zhu, D. *J. Am. Chem. Soc.* **2012**, *134*, 4084.
- (134) Pron, A.; Leclerc, M. *Prog. Polym. Sci.* **2013**, *38*, 1815.
- (135) Kang, I.; Yun, H.-J.; Chung, D. S.; Kwon, S.-K.; Kim, Y.-H. *J. Am. Chem. Soc.* **2013**, *135*, 14896.
- (136) Kim, R.; Amegadze, P. S. K.; Kang, I.; Yun, H.-J.; Noh, Y.-Y.; Kwon, S.-K.; Kim, Y.-H. *Adv. Funct. Mater.* **2013**, *23*, 5719.
- (137) Lei, T.; Xia, X.; Wang, J.-Y.; Liu, C.; Pei, J. *J. Am. Chem. Soc.* **2014**, *136*, 2135.
- (138) Lee, J.; Han, A. R.; Yu, H.; Shin, T. J.; Yang, C.; Oh, J. H. *J. Am. Chem. Soc.* **2013**, *135*, 9540.
- (139) Cabanatos, C.; El Labban, A.; Bartelt, J. A.; Douglas, J. D.; Mateker, W. R.; Fréchet, J. M. J.; McGehee, M. D.; Beaujuge, P. M. *J. Am. Chem. Soc.* **2013**, *135*, 4656.
- (140) Hendriks, K. H.; Heintges, G. H. L.; Gevaerts, V. S.; Wienk, M. M.; Janssen, R. A. J. *Angew. Chem., Int. Ed.* **2013**, *52*, 8341.
- (141) Deng, Y.; Liu, J.; Wang, J.; Liu, L.; Li, W.; Tian, H.; Zhang, X.; Xie, Z.; Geng, Y.; Wang, F. *Adv. Mater.* **2014**, *26*, 471.
- (142) Facchetti, A. *Mater. Today* **2013**, *16*, 123.
- (143) Kardos, M. Vat Dye. German Patent 276357, June 14, 1913.
- (144) Herbst, W.; Hunger, K. *Industrial Organic Pigments; production, properties, applications*, 2nd ed.; Wiley-VCH: Weinheim, 1997.
- (145) Huang, C.; Barlow, S.; Marder, S. R. *J. Org. Chem.* **2011**, *76*, 2386.
- (146) Würthner, F. *Chem. Commun.* **2004**, 1564.
- (147) Zollinger, H. *Color Chemistry*, 3rd ed.; Wiley-VCH: Weinheim, 2003.
- (148) Struijk, C. W.; Sieval, A. B.; Dakhorst, J. E. J.; van Dijk, M.; Kimkes, P.; Koehorst, R. B. M.; Donker, H.; Schaafsma, T. J.; Picken, S. J.; van de Craats, A. M.; Warman, J. M.; Zuilhof, H.; Sudhölter, E. J. R. J. *Am. Chem. Soc.* **2000**, *122*, 11057.

- (149) Schmidt-Mende, L.; Fechtenkötter, A.; Müllen, K.; Moons, E.; Friend, R. H.; MacKenzie, J. D. *Science* **2001**, *293*, 1119.
- (150) Zhang, X.; Lu, Z.; Ye, L.; Zhan, C.; Hou, J.; Zhang, S.; Jiang, B.; Zhao, Y.; Huang, J.; Zhang, S.; Liu, Y.; Shi, Q.; Liu, Y.; Yao, J. *Adv. Mater.* **2013**, *25*, 5791.
- (151) Ego, C.; Marsitzky, D.; Becker, S.; Zhang, J.; Grimsdale, A. C.; Müllen, K.; MacKenzie, J. D.; Silva, C.; Friend, R. H. *J. Am. Chem. Soc.* **2002**, *125*, 437.
- (152) Würthner, F.; Stepanenko, V.; Chen, Z.; Saha-Möller, C. R.; Kocher, N.; Stalke, D. *J. Org. Chem.* **2004**, *69*, 7933.
- (153) Bohm, A.; Arms, H.; Henning, G.; Blasckha, P. B. *Chem. Abstr.* **1997**, *127*, 96569g.
- (154) Rajasingh, P.; Cohen, R.; Shirman, E.; Shimon, L. J. W.; Rybtchinski, B. *J. Org. Chem.* **2007**, *72*, S973.
- (155) Wescott, L. D.; Mattern, D. L. *J. Org. Chem.* **2003**, *68*, 10058.
- (156) Zhan, X.; Tan, Z. A.; Domercq, B.; An, Z.; Zhang, X.; Barlow, S.; Li, Y.; Zhu, D.; Kippelen, B.; Marder, S. R. *J. Am. Chem. Soc.* **2007**, *129*, 7246.
- (157) Zhang, L.; Di, C.-A.; Zhao, Y.; Guo, Y.; Sun, X.; Wen, Y.; Zhou, W.; Zhan, X.; Yu, G.; Liu, Y. *Adv. Mater.* **2010**, *22*, 3537.
- (158) Chen, Z.; Zheng, Y.; Yan, H.; Facchetti, A. *J. Am. Chem. Soc.* **2008**, *131*, 8.
- (159) Zhang, S.; Wen, Y.; Zhou, W.; Guo, Y.; Ma, L.; Zhao, X.; Zhao, Z.; Barlow, S.; Marder, S. R.; Liu, Y.; Zhan, X. *J. Polym. Sci., Part A: Polym. Chem.* **2013**, *51*, 1550.
- (160) Zhou, W.; Wen, Y.; Ma, L.; Liu, Y.; Zhan, X. *Macromolecules* **2012**, *45*, 4115.
- (161) Zhao, X.; Wen, Y.; Ren, L.; Ma, L.; Liu, Y.; Zhan, X. *J. Polym. Sci., Part A: Polym. Chem.* **2012**, *50*, 4266.
- (162) Popere, B. C.; Della Pelle, A. M.; Thayumanavan, S. *Macromolecules* **2011**, *44*, 4767.
- (163) Hahm, S. G.; Rho, Y.; Jung, J.; Kim, S. H.; Sajoto, T.; Kim, F. S.; Barlow, S.; Park, C. E.; Jenekhe, S. A.; Marder, S. R.; Ree, M. *Adv. Funct. Mater.* **2013**, *23*, 2060.
- (164) Hou, J.; Tan, Z. a.; Yan, Y.; He, Y.; Yang, C.; Li, Y. *J. Am. Chem. Soc.* **2006**, *128*, 4911.
- (165) Liu, Y.; Larsen-Olsen, T. T.; Zhao, X.; Andreasen, B.; Søndergaard, R. R.; Helgesen, M.; Norrman, K.; Jørgensen, M.; Krebs, F. C.; Zhan, X. *Sol. Energy Mater. Sol. Cells* **2013**, *112*, 157.
- (166) Cheng, P.; Ye, L.; Zhao, X.; Hou, J.; Li, Y.; Zhan, X. *Energy Environ. Sci.* **2013**, *7*, 1351.
- (167) Zhan, X.; Tan, Z. A.; Zhou, E.; Li, Y.; Misra, R.; Grant, A.; Domercq, B.; Zhang, X.-H.; An, Z.; Zhang, X.; Barlow, S.; Kippelen, B.; Marder, S. R. *J. Mater. Chem.* **2009**, *19*, 5794.
- (168) Huang, J.; Wu, Y.; Fu, H.; Zhan, X.; Yao, J.; Barlow, S.; Marder, S. R. *J. Phys. Chem. A* **2009**, *113*, 5039.
- (169) Kozma, E.; Kotowski, D.; Bertini, F.; Luzzati, S.; Catellani, M. *Polymer* **2010**, *51*, 2264.
- (170) Zhou, E.; Cong, J.; Wei, Q.; Tajima, K.; Yang, C.; Hashimoto, K. *Angew. Chem., Int. Ed.* **2011**, *50*, 2799.
- (171) Zhou, Y.; Kurosawa, T.; Ma, W.; Guo, Y.; Fang, L.; Vandewal, K.; Diao, Y.; Wang, C.; Yan, Q.; Reinspach, J.; Mei, J.; Appleton, A. L.; Koleilat, G. I.; Gao, Y.; Mannsfeld, S. C. B.; Salleo, A.; Ade, H.; Zhao, D.; Bao, Z. *Adv. Mater.* **2014**, *26*, 3767.
- (172) Lei, T.; Cao, Y.; Fan, Y.; Liu, C.-J.; Yuan, S.-C.; Pei, J. *J. Am. Chem. Soc.* **2011**, *133*, 6099.
- (173) Fang, L.; Zhou, Y.; Yao, Y.-X.; Diao, Y.; Lee, W.-Y.; Appleton, A. L.; Allen, R.; Reinspach, J.; Mannsfeld, S. C. B.; Bao, Z. *Chem. Mater.* **2013**, *25*, 4874.
- (174) Zhou, E.; Tajima, K.; Yang, C.; Hashimoto, K. *J. Mater. Chem.* **2010**, *20*, 2362.
- (175) Usta, H.; Newman, C.; Chen, Z.; Facchetti, A. *Adv. Mater.* **2012**, *24*, 3678.
- (176) Eversloh, C. L.; Li, C.; Müllen, K. *Org. Lett.* **2011**, *13*, 4148.
- (177) Yuan, Z.; Xiao, Y.; Yang, Y.; Xiong, T. *Macromolecules* **2011**, *44*, 1788.
- (178) Wong, W. W. H.; Singh, T. B.; Vak, D.; Pisula, W.; Yan, C.; Feng, X.; Williams, E. L.; Chan, K. L.; Mao, Q.; Jones, D. J.; Ma, C.-Q.; Müllen, K.; Bäuerle, P.; Holmes, A. B. *Adv. Funct. Mater.* **2010**, *20*, 927.
- (179) Guo, X.; Watson, M. D. *Org. Lett.* **2008**, *10*, 5333.
- (180) Zhou, W.; Zhang, Z.-G.; Ma, L.; Li, Y.; Zhan, X. *Sol. Energy Mater. Sol. Cells* **2013**, *112*, 13.
- (181) Zhang, Z.-G.; Zhang, S.; Min, J.; Chui, C.; Zhang, J.; Zhang, M.; Li, Y. *Macromolecules* **2011**, *45*, 113.
- (182) Sommer, M.; Huettner, S.; Thelakkat, M. *J. Mater. Chem.* **2010**, *20*, 10788.
- (183) Huttner, S.; Sommer, M.; Thelakkat, M. *Appl. Phys. Lett.* **2008**, *92*, 093302.
- (184) Finlayson, C. E.; Friend, R. H.; Otten, M. B. J.; Schwartz, E.; Cornelissen, J. J. L. M.; Nolte, R. J. M.; Rowan, A. E.; Samori, P.; Palermo, V.; Liscio, A.; Peneva, K.; Müllen, K.; Trapani, S.; Beljonne, D. *Adv. Funct. Mater.* **2008**, *18*, 3947.
- (185) Liu, Y.; Yang, C.; Li, Y.; Li, Y.; Wang, S.; Zhuang, J.; Liu, H.; Wang, N.; He, X.; Li, Y.; Zhu, D. *Macromolecules* **2005**, *38*, 716.
- (186) Mikroyannidis, J. A.; Stylianakis, M. M.; Sharma, G. D.; Balraju, P.; Roy, M. S. *J. Phys. Chem. C* **2009**, *113*, 7904.
- (187) Raj, M. R.; Ramkumar, S.; Anandan, S. *RSC Adv.* **2013**, *3*, 5108.
- (188) Röger, C.; Miloslavina, Y.; Brunner, D.; Holzwarth, A. R.; Würthner, F. *J. Am. Chem. Soc.* **2008**, *130*, 5929.
- (189) Lindner, S. M.; Hüttner, S.; Chiche, A.; Thelakkat, M.; Krausch, G. *Angew. Chem., Int. Ed.* **2006**, *45*, 3364.
- (190) Zhang, Q.; Cirpan, A.; Russell, T. P.; Emrick, T. *Macromolecules* **2009**, *42*, 1079.
- (191) Huettner, S.; Sommer, M.; Hodgkiss, J.; Kohn, P.; Thurn-Albrecht, T.; Friend, R. H.; Steiner, U.; Thelakkat, M. *ACS Nano* **2011**, *5*, 3506.
- (192) Huang, C.; Potscavage, W. J.; Tiwari, S. P.; Sutcu, S.; Barlow, S.; Kippelen, B.; Marder, S. R. *Polym. Chem.* **2012**, *3*, 2996.
- (193) Thalacker, C.; Röger, C.; Würthner, F. *J. Org. Chem.* **2006**, *71*, 8098.
- (194) Vollmann, H.; Becker, H.; Corell, M.; Streeck, H. *Liebigs Ann.* **1937**, *531*, 1.
- (195) Gsänger, M.; Oh, J. H.; Könemann, M.; Höffken, H. W.; Krause, A.-M.; Bao, Z.; Würthner, F. *Angew. Chem., Int. Ed.* **2010**, *49*, 740.
- (196) Guo, X.; Kim, F. S.; Seger, M. J.; Jenekhe, S. A.; Watson, M. D. *Chem. Mater.* **2012**, *24*, 1434.
- (197) Yan, H.; Chen, Z.; Zheng, Y.; Newman, C.; Quinn, J. R.; Dotz, F.; Kastler, M.; Facchetti, A. *Nature* **2009**, *457*, 679.
- (198) Durban, M. M.; Kazarinoff, P. D.; Luscombe, C. K. *Macromolecules* **2010**, *43*, 6348.
- (199) Yuan, M.; Durban, M. M.; Kazarinoff, P. D.; Zeigler, D. F.; Rice, A. H.; Segawa, Y.; Luscombe, C. K. *J. Polym. Sci., Part A: Polym. Chem.* **2013**, *51*, 4061.
- (200) Huang, H.; Chen, Z.; Ortiz, R. P.; Newman, C.; Usta, H.; Lou, S.; Youn, J.; Noh, Y.-Y.; Baeg, K.-J.; Chen, L. X.; Facchetti, A.; Marks, T. J. *Am. Chem. Soc.* **2012**, *134*, 10966.
- (201) Hwang, Y.-J.; Ren, G.; Murari, N. M.; Jenekhe, S. A. *Macromolecules* **2012**, *45*, 9056.
- (202) Hwang, Y.-J.; Murari, N. M.; Jenekhe, S. A. *Polym. Chem.* **2013**, *4*, 3187.
- (203) Sajoto, T.; Tiwari, S. P.; Li, H.; Risko, C.; Barlow, S.; Zhang, Q.; Cho, J.-Y.; Brédas, J.-L.; Kippelen, B.; Marder, S. R. *Polymer* **2012**, *53*, 1072.
- (204) Kola, S.; Kim, J. H.; Ireland, R.; Yeh, M.-L.; Smith, K.; Guo, W.; Katz, H. E. *ACS Macro Lett.* **2013**, *2*, 664.
- (205) Guo, X.; Watson, M. D. *Macromolecules* **2011**, *44*, 6711.
- (206) Durban, M. M.; Kazarinoff, P. D.; Segawa, Y.; Luscombe, C. K. *Macromolecules* **2011**, *44*, 4721.
- (207) Kim, Y.; Hong, J.; Oh, J. H.; Yang, C. *Chem. Mater.* **2013**, *25*, 3251.
- (208) Lei, T.; Cao, Y.; Zhou, X.; Peng, Y.; Bian, J.; Pei, J. *Chem. Mater.* **2012**, *24*, 1762.
- (209) Kim, F. S.; Guo, X.; Watson, M. D.; Jenekhe, S. A. *Adv. Mater.* **2010**, *22*, 478.
- (210) Guo, X.; Quinn, J.; Chen, Z.; Usta, H.; Zheng, Y.; Xia, Y.; Hennek, J. W.; Ortiz, R. P.; Marks, T. J.; Facchetti, A. *J. Am. Chem. Soc.* **2013**, *135*, 1986.
- (211) Gu, C.; Hu, W.; Yao, J.; Fu, H. *Chem. Mater.* **2013**, *25*, 2178.

- (212) Chen, H.; Guo, Y.; Mao, Z.; Yu, G.; Huang, J.; Zhao, Y.; Liu, Y. *Chem. Mater.* **2013**, *25*, 3589.
- (213) Baeg, K.-J.; Khim, D.; Jung, S.-W.; Kang, M.; You, I.-K.; Kim, D.-Y.; Facchetti, A.; Noh, Y.-Y. *Adv. Mater.* **2012**, *24*, 5433.
- (214) Fabiano, S.; Chen, Z.; Vahedi, S.; Facchetti, A.; Pignataro, B.; Loi, M. A. *J. Mater. Chem.* **2011**, *21*, 5891.
- (215) Szendrei, K.; Jarzab, D.; Chen, Z.; Facchetti, A.; Loi, M. A. *J. Mater. Chem.* **2010**, *20*, 1317.
- (216) Moore, J. R.; Albert-Seifried, S.; Rao, A.; Massip, S.; Watts, B.; Morgan, D. J.; Friend, R. H.; McNeill, C. R.; Sirringhaus, H. *Adv. Energy Mater.* **2011**, *1*, 230.
- (217) Schubert, M.; Dolfen, D.; Frisch, J.; Roland, S.; Steyrlleuthner, R.; Stiller, B.; Chen, Z.; Scherf, U.; Koch, N.; Facchetti, A.; Neher, D. *Adv. Energy Mater.* **2012**, *2*, 369.
- (218) Liang, Y.; Xu, Z.; Xia, J.; Tsai, S.-T.; Wu, Y.; Li, G.; Ray, C.; Yu, L. *Adv. Mater.* **2010**, *22*, E135.
- (219) Tang, Y.; McNeill, C. R. *J. Polym. Sci., Part B: Polym. Phys.* **2013**, *51*, 403.
- (220) Zhou, N.; Lin, H.; Lou, S. J.; Yu, X.; Guo, P.; Manley, E. F.; Loser, S.; Hartnett, P.; Huang, H.; Wasielewski, M. R.; Chen, L. X.; Chang, R. P. H.; Facchetti, A.; Marks, T. J. *Adv. Energy Mater.* **2013**, DOI: 10.1002/aenm.201300785.
- (221) Mori, D.; Benten, H.; Okada, I.; Ohkita, H.; Ito, S. *Adv. Energy Mater.* **2013**, DOI: 10.1002/aenm.201301006.
- (222) Earmme, T.; Hwang, Y.-J.; Murari, N. M.; Subramaniyan, S.; Jenekhe, S. A. *J. Am. Chem. Soc.* **2013**, *135*, 14960.
- (223) Zhou, E.; Cong, J.; Zhao, M.; Zhang, L.; Hashimoto, K.; Tajima, K. *Chem. Commun.* **2012**, *48*, 5283.
- (224) Zhou, E.; Cong, J.; Hashimoto, K.; Tajima, K. *Adv. Mater.* **2013**, *25*, 6991.
- (225) Nakabayashi, K.; Mori, H. *Macromolecules* **2012**, *45*, 9618.
- (226) Zhao, Z.; Zhang, F.; Zhang, X.; Yang, X.; Li, H.; Gao, X.; Di, C.-A.; Zhu, D. *Macromolecules* **2013**, *46*, 7705.
- (227) Lee, S. J.; Park, J. S.; Yoon, K.-J.; Kim, Y.-I.; Jin, S.-H.; Kang, S. K.; Gal, Y.-S.; Kang, S.; Lee, J. Y.; Kang, J.-W.; Lee, S.-H.; Park, H.-D.; Kim, J.-J. *Adv. Funct. Mater.* **2008**, *18*, 3922.
- (228) Chen, S.-C.; Zheng, Q.; Zhang, Q.; Cai, D.; Wang, J.; Yin, Z.; Tang, C. *J. Polym. Sci., Part A: Polym. Chem.* **2013**, *51*, 1999.
- (229) Fukutomi, Y.; Nakano, M.; Hu, J.-Y.; Osaka, I.; Takimiya, K. *J. Am. Chem. Soc.* **2013**, *135*, 11445.
- (230) Arnold, F. E.; Van Deusen, R. L. *Macromolecules* **1969**, *2*, 497.
- (231) Babel, A.; Jenekhe, S. A. *J. Am. Chem. Soc.* **2003**, *125*, 13656.
- (232) Li, Y.; Zhang, G.; Yang, G.; Guo, Y.; Di, C. a.; Chen, X.; Liu, Z.; Liu, H.; Xu, Z.; Xu, W.; Fu, H.; Zhang, D. *J. Org. Chem.* **2013**, *78*, 2926.
- (233) Li, Y.; Zhang, G.; Liu, Z.; Chen, X.; Wang, J.; Di, C. a.; Zhang, D. *Macromolecules* **2013**, *46*, 5504.
- (234) Hopff, H.; Doswald, P.; Manukian, B. K. *Helv. Chim. Acta* **1961**, *44*, 1231.
- (235) Rhee, T. H.; Choi, T.; Chung, E. Y.; Suh, D. H. *Macromol. Chem. Phys.* **2001**, *202*, 906.
- (236) Kola, S.; Tremblay, N. J.; Yeh, M.-L.; Katz, H. E.; Kirschner, S. B.; Reich, D. H. *ACS Macro Lett.* **2011**, *1*, 136.
- (237) Zhou, X.; Cao, Y.; Wang, X.-Y.; Guo, Z.-H.; Wang, J.-Y.; Pei, J. *Asian J. Org. Chem.* **2014**, *3*, 209.
- (238) Witzel, S.; Ott, C.; Klemm, E. *Macromol. Rapid Commun.* **2005**, *26*, 889.
- (239) Dierschke, F.; Jacob, J.; Müllen, K. *Synth. Met.* **2006**, *156*, 433.
- (240) Allen, C. F. H.; Frame, G. F.; Wilson, C. V. *J. Org. Chem.* **1941**, *6*, 732.
- (241) Guo, X.; Ortiz, R. P.; Zheng, Y.; Kim, M.-G.; Zhang, S.; Hu, Y.; Lu, G.; Facchetti, A.; Marks, T. J. *J. Am. Chem. Soc.* **2011**, *133*, 13685.
- (242) Chen, D.; Zhao, Y.; Zhong, C.; Gao, S.; Yu, G.; Liu, Y.; Qin, J. *J. Mater. Chem.* **2012**, *22*, 14639.
- (243) Huang, J.; Zhao, Y.; He, W.; Jia, H.; Lu, Z.; Jiang, B.; Zhan, C.; Pei, Q.; Liu, Y.; Yao, J. *Polym. Chem.* **2012**, *3*, 2832.
- (244) Kim, J.; Baeg, K.-J.; Khim, D.; James, D. T.; Kim, J.-S.; Lim, B.; Yun, J.-M.; Jeong, H.-G.; Amegadze, P. S. K.; Noh, Y.-Y.; Kim, D.-Y. *Chem. Mater.* **2013**, *25*, 1572.
- (245) Khim, D.; Han, H.; Baeg, K.-J.; Kim, J.; Kwak, S.-W.; Kim, D.-Y.; Noh, Y.-Y. *Adv. Mater.* **2013**, *25*, 4302.
- (246) Khim, D.; Baeg, K.-J.; Kim, J.; Yeo, J.-S.; Kang, M.; Amegadzea, P. S. K.; Kim, M.-G.; Cho, J.; Lee, J. H.; Kim, D.-Y.; Noh, Y.-Y. *J. Mater. Chem.* **2012**, *22*, 16979.
- (247) Xin, H.; Guo, X.; Kim, F. S.; Ren, G.; Watson, M. D.; Jenekhe, S. A. *J. Mater. Chem.* **2009**, *19*, 5303.
- (248) Xin, H.; Guo, X.; Ren, G.; Watson, M. D.; Jenekhe, S. A. *Adv. Energy Mater.* **2012**, *2*, 575.
- (249) Lee, J. Y.; Song, K. W.; Ku, J. R.; Sung, T. H.; Moon, D. K. *Sol. Energy Mater. Sol. Cells* **2011**, *95*, 3377.
- (250) Lee, J. Y.; Lee, S. M.; Song, K. W.; Moon, D. K. *Eur. Polym. J.* **2012**, *48*, 532.
- (251) Zhang, M.; Guo, X.; Zhang, Z.-G.; Li, Y. *Polymer* **2011**, *52*, 5464.
- (252) Yue, W.; Larsen-Olsen, T. T.; Hu, X.; Shi, M.; Chen, H.; Hinge, M.; Fojan, P.; Krebs, F. C.; Yu, D. *J. Mater. Chem. A* **2013**, *1*, 1785.
- (253) Zhang, G.; Fu, Y.; Zhang, Q.; Xie, Z. *Macromol. Chem. Phys.* **2010**, *211*, 2596.
- (254) Huang, J.; Wang, X.; Zhan, C.; Zhao, Y.; Sun, Y.; Pei, Q.; Liu, Y.; Yao, J. *Polym. Chem.* **2013**, *4*, 2174.
- (255) Kim, J.; Yeo, J.-S.; Jeong, H.-G.; Yun, J.-M.; Kim, Y.-A.; Kim, D.-Y. *Sol. Energy Mater. Sol. Cells* **2014**, *125*, 253.
- (256) You, J.; Dou, L.; Yoshimura, K.; Kato, T.; Ohya, K.; Moriarty, T.; Emery, K.; Chen, C.-C.; Gao, J.; Li, G.; Yang, Y. *Nat. Commun.* **2013**, *4*, 1446.
- (257) Zhang, Q. T.; Tour, J. M. *J. Am. Chem. Soc.* **1997**, *119*, 5065.
- (258) Sicé, J. *J. Org. Chem.* **1954**, *19*, 70.
- (259) Dimmler, M.; Eilingsfeld, H. 2,5-Diphenylthiophene-3,4-dicarboximides. German Patent 2538951, March 10, 1977.
- (260) Nielsen, C. B.; Bjornholm, T. *Org. Lett.* **2004**, *6*, 3381.
- (261) Berrouard, P.; Dufresne, S.; Pron, A.; Veilleux, J.; Leclerc, M. *J. Org. Chem.* **2012**, *77*, 8167.
- (262) Guo, X.; Xin, H.; Kim, F. S.; Liyanage, A. D. T.; Jenekhe, S. A.; Watson, M. D. *Macromolecules* **2010**, *44*, 269.
- (263) Berrouard, P.; Najari, A.; Pron, A.; Gendron, D.; Morin, P.-O.; Pouliot, J.-R.; Veilleux, J.; Leclerc, M. *Angew. Chem., Int. Ed.* **2012**, *51*, 2068.
- (264) Wu, Q.; Wang, M.; Qiao, X.; Xiong, Y.; Huang, Y.; Gao, X.; Li, H. *Macromolecules* **2013**, *46*, 3887.
- (265) Yuan, J.; Zang, Y.; Dong, H.; Liu, G.; Di, C.; Li, Y.; Ma, W. *Polym. Chem.* **2013**, *4*, 4199.
- (266) Woo, C. H.; Beaujuge, P. M.; Holcombe, T. W.; Lee, O. P.; Fréchet, J. M. J. *J. Am. Chem. Soc.* **2010**, *132*, 15547.
- (267) Deng, Y.; Chen, Y.; Zhang, X.; Tian, H.; Bao, C.; Yan, D.; Geng, Y.; Wang, F. *Macromolecules* **2012**, *45*, 8621.
- (268) Shi, S.; Xie, X.; Qu, R.; Chen, S.; Wang, L.; Wang, M.; Wang, H.; Li, X.; Yu, G. *RSC Adv.* **2013**, *3*, 18944.
- (269) Grenier, F.; Berrouard, P.; Pouliot, J.-R.; Tseng, H.-R.; Heeger, A. J.; Leclerc, M. *Polym. Chem.* **2013**, *4*, 1836.
- (270) Kim, G.; Han, A. R.; Lee, H. R.; Lee, J.; Oh, J. H.; Yang, C. *Chem. Commun.* **2014**, *50*, 2180.
- (271) Zou, Y.; Najari, A.; Berrouard, P.; Beaupré, S.; Réda Aïch, B.; Tao, Y.; Leclerc, M. *J. Am. Chem. Soc.* **2010**, *132*, 5330.
- (272) Zhang, Y.; Hau, S. K.; Yip, H.-L.; Sun, Y.; Acton, O.; Jen, A. K. Y. *Chem. Mater.* **2010**, *22*, 2696.
- (273) Zhang, G.; Fu, Y.; Zhang, Q.; Xie, Z. *Chem. Commun.* **2010**, *46*, 4997.
- (274) Piliego, C.; Holcombe, T. W.; Douglas, J. D.; Woo, C. H.; Beaujuge, P. M.; Fréchet, J. M. J. *J. Am. Chem. Soc.* **2010**, *132*, 7595.
- (275) Aich, B. R.; Lu, J.; Beaupré, S.; Leclerc, M.; Tao, Y. *Org. Electron.* **2012**, *13*, 1736.
- (276) Hoke, E. T.; Vandewal, K.; Bartelt, J. A.; Mateker, W. R.; Douglas, J. D.; Noriega, R.; Graham, K. R.; Fréchet, J. M. J.; Salleo, A.; McGehee, M. D. *Adv. Energy Mater.* **2013**, *3*, 220.
- (277) Bartelt, J. A.; Beiley, Z. M.; Hoke, E. T.; Mateker, W. R.; Douglas, J. D.; Collins, B. A.; Tumbleston, J. R.; Graham, K. R.; Amassian, A.; Ade, H.; Fréchet, J. M. J.; Toney, M. F.; McGehee, M. D. *Adv. Energy Mater.* **2013**, *3*, 364.

- (278) Griffini, G.; Douglas, J. D.; Piliego, C.; Holcombe, T. W.; Turri, S.; Fréchet, J. M. J.; Mynar, J. L. *Adv. Mater.* **2011**, *23*, 1660.
- (279) Zhou, E.; Cong, J.; Hashimoto, K.; Tajima, K. *Energy Environ. Sci.* **2012**, *5*, 9756.
- (280) Yuan, J.; Zhai, Z.; Dong, H.; Li, J.; Jiang, Z.; Li, Y.; Ma, W. *Adv. Funct. Mater.* **2013**, *23*, 885.
- (281) Warnan, J.; Cabanetos, C.; Bude, R.; El Labban, A.; Li, L.; Beaujuge, P. M. *Chem. Mater.* **2014**, *26*, 2829.
- (282) Vanormelingen, W.; Kesters, J.; Verstappen, P.; Drijkoningen, J.; Kudrjasova, J.; Koudjina, S.; Liegeois, V.; Champagne, B.; Manca, J.; Lutzen, L.; Vanderzande, D.; Maes, W. *J. Mater. Chem. A* **2014**, *2*, 7535.
- (283) Najari, A.; Beaupré, S.; Berrouard, P.; Zou, Y.; Pouliot, J.-R.; Lepage-Pérusse, C.; Leclerc, M. *Adv. Funct. Mater.* **2011**, *21*, 718.
- (284) Chen, Y.-L.; Chang, C.-Y.; Cheng, Y.-J.; Hsu, C.-S. *Chem. Mater.* **2012**, *24*, 3964.
- (285) Hou, J.; Chen, H.-Y.; Zhang, S.; Li, G.; Yang, Y. *J. Am. Chem. Soc.* **2008**, *130*, 16144.
- (286) Allard, N.; Beaupré, S.; Aich, B. R. d.; Najari, A.; Tao, Y.; Leclerc, M. *Macromolecules* **2011**, *44*, 7184.
- (287) Chen, S.; Small, C. E.; Amb, C. M.; Subbiah, J.; Lai, T.-h.; Tsang, S.-W.; Manders, J. R.; Reynolds, J. R.; So, F. *Adv. Energy Mater.* **2012**, *2*, 1333.
- (288) Manders, J. R.; Tsang, S.-W.; Hartel, M. J.; Lai, T.-H.; Chen, S.; Amb, C. M.; Reynolds, J. R.; So, F. *Adv. Funct. Mater.* **2013**, *23*, 2993.
- (289) Zhong, H.; Li, Z.; Deledalle, F.; Fregoso, E. C.; Shahid, M.; Fei, Z.; Nielsen, C. B.; Yaacobi-Gross, N.; Rossbauer, S.; Anthopoulos, T. D.; Durrant, J. R.; Heeney, M. *J. Am. Chem. Soc.* **2013**, *135*, 2040.
- (290) Zhang, Y.; Zou, J.; Yip, H.-L.; Sun, Y.; Davies, J. A.; Chen, K.-S.; Acton, O.; Jen, A. K. *J. Mater. Chem.* **2011**, *21*, 3895.
- (291) Li, Z.; Tsang, S.-W.; Du, X.; Scoles, L.; Robertson, G.; Zhang, Y.; Toll, F.; Tao, Y.; Lu, J.; Ding, J. *Adv. Funct. Mater.* **2011**, *21*, 3331.
- (292) Najari, A.; Berrouard, P.; Ottone, C.; Boivin, M.; Zou, Y.; Gendron, D.; Caron, W.-O.; Legros, P.; Allen, C. N.; Sadki, S.; Leclerc, M. *Macromolecules* **2012**, *45*, 1833.
- (293) Donaghey, J. E.; Ashraf, R. S.; Kim, Y.; Huang, Z. G.; Nielsen, C. B.; Zhang, W.; Schroeder, B.; Grenier, C. R. G.; Brown, C. T.; D'Angelo, P.; Smith, J.; Watkins, S.; Song, K.; Anthopoulos, T. D.; Durrant, J. R.; Williams, C. K.; McCulloch, I. *J. Mater. Chem.* **2011**, *21*, 18744.
- (294) Yuan, M.-C.; Chiu, M.-Y.; Liu, S.-P.; Chen, C.-M.; Wei, K.-H. *Macromolecules* **2010**, *43*, 6936.
- (295) Jo, J.; Pron, A.; Berrouard, P.; Leong, W. L.; Yuen, J. D.; Moon, J. S.; Leclerc, M.; Heeger, A. J. *Adv. Energy Mater.* **2012**, *2*, 1397.
- (296) Wang, D. H.; Pron, A.; Leclerc, M.; Heeger, A. J. *Adv. Funct. Mater.* **2013**, *23*, 1297.
- (297) Chen, G.-Y.; Cheng, Y.-H.; Chou, Y.-J.; Su, M.-S.; Chen, C.-M.; Wei, K.-H. *Chem. Commun.* **2011**, *47*, 5064.
- (298) Kuo, C.-Y.; Su, M.-S.; Chen, G.-Y.; Ku, C.-S.; Lee, H.-Y.; Wei, K.-H. *Energy Environ. Sci.* **2011**, *4*, 2316.
- (299) Abdalla, M. A.; Bayer, J.; Rädler, J. O.; Müllen, K. *Angew. Chem., Int. Ed.* **2004**, *43*, 3967.
- (300) Sirringhaus, H. *Adv. Mater.* **2009**, *21*, 3859.
- (301) Usta, H.; Risko, C.; Wang, Z.; Huang, H.; Deliomeroglu, M. K.; Zhukhovitskiy, A.; Faccetti, A.; Marks, T. J. *J. Am. Chem. Soc.* **2009**, *131*, 5586.
- (302) Gendron, D.; Morin, P.-O.; Berrouard, P.; Allard, N.; Aich, B. R.; Garon, C. N.; Tao, Y.; Leclerc, M. *Macromolecules* **2011**, *44*, 7188.
- (303) Ko, S.; Hoke, E. T.; Pandey, L.; Hong, S.; Mondal, R.; Risko, C.; Yi, Y.; Noriega, R.; McGehee, M. D.; Brédas, J.-L.; Salleo, A.; Bao, Z. *J. Am. Chem. Soc.* **2012**, *134*, 5222.
- (304) Meng, H.; Wudl, F. *Macromolecules* **2001**, *34*, 1810.
- (305) Braunecker, W. A.; Owczarczyk, Z. R.; Garcia, A.; Kopidakis, N.; Larsen, R. E.; Hammond, S. R.; Ginley, D. S.; Olson, D. C. *Chem. Mater.* **2012**, *24*, 1346.
- (306) Hsu, D.-T.; Lin, C.-H. *J. Org. Chem.* **2009**, *74*, 9180.
- (307) Douglas, J. D.; Griffini, G.; Holcombe, T. W.; Young, E. P.; Lee, O. P.; Chen, M. S.; Fréchet, J. M. J. *Macromolecules* **2012**, *45*, 4069.
- (308) Braunecker, W. A.; Oosterhout, S. D.; Owczarczyk, Z. R.; Larsen, R. E.; Larson, B. W.; Ginley, D. S.; Boltalina, O. V.; Strauss, S. H.; Kopidakis, N.; Olson, D. C. *Macromolecules* **2013**, *46*, 3367.
- (309) Wu, Y.; Jing, Y.; Guo, X.; Zhang, S.; Zhang, M.; Huo, L.; Hou, J. *Polym. Chem.* **2013**, *4*, 536.
- (310) Li, H.; Sun, S.; Salim, T.; Bomma, S.; Grimsdale, A. C.; Lam, Y. M. *J. Polym. Sci., Part A: Polym. Chem.* **2012**, *50*, 250.
- (311) Farnum, D. G.; Mehta, G.; Moore, G. G. I.; Siegal, F. P. *Tetrahedron Lett.* **1974**, *15*, 2549.
- (312) Iqbal, A.; Cassar, L. Process for Dyeing High-Molecular Organic Material, and Novel Polycyclic Pigments. U.S. Patent 4415685, Nov 15, 1983.
- (313) Hao, Z.; Iqbal, A. *Chem. Soc. Rev.* **1997**, *26*, 203.
- (314) Chan, W. K.; Chen, Y.; Peng, Z.; Yu, L. *J. Am. Chem. Soc.* **1993**, *115*, 11735.
- (315) Wienk, M. M.; Turbiez, M.; Gilot, J.; Janssen, R. A. J. *Adv. Mater.* **2008**, *20*, 2556.
- (316) Li, Y.; Sonar, P.; Murphy, L.; Hong, W. *Energy Environ. Sci.* **2013**, *6*, 1684.
- (317) Qu, S.; Tian, H. *Chem. Commun.* **2012**, *48*, 3039.
- (318) Rochat, A. C.; Cassar, L.; Iqbal, A. Preparation of Pyrrolo[3,4-c] pyrroles. U.S. Patent 4579949, Apr 1, 1986.
- (319) Bürgi, L.; Turbiez, M.; Pfeiffer, R.; Bienewald, F.; Kirner, H.-J.; Winnewisser, C. *Adv. Mater.* **2008**, *20*, 2217.
- (320) Bijleveld, J. C.; Zoombelt, A. P.; Mathijssen, S. G. J.; Wienk, M. M.; Turbiez, M.; de Leeuw, D. M.; Janssen, R. A. J. *J. Am. Chem. Soc.* **2009**, *131*, 16616.
- (321) Shahid, M.; McCarthy-Ward, T.; Labram, J.; Rossbauer, S.; Domingo, E. B.; Watkins, S. E.; Stingelin, N.; Anthopoulos, T. D.; Heeney, M. *Chem. Sci.* **2012**, *3*, 181.
- (322) Kaur, M.; Seul Yang, D.; Shin, J.; Wan Lee, T.; Choi, K.; Ju Cho, M.; Hoon Choi, D. *Chem. Commun.* **2013**, *49*, 5495.
- (323) Mei, J.; Kim, D. H.; Ayzner, A. L.; Toney, M. F.; Bao, Z. *J. Am. Chem. Soc.* **2011**, *133*, 20130.
- (324) Lee, J.; Han, A. R.; Kim, J.; Kim, Y.; Oh, J. H.; Yang, C. *J. Am. Chem. Soc.* **2012**, *134*, 20713.
- (325) Wu, P.-T.; Kim, F. S.; Jenekhe, S. A. *Chem. Mater.* **2011**, *23*, 4618.
- (326) Li, Y.; Singh, S. P.; Sonar, P. *Adv. Mater.* **2010**, *22*, 4862.
- (327) Chen, Z.; Lee, M. J.; Shahid Ashraf, R.; Gu, Y.; Albert-Seifried, S.; Meedom Nielsen, M.; Schroeder, B.; Anthopoulos, T. D.; Heeney, M.; McCulloch, I.; Sirringhaus, H. *Adv. Mater.* **2012**, *24*, 647.
- (328) Li, J.; Zhao, Y.; Tan, H. S.; Guo, Y.; Di, C.-A.; Yu, G.; Liu, Y.; Lin, M.; Lim, S. H.; Zhou, Y.; Su, H.; Ong, B. S. *Sci. Rep.* **2012**, *2*, 754.
- (329) Bijleveld, J. C.; Verstrijden, R. A. M.; Wienk, M. M.; Janssen, R. A. J. *J. Mater. Chem.* **2011**, *21*, 9224.
- (330) Li, Y.; Sonar, P.; Singh, S. P.; Soh, M. S.; van Meurs, M.; Tan, J. *J. Am. Chem. Soc.* **2011**, *133*, 2198.
- (331) Ha, J. S.; Kim, K. H.; Choi, D. H. *J. Am. Chem. Soc.* **2011**, *133*, 10364.
- (332) Yi, Z.; Sun, X.; Zhao, Y.; Guo, Y.; Chen, X.; Qin, J.; Yu, G.; Liu, Y. *Chem. Mater.* **2012**, *24*, 4350.
- (333) Li, Y.; Sonar, P.; Singh, S. P.; Zeng, W.; Soh, M. S. *J. Mater. Chem.* **2011**, *21*, 10829.
- (334) Jung, J. W.; Liu, F.; Russell, T. P.; Jo, W. H. *Energy Environ. Sci.* **2012**, *5*, 6857.
- (335) Li, J.; Qin, F.; Li, C. M.; Bao, Q.; Chan-Park, M. B.; Zhang, W.; Qin, J.; Ong, B. S. *Chem. Mater.* **2008**, *20*, 2057.
- (336) Liu, J.; Zhang, R.; Sauvé, G.; Kowalewski, T.; McCullough, R. D. *J. Am. Chem. Soc.* **2008**, *130*, 13167.
- (337) Nelson, T. L.; Young, T. M.; Liu, J.; Mishra, S. P.; Belot, J. A.; Balliet, C. L.; Javier, A. E.; Kowalewski, T.; McCullough, R. D. *Adv. Mater.* **2010**, *22*, 4617.
- (338) Chen, H.; Guo, Y.; Yu, G.; Zhao, Y.; Zhang, J.; Gao, D.; Liu, H.; Liu, Y. *Adv. Mater.* **2012**, *24*, 4618.
- (339) Kronemeijer, A. J.; Gili, E.; Shahid, M.; Rivnay, J.; Salleo, A.; Heeney, M.; Sirringhaus, H. *Adv. Mater.* **2012**, *24*, 1558.
- (340) Kang, I.; An, T. K.; Hong, J.-a.; Yun, H.-J.; Kim, R.; Chung, D. S.; Park, C. E.; Kim, Y.-H.; Kwon, S.-K. *Adv. Mater.* **2013**, *25*, 524.
- (341) Bronstein, H.; Chen, Z.; Ashraf, R. S.; Zhang, W.; Du, J.; Durrant, J. R.; Shakya Tuladhar, P.; Song, K.; Watkins, S. E.; Geerts, Y.; Wienk, M. M.; Janssen, R. A. J.; Anthopoulos, T.; Sirringhaus, H.; Heeney, M.; McCulloch, I. *J. Am. Chem. Soc.* **2011**, *133*, 3272.

- (342) Sonar, P.; Singh, S. P.; Li, Y.; Ooi, Z.-E.; Ha, T.-J.; Wong, I.; Soh, M. S.; Dodabalapur, A. *Energy Environ. Sci.* **2011**, *4*, 2288.
- (343) Lee, H.-S.; Lee, J. S.; Cho, S.; Kim, H.; Kwak, K.-W.; Yoon, Y.; Son, S. K.; Kim, H.; Ko, M. J.; Lee, D.-K.; Kim, J. Y.; Park, S.; Choi, D. H.; Oh, S. Y.; Cho, J. H.; Kim, B. *J. Phys. Chem. C* **2012**, *116*, 26204.
- (344) Lee, D. H.; Shin, J.; Cho, M. J.; Choi, D. H. *Chem. Commun.* **2013**, *49*, 3896.
- (345) Lee, J. B.; Kim, K. H.; Hong, C. S.; Choi, D. H. *J. Polym. Sci., Part A: Polym. Chem.* **2012**, *50*, 2809.
- (346) Jiang, Y.; Mei, J.; Ayzner, A. L.; Toney, M. F.; Bao, Z. *Chem. Commun.* **2012**, *48*, 7286.
- (347) Jiang, Y.; Okamoto, T.; Becerril, H. A.; Hong, S.; Tang, M. L.; Mayer, A. C.; Parmer, J. E.; McGehee, M. D.; Bao, Z. *Macromolecules* **2010**, *43*, 6361.
- (348) Chen, H.; Guo, Y.; Sun, X.; Gao, D.; Liu, Y.; Yu, G. *J. Polym. Sci., Part A: Polym. Chem.* **2013**, *51*, 2208.
- (349) Zou, Y.; Gendron, D.; Badrou-Aïch, R. d.; Najari, A.; Tao, Y.; Leclerc, M. *Macromolecules* **2009**, *42*, 2891.
- (350) Ashraf, R. S.; Chen, Z.; Leem, D. S.; Bronstein, H.; Zhang, W.; Schroeder, B.; Geerts, Y.; Smith, J.; Watkins, S.; Anthopoulos, T. D.; Sirringhaus, H.; de Mello, J. C.; Heeney, M.; McCulloch, I. *Chem. Mater.* **2010**, *23*, 768.
- (351) Yamaguchi, S.; Tamao, K. *J. Chem. Soc., Dalton Trans.* **1998**, 3693.
- (352) Wang, X.; Luo, H.; Sun, Y.; Zhang, M.; Li, X.; Yu, G.; Liu, Y.; Li, Y.; Wang, H. *J. Polym. Sci., Part A: Polym. Chem.* **2012**, *50*, 371.
- (353) Yuen, J. D.; Fan, J.; Seifter, J.; Lim, B.; Hufschmid, R.; Heeger, A. J.; Wudl, F. *J. Am. Chem. Soc.* **2011**, *133*, 20799.
- (354) Sonar, P.; Singh, S. P.; Li, Y.; Soh, M. S.; Dodabalapur, A. *Adv. Mater.* **2010**, *22*, 5409.
- (355) Chen, Z.; Lemke, H.; Albert-Seifried, S.; Caironi, M.; Nielsen, M. M.; Heeney, M.; Zhang, W.; McCulloch, I.; Sirringhaus, H. *Adv. Mater.* **2010**, *22*, 2371.
- (356) Patra, A.; Bendikov, M. *J. Mater. Chem.* **2010**, *20*, 422.
- (357) Lee, J.; Cho, S.; Seo, J. H.; Anant, P.; Jacob, J.; Yang, C. *J. Mater. Chem.* **2012**, *22*, 1504.
- (358) Mohebbi, A. R.; Wudl, F. *Chem.—Eur. J.* **2011**, *17*, 2642.
- (359) Mohebbi, A. R.; Yuen, J.; Fan, J.; Munoz, C.; Wang, M. f.; Shirazi, R. S.; Seifter, J.; Wudl, F. *Adv. Mater.* **2011**, *23*, 4644.
- (360) Hong, W.; Sun, B.; Aziz, H.; Park, W.-T.; Noh, Y.-Y.; Li, Y. *Chem. Commun.* **2012**, *48*, 8413.
- (361) Zoombelt, A. P.; Mathijssen, S. G. J.; Turbiez, M. G. R.; Wienk, M. M.; Janssen, R. A. *J. Mater. Chem.* **2010**, *20*, 2240.
- (362) Li, Y.; Sun, B.; Sonar, P.; Singh, S. P. *Org. Electron.* **2012**, *13*, 1606.
- (363) Mei, J.; Bao, Z. *Chem. Mater.* **2014**, *26*, 604.
- (364) Lei, T.; Wang, J.-Y.; Pei, J. *Chem. Mater.* **2013**, *26*, 594.
- (365) Kanimozhhi, C.; Yaacobi-Gross, N.; Chou, K. W.; Amassian, A.; Anthopoulos, T. D.; Patil, S. *J. Am. Chem. Soc.* **2012**, *134*, 16532.
- (366) Dhar, J.; Venkatramiah, N.; A, A.; Patil, S. *J. Mater. Chem. C* **2014**, *2*, 3457.
- (367) Jung, J. W.; Liu, F.; Russell, T. P.; Jo, W. H. *Chem. Commun.* **2013**, *49*, 8495.
- (368) Sun, B.; Hong, W.; Yan, Z.; Aziz, H.; Li, Y. *Adv. Mater.* **2014**, *26*, 2636.
- (369) Li, W.; Furlan, A.; Hendriks, K. H.; Wienk, M. M.; Janssen, R. A. *J. Am. Chem. Soc.* **2013**, *135*, 5529.
- (370) Chen, M. S.; Lee, O. P.; Niskala, J. R.; Yiu, A. T.; Tassone, C. J.; Schmidt, K.; Beaujuge, P. M.; Onishi, S. S.; Toney, M. F.; Zettl, A.; Fréchet, J. M. J. *J. Am. Chem. Soc.* **2013**, *135*, 19229.
- (371) Schmidt, K.; Tassone, C. J.; Niskala, J. R.; Yiu, A. T.; Lee, O. P.; Weiss, T. M.; Wang, C.; Fréchet, J. M. J.; Beaujuge, P. M.; Toney, M. F. *Adv. Mater.* **2014**, *26*, 300.
- (372) Yiu, A. T.; Beaujuge, P. M.; Lee, O. P.; Woo, C. H.; Toney, M. F.; Fréchet, J. M. J. *J. Am. Chem. Soc.* **2011**, *134*, 2180.
- (373) Lei, T.; Dou, J.-H.; Pei, J. *Adv. Mater.* **2012**, *24*, 6457.
- (374) Meager, I.; Ashraf, R. S.; Mollinger, S.; Schroeder, B. C.; Bronstein, H.; Beatrup, D.; Vezie, M. S.; Kirchartz, T.; Salleo, A.; Nelson, J.; McCulloch, I. *J. Am. Chem. Soc.* **2013**, *135*, 11537.
- (375) Li, J.; Ong, K.-H.; Lim, S.-L.; Ng, G.-M.; Tan, H.-S.; Chen, Z.-K. *Chem. Commun.* **2011**, *47*, 9480.
- (376) Zeng, Z.; Li, Y.; Deng, J.; Huang, Q.; Peng, Q. *J. Mater. Chem. A* **2014**, *2*, 653.
- (377) Huo, L.; Hou, J.; Chen, H.-Y.; Zhang, S.; Jiang, Y.; Chen, T. L.; Yang, Y. *Macromolecules* **2009**, *42*, 6564.
- (378) Li, W.; Roelofs, W. S. C.; Turbiez, M.; Wienk, M. M.; Janssen, R. A. *J. Adv. Mater.* **2014**, *26*, 3304.
- (379) Blouin, N.; Michaud, A.; Gendron, D.; Wakim, S.; Blair, E.; Neagu-Plesu, R.; Belletête, M.; Durocher, G.; Tao, Y.; Leclerc, M. *J. Am. Chem. Soc.* **2007**, *130*, 732.
- (380) Jo, J.; Gendron, D.; Najari, A.; Moon, J. S.; Cho, S.; Leclerc, M.; Heeger, A. J. *Appl. Phys. Lett.* **2010**, *97*, 203303.
- (381) Deng, Y.; Chen, Y.; Liu, J.; Liu, L.; Tian, H.; Xie, Z.; Geng, Y.; Wang, F. *ACS Appl. Mater. Interfaces* **2013**, *5*, 5741.
- (382) Li, Z.; Zhang, Y.; Tsang, S.-W.; Du, X.; Zhou, J.; Tao, Y.; Ding, J. *J. Phys. Chem. C* **2011**, *115*, 18002.
- (383) Venkataraman, D.; Yurt, S.; Venkatraman, B. H.; Gavvalapalli, N. *J. Phys. Chem. Lett.* **2010**, *1*, 947.
- (384) Jung, J. W.; Jo, J. W.; Liu, F.; Russell, T. P.; Jo, W. H. *Chem. Commun.* **2012**, *48*, 6933.
- (385) Huo, L.; Zhang, S.; Guo, X.; Xu, F.; Li, Y.; Hou, J. *Angew. Chem., Int. Ed.* **2011**, *50*, 9697.
- (386) Dou, L.; Gao, J.; Richard, E.; You, J.; Chen, C.-C.; Cha, K. C.; He, Y.; Li, G.; Yang, Y. *J. Am. Chem. Soc.* **2012**, *134*, 10071.
- (387) Dou, L.; Chang, W.-H.; Gao, J.; Chen, C.-C.; You, J.; Yang, Y. *Adv. Mater.* **2013**, *25*, 825.
- (388) Chang, W.-H.; Gao, J.; Dou, L.; Chen, C.-C.; Liu, Y.; Yang, Y. *Adv. Energy Mater.* **2013**, DOI: 10.1002/aenm.201300864.
- (389) Bijleveld, J. C.; Gevaerts, V. S.; Di Nuzzo, D.; Turbiez, M.; Mathijssen, S. G. J.; de Leeuw, D. M.; Wienk, M. M.; Janssen, R. A. *J. Adv. Mater.* **2010**, *22*, E242.
- (390) Li, W.; Hendriks, K. H.; Furlan, A.; Roelofs, W. S. C.; Meskers, S. C. J.; Wienk, M. M.; Janssen, R. A. *J. Adv. Mater.* **2014**, *26*, 1565.
- (391) Jo, J.; Pouliot, J.-R.; Wynands, D.; Collins, S. D.; Kim, J. Y.; Nguyen, T. L.; Woo, H. Y.; Sun, Y.; Leclerc, M.; Heeger, A. J. *Adv. Mater.* **2013**, *25*, 4783.
- (392) Li, W.; Furlan, A.; Roelofs, W. S. C.; Hendriks, K.; Van Pruisen, G. W. P.; Wienk, M. M.; Janssen, R. A. *J. Chem. Commun.* **2014**, *50*, 679.
- (393) Li, W.; Lee, T.; Oh, S. J.; Kagan, C. R. *ACS Appl. Mater. Interfaces* **2011**, *3*, 3874.
- (394) Falzon, M.-F.; Zoombelt, A. P.; Wienk, M. M.; Janssen, R. A. *J. Phys. Chem. Chem. Phys.* **2011**, *13*, 8931.
- (395) Fitzhugh, E. W. *Artists' Pigments*; Oxford University Press: New York, 1997.
- (396) Stalder, R.; Mei, J.; Graham, K. R.; Estrada, L. A.; Reynolds, J. R. *Chem. Mater.* **2013**, *26*, 664.
- (397) Mei, J.; Graham, K. R.; Stalder, R.; Reynolds, J. R. *Org. Lett.* **2010**, *12*, 660.
- (398) Deng, P.; Zhang, Q. *Polym. Chem.* **2014**, *5*, 3298.
- (399) Rivnay, J.; Toney, M. F.; Zheng, Y.; Kauvar, I. V.; Chen, Z.; Wagner, V.; Facchetti, A.; Salleo, A. *Adv. Mater.* **2010**, *22*, 4359.
- (400) Shin, J.; Um, H. A.; Lee, D. H.; Lee, T. W.; Cho, M. J.; Choi, D. H. *Polym. Chem.* **2013**, *4*, 5688.
- (401) Sonar, P.; Tan, H.-S.; Sun, S.; Lam, Y. M.; Dodabalapur, A. *Polym. Chem.* **2013**, *4*, 1983.
- (402) Allard, N.; Najari, A.; Pouliot, J.-R.; Pron, A.; Grenier, F.; Leclerc, M. *Polym. Chem.* **2012**, *3*, 2875.
- (403) Lei, T.; Dou, J.-H.; Ma, Z.-J.; Yao, C.-H.; Liu, C.-J.; Wang, J.-Y.; Pei, J. *J. Am. Chem. Soc.* **2012**, *134*, 20025.
- (404) Lei, T.; Dou, J.-H.; Ma, Z.-J.; Liu, C.-J.; Wang, J.-Y.; Pei, J. *Chem. Sci.* **2013**, *4*, 2447.
- (405) Zhang, G.; Fu, Y.; Xie, Z.; Zhang, Q. *Macromolecules* **2011**, *44*, 1414.
- (406) Liu, B.; Zou, Y.; Peng, B.; Zhao, B.; Huang, K.; He, Y.; Pan, C. *Polym. Chem.* **2011**, *2*, 1156.
- (407) Cao, K.; Wu, Z.; Li, S.; Sun, B.; Zhang, G.; Zhang, Q. *J. Polym. Sci., Part A: Polym. Chem.* **2013**, *51*, 94.

- (408) Veldman, D.; Meskers, S. C. J.; Janssen, R. A. *J. Adv. Funct. Mater.* **2009**, *19*, 1939.
- (409) Ma, Z.; Wang, E.; Jarvid, M. E.; Henriksson, P.; Inganas, O.; Zhang, F.; Andersson, M. R. *J. Mater. Chem.* **2012**, *22*, 2306.
- (410) Zhuang, W.; Bolognesi, M.; Seri, M.; Henriksson, P.; Gedefaw, D.; Kroon, R.; Jarvid, M.; Lundin, A.; Wang, E.; Muccini, M.; Andersson, M. R. *Macromolecules* **2013**, *46*, 8488.
- (411) Yang, Y.; Wu, R.; Wang, X.; Xu, X.; Li, Z.; Li, K.; Peng, Q. *Chem. Commun.* **2014**, *50*, 439.
- (412) Ma, Z.; Dang, D.; Tang, Z.; Gedefaw, D.; Bergqvist, J.; Zhu, W.; Mammo, W.; Andersson, M. R.; Inganäs, O.; Zhang, F.; Wang, E. *Adv. Energy Mater.* **2013**, DOI: 10.1002/aenm.201301455.
- (413) Wang, E.; Ma, Z.; Zhang, Z.; Henriksson, P.; Inganas, O.; Zhang, F.; Andersson, M. R. *Chem. Commun.* **2011**, *47*, 4908.
- (414) Kim, D. H.; Ayzner, A. L.; Appleton, A. L.; Schmidt, K.; Mei, J.; Toney, M. F.; Bao, Z. *Chem. Mater.* **2012**, *25*, 431.
- (415) Barbarella, G.; Zambianchi, M.; Antolini, L.; Ostoja, P.; Maccagnani, P.; Bongini, A.; Marseglia, E. A.; Tedesco, E.; Gigli, G.; Cingolani, R. *J. Am. Chem. Soc.* **1999**, *121*, 8920.
- (416) Wang, Y.; Watson, M. D. *Macromolecules* **2008**, *41*, 8643.
- (417) Kim, D. H.; Lee, B.-L.; Moon, H.; Kang, H. M.; Jeong, E. J.; Park, J.-I.; Han, K.-M.; Lee, S.; Yoo, B. W.; Koo, B. W.; Kim, J. Y.; Lee, W. H.; Cho, K.; Becerril, H. A.; Bao, Z. *J. Am. Chem. Soc.* **2009**, *131*, 6124.
- (418) Jung, E. H.; Jo, W. H. *Energy Environ. Sci.* **2014**, *7*, 650.
- (419) Wang, E.; Ma, Z.; Zhang, Z.; Vandewal, K.; Henriksson, P.; Inganäs, O.; Zhang, F.; Andersson, M. R. *J. Am. Chem. Soc.* **2011**, *133*, 14244.
- (420) Ma, Z.; Sun, W.; Himmelberger, S.; Vandewal, K.; Tang, Z.; Bergqvist, J.; Salleo, A.; Andreassen, J. W.; Inganas, O.; Andersson, M. R.; Muller, C.; Zhang, F.; Wang, E. *Energy Environ. Sci.* **2014**, *7*, 361.
- (421) Xu, X.; Cai, P.; Lu, Y.; Choon, N. S.; Chen, J.; Hu, X.; Ong, B. S. *J. Polym. Sci., Part A: Polym. Chem.* **2013**, *51*, 424.
- (422) Stalder, R.; Grand, C.; Subbiah, J.; So, F.; Reynolds, J. R. *J. Polym. Chem.* **2012**, *3*, 89.
- (423) Dang, D.; Chen, W.; Yang, R.; Zhu, W.; Mammo, W.; Wang, E. *Chem. Commun.* **2013**, *49*, 9335.
- (424) Sun, W.; Ma, Z.; Dang, D.; Zhu, W.; Andersson, M. R.; Zhang, F.; Wang, E. *J. Mater. Chem. A* **2013**, *1*, 11141.
- (425) Wang, C.; Zhao, B.; Cao, Z.; Shen, P.; Tan, Z.; Li, X.; Tan, S. *Chem. Commun.* **2013**, *49*, 3857.
- (426) Hou, J.; Park, M.-H.; Zhang, S.; Yao, Y.; Chen, L.-M.; Li, J.-H.; Yang, Y. *Macromolecules* **2008**, *41*, 6012.
- (427) Stalder, R.; Mei, J.; Subbiah, J.; Grand, C.; Estrada, L. A.; So, F.; Reynolds, J. R. *Macromolecules* **2011**, *44*, 6303.
- (428) Ashraf, R. S.; Kronemeijer, A. J.; James, D. I.; Sirringhaus, H.; McCulloch, I. *Chem. Commun.* **2012**, *48*, 3939.
- (429) Dutta, G. K.; Han, A. R.; Lee, J.; Kim, Y.; Oh, J. H.; Yang, C. *Adv. Funct. Mater.* **2013**, *23*, 5317.
- (430) Chen, M. S.; Niskala, J. R.; Unruh, D. A.; Chu, C. K.; Lee, O. P.; Fréchet, J. M. J. *Chem. Mater.* **2013**, *25*, 4088.
- (431) Yan, Z.; Sun, B.; Li, Y. *Chem. Commun.* **2013**, *49*, 3790.
- (432) Lei, T.; Dou, J.-H.; Cao, X.-Y.; Wang, J.-Y.; Pei, J. *J. Am. Chem. Soc.* **2013**, *135*, 12168.
- (433) Lei, T.; Dou, J.-H.; Cao, X.-Y.; Wang, J.-Y.; Pei, J. *Adv. Mater.* **2013**, *25*, 6589.
- (434) Li, S.; Yuan, Z.; Yuan, J.; Deng, P.; Zhang, Q.; Sun, B. *J. Mater. Chem. A* **2014**, *2*, 5427.
- (435) Irimia-Vladu, M.; Glowacki, E. D.; Troshin, P. A.; Schwabegger, G.; Leonat, L.; Susarova, D. K.; Krystal, O.; Ullah, M.; Kanbur, Y.; Bodea, M. A.; Razumov, V. F.; Sitter, H.; Bauer, S.; Sariciftci, N. S. *Adv. Mater.* **2014**, *24*, 375.
- (436) Guo, C.; Sun, B.; Quinn, J.; Yan, Z.; Li, Y. *J. Mater. Chem. C* **2014**, *2*, 4289.
- (437) Greenhalgh, C. W.; Carey, J. L.; Newton, D. F. *Dyes Pigm.* **1980**, *1*, 103.
- (438) Cui, W.; Yuen, J.; Wudl, F. *Macromolecules* **2011**, *44*, 7869.
- (439) Hong, W.; Guo, C.; Li, Y.; Zheng, Y.; Huang, C.; Lu, S.; Facchetti, A. *J. Mater. Chem.* **2012**, *22*, 22282.
- (440) Van Pruissen, G. W. P.; Pidko, E. A.; Wienk, M. M.; Janssen, R. A. *J. Mater. Chem. C* **2013**, *2*, 731.
- (441) Street, R. A.; Salleo, A. *Appl. Phys. Lett.* **2002**, *81*, 2887.
- (442) Deng, P.; Liu, L.; Ren, S.; Li, H.; Zhang, Q. *Chem. Commun.* **2012**, *48*, 6960.
- (443) Rumer, J. W.; Levick, M.; Dai, S.-Y.; Rossbauer, S.; Huang, Z.; Biniek, L.; Anthopoulos, T. D.; Durrant, J. R.; Procter, D. J.; McCulloch, I. *Chem. Commun.* **2013**, *49*, 4465.
- (444) Cui, W.; Wudl, F. *Macromolecules* **2013**, *46*, 7232.
- (445) Hong, W.; Sun, B.; Guo, C.; Yuen, J.; Li, Y.; Lu, S.; Huang, C.; Facchetti, A. *Chem. Commun.* **2013**, *49*, 484.
- (446) Yue, W.; Huang, X.; Yuan, J.; Ma, W.; Krebs, F. C.; Yu, D. J. *Mater. Chem. A* **2013**, *1*, 10116.
- (447) Li, H.; Kim, F. S.; Ren, G.; Jenekhe, S. A. *J. Am. Chem. Soc.* **2013**, *135*, 14920.
- (448) Wang, H.; Shi, Q.; Lin, Y.; Fan, H.; Cheng, P.; Zhan, X.; Li, Y.; Zhu, D. *Macromolecules* **2011**, *44*, 4213.
- (449) Wang, L.; Cai, D.; Zheng, Q.; Tang, C.; Chen, S.-C.; Yin, Z. *ACS Macro Lett.* **2013**, *2*, 605.
- (450) Li, D.; Qian, G.; Wang, Z. Y. *Polymer* **2013**, *54*, 5543.
- (451) Dutta, T.; Li, Y.; Thornton, A. L.; Zhu, D.-M.; Peng, Z. *J. Polym. Sci., Part A: Polym. Chem.* **2013**, *51*, 3818.
- (452) Kim, S.-O.; Kim, Y.-S.; Yun, H.-J.; Kang, I.; Yoon, Y.; Shin, N.; Son, H. J.; Kim, H.; Ko, M. J.; Kim, B.; Kim, K.; Kim, Y.-H.; Kwon, S.-K. *Macromolecules* **2013**, *46*, 3861.
- (453) Tamilavan, V.; Song, M.; Agneeswari, R.; Kang, J.-W.; Hwang, D.-H.; Hyun, M. H. *Polymer* **2013**, *54*, 6125.
- (454) Cao, J.; Liao, Q.; Du, X.; Chen, J.; Xiao, Z.; Zuo, Q.; Ding, L. *Energy Environ. Sci.* **2013**, *6*, 3224.
- (455) Poduval, M. K.; Burrezo, P. M.; Casado, J.; López Navarrete, J. T.; Ortiz, R. P.; Kim, T.-H. *Macromolecules* **2013**, *46*, 9220.
- (456) Cao, Y.; Guo, Z.-H.; Chen, Z.-Y.; Yuan, J.-S.; Dou, J.-H.; Zheng, Y.-Q.; Wang, J.-Y.; Pei, J. *Polym. Chem.* **2014**, *5*, 5369.
- (457) Liu, M.; Liang, Y.; Chen, P.; Chen, D.; Liu, K.; Li, Y.; Liu, S.; Gong, X.; Huang, F.; Su, S.-J.; Cao, Y. *J. Mater. Chem. A* **2014**, *2*, 321.
- (458) Fürstenwerth, H. Pyrrolo[3,2-b]pyrrolidine Pigments for Plastic Resins. German Patent 3525109 A1, Jan 15, 1987.
- (459) Welterlich, I.; Charov, O.; Tieke, B. *Macromolecules* **2012**, *45*, 4511.
- (460) Kirkus, M.; Knippenberg, S.; Beljonne, D.; Cornil, J.; Janssen, R. A. J.; Meskers, S. C. J. *J. Phys. Chem. A* **2013**, *117*, 2782.
- (461) Lu, S.; Drees, M.; Yao, Y.; Boudinet, D.; Yan, H.; Pan, H.; Wang, J.; Li, Y.; Usta, H.; Facchetti, A. *Macromolecules* **2013**, *46*, 3895.
- (462) Rumer, J. W.; Dai, S.-Y.; Levick, M.; Kim, Y.; Madec, M.-B.; Ashraf, R. S.; Huang, Z.; Rossbauer, S.; Schroeder, B.; Biniek, L.; Watkins, S. E.; Anthopoulos, T. D.; Janssen, R. A. J.; Durrant, J. R.; Procter, D. J.; McCulloch, I. *J. Mater. Chem. C* **2013**, *1*, 2711.
- (463) Cai, Z.; Guo, Y.; Yang, S.; Peng, Q.; Luo, H.; Liu, Z.; Zhang, G.; Liu, Y.; Zhang, D. *Chem. Mater.* **2013**, *25*, 471.
- (464) von Pechmann, H. *Chem. Ber.* **1882**, *15*, 881.
- (465) Cai, Z.; Luo, H.; Qi, P.; Wang, J.; Zhang, G.; Liu, Z.; Zhang, D. *Macromolecules* **2014**, *47*, 2899.
- (466) Wang, J.; Chen, X.; Cai, Z.; Luo, H.; Li, Y.; Liu, Z.; Zhang, G.; Zhang, D. *Polym. Chem.* **2013**, *4*, 5283.